# Evolving ocean basins in the Early Cretaceous greenhouse: A climate model-proxy synthesis of circulation, surface temperatures and carbon burial

Dissertation
zur Erlangung des Doktorgrades
der Mathematisch-Naturwissenschaftlichen Fakultät
der Christian-Albrechts-Universität zu Kiel

vorgelegt von
Sebastian Steinig

Kiel, 2019

Erster Gutacher: Prof. Dr. Martin Frank

Zweite Gutachterin: Prof. Dr. Birgit Schneider

Tag der mündlichen Prüfung: 02.08.2019

# Abstract

Greenhouse climates with global mean temperatures significantly higher than today prevailed during large parts of the geological history. They provide direct evidence for the adaptation of the climate system to enhanced greenhouse gas forcing during the past and represent the only possibility to constrain model-derived projections of future anthropogenic warming. The Early Cretaceous (∼145-100.5 Ma) provides a special opportunity to test our understanding of past greenhouse dynamics, as the long-term warmth was punctuated by severe perturbations of the global carbon cycle and episodes of transient cooling. Young and restricted ocean basins, emerging from the break-up of Gondwana, are a possible driver of both short- and long-term carbon cycle dynamics due to their enhanced organic carbon burial potential.

This thesis aims to better constrain the main drivers of the Early Cretaceous greenhouse climate and to assess how they differed from the present-day dynamics. Dedicated climate model simulations of the Early Cretaceous were integrated with paleoceanographic records of water mass mixing, surface temperatures and organic carbon burial to assess both the causes for the mean state warming, as well as to reconstruct the tectonically driven ocean circulation and carbon cycle changes.

In a first step, the individual processes that controlled the simulated global mean warming and the meridional temperature gradient (MTG) response to the increased greenhouse gas forcing and changed paleogeography were quantified. The Early Aptian (∼125 Ma) surface warming was driven by higher atmospheric greenhouse gas levels (70%) and surface albedo changes (30%). The lower elevation and surface albedo of ice-free Antarctica formed the largest contribution to the up to 38% reduction of the MTG. Cloud cover changes did not influence the global mean temperature change, but their latitudinal variations were the only feedback strengthening the MTG. A comparison with a model ensemble forced under the present-day geography confirms the stabilising cloud influence as a robust response across the two time periods.

In a second step, the model results were used to test the internal consistency of the Cretaceous upper-ocean temperature record. It is demonstrated that the restricted circulation of the evolving North and South Atlantic led to a systematic overestimation of local Early Cretaceous temperatures in the $TEX_{86}$ proxy. Applying an adjusted calibration significantly improves the model-data fit and the overall comparison with other temperature proxies for the Early Cretaceous. The combination of both studies implies that the MTG during the Early Aptian was significantly lower than today, but can be reproduced with the current generation of climate models.

A third study simulated the Aptian to Albian progressive opening of two marine gateways between the emerging South Atlantic and Southern Ocean to assess their influence on the water mass exchange between both basins and to derive possible implications for the organic carbon burial. A large model ensemble demonstrates the enhanced influence of boundary condition uncertainties on the simulated regional circulation. The test against geochemical data allowed to constrain the most likely depth of the proto-Drake Passage to $\sim$200 m and therefore improves our understanding of the large-scale oceanographic setting of the Early Cretaceous Southern Ocean. The results show a dominant geographic control on the reconstructed circulation changes. The opening of the Falkland Plateau initially started convection and ventilation in the Weddell Sea, while the subsequent opening of the Georgia Basin Gateway enabled deep water exchange between the South Atlantic and Southern Ocean that ultimately terminated enhanced organic carbon burial in the Cape Basin. The results provide the basis for future biogeochemical modelling to quantify the influence of the regional carbon burial changes on the global carbon cycle and the transient climate evolution of the Early Cretaceous.

# Zusammenfassung

Treibhausklimata mit deutlich höheren globalen Durchschnittstemperaturen als heutzutage dominierten weite Teile der geologischen Geschichte. Sie liefern direkte Hinweise auf die Anpassung des Klimasystems an erhöhte Treibhausgaskonzentrationen in der Vergangenheit und stellen die einzige Möglichkeit dar, die Spanne modellbasierter Prognosen der zukünftigen anthropogenen Erwärmung zu begrenzen. Die frühe Kreide ($\sim$145-100.5 Ma) bietet eine besondere Möglichkeit unser Verständnis vergangener Treibhausdynamiken zu testen, da die langfristige Wärme durch starke Störungen des globalen Kohlenstoffkreislaufes und Episoden vorübergehender Abkühlung unterbrochen wurde. Junge Ozeanbecken mit eingeschränkter Zirkulation, die durch den Zerfall Gondwanas entstanden, sind aufgrund ihres erhöhten Potenzials für die Ablagerung von organischem Kohlenstoff ein möglicher Antrieb für sowohl kurz- als auch langfristige Schwankungen des Kohlenstoffkreislaufes.

Diese Arbeit zielt darauf ab die primären Antriebe des Treibhausklimas der frühen Kreide besser einzugrenzen und zu beurteilen, inwiefern sie sich von den heutigen Dynamiken unterschieden. Klimamodellsimulationen der frühen Kreidezeit wurden mit paläozeanographischen Rekonstruktionen der Wassermassenmischung, Oberflächentemperaturen und organischer Kohlenstoffablagerung zusammengeführt, um sowohl die Ursachen für die mittlere Erwärmung als auch die tektonisch bedingten Veränderungen der Ozeanzirkulation und des Kohlenstoffkreislaufes zu rekonstruieren.

In einem ersten Schritt wurden die einzelnen Prozesse quantifiziert, die die simulierte mittlere globale Erwärmung und die Änderungen des meridionalen Temperaturgradienten (MTG) in Folge des erhöhten Treibhauseffektes und der veränderten Paläogeographie kontrollierten. Die Oberflächenerwärmung im frühen Apt ($\sim$125 Ma) wurde durch die erhöhten Treibhausgaskonzentrationen (70%) und Änderungen der Oberflächenalbedo (30%) angetrieben. Die reduzierte Höhe und Oberflächenalbedo der eisfreien Antarktis trugen den Großteil zur bis zu 38-prozentigen Abnahme des MTG bei. Änderungen der Wolkenbedeckung hatten keinen Einfluss auf die Änderung der globalen Mitteltemperatur, aber ihre latitudinalen Veränderungen bildeten den einzigen Prozess, der den MTG verstärkte. Der Vergleich mit einem Modellensemble, angetrieben unter der heutigen Geographie, bestätigt, dass der stabilisierende Wolkeneinfluss eine robuste Modellantwort für beide Zeitperioden darstellt.

In einem zweiten Schritt wurden die Modellergebnisse genutzt, um die interne Konsistenz der rekonstruierten Kreidetemperaturen des oberen Ozeans zu testen. Es wird gezeigt, dass die limitierte Zirkulation im gerade entstehenden Nord- und Südatlantik dazu geführt hat, dass die lokalen Temperaturen der frühen Kreide im $TEX_{86}$-Proxy überschätzt werden. Das Verwenden einer angepassten Kalibration führte dazu, dass sowohl die Übereinstimmung von Modell und Daten als auch die allgemeine Übereinstimmung mit anderen Proxies für die frühe Kreide zunahm. Die Kombination beider Studien impliziert, dass der MTG im frühen Apt zwar deutlich geringer war als heutzutage, er jedoch mit der aktuellen Generation von Klimamodellen reproduzierbar ist.

Eine dritte Studie simulierte die schrittweise Öffnung zweier Meeresverbindungen zwischen dem Südatlantik und dem Südozean im Zeitraum vom Abt bis zum Alb, um ihren Einfluss auf den Wassermassenaustausches zwischen beiden Becken zu rekonstruieren und um mögliche Auswirkungen auf die organische Kohlenstoffablagerung abzuleiten. Ein großes Modellensemble verdeutlicht den verstärkten Einfluss von Unsicherheiten in den verfügbaren Randbedingungen auf die simulierte regionale Zirkulation. Ein Abgleich mit geochemischen Daten ermöglichte eine Eingrenzung der wahrscheinlichsten Tiefe der frühen Drake-Passage auf $\sim$200 m und verbessert damit unser Verständnis der großräumigen ozeanographischen Begebenheiten des Südozeans während der frühen Kreide. Die Ergebnisse unterstützen die Annahme einer besonders wichtigen Rolle der Paläogeographie bei den rekonstruierten Zirkulationsänderungen. Die Öffnung des Falkland Plateaus ermöglichte das Einsetzen von Konvektion und Belüftung im Weddell-Meer, während die darauffolgende Öffnung einer Tiefenwasserverbindung den Wassermassenaustausch zwischen dem Südatlantik und Südozean ermöglichte und schließlich zum Ende der erhöhten Kohlenstoffablagerungen führte. Die Ergebnisse liefern die Grundlagen für zukünftige biogeochemische Modellierungen um den Einfluss der regionalen Änderungen der Kohlenstoffablagerungen auf den globalen Kohlenstoffkreislauf und damit den zeitlichen Verlauf der Klimaentwicklung der frühen Kreide zu quantifizieren.

# Contents

# 1 Introduction

## 1.1 Motivation

Children born in the year 2018 will most likely experience climatic conditions unprecedented for the past 3 million years within their lifetime (Burke et al., 2018). If the current rate of unmitigated global warming continues, a 50 million-year-long cooling trend could be reversed by the end of the next century (Burke et al., 2018). The only direct evidence of how the near-future climate system will adapt to the ongoing emissions of atmospheric greenhouse gases come from the geologic past. In fact, most of the Phanerozoic, i.e. the last 514 million years (Ma), were characterised by atmospheric $CO_2$ concentrations and global mean surface temperatures above present-day levels (e.g., Huber and Thomas, 2010; Veizer and Prokoph, 2015; Song et al., 2019). One of the longest and best-documented examples of these past "greenhouse" climates was the Cretaceous, lasting from $\sim$145 to 66 Ma. The Cretaceous gained particular interest due to its prolonged greenhouse conditions with peak global mean temperatures of more than 10 °C above modern (Huber and Thomas, 2010). Furthermore, as most parts of the Earth's ocean floor older than 180 Ma have been subducted (Hay, 2017), the Cretaceous provides the first example of a greenhouse interval for which reliable reconstructions of the plate tectonic history and age of the ocean floor are available (Müller et al., 2008).

No past warm period is a perfect analogue for a future anthropogenic warming (Haywood et al., 2011). One fundamental limitation for the comparability is that the climate sensitivity itself, i.e. how the temperature changes with increasing $CO_2$, will be modulated by the respective paleotopography and potentially changes on geological time scales (Haywood et al., 2011). Therefore, a profound understanding of the processes that characterise the climatic response of individual time periods to enhanced greenhouse forcing is essential to separate them from the more invariant controls on greenhouse dynamics. This will ultimately help to assess which mechanisms of past warm periods might also be the potential drivers of any future anthropogenic warming. This thesis aims to identify and better constrain these main time-slice characteristics for the Early Cretaceous ($\sim$145 to 100.5 Ma) and to assess how comparable they were to the present-day dynamics. The following section will give a brief introduction on some of the specific features of the Early Cretaceous climate system and how they lead to the main research questions addressed in this thesis.

## 1.2 What was special about the Cretaceous?

### 1.2.1 Greenhouse climate

The Cretaceous is classically described as a prime example of a greenhouse climate with long-term maxima in global temperatures (Barron, 1983; Huber and Thomas, 2010; Price et al., 2013). Low-latitude sea surface temperatures exceeded 30 °C for most of the time (see review in O'Brien et al., 2017) and bottom water temperatures ranged between 10 and at times more than 20 °C (Friedrich et al., 2012). Although the whole of the Cretaceous is considered a greenhouse climate (Huber and Thomas, 2010), global temperatures peaked around the mid-Cretaceous Cenomanian to Turonian (Voigt et al., 2004; Friedrich et al., 2012; MacLeod et al., 2013; Huber et al., 2018). While there is a general consensus that the polar regions during this Cretaceous Thermal Maximum were ice-free (Moriya et al., 2007; Ando et al., 2009; Huber et al., 2018), the possibility of at least temporary continental ice sheets during cooler episodes of the Early and Late Cretaceous can not be ruled out (Alley and Frakes, 2003; Price and Nunn, 2010; Alley et al., 2019). The overall reduced amount of land ice in combination with tectonically driven changes in the ocean basin volume led to an eustatic sea level highstand of $\sim$75-250 m above the present-day level (Haq, 2014).

High concentrations of atmospheric $CO_2$ are commonly considered as the main driver of the sustained warmth (Berner, 2001; Huber and Thomas, 2010; Price et al., 2013) with values above $\sim$500 ppmv throughout the Cretaceous (Wang et al., 2014). In accordance with the temperature maximum, generally higher $CO_2$ levels in the range of 1000-2000 ppmv were reconstructed for the mid-Cretaceous (Caldeira and Rampino, 1991; Berner, 1990; Bice et al., 2006; Wang et al., 2014), but also for parts of the Aptian (Wallmann, 2001; Naafs et al., 2016). Most studies indicate that the high $CO_2$ levels were maintained by enhanced tectonic and volcanic activity (e.g., Arthur et al., 1985; Wallmann, 2001; Van Der Meer et al., 2014) expressed as increased oceanic crust production (Larson, 1991; Seton et al., 2009) and the emplacement of large igneous provinces (Coffin and Eldholm, 1994).

A characteristic feature of the Cretaceous greenhouse climate is that the reconstructed warming was particularly pronounced in the high latitudes of both hemispheres. The associated strong reduction of the meridional temperature gradient (Barron, 1983; Huber et al., 1995; Littler et al., 2011) led to the idea that an "equable" climate characterised large parts of the Cretaceous (Barron, 1983). Evidence for mean annual temperatures in excess of 10 °C and above-freezing winter temperatures in the polar regions mainly come from the presence of crocodile-like reptiles (Tarduno et al., 1998) and plant fossils from the Arctic (Parrish and Spicer, 1988; Spicer and Herman, 2010) and the Antarctic Peninsula (Francis and Poole, 2002). Reproducing this polar amplification and reduced seasonality in continental interiors without the need of unrealistically high $CO_2$ levels has been a serious problem for global climate models for decades (Sloan and Barron, 1990; DeConto et al., 1999; DeConto et al., 2000; Sellwood and Valdes, 2006; Spicer et al., 2008; Niezgodzki et al., 2017). This long-lasting model-proxy mismatch could either indicate that the high-latitude warming is overestimated in the proxy reconstructions or that our knowledge about the deep-time boundary conditions used to force the models is insufficient. A third explanation, arguably with the more serious implications for our understanding of future climates, is that our current climate models are lacking fundamental dynamical feedbacks active in greenhouse climates (Spicer et al., 2008). This would genuinely question the robustness of our current projections of future anthropogenic warming. Furthermore, a reliable simulation of the mean state of past warm periods is essential to unravel the causes of any recorded climate variability. One of the fundamental advantages of coupled climate models is the ability to study the response of the climate system to a defined forcing on a global, physically consistent scale. In a first step, this thesis aims to assess the physical processes that caused the Early Cretaceous surface warming. Implementing our current knowledge about the Early Cretaceous boundary conditions in a state-of-the-art climate model will address the question: **(1) What controlled the simulated surface temperature distribution during the Early Cretaceous greenhouse?**

While it is certainly of interest to better understand the simulated physical changes of greenhouse climates, only a direct validation against the available proxy record will allow to constrain the numerical results and ultimately improve our understanding of past dynamics and enhance the credibility of future projections. Three main problems limit the model-proxy comparability for the Early Cretaceous. First, much of the Early Cretaceous falls within a period of a long-term stability of the geomagnetic field polarity, called the Cretaceous Normal Superchron (Granot et al., 2012). This severely reduces the accuracy and robustness of available plate tectonic models and therefore also limits the quality of paleogeographic reconstructions and stratigraphic controls for proxy records. Second, the reduced abundance of planktonic foraminifera in combination with poor preservation and diagenetic alteration of many samples (Pearson et al., 2001) limit the applicability of the classic oxygen isotope temperature proxy. This makes the organic paleothermometer $TEX_{86}$ the only widely used proxy for quantitative reconstructions of marine surface temperatures for large parts of the Early Cretaceous (O'Brien et al., 2017). Consequently, this also ties much of our understanding of the Early Cretaceous temperature evolution to the uncertainties and limitations associated with a single proxy technique. The third and closely related problem is that all temperature proxy methods rely on assumptions about the prevailing paleoenvironmental conditions during the actual signal formation. In the case of the $TEX_{86}$ proxy, the mechanism itself that relates the measured sedimentary signal to the actual surface temperatures is still not completely understood (see review in O'Brien et al., 2017). Uncertainties arise in part from different assumptions about the export depth of the signal (Kim et al., 2012; Taylor et al., 2013; Hernández-Sánchez et al., 2014; Ho and Laepple, 2016; Zhang and Liu, 2018) and demonstrated regional differences even in the present-day core-top sediments (Tierney and Tingley, 2014). Areas with known deviations from the global $TEX_{86}$-temperature relation are the (sub)polar oceans (Kim et al., 2010; Tierney

**Figure 1.1:** OAE 2 (∼ 94 Ma) organic-rich shales (dark gray, ∼1 m layer thickness) inbetween light-coloured carbonates at the Furlo section, Italy. Photo by S. Steinig.

and Tingley, 2014) and the Mediterranean and Red Sea (Trommer et al., 2009; Kim et al., 2015; Kim et al., 2016) and led to the formulation of spatially varying calibrations for the present-day continental configuration (Tierney and Tingley, 2014; Tierney and Tingley, 2015). For deep-time applications, on the other hand, the definition of these best modern analogue environments is difficult and depends on a priori assumptions. In consequence, only global core-top calibrations are commonly applied, even though the direct comparison with other temperature proxies reveals systematic offsets of the $TEX_{86}$-derived temperatures (Hollis et al., 2012; Taylor et al., 2013; Polik et al., 2018). Climate models could bridge this gap and evaluate the regional oceanographic setting of individual study sites to find the respective best present-day analogue and therefore $TEX_{86}$-temperature relation. Given the important role of the $TEX_{86}$ proxy for Early Cretaceous temperature reconstructions, this leads to the question: **(2) Can climate models reveal systematic biases in the Early Cretaceous temperature record?**

### 1.2.2 Evolving ocean basins and carbon cycle perturbations

The traditional view of a warm and equable Cretaceous climate is challenged by an increasing amount of evidence for a rather complex succession of dynamic transitions between cooler intervals and hothouse states around the mean greenhouse climate (Price, 1999; Price and Nunn, 2010; Bodin et al., 2015; Herrle et al., 2015; Jenkyns, 2018). Changes in the global carbon cycle are commonly viewed as drivers of both short-term and long-term variations of the Cretaceous climate system (Weissert and Erba, 2004; Huber and Thomas, 2010; Price et al., 2013; Bodin et al., 2015).

Two of the most significant perturbations with estimated durations of close to 1 Ma (Jenkyns, 2018) were the Early Aptian Oceanic Anoxic Event (OAE) 1a and OAE 2 during the Cenomanian–Turonian boundary. Both were characterised by long-term maxima in global temperatures (O'Brien et al., 2017; Jenkyns, 2018), widespread oxygen depleted water masses (Schlanger and Jenkyns, 1976; Bralower et al., 1994; Jenkyns, 2010) and large-scale deposition of marine organic-rich black shales (Fig. 1.1; Schlanger and Jenkyns, 1976; Jenkyns, 1980; Arthur et al., 1988). The rapid surface temperature increase accompanying the onset of OAE 1a was most likely related to $CO_2$ degassing during the emplacement of the Ontong Java Plateau (Larson and Erba, 1999; Bottini et al., 2012; Charbonnier and Föllmi, 2017), the largest magmatic event on record (Fitton et al., 2004). The initial warming was followed by increased organic carbon burial and potentially related multiple episodes of transient global cooling (Bodin et al., 2015; Bottini et al., 2015; Jenkyns, 2018).

In addition to the global occurrence of OAEs, widespread deposition of organic-carbon-rich sediments during the Early Cretaceous occurred predominantly in the young North and South Atlantic (Arthur and Natland, 1979; Weissert, 1981; Stein et al., 1986; Zimmerman et al., 1987; Wagner et al., 2013). The South Atlantic emerged in the first stages of seafloor spreading between Africa and South America (Fig. 1.2) that started in the Late Jurassic in the course of the breakup of Pangea (Torsvik et al., 2009). Initial water mass exchange with the Southern Ocean was severely limited by the presence of the Falkland Plateau (Fig. 1.2b, Pérez-Díaz and Eagles, 2017). Simultaneously, hotspot volcanism led to the formation of the Walvis Ridge that separated the southern Cape-Argentine Basin from the northern Angola Basin (Dingle, 1999; Hoernle et al., 2015). The restricted circulation and large shelf areas of these young ocean basins formed ideal environments for enhanced biogeochemical turnover rates, the formation of oxygen-deficient water masses and increased organic carbon burial (Trabucho-Alexandre et al., 2012). This turned the evolving ocean basins into efficient carbon sinks with the potential to influence or even trigger global climate trends (McAnena et al., 2013). Besides OAE 1a, the Aptian (∼125 to 113 Ma) was characterised by at least one other global carbon cycle perturbation—the so-called Late Aptian Cold Spell (LACS). This period of enhanced carbon burial and global cooling was also associated with a marine biotic crisis (Mutterlose et al., 2009; McAnena et al., 2013; Bottini et al., 2015). Biogeochemical modelling indicates a dominant role of the emerging South Atlantic and Southern Ocean basins in the excessive sequestration of atmospheric carbon and therefore in driving the ∼2.5 Ma long cooling trend (McAnena et al., 2013). Nevertheless, the underlying processes that caused the transient oceanographic and biogeochemical changes are poorly understood. The potential influence of the emerging South Atlantic on global-scale climate perturbations leads to the question: **(3) What controlled the circulation and carbon burial in the Early Cretaceous South Atlantic and Southern Ocean?**

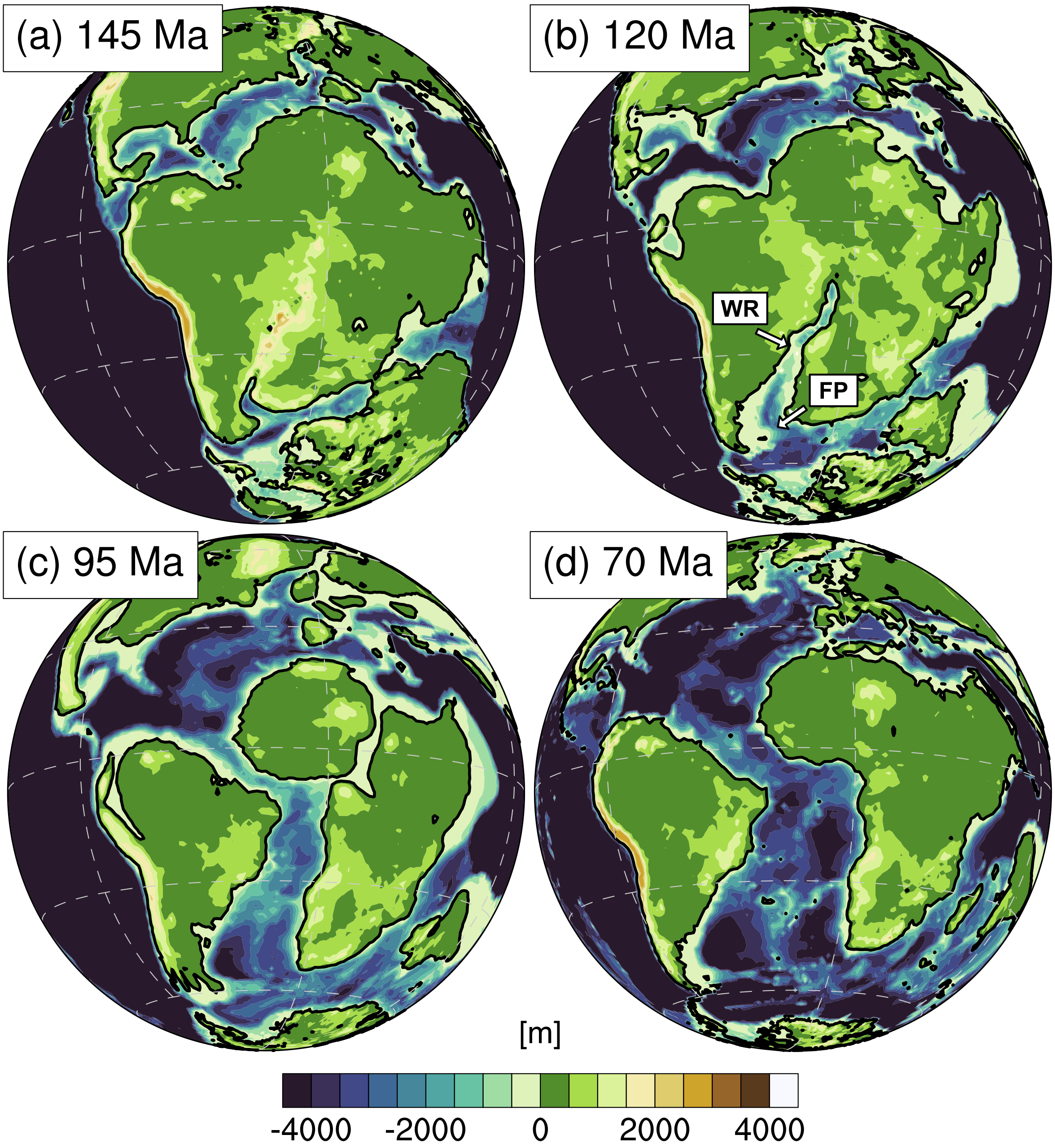

**Figure 1.2:** Paleogeographic maps for four time slices of the Cretaceous. Paleobathymetry and paleotopography reconstructions are from Scotese and Wright (2018) with highlighted positions of the Falkland Plateau (FP) and Walvis Ridge (WR). Contour interval is 500 m.

## 1.3 Strategy and outline of the thesis

The three questions raised in section 1.2 will be addressed in three individual studies presented in chapters 2 to 4. While climate model simulations with the Kiel Climate Model (KCM, Park et al., 2009), adapted to the Early Cretaceous boundary conditions, form the backbone of each study, they are complemented by different data sets to increase the validity of the presented results. In particular, this thesis is integrated in a joint project to assess the influence of the transient carbon burial changes in the South Atlantic and Southern Ocean on the global carbon cycle and Early Cretaceous climate evolution. New geochemical data generated within this project are directly integrated in chapters 3 and 4. The following will give a brief overview of the different approaches used to answer the three main research questions of this thesis.

### (1) What controlled the simulated surface temperature distribution during the Early Cretaceous greenhouse?

Chapter 2 introduces a suite of new KCM simulations for Early Aptian (∼125 Ma) boundary conditions to assess the model-predicted peak warming during OAE 1a. An energy balance model analysis is applied to quantify the contribution of individual processes both to the global mean warming and to the changes of the meridional temperature gradient. Furthermore, a separation of the respective warming into a part caused by the changed paleogeography and one solely induced by the increased atmospheric $CO_2$ concentrations allows the comparison of the Cretaceous climate sensitivity to other time periods. In particular, the robustness of the results is tested against models participating in the Coupled Model Intercomparison Project phase 5 (CMIP5).

### (2) Can climate models reveal systematic biases in the Early Cretaceous temperature record?

Chapter 3 compares the simulated surface temperatures against the available $TEX_{86}$ proxy record for OAE 1a. The proxy data includes a recent compilation of published records and new data generated within the project. A particular focus lies on the internal consistency of the available $TEX_{86}$ data that can be tested against the regional temperature distribution in the simulations. Systematic differences in the $TEX_{86}$ ratios are explained by the simulated oceanographic setting of individual study sites. Finally, the refined absolute temperatures are discussed in the context of the long-term Cretaceous temperature evolution.

### (3) What controlled the circulation and carbon burial in the Early Cretaceous South Atlantic and Southern Ocean?

Chapter 4 builds on the previously described global model, but refines the regional bathymetry of the South Atlantic and Southern Ocean. Three pseudo-transient stages are designed to represent the hypothesised opening history of the Falkland Plateau in the KCM. An ensemble of simulations for each stage is used to account for the large range in the available boundary conditions for key oceanic gateways and atmospheric $CO_2$ levels. The results are discussed in the context of reconstructed water mass mixing and carbon burial across the region to constrain the simulated circulation and to test hypotheses generated from the proxy data. Finally, the results are combined with a regional stratigraphic framework to derive an integrated ocean circulation and carbon burial history for the Early Cretaceous South Atlantic and Southern Ocean.

Chapter 5 presents a summary of the results in the form of answers to the three main research questions and derives an outlook for future work.

## References

Alley, N. F. and L. A. Frakes (2003). “First known Cretaceous glaciation: Livingston tillite member of the Cadna-owie Formation, South Australia”. In: *Australian Journal of Earth Sciences* 50.2, pp. 139–144. DOI: `10.1046/j.1440-0952.2003.00984.x`.

Alley, N. F., S. B. Hore, and L. A. Frakes (2019). “Glaciations at high-latitude Southern Australia during the Early Cretaceous”. In: *Australian Journal of Earth Sciences*, pp. 1–51. DOI: `10.1080/08120099.2019.1590457`.

Ando, Atsushi, Brian T. Huber, Kenneth G. MacLeod, Tomoko Ohta, and Boo Keun Khim (2009). “Blake Nose stable isotopic evidence against the mid-Cenomanian glaciation hypothesis”. In: *Geology* 37.5, pp. 451–454. DOI: `10.1130/G25580A.1`.

Arthur, M. A., W. E. Dean, and S. O. Schlanger (1985). “Variations in the Global Carbon Cycle During the Cretaceous Related to Climate, Volcanism, and Changes in Atmospheric CO 2”. In: *Geophysical Monograph Series*. Vol. 32, pp. 504–529. DOI: `10.1029/GM032p0504`.

Arthur, Michael A., Walter E. Dean, and Lisa M. Pratt (1988). “Geochemical and climatic effects of increased marine organic carbon burial at the Cenomanian/Turonian boundary”. In: *Nature* 335.6192, pp. 714–717. DOI: `10.1038/335714a0`.

Arthur, Michael A. and James H. Natland (1979). “Carbonaceous sediments in the North and South Atlantic: The role of salinity in stable stratification of early Cretaceous basins”. In: *Deep drilling results in the Atlantic Ocean: Continental Margins and Paleoenvironment*. Vol. 3, pp. 375–401. DOI: `10.1029/ME003p0375`.

Barron, Eric J. (1983). “A warm, equable Cretaceous: The nature of the problem”. In: *Earth-Science Reviews* 19.4, pp. 305–338. DOI: `10.1016/0012-8252(83)90001-6`.

Berner, R. a. (2001). "GEOCARB III: A revised model of atmospheric CO2 over Phanerozoic time". In: *American Journal of Science* 301.2, pp. 182–204. DOI: `10.2475/ajs.301.2.182`.

Berner, Robert A (1990). "Atmospheric Carbon Dioxide Levels Over Phanerozoic Time". In: *Science* 249.4975, pp. 1382–1386. DOI: `10.1126/science.249.4975.1382`.

Bice, Karen L., Daniel Birgel, Philip A. Meyers, Kristina A. Dahl, Kai Uwe Hinrichs, and Richard D. Norris (2006). "A multiple proxy and model study of Cretaceous upper ocean temperatures and atmospheric CO2concentrations". In: *Paleoceanography*. DOI: `10.1029/2005PA001203`.

Bodin, Stéphane, Philipp Meissner, Nico M.M. Janssen, Thomas Steuber, and Jörg Mutterlose (2015). "Large igneous provinces and organic carbon burial: Controls on global temperature and continental weathering during the Early Cretaceous". In: *Global and Planetary Change* 133, pp. 238–253. DOI: `10.1016/j.gloplacha.2015.09.001`.

Bottini, C., E. Erba, D. Tiraboschi, H. C. Jenkyns, S. Schouten, and J. S. Sinninghe Damsté (2015). "Climate variability and ocean fertility during the Aptian Stage". In: *Climate of the Past* 11.3, pp. 383–402. DOI: `10.5194/cp-11-383-2015`.

Bottini, Cinzia, Anthony S Cohen, Elisabetta Erba, Hugh C Jenkyns, and Angela L Coe (2012). "Osmium-isotope evidence for volcanism, weathering, and ocean mixing during the early Aptian OAE 1a". In: *Geology* 40.7, pp. 583–586. DOI: `10.1130/G33140.1`.

Bralower, Timothy J., Seymour O. Schlanger, William V. Sliter, David J. Allard, R. Mark Leckie, and Michael A. Arthur (1994). "Timing and Paleoceanography of Oceanic Dysoxia/Anoxia in the Late Barremian to Early Aptian (Early Cretaceous)". In: *Palaios* 9.4, pp. 335–369. DOI: `10.2307/3515055`.

Burke, K. D., J. W. Williams, M. A. Chandler, A. M. Haywood, D. J. Lunt, and B. L. Otto-Bliesner (2018). "Pliocene and Eocene provide best analogs for near-future climates". In: *Proceedings of the National Academy of Sciences* 115.52, pp. 13288–13293. DOI: `10.1073/pnas.1809600115`.

Caldeira, Ken and Michael R. Rampino (1991). "The Mid-Cretaceous Super Plume, carbon dioxide, and global warming". In: *Geophysical Research Letters* 18.6, pp. 987–990. DOI: `10.1029/91GL01237`.

Charbonnier, Guillaume and Karl B Föllmi (2017). "Mercury enrichments in lower Aptian sediments support the link between Ontong Java large igneous province activity and oceanic anoxic episode 1a". In: *Geology* 45.1, pp. 63–66. DOI: `10.1130/G38207.1`.

Coffin, Millard F. and Olav Eldholm (1994). "Large Igneous Provinces : Crustal Structure , Dimensions ". In: *Reviews of Geophysics* 32.1, pp. 1–36. DOI: `10.1029/93RG02508`.

DeConto, Robert M., Esther C. Brady, Jon Bergengren, and William W. Hay (2000). "Late Cretaceous climate, vegetation, and ocean interactions". In: *Warm Climates in Earth History*. Ed. by Brian T. Huber, Kenneth G. Macleod, and Scott L. Wing. Cambridge: Cambridge University Press, pp. 275–296. DOI: `10.1017/CBO9780511564512.010`.

DeConto, Robert M., William W. Hay, Stanley L. Thompson, and Jon Bergengren (1999). "Late Cretaceous climate and vegetation interactions: Cold continental interior paradox". In: *Special Paper 332: Evolution of the Cretaceous Ocean-Climate System*. Geological Society of America, pp. 391–406. DOI: `10.1130/0-8137-2332-9.391`.

Dingle, R V (1999). “Walvis Ridge barrier: its influence on palaeoenvironments and source rock generation deduced from ostracod distributions in the early South Atlantic Ocean”. In: *Geological Society, London, Special Publications* 153.1, pp. 293–302. DOI: `10.1144/GSL.SP.1999.153.01.18`.

Fitton, J. Godfrey, John J. Mahoney, Paul J. Wallace, and Andrew D. Saunders (2004). “Origin and evolution of the Ontong Java Plateau: introduction”. In: *Geological Society, London, Special Publications* 229.1, pp. 1–8. DOI: `10.1144/GSL.SP.2004.229.01.01`.

Francis, Jane E. and Imogen Poole (2002). “Cretaceous and early Tertiary climates of Antarctica: evidence from fossil wood”. In: *Palaeogeography, Palaeoclimatology, Palaeoecology* 182.1-2, pp. 47–64. DOI: `10.1016/S0031-0182(01)00452-7`.

Friedrich, Oliver, Richard D. Norris, and Jochen Erbacher (2012). “Evolution of middle to late Cretaceous oceans-A 55 m.y. Record of Earth’s temperature and carbon cycle”. In: *Geology* 40.2, pp. 107–110. DOI: `10.1130/G32701.1`.

Granot, Roi, Jérôme Dyment, and Yves Gallet (2012). “Geomagnetic field variability during the Cretaceous Normal Superchron”. In: *Nature Geoscience* 5.3, pp. 220–223. DOI: `10.1038/ngeo1404`.

Haq, Bilal U. (2014). “Cretaceous eustasy revisited”. In: *Global and Planetary Change* 113, pp. 44–58. DOI: `10.1016/j.gloplacha.2013.12.007`.

Hay, William W. (2017). “Toward understanding Cretaceous climate—An updated review”. In: *Science China Earth Sciences* 60.1, pp. 5–19. DOI: `10.1007/s11430-016-0095-9`.

Haywood, Alan M., Andy Ridgwell, Daniel J. Lunt, Daniel J. Hill, Matthew J. Pound, Harry J. Dowsett, Aisling M. Dolan, Jane E. Francis, and Mark Williams (2011). “Are there pre-Quaternary geological analogues for a future greenhouse warming?” In: *Philosophical Transactions of the Royal Society A: Mathematical, Physical and Engineering Sciences* 369.1938, pp. 933–956. DOI: `10.1098/rsta.2010.0317`.

Hernández-Sánchez, M. T., E. M.S. Woodward, K. W.R. Taylor, G. M. Henderson, and R. D. Pancost (2014). “Variations in GDGT distributions through the water column in the South East Atlantic Ocean”. In: *Geochimica et Cosmochimica Acta*. DOI: `10.1016/j.gca.2014.02.009`.

Herrle, Jens O., Claudia J. Schröder-Adams, William Davis, Adam T. Pugh, Jennifer M. Galloway, and Jared Fath (2015). “Mid-Cretaceous High Arctic stratigraphy, climate, and Oceanic Anoxic Events”. In: *Geology* 43.5, pp. 403–406. DOI: `10.1130/G36439.1`.

Ho, Sze Ling and Thomas Laepple (2016). “Flat meridional temperature gradient in the early Eocene in the subsurface rather than surface ocean”. In: *Nature Geoscience* 9.8, pp. 606–610. DOI: `10.1038/ngeo2763`.

Hoernle, Kaj, Joana Rohde, Folkmar Hauff, Dieter Garbe-Schönberg, Stephan Homrighausen, Reinhard Werner, and Jason P Morgan (2015). “How and when plume zonation appeared during the 132 Myr evolution of the Tristan Hotspot”. In: *Nature Communications* 6.1, p. 7799. DOI: `10.1038/ncomms8799`.

Hollis, Christopher J., Kyle W.R. Taylor, Luke Handley, Richard D. Pancost, Matthew Huber, John B. Creech, Benjamin R. Hines, Erica M. Crouch, Hugh E.G. Morgans, James S. Crampton, Samantha Gibbs, Paul N. Pearson, and James C. Zachos (2012). “Early Paleogene temperature history of the Southwest Pacific Ocean: Reconciling proxies and models". In: *Earth and Planetary Science Letters* 349-350, pp. 53–66. DOI: `10.1016/j.epsl.2012.06.024`.

Huber, B. T., D. A. Hodell, and C. P. Hamilton (1995). "Middle-late Cretaceous climate of the southern high latitudes: stable isotopic evidence for minimal equator-to-pole thermal gradients". In: *Geological Society of America Bulletin* 107.10, pp. 1164–1191. DOI: `10.1130/0016-7606(1995)107<1164:MLCCOT>2.3.CO;2`. arXiv: `1210.4576`.

Huber, Brian T., Kenneth G. MacLeod, David K. Watkins, and Millard F. Coffin (2018). "The rise and fall of the Cretaceous Hot Greenhouse climate". In: *Global and Planetary Change* 167, pp. 1–23. DOI: `10.1016/j.gloplacha.2018.04.004`.

Huber, M. and E. Thomas (2010). "Paleoceanography: The Greenhouse World". In: *Encyclopedia of Ocean Sciences* 86, pp. 319–329. DOI: `10.1016/B978-012374473-9.00701-3`.

Jenkyns, H. C. (1980). "Cretaceous anoxic events: from continents to oceans". In: *Journal of the Geological Society* 137.2, pp. 171–188. DOI: `10.1144/gsjgs.137.2.0171`.

Jenkyns, Hugh C (2018). "Transient cooling episodes during Cretaceous Oceanic Anoxic Events with special reference to OAE 1a ( Early Aptian )". In: *Philosophical Transactions of the Royal Society A* 376.20170073, pp. 1–26. DOI: `10.1098/rsta.2017.0073`.

— (2010). "Geochemistry of oceanic anoxic events". In: *Geochemistry, Geophysics, Geosystems* 11.3, pp. 1–30. DOI: `10.1029/2009GC002788`.

Kim, Jung Hyun, Jaap van der Meer, Stefan Schouten, Peer Helmke, Veronica Willmott, Francesca Sangiorgi, Nalân Koç, Ellen C. Hopmans, and Jaap S Sinninghe Damsté (2010). "New indices and calibrations derived from the distribution of crenarchaeal isoprenoid tetraether lipids: Implications for past sea surface temperature reconstructions". In: *Geochimica et Cosmochimica Acta* 74.16, pp. 4639–4654. DOI: `10.1016/j.gca.2010.05.027`.

Kim, Jung Hyun, Oscar E. Romero, Gerrit Lohmann, Barbara Donner, Thomas Laepple, Eddie Haam, and Jaap S. Sinninghe Damsté (2012). "Pronounced subsurface cooling of North Atlantic waters off Northwest Africa during Dansgaard-Oeschger interstadials". In: *Earth and Planetary Science Letters* 339-340, pp. 95–102. DOI: `10.1016/j.epsl.2012.05.018`.

Kim, Jung Hyun, Stefan Schouten, Marta Rodrigo-Gámiz, Sebastiaan Rampen, Gianluca Marino, Carme Huguet, Peer Helmke, Roselyne Buscail, Ellen C. Hopmans, Jörg Pross, Francesca Sangiorgi, Jack B M Middelburg, and Jaap S. Sinninghe Damsté (2015). "Influence of deep-water derived isoprenoid tetraether lipids on the TEX86H paleothermometer in the Mediterranean Sea". In: *Geochimica et Cosmochimica Acta* 150, pp. 125–141. DOI: `10.1016/j.gca.2014.11.017`.

Kim, Jung Hyun, Laura Villanueva, Claudia Zell, and Jaap S. Sinninghe Damsté (2016). "Biological source and provenance of deep-water derived isoprenoid tetraether lipids along the Portuguese continental margin". In: *Geochimica et Cosmochimica Acta* 172, pp. 177–204. DOI: `10.1016/j.gca.2015.09.010`.

Larson, R. L. (1991). "Latest pulse of Earth: Evidence for a mid-Cretaceous superplume". In: *Geology* 19.6, p. 547. DOI: `10.1130/0091-7613(1991)019<0547:LPOEEF>2.3.CO;2`.

Larson, Roger L. and Elisabetta Erba (1999). "Onset of the Mid-Cretaceous greenhouse in the Barremian-Aptian: Igneous events and the biological, sedimentary, and geochemical responses". In: *Paleoceanography* 14.6, pp. 663–678. DOI: `10.1029/1999PA900040`.

Littler, Kate, Stuart A. Robinson, Paul R. Bown, Alexandra J. Nederbragt, and Richard D. Pancost (2011). “High sea-surface temperatures during the Early Cretaceous Epoch”. In: *Nature Geoscience* 4.3, pp. 169–172. DOI: `10.1038/ngeo1081`.

MacLeod, Kenneth G., Brian T. Huber, Álvaro Jiménez Berrocoso, and Ines Wendler (2013). “A stable and hot Turonian without glacial $\delta$18O excursions is indicated by exquisitely preserved Tanzanian foraminifera”. In: *Geology* 41.10, pp. 1083–1086. DOI: `10.1130/G34510.1`.

McAnena, A., S. Flögel, P. Hofmann, J. O. Herrle, A. Griesand, J. Pross, H. M. Talbot, J. Rethemeyer, K. Wallmann, and T. Wagner (2013). “Atlantic cooling associated with a marine biotic crisis during the mid-Cretaceous period”. In: *Nature Geoscience* 6.7, pp. 558–561. DOI: `10.1038/ngeo1850`.

Moriya, Kazuyoshi, Paul A. Wilson, Oliver Friedrich, Jochen Erbacher, and Hodaka Kawahata (2007). “Testing for ice sheets during the mid-Cretaceous greenhouse using glassy foraminiferal calcite from the mid-Cenomanian tropics on Demerara Rise”. In: *Geology* 35.7, p. 615. DOI: `10.1130/G23589A.1`.

Müller, R. Dietmar, Maria Sdrolias, Carmen Gaina, Bernhard Steinberger, and Christian Heine (2008). “Long-term sea-level fluctuations driven by ocean basin dynamics”. In: *Science* 319.5868, pp. 1357–1362. DOI: `10.1126/science.1151540`.

Mutterlose, Jörg, André Bornemann, and Jens Herrle (2009). “The Aptian – Albian cold snap: Evidence for "mid" Cretaceous icehouse interludes”. In: *Neues Jahrbuch für Geologie und Paläontologie - Abhandlungen* 252.2, pp. 217–225. DOI: `10.1127/0077-7749/2009/0252-0217`.

Naafs, B. D.A., J. M. Castro, G. A. De Gea, M. L. Quijano, D. N. Schmidt, and R. D. Pancost (2016). “Gradual and sustained carbon dioxide release during Aptian Oceanic Anoxic Event 1a”. In: *Nature Geoscience* 9.2, pp. 135–139. DOI: `10.1038/ngeo2627`.

Niezgodzki, Igor, Gregor Knorr, Gerrit Lohmann, Jarosław Tyszka, and Paul J. Markwick (2017). “Late Cretaceous climate simulations with different CO2levels and subarctic gateway configurations: A model-data comparison”. In: *Paleoceanography* 32.9, pp. 980–998. DOI: `10.1002/2016PA003055`.

O’Brien, Charlotte L., Stuart A. Robinson, Richard D. Pancost, Jaap S. Sinninghe Damsté, Stefan Schouten, Daniel J. Lunt, Heiko Alsenz, André Bornemann, Cinzia Bottini, Simon C. Brassell, Alexander Farnsworth, Astrid Forster, Brian T. Huber, Gordon N. Inglis, Hugh C. Jenkyns, Christian Linnert, Kate Littler, Paul Markwick, Alison McAnena, Jörg Mutterlose, B. David A. Naafs, Wilhelm Püttmann, Appy Sluijs, Niels A.G.M. van Helmond, Johan Vellekoop, Thomas Wagner, and Neil E. Wrobel (2017). “Cretaceous sea-surface temperature evolution: Constraints from TEX86 and planktonic foraminiferal oxygen isotopes”. In: *Earth-Science Reviews* 172, pp. 224–247. DOI: `10.1016/j.earscirev.2017.07.012`.

Park, W., N. Keenlyside, M. Latif, A. Ströh, R. Redler, E. Roeckner, and G. Madec (2009). “Tropical Pacific Climate and Its Response to Global Warming in the Kiel Climate Model”. In: *Journal of Climate* 22.1, pp. 71–92. DOI: `10.1175/2008JCLI2261.1`.

Parrish, Judith Totman and Robert A. Spicer (1988). “Late Cretaceous terrestrial vegetation: A near-polar temperature curve”. In: *Geology* 16.1, p. 22. DOI: `10.1130/0091-7613(1988)016<0022:LCTVAN>2.3.CO;2`.

Pearson, Paul N., Peter W. Ditchfield, Joyce Singano, Katherine G. Harcourt-Brown, Christopher J. Nicholas, Richard K. Olsson, Nicholas J. Shackleton, and Mike A. Hall (2001). *Warm tropical sea surface temperatures in the Late Cretaceous and Eocene epochs*. DOI: `10.1038/35097000`.

Pérez-Díaz, Lucía and Graeme Eagles (2017). "South Atlantic paleobathymetry since early Cretaceous". In: *Scientific Reports* 7.1. DOI: `10.1038/s41598-017-11959-7`.

Polik, Catherine A., Felix J. Elling, and Ann Pearson (2018). "Impacts of Paleoecology on the TEX86 Sea Surface Temperature Proxy in the Pliocene-Pleistocene Mediterranean Sea". In: *Paleoceanography and Paleoclimatology* 33.12, pp. 1472–1489. DOI: `10.1029/2018PA003494`.

Price, Gregory D. (1999). "The evidence and implications of polar ice during the Mesozoic". In: *Earth Science Reviews* 48.3, pp. 183–210. DOI: `10.1016/S0012-8252(99)00048-3`.

Price, Gregory D. and Elizabeth V. Nunn (2010). "Valanginian isotope variation in glendonites and belemnites from Arctic Svalbard: Transient glacial temperatures during the Cretaceous greenhouse". In: *Geology* 38.3, pp. 251–254. DOI: `10.1130/G30593.1`.

Price, Gregory D., Richard J. Twitchett, James R. Wheeley, and Giuseppe Buono (2013). "Isotopic evidence for long term warmth in the Mesozoic". In: *Scientific Reports* 3, pp. 1–5. DOI: `10.1038/srep01438`.

Schlanger, S. O. and H. C. Jenkyns (1976). "Createaceous oceanic anoxic events: causes and consequences". In: *Geologie en mijbouw* 55.3-4, pp. 179–184.

Scotese, C.R. and N. Wright (2018). "PALEOMAP Paleodigital Elevation Models (PaleoDEMS) for the Phanerozoic PALEOMAP Project, https://www.earthbyte.org/paleodem-resource-scotese-and-wright-2018".

Sellwood, Bruce W. and Paul J. Valdes (2006). "Mesozoic climates: General circulation models and the rock record". In: *Sedimentary Geology* 190.1-4, pp. 269–287. DOI: `10.1016/j.sedgeo.2006.05.013`.

Seton, Maria, C. Gaina, R. D. Müller, and C. Heine (2009). "Mid-Cretaceous seafloor spreading pulse: Fact or fiction?" In: *Geology* 37.8, pp. 687–690. DOI: `10.1130/G25624A.1`.

Sloan, L. Cirbus and Eric J. Barron (1990). ""Equable" climates during Earth history?" In: *Geology* 18.6, pp. 489–492. DOI: `10.1130/0091-7613(1990)018<0489:ECDEH>2.3.CO;2`.

Song, Haijun, Paul B. Wignall, Huyue Song, Xu Dai, and Daoliang Chu (2019). "Seawater Temperature and Dissolved Oxygen over the Past 500 Million Years". In: *Journal of Earth Science* 30.2, pp. 236–243. DOI: `10.1007/s12583-018-1002-2`.

Spicer, Robert A., Anders Ahlberg, Alexei B. Herman, Christa Charlotte Hofmann, Michail Raikevich, Paul J. Valdes, and Paul J. Markwick (2008). "The Late Cretaceous continental interior of Siberia: A challenge for climate models". In: *Earth and Planetary Science Letters* 267.1-2, pp. 228–235. DOI: `10.1016/j.epsl.2007.11.049`.

Spicer, Robert A. and Alexei B. Herman (2010). "The Late Cretaceous environment of the Arctic: A quantitative reassessment based on plant fossils". In: *Palaeogeography, Palaeoclimatology, Palaeoecology* 295.3-4, pp. 423–442. DOI: `10.1016/j.palaeo.2010.02.025`.

Stein, Rüdiger, Jürgen Rullkötter, and Dietrich H. Welte (1986). "Accumulation of organic-carbon-rich sediments in the Late Jurassic and Cretaceous Atlantic Ocean — A synthesis". In: *Chemical Geology* 56.1-2, pp. 1–32. DOI: `10.1016/0009-2541(86)90107-5`.

Tarduno, J. A., D. B. Brinkman, P. R. Renne, R. D. Cottrell, H. Scher, and P. Castillo (1998). "Evidence for Extreme Climatic Warmth from Late Cretaceous Arctic Vertebrates". In: *Science* 282.5397, pp. 2241–2243. DOI: `10.1126/science.282.5397.2241`.

Taylor, Kyle W.R., Matthew Huber, Christopher J. Hollis, Maria T. Hernandez-Sanchez, and Richard D. Pancost (2013). "Re-evaluating modern and Palaeogene GDGT distributions: Implications for SST reconstructions". In: *Global and Planetary Change* 108, pp. 158–174. DOI: `10.1016/j.gloplacha.2013.06.011`.

Tierney, Jessica E. and Martin P. Tingley (2014). "A Bayesian, spatially-varying calibration model for the TEX86 proxy". In: *Geochimica et Cosmochimica Acta* 127, pp. 83–106. DOI: `10.1016/j.gca.2013.11.026`.

— (2015). "A TEX86 surface sediment database and extended Bayesian calibration". In: *Scientific Data* 2, pp. 1–10. DOI: `10.1038/sdata.2015.29`.

Torsvik, Trond H., Sonia Rousse, Cinthia Labails, and Mark A. Smethurst (2009). "A new scheme for the opening of the South Atlantic Ocean and the dissection of an Aptian salt basin". In: *Geophysical Journal International* 177.3, pp. 1315–1333. DOI: `10.1111/j.1365-246X.2009.04137.x`.

Trabucho-Alexandre, J., W. W. Hay, and P. L. De Boer (2012). "Phanerozoic environments of black shale deposition and the Wilson Cycle". In: *Solid Earth* 3.1, pp. 29–42. DOI: `10.5194/se-3-29-2012`.

Trommer, Gabriele, Michael Siccha, Marcel T.J. van der Meer, Stefan Schouten, Jaap S. Sinninghe Damsté, Hartmut Schulz, Christoph Hemleben, and Michal Kucera (2009). "Distribution of Crenarchaeota tetraether membrane lipids in surface sediments from the Red Sea". In: *Organic Geochemistry* 40.6, pp. 724–731. DOI: `10.1016/j.orggeochem.2009.03.001`.

Van Der Meer, D. G., R. E. Zeebe, D. J. J. van Hinsbergen, A. Sluijs, W. Spakman, and T. H. Torsvik (2014). "Plate tectonic controls on atmospheric CO2 levels since the Triassic". In: *Proceedings of the National Academy of Sciences* 111.12, pp. 4380–4385. DOI: `10.1073/pnas.1315657111`.

Veizer, Jan and Andreas Prokoph (2015). "Temperatures and oxygen isotopic composition of Phanerozoic oceans". In: *Earth-Science Reviews* 146, pp. 92–104. DOI: `10.1016/j.earscirev.2015.03.008`.

Voigt, Silke, Andrew S. Gale, and Sascha Flögel (2004). "Midlatitude shelf seas in the Cenomanian-Turonian greenhouse world: Temperature evolution and North Atlantic circulation". In: *Paleoceanography* 19.4, pp. 1–17. DOI: `10.1029/2004PA001015`.

Wagner, T., P. Hofmann, and S. Flögel (2013). "Marine black shale deposition and Hadley Cell dynamics: A conceptual framework for the Cretaceous Atlantic Ocean". In: *Marine and Petroleum Geology* 43, pp. 222–238. DOI: `10.1016/j.marpetgeo.2013.02.005`.

Wallmann, K. (2001). "Controls on the Cretaceous and Cenozoic evolution of seawater composition, atmospheric CO2 and climate". In: *Geochimica et Cosmochimica Acta* 65.18, pp. 3005–3025. DOI: `10.1016/S0016-7037(01)00638-X`.

Wang, Yongdong, Chengmin Huang, Bainian Sun, Cheng Quan, Jingyu Wu, and Zhicheng Lin (2014). "Paleo-CO2 variation trends and the Cretaceous greenhouse climate". In: *Earth-Science Reviews* 129, pp. 136–147. DOI: `10.1016/j.earscirev.2013.11.001`.

Weissert, Helmut (1981). “The environment of deposition of black shales in the Early Cretaceous: an ongoing controversy”. In: *The Deep Sea Drilling Project: A Decade of Progress*. January 1981. SEPM (Society for Sedimentary Geology), pp. 547–560. DOI: `10.2110/pec.81.32.0547`.

Weissert, Helmut and Elisabetta Erba (2004). “Volcanism, CO2 and palaeoclimate: a Late Jurassic–Early Cretaceous carbon and oxygen isotope record”. In: *Journal of the Geological Society* 161.4, pp. 695–702. DOI: `10.1144/0016-764903-087`.

Zhang, Yi Ge and Xiaoqing Liu (2018). “Export Depth of the TEX86 Signal”. In: *Paleoceanography and Paleoclimatology* 33.7, pp. 666–671. DOI: `10.1029/2018PA003337`.

Zimmerman, H. B., A. Boersma, and F. W. McCoy (1987). “Carbonaceous sediments and palaeoenvironment of the Cretaceous South Atlantic Ocean”. In: *Geological Society, London, Special Publications* 26.1, pp. 271–286. DOI: `10.1144/GSL.SP.1987.026.01.19`.

# 2 Clouds maintain the meridional temperature gradient during the Early Cretaceous greenhouse climate

Sebastian Steinig, Wonsun Park, Mojib Latif and Sascha Flögel

**Declaration:** *This chapter is in preparation for submission. I designed the study with support from Sascha Flögel. Wonsun Park provided one Cretaceous simulation and the pre-industrial reference simulation. I carried out all other model experiments. I performed the analysis, produced all figures and wrote the chapter.*

## 2.1 Abstract

Greenhouse climates with global mean temperatures significantly above the present day prevailed during large parts of the Phanerozoic and are especially well documented for the Cretaceous Period (∼145-66 Ma). Paleoclimate records indicate that the overall warming was, at least temporarily, amplified at higher latitudes and associated with ice-free polar regions and warm continental interiors during winter. Reproducing and explaining this polar warmth is still a challenging task for state-of-the-art climate models. Here we quantify individual processes that influence the meridional temperature gradient (MTG) response to increased greenhouse gas forcing and therefore determine the simulated large-scale atmospheric and oceanic circulation during the Early Cretaceous. We employ the Kiel Climate Model, a coupled atmosphere-ocean-sea ice general circulation model, under Early Aptian (∼125 Ma) boundary conditions. We perform equilibrium integrations with different atmospheric $CO_2$ levels and a pre-industrial reference run to distinguish between changes induced by the increased greenhouse gas concentrations and the changed paleogeography. An energy balance model analysis is applied to enable a comparison of the Early Cretaceous results with models participating in the Coupled Model Intercomparison Project phase 5 (CMIP5). We thereby identify similarities and differences in the climatic response to enhanced greenhouse gas forcing for the Cretaceous and present-day geography. Global mean surface temperatures at peak $CO_2$ concentrations of 1200 ppmv are elevated by 9.6 °C compared to pre-industrial. The surface warming is mainly radiatively driven by the higher atmospheric greenhouse gas levels (∼70% of the warming) and surface albedo changes (∼30% of the warming). The lower elevation and surface albedo of ice-free Antarctica forms the largest contribution to the 38% reduction of the MTG. In fact, the MTG at the same pre-industrial $CO_2$ level was already 24% lower during the Cretaceous than for the present-day geography. Adjustments of the meridional heat transport influence local temperatures in the restricted Arctic Ocean, but are negligible on the global scale. Cloud feedbacks show little influence on the global mean temperature change, but their pronounced latitudinal variations significantly influence the strength of the MTG. Weaker tropical deep convection reduces low-latitude cloud cover and leads to a net cloud-induced warming in the tropics. The absence of polar ice caps prevents high-latitude atmospheric subsidence resulting in thicker, low-level clouds that reflect incoming shortwave radiation and consequently cool the surface. These cloud radiative feedbacks partly compensate the geographically driven reduction of the MTG and reduce its sensitivity to $CO_2$ changes. Additionally, the seasonality of the cloud feedbacks increases for the ice-free Early Cretaceous which in turn enhances the interhemispheric differences in the annual temperature cycle between the Arctic Ocean and continental Antarctica. The strength of the radiatively driven changes of the global MTG, including the stabilising cloud influence, is similar both for the Early Cretaceous and the present-day CMIP5 model ensemble. They therefore represent robust features of the simulated response to enhanced greenhouse gas forcing that are less sensitive to the applied model geography. Additionally, the regional climatic response can be modulated by the paleogeography and can therefore potentially differ from the present-day dynamics.

## 2.2 Introduction

The geologic past provides examples of multiple time periods where global mean temperatures were significantly higher than today (e.g., Song et al., 2019). The Cretaceous Period ($\sim$145-66 Ma) represents one of the warmest and best-documented greenhouse periods of the whole Phanerozoic (Huber and Thomas, 2010). Global mean temperatures were about 6-12 °C higher than today (Barron et al., 1995) and are commonly associated with the predominant absence of larger continental ice sheets (e.g., Huber et al., 2002; MacLeod et al., 2013) and an eustatic sea level highstand (Haq et al., 1987; Miller et al., 2005). Elevated concentrations of atmospheric $CO_2$ are widely accepted as the main driver of Cretaceous warmth (e.g., Royer, 2006; Fletcher et al., 2008; Price et al., 2013), even though this causal relation might have changed over the course of the Phanerozoic (Veizer et al., 2000). Estimates of Cretaceous $CO_2$ concentrations typically range between 500-2000 ppmv (Wang et al., 2014) with the highest levels during the mid-Cretaceous Cenomanian to Turonian (Hong and Lee, 2012). The high $CO_2$ levels were most likely maintained and controlled by increased volcanic activity in the form of enhanced oceanic crust production and the formation of large igneous provinces (Arthur et al., 1985; Larson, 1991; Van Der Meer et al., 2014).

Several lines of evidence suggest a particular strong warming in the polar regions of both hemispheres leading to the assumption of an equable Cretaceous climate with a strongly reduced meridional temperature gradient (MTG; Barron, 1983; Huber et al., 2002; Littler et al., 2011). Mean annual temperatures of $> 14$ °C for the mid-Cretaceous Arctic Ocean have been reconstructed on the basis of vertebrate assemblages (Tarduno et al., 1998) and are supported by paleofloral evidence (Spicer and Herman, 2010). MTGs (latitudes $< 30°$ minus latitudes $> 48°$) reconstructed from the oxygen isotope and $TEX_{86}$ paleothermometers vary considerably throughout the Cretaceous and range from 19-21 °C in the Campanian to Maastrichtian to a minimum of only 3-5 °C in the Aptian (O'Brien et al., 2017). This is a remarkable result, as the lowest MTG during the Early Cretaceous would also imply a decoupling of the MTG strength from the global mean temperatures that peaked during the mid-Cretaceous (O'Brien et al., 2017). On the other hand, $\delta^{18}O$ values of phosphate from vertebrates and fish teeth from the Late Cretaceous indicate only a small MTG reduction (Amiot et al., 2004) or even a low- to mid-latitude thermal gradient that was very similar to the present day (Pucéat et al., 2007).

The apparent strength and duration of the Cretaceous greenhouse conditions and the overall evidence for a, at least intermittent, polar amplification of the warming has motivated extensive research on the dominant influences on the Cretaceous surface temperature distribution. Pioneering numerical modelling, starting in the 1980s, identified changes in atmospheric $CO_2$, geography and oceanic heat transport as the major controls on mid-Cretaceous climate (Barron et al., 1981; Barron and Washington, 1984; Barron and Washington, 1985; Barron and Peterson, 1989) . A combination of these three factors produced the best model-data fit for mid-Cretaceous surface temperatures (Barron et al., 1995). Other proposed mechanisms for an enhanced high-latitude warming include atmosphere-vegetation feedbacks (Otto-Bliesner and Upchurch, 1997; Upchurch et al., 1998; DeConto et al., 2000) and local cloud radiative feedbacks (Sloan and Pollard, 1998; Abbot and Tziperman, 2008; Kump and Pollard, 2008).

The relative importance of these individual variables is still not clear and probably changed throughout the Cretaceous (Barron et al., 1993; Poulsen et al., 1999; Poulsen et al., 2003; Donnadieu et al., 2006). Uncertainties arise in part from the simultaneous occurrence of the long-term maxima in atmospheric $CO_2$ concentrations with the continuing breakup of Pangea (Blakey, 2008). The large-scale reorganisation of the land-sea distribution had a profound influence on the temporal evolution of the atmospheric circulation, the seasonal temperature cycle and monsoon precipitation (Kutzbach and Gallimore, 1989; Donnadieu et al., 2006; Fluteau et al., 2007; Ohba and Ueda, 2010), as well as on the ocean circulation (Poulsen et al., 1999; Poulsen et al., 2001; Otto-Bliesner, 2002; Poulsen et al., 2003) and deep water ventilation (Donnadieu et al., 2016). This highlights the need for a precise assessment of the mechanisms that controlled the surface temperatures during individual time periods and how they changed over time. Ultimately, this provides the basis to separate the common climatic responses of past warm periods from the time-slice-dependent modulation of the temperature distribution.

This becomes even more important as the global MTG ultimately controls the strength and position of the large-scale circulation features in the ocean and atmosphere. Shifts in the latitudinal positions of the Hadley cells or the jet streams in response to increased atmospheric $CO_2$ are proposed for the present-day climate (e.g., Kushner et al., 2001; Lu et al., 2007; Son et al., 2018) and also commonly invoked in explaining orbitally induced changes in Cretaceous depositional environments (Flögel et al., 2008; Hofmann and Wagner, 2011; Wagner et al., 2013; Behrooz et al., 2018). Furthermore, estimates of the Cretaceous Hadley cell location based on desert distribution reconstructions indicate a potential drastic, non-linear shrinking of its width for a certain $CO_2$ threshold that was possibly reached during the mid-Cretaceous (Hasegawa et al., 2012).

The interpretation of reconstructed changes in the paleorecord rely on robust estimates of surface temperatures, the position of large-scale atmospheric features and their sensitivity to geographical and radiative changes. The proposed weak MTG, especially during the Early Cretaceous (O'Brien et al., 2017), still challenges our understanding of the physical mechanisms that govern the climate dynamics during past greenhouse climates. The aim of this study is to quantify the processes that drove the Early Cretaceous surface warming and shaped the global MTG and atmospheric circulation with the help of numerical modelling. We choose the Early Aptian ($\sim$125 Ma) as a modelling target due to two reasons. First, a recent review of available proxy temperature data concludes that the low-to-higher mid-latitudinal temperature gradient of 3-5 °C during the Aptian was the lowest of the whole Cretaceous, even though mean surface temperatures peaked during the mid-Cretaceous (O'Brien et al., 2017). Second, the Early Aptian is characterised by

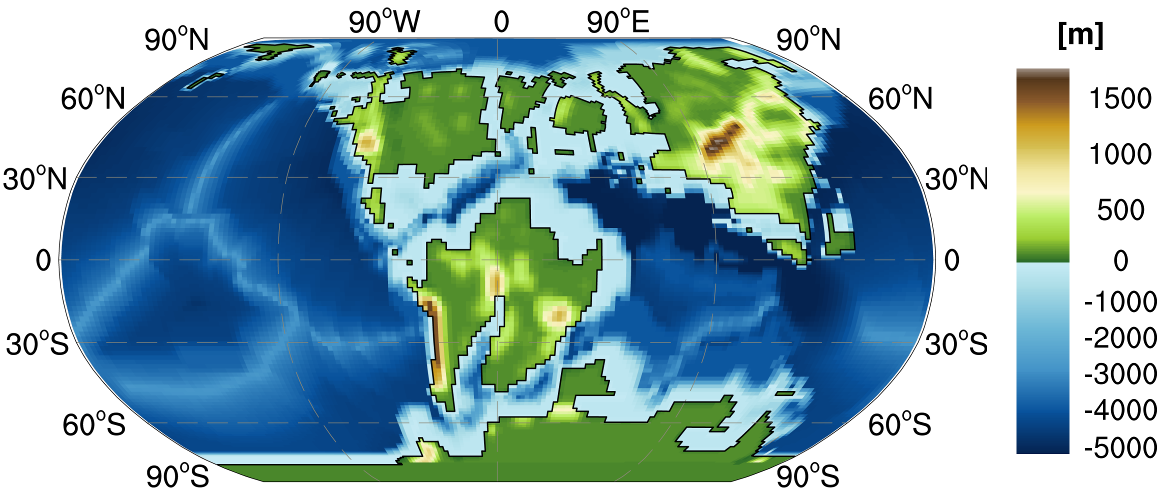

**Figure 2.1:** Early Aptian (∼125 Ma) model topography and bathymetry. Values are in meters.

the widespread deposition of organic-rich black shales during the Oceanic Anoxic Event 1a (OAE 1a; Jenkyns, 2010). This large disturbance of the global carbon cycle stimulated wide-ranging research on the causes and consequences for the the intermittent occurrence of widespread bottom water anoxia. Changes in surface temperatures and resulting upper ocean stratification possibly contributed to the development of OAEs (Schlanger and Jenkyns, 1976; Bralower, 2008; Bentum et al., 2009). An improved understanding of the controls on Early Aptian temperatures will therefore provide a new framework to evaluate the extensive OAE 1a literature.

We use a global climate model, the Kiel Climate Model, both in an Aptian and present-day configuration at a range of atmospheric $CO_2$ concentrations to separate the influence of geographical and radiative changes on the simulated temperature distribution. This increases the comparability of our Early Cretaceous results to other geological time periods and to the present-day and near-future climate. We are thereby able to use model output of the Coupled Model Intercomparison Project Phase 5 (Taylor et al., 2012) to validate the proposed changes of the MTG and large-scale atmospheric circulation and to identify common features and discrepancies between the Early Cretaceous and present-day climatic response to increased $CO_2$ concentrations..

## 2.3 Methods

### 2.3.1 Model description and experimental design

All experiments use the Kiel Climate Model (KCM; Park et al., 2009), consisting of the ECHAM5 atmosphere general circulation model (Roeckner et al., 2003) coupled to the ocean-sea ice component NEMO (Madec, 2008). The atmospheric model uses a spectral T42 horizontal grid (i.e. ∼2.8° x 2.8°) with 19 vertical levels. The ocean is discretised on a 2° Mercator mesh with an increased meridional resolution of 0.5° around the equator (ORCA2). Experiments with this configuration

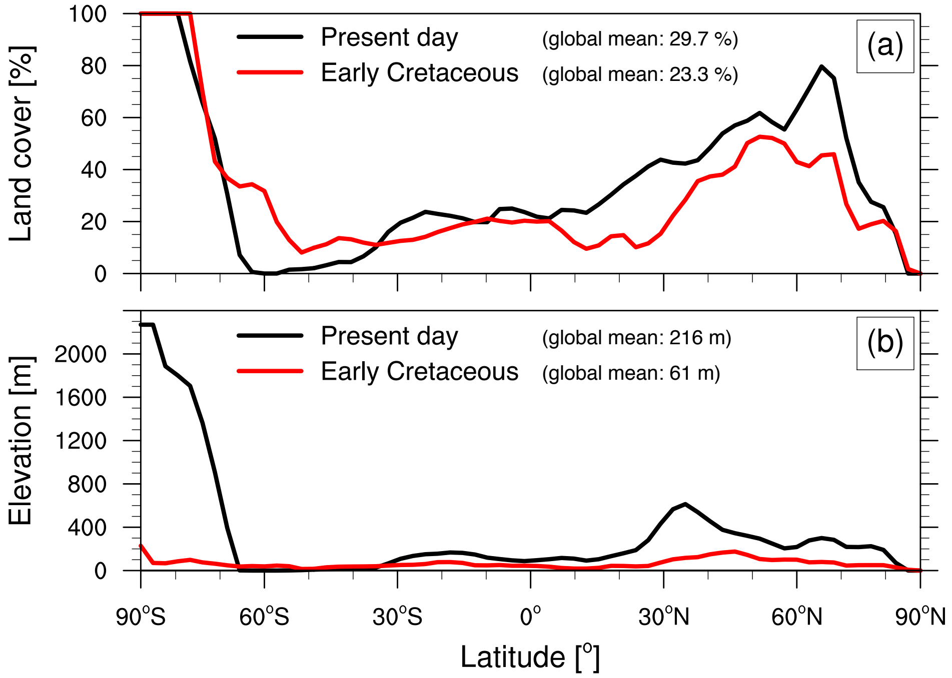

**Figure 2.2:** Comparison of zonal mean (a) land cover and (b) mean elevation between the present-day and Cretaceous model geography.

under present-day boundary conditions are described in Park and Latif (2019). Land topography and ocean bathymetry for the Early Aptian configuration (Fig. 2.1) are adapted from Müller et al. (2008) and Blakey (2008) and are described in Blöhdorn (2013). Main features include an increased interhemispheric symmetry of the continental land masses (Fig. 2.2a) and significantly reduced mean elevations, especially over Antarctica (Fig. 2.2b). Freshwater routing from the continents to the ocean is determined from the orography (Hagemann and Dümenil, 1998). The continents are assumed ice-free to represent evidence from oxygen isotopic records (Moriya et al., 2007; Ando et al., 2009; MacLeod et al., 2013), even though this is still under debate for some cooler intervals of the Cretaceous (Alley and Frakes, 2003; Bowman et al., 2013; Alley et al., 2019). Surface vegetation is prescribed as simplified climate-zone dependent properties with no zonal variations (Blöhdorn, 2013).

We perform Early Aptian integrations with three different atmospheric $CO_2$ concentrations. Two simulations with 600 and 1200 ppmv (hereafter $CRET_{600}$ and $CRET_{1200}$) are used to cover the range of the reported Aptian $CO_2$ reconstructions (Wang et al., 2014; Jing and Bainian, 2018), while we isolate the changes solely induced by the changed paleogeography in a third experiment with the pre-industrial $CO_2$ concentration of 286 ppmv (hereafter $CRET_{286}$). Remaining atmospheric trace gases are set to pre-industrial values. The solar constant for all Cretaceous experiments is lowered from 1365 to 1350 $W/m^2$ to account for a gradual increase in solar luminosity (Gough, 1981; Caldeira and Kasting, 1992). Additionally, we use a KCM reference simulation with the modern geography at a pre-industrial $CO_2$ concentration (hereafter $PD_{286}$). Throughout this study we differentiate between the geographically and radiatively induced temperature changes defined as:

- $\Delta$GEO: Temperature difference due to changed geographical boundary conditions (different land-sea distribution, no continental ice sheets, reduced land elevation and changed land surface),

  i.e. $\Delta$GEO = CRET$_{286}$ - PD$_{286}$

- $\Delta$RAD: Temperature difference due to an approximate quadrupling of the atmospheric CO$_2$ concentration,

  i.e. $\Delta$RAD = CRET$_{1200}$ - CRET$_{286}$

### 2.3.2 Energy balance analysis

By design, climate models simulate the complex interactions of multiple components of the radiation balance in response to changes of the external forcing. This makes a direct assessment of the main controls on the simulated warming and a comparison to other models difficult. We therefore use a 1-D energy balance analysis to quantify the contributions of individual processes to the global mean warming and the changes of the MTG. We closely follow the methodology proposed by Heinemann et al. (2009) and refined by Lunt et al. (2012) and recall the main equations in the following. The zonal mean radiative fluxes from the KCM are used to formulate a simple Energy Balance Model (EBM) in which the incoming shortwave solar radiation is balanced by the outgoing longwave radiation. Local meridional heat transport is assumed to close any difference between the two terms leading to:

$$SW_t^{\downarrow}(1-\alpha) + H = \epsilon\sigma\tau^4 \tag{2.1}$$

where $SW_t^{\downarrow}$ is the incoming solar radiation at the top of the atmosphere, $\alpha$ is the planetary albedo, H is the net meridional heat transport convergence, $\epsilon$ is the longwave emissivity, $\sigma$ is the Stefan–Boltzmann constant and $\tau$ is the EBM surface temperature. The planetary albedo and longwave emissivity for each experiment are calculated with zonal mean radiative fluxes from the KCM as:

$$\alpha = \frac{SW_t^{\uparrow}}{SW_t^{\downarrow}} \tag{2.2}$$

and

$$\epsilon = \frac{LW_t^{\uparrow}}{LW_s^{\uparrow}} \tag{2.3}$$

where $SW_t^{\uparrow}$ and $SW_t^{\downarrow}$ are the upward and downward shortwave fluxes at the top of the atmosphere and $LW_t^{\uparrow}$ and $LW_s^{\uparrow}$ are the upward longwave fluxes at the top of the atmosphere and the surface, respectively. Assuming a black-body radiation of the surface , i.e. $LW_s^{\uparrow} = \sigma\tau^4$, the respective terms in equation 2.1 can be substituted. The use of $SW_t^{net} = SW_t^{\downarrow} - SW_t^{\uparrow}$ and $LW_t^{net} = - LW_t^{\uparrow}$ leads to the convergence of the total meridional heat transport as:

$$H = -(SW_t^{net} + LW_t^{net}) \tag{2.4}$$

Following the definition from Lunt et al. (2012), the EBM surface temperature for each experiment and latitude can therefore be defined as:

$$\tau = (\frac{1}{\epsilon\sigma}(SW_t^{\downarrow}(1-\alpha) + H)^{0.25}) \equiv E(\epsilon, \alpha, H, SW_t^{\downarrow}) \tag{2.5}$$

By comparison of the EBM derived temperatures for the Cretaceous, $E(\epsilon, \alpha, H, SW_t^{\downarrow})$, with those of the present-day configuration, $E(\epsilon', \alpha', H', SW_t^{\downarrow'})$, we can quantify the difference associated with individual EBM input parameters as:

$$\Delta T_{emm} = E(\epsilon, \alpha, H, SW_t^{\downarrow}) - E(\epsilon', \alpha, H, SW_t^{\downarrow}) \tag{2.6}$$

$$\Delta T_{alb} = E(\epsilon, \alpha, H, SW_t^{\downarrow}) - E(\epsilon, \alpha', H, SW_t^{\downarrow}) \tag{2.7}$$

$$\Delta T_{tran} = E(\epsilon, \alpha, H, SW_t^{\downarrow}) - E(\epsilon, \alpha, H', SW_t^{\downarrow}) \tag{2.8}$$

$$\Delta T_{sol} = E(\epsilon, \alpha, H, SW_t^{\downarrow}) - E(\epsilon, \alpha, H, SW_t^{\downarrow'}) \tag{2.9}$$

where $\Delta T_{emm}$, $\Delta T_{alb}$, $\Delta T_{tran}$ and $\Delta T_{sol}$ are the temperature differences between the Early Cretaceous and present-day EBM solely caused by changes in the atmospheric emissivity, the planetary albedo, the meridional heat transport and the solar constant, respectively. The atmospheric emissivity changes are caused by a combination of greenhouse gas changes ($\Delta T_{gg}$), longwave cloud radiative effects ($\Delta T_{lwc}$) and surface elevation differences ($\Delta T_{topo}$):

$$\Delta T_{emm} = \Delta T_{gg} + \Delta T_{lwc} + \Delta T_{topo} \tag{2.10}$$

To derive $\Delta T_{topo}$, we first extrapolate the surface temperatures to the potential temperatures at the global mean surface pressure using a dry adiabatic lapse rate of 9.8 °C/km (as proposed in Heinemann et al., 2009). $\Delta T_{topo}$ is then defined as the difference between the surface and potential temperature change between two experiments. Furthermore, we use the clear-sky (cs) radiative fluxes from the KCM to exclude the influence of cloud radiative effects (CRE). Emissivity changes under clear-sky conditions are only caused by the topographic and greenhouse gas changes. Clear-sky albedo changes can be attributed to surface albedo changes $\Delta T_{salb}$, leading to:

$$\Delta T_{gg} = E(\epsilon_{cs}, \alpha_{cs}, H_{cs}, SW_t^{\downarrow}{}_{cs}) - E(\epsilon'_{cs}, \alpha_{cs}, H_{cs}, SW_t^{\downarrow}{}_{cs}) - \Delta T_{topo} \tag{2.11}$$

$$\Delta T_{salb} = E(\epsilon_{cs}, \alpha_{cs}, H_{cs}, SW_t^{\downarrow}{}_{cs}) - E(\epsilon_{cs}, \alpha'_{cs}, H_{cs}, SW_t^{\downarrow}{}_{cs}) \tag{2.12}$$

Finally, the remaining changes are caused by longwave ($\Delta T_{lwc}$) and shortwave ($\Delta T_{swc}$) cloud effects:

$$\Delta T_{lwc} = \Delta T_{emm} - \Delta T_{gg} - \Delta T_{topo} \tag{2.13}$$

$$\Delta T_{swc} = \Delta T_{alb} - \Delta T_{salb} \tag{2.14}$$

The total, zonal mean surface temperature change between the Cretaceous and present-day experiments can therefore be expressed as the sum of 7 individual components:

$$\Delta T = \Delta T_{gg} + \Delta T_{salb} + \Delta T_{swc} + \Delta T_{lwc} + \Delta T_{topo} + \Delta T_{tran} + \Delta T_{sol} \tag{2.15}$$

### 2.3.3 CMIP5 data

Our analysis aims to separate the Early Cretaceous surface warming into geographically and radiatively driven changes. Some of these, e.g. cloud radiative processes, might be particular sensitive to the choice of the applied model and parameterisation scheme, thereby questioning the robustness of our results. We therefore use a large ensemble of 22 CMIP5 climate models for comparison. We include all models that provide data for the "abrupt4x$CO_2$" experiment, imposing an instantaneous quadrupling of atmospheric CO2, and the corresponding pre-industrial control run "piControl" (Taylor et al., 2012). We use the difference between model years 121-140 of the 4x$CO_2$ experiment and the control run climatology as an estimate of the fast response of the models to enhanced greenhouse gas forcing. We apply the same EBM flux analysis as described in Section 2.3.2 to compare the KCM and CMIP5 results.

## 2.4 Results

### 2.4.1 A note on the choice of initial conditions

To investigate the simulated Early Cretaceous mean state, $CRET_{1200}$ has been initialised with a homogeneous ocean salinity of 35 and temperature of 10 °C and integrated for 6000 model years. Experiments $CRET_{600}$ and $CRET_{286}$ are branched off from $CRET_{1200}$ at model year 1000 and integrated for a further 5000 model years. During the spin-up we noticed a sensitivity of the atmospheric temperatures to the applied numerical time step in ECHAM5 at high $CO_2$ concentrations. We therefore reduced the time step in ECHAM5 from 1800 s to 1200 s for the last 3000 years for all integrations. Results are averaged over the last 500 simulation years. Defining the model steady state is a rather subjective process, but of uttermost importance especially for deep-time simulations where the adjustments from the initial conditions are substantial and take an increased amount of computation time. Commonly used criteria are based on globally averaged surface or deep ocean temperature trends falling below a certain threshold value. Even if we assume that different initial conditions will eventually converge to the same steady state, the needed simulation years to reach this point potentially depend on our choice of initial values and therefore on the initial water column stratification. To test this hypothesis we compare two separate, multi-millennia spin-up realisations of $CRET_{1200}$. Both experiments differ only in the initial temperature and salinity distribution, the applied boundary conditions are the same. One experiment is started from a homo-

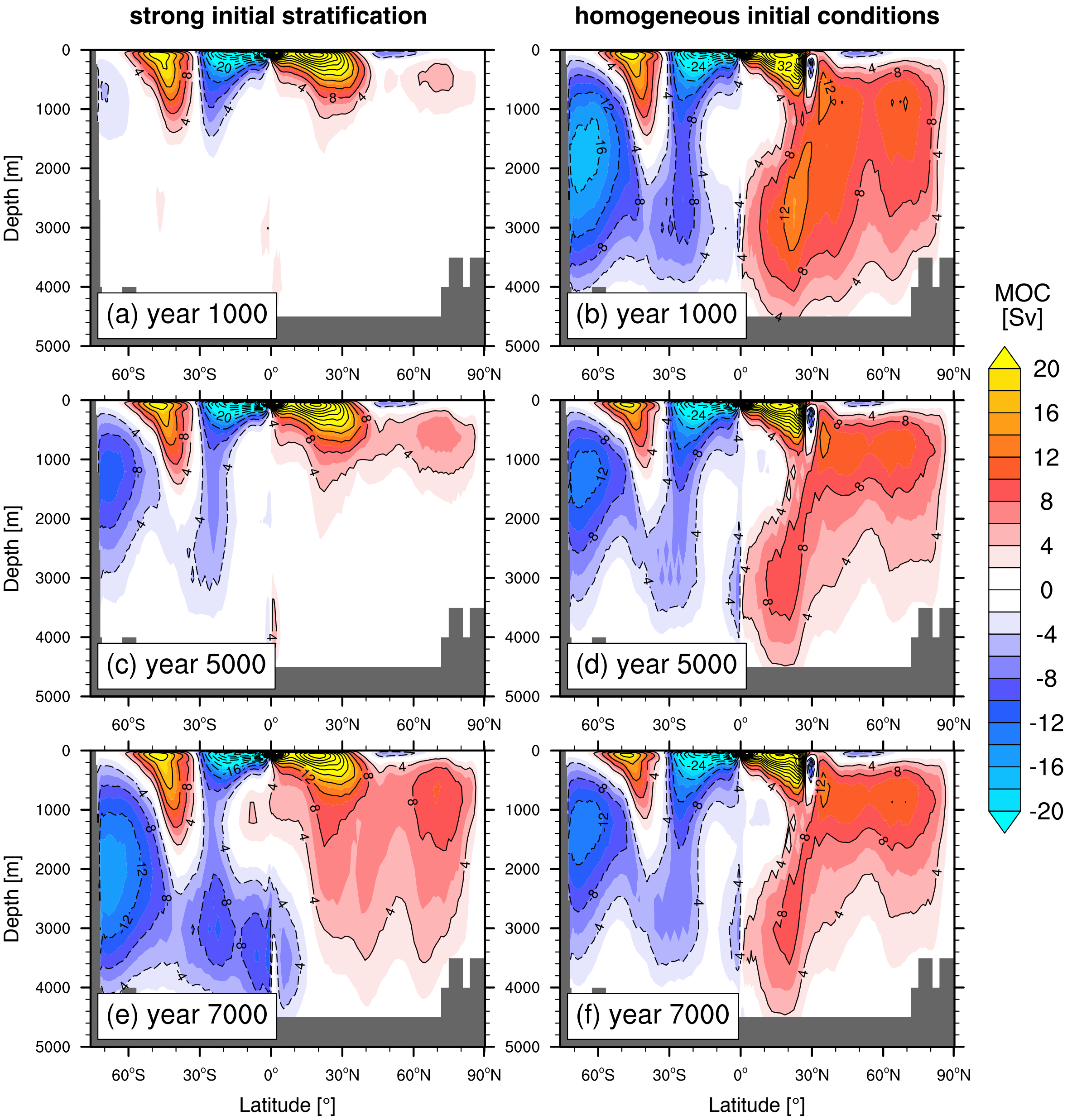

**Figure 2.3:** Evolution of the global meridional overturning streamfunctions for two different CRET$_{1200}$ spin-ups. Both simulations use the same boundary conditions, but different initial conditions. The model is started from either (left) a stratified ocean as used in Blöhdorn (2013) or (right) from a homogeneous temperature and salinity distribution. For comparability, both integrations used the same atmospheric model time step of 1800 s. Fields are averaged for the respective 100 years before the shown date and expressed in Sv (1 Sv = $10^6$ m$^3$/s). Shading interval is 2 Sv, with black contour lines every 4 Sv.

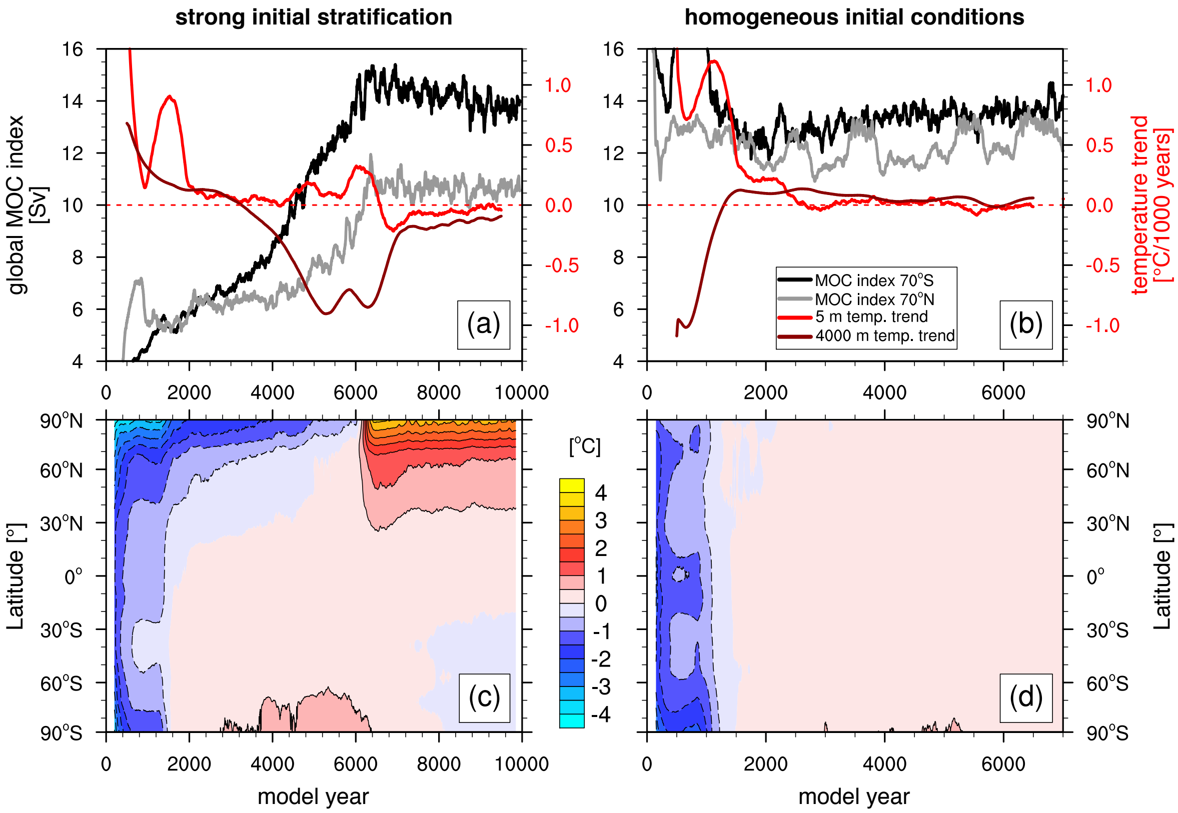

**Figure 2.4:** Evolution of global mean temperature trends and meridional overturning circulation (MOC) for two different CRET$_{1200}$ spin-ups. Simulations are the same as in Figure 2.3. Panels show (a-b) the absolute values of the maximum strength of the MOC at 70°S and 70°N and the global mean ocean temperature trend per 1000 years at 5 m and 4000 m and (c-d) Hovmöller diagrams of the zonal mean surface air temperature expressed as an anomaly to the long-term mean value at each latitude. Globally averaged temperature trends are calculated for a sliding window of 500 years before and after the respective year.

geneous temperature of 10 °C and homogeneous salinity of 35. The second version is a restart from the experiment presented in Blöhdorn (2013). It was initialised with the zonal mean output of a 1000 year-long spin-up with a modern land-sea mask and present-day initial conditions, but forced with the Cretaceous $CO_2$ concentration of 1200 ppmv. High surface freshwater inputs acted to significantly enhance the initial vertical water column stratification. We increased the minimum ocean temperature to 8 °C to accelerate the deep ocean adjustment.

The fundamentally different evolution of the global meridional overturning circulation (MOC) for both spin-up procedures is shown in Fig. 2.3, with the time series of Northern and Southern Hemisphere overturning shown in Fig. 2.4. The ocean surface and bottom water temperature trends for both simulations are close to zero after about 3000 model years and therefore fulfil the commonly applied criteria to define a model equilibrium. In contrast, the comparison of the MOC strength shows that the overturning is still building up for the initially stratified experiment (Fig. 2.4a), while it is already fully developed in the homogeneous spin-up (Fig. 2.4b). The stronger initial stratification, together with the higher surface freshwater forcing caused by the enhanced hydrological cycle, leads to a drastic reduction in global deep water formation (Fig. 2.3a). The steep salinity gradient is only slowly reduced, allowing for a gradual intensification of the MOC in both hemispheres (Fig. 2.3c,e). This process is especially important in the restricted Arctic Ocean which shows a sudden switch from a thermodynamically fresh water system to the onset of deep convection after about 6000 model years (Fig. 2.4a). Resulting deep water export into the proto-Pacific Ocean increases heat advection in the surface layer via mass conservation and warms the high latitudes of the Northern Hemisphere by as much as 3-4 °C (Fig. 2.4c). The resulting ocean temperature adjustments require a total integration time of nearly 10000 model years (Fig. 2.4a), while temperatures in the homogeneous spin-up are already constant after ∼3000 years. The resulting mean state MOC is in both cases dominated by high-latitude deep water formation in both hemispheres. Apart from that, the different initial conditions still lead to a slightly different mean state overturning. Mainly, the homogeneous initial conditions cause to a stronger Northern Hemisphere cell, while the Southern Hemisphere deep cell dominates in the stratified spin-up. Together with the small remaining model drift in the MOC indices (Fig. 2.4a-b), this indicates that even 10000 years of spin-up are not sufficient to completely eliminate differences in the initial conditions, at least not for the deep ocean. The results highlight, that due to the tight coupling between high-latitude deep water formation and the meridional heat transport, a sufficient spin-up of the ocean dynamics is essential for a meaningful analysis of the MTG.

### 2.4.2 Quantifying the surface warming

The simulated annual mean surface temperatures for the pre-industrial and Early Cretaceous simulations are shown in Fig. 2.5. Low-latitude temperatures in $CRET_{286}$ are slightly lower than in $PD_{286}$ due to the reduced solar constant. In contrast, polar regions are significantly warmer. The largest differences are simulated for Antarctica, where the reduced surface elevations (Fig. 2.2b) and the removal of land ice already increase the surface temperatures by more than 20 °C (Fig. 2.6a). The resulting global mean temperature is increased by 0.9 °C, while the geographically driven high-latitude warming reduces the MTG (difference of surface temperatures averaged between 30°S to 30°N and those poleward of 60°S and 60°N) by 24% (Table 2.1). At the low $CO_{286}$ levels, annual mean temperatures fall below 0 °C poleward of ∼55-60°S/N. This latitude range is roughly the same for the modern and Early Cretaceous geography. The 0 °C isotherm is shifted polewards by

**Table 2.1:** Simulated annual mean global mean surface temperatures (GMST) and meridional temperature gradients (MTG). The gradient is defined as the difference between temperatures averaged between 30°S and 30°N and those poleward of 60 °S and 60°N (Fig. 2.6a). Results are shown for the present-day (PD) and Cretaceous (CRET) geographies and reported in °C. Subscripts indicate atmospheric $CO_2$ for the respective simulation.

| Experiment | GMST | MTG land | MTG ocean | MTG land & ocean |
|---|---|---|---|---|
| $PD_{286}$ | 13.3 | 44.9 | 25.3 | 38.9 |
| $CRET_{286}$ | 14.2 (+ 0.9) | 32.6 (-27.4%) | 23.1 (-8.9%) | 29.5 (-24.2%) |
| $CRET_{600}$ | 17.7 (+ 4.4) | 31.3 (-30.3%) | 23.0 (-9.1%) | 26.8 (-31.2%) |
| $CRET_{1200}$ | 22.9 (+ 9.6) | 29.8 (-33.8%) | 21.6 (-14.4%) | 24.1 (-38.0%) |

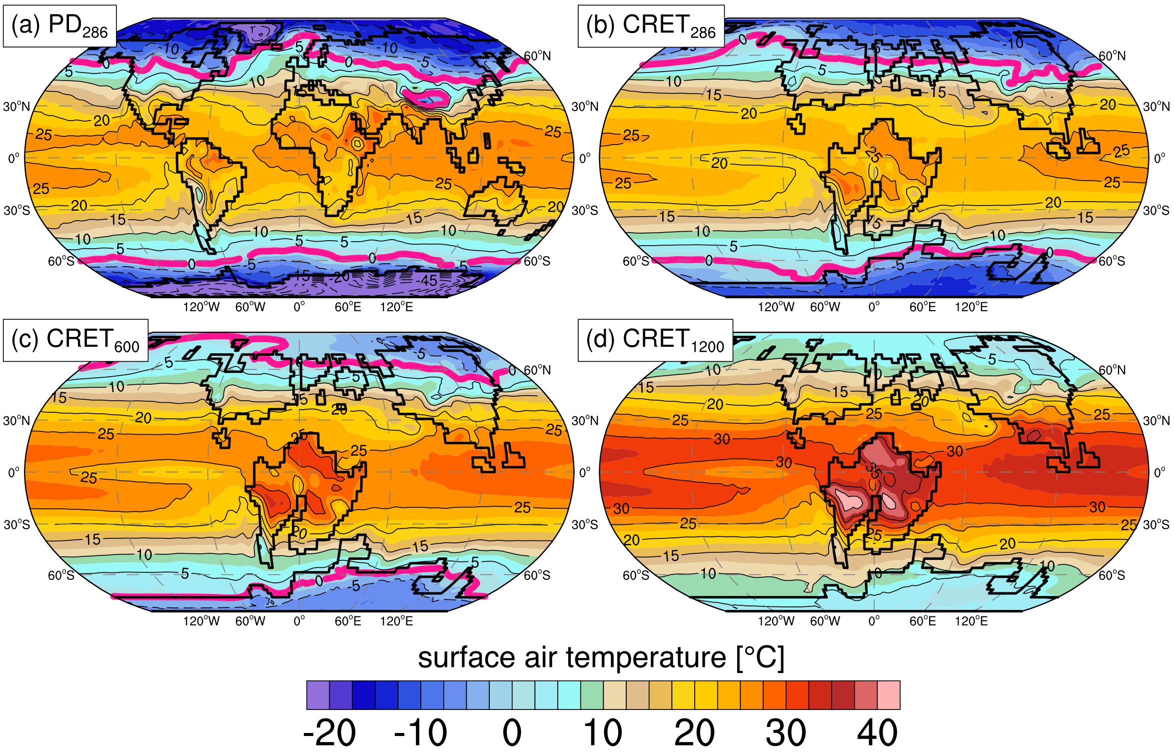

**Figure 2.5:** Simulated annual mean 2 m temperatures for experiments (a) $PD_{286}$, (b) $CRET_{286}$, (c) $CRET_{600}$ and (d) $CRET_{1200}$. Shading interval is 2.5 °C and black contours are shown every 5 °C. Thick pink line indicates the 0 °C isotherm.

$\sim$ 10° in $CRET_{600}$ (Fig. 2.6a). Global mean temperatures are 4.4 °C higher than in $PD_{286}$ and the MTG is reduced by 31%. Strongest surface warming of 9.6 °C is simulated for $CRET_{1200}$, associated with a MTG reduction of 38%. The relative MTG decrease in $CRET_{1200}$ compared to $CRET_{600}$ is higher over the ocean than over the land (Table 2.1). Together with the reduced global land fraction in the Aptian land-sea mask (Fig. 2.2a) this increases the oceanic contribution to the MTG reduction compared to $CRET_{600}$. This explains the strong reduction of the overall MTG of 38%, while the individual decreases over the land (34%) and ocean (14%) are smaller. Overall, annual mean surface temperatures are above freezing for the whole globe in $CRET_{1200}$ (Fig. 2.5d).

The highest global mean temperatures and weakest MTG are simulated for $CRET_{1200}$. The EBM analysis (see Section 2.3.2) allows a direct quantification of the individual processes influencing the surface temperature distribution (Fig. 2.6b). Over 70% of the total global mean warming (7.3 of 9.6 °C) is caused by a greenhouse-gas-induced reduction of the atmospheric emissivity. This includes the direct contribution from the elevated $CO_2$ concentrations and a second, even stronger component, induced by the positive feedback due to the increased atmospheric water vapour content in the warmer atmosphere. Largest greenhouse gas warming is simulated for the Arctic Ocean, in accordance to an enhanced contribution of the lapse-rate feedback. This leads to an overall small reduction of the MTG of 2.5 °C that increases with atmospheric $CO_2$ (Fig. 2.7). The effect of the lapse-rate feedback is masked over Antarctica due to the substantial reduction in surface elevation, quantified as the topographic influence on the surface temperature. While the reduced global mean

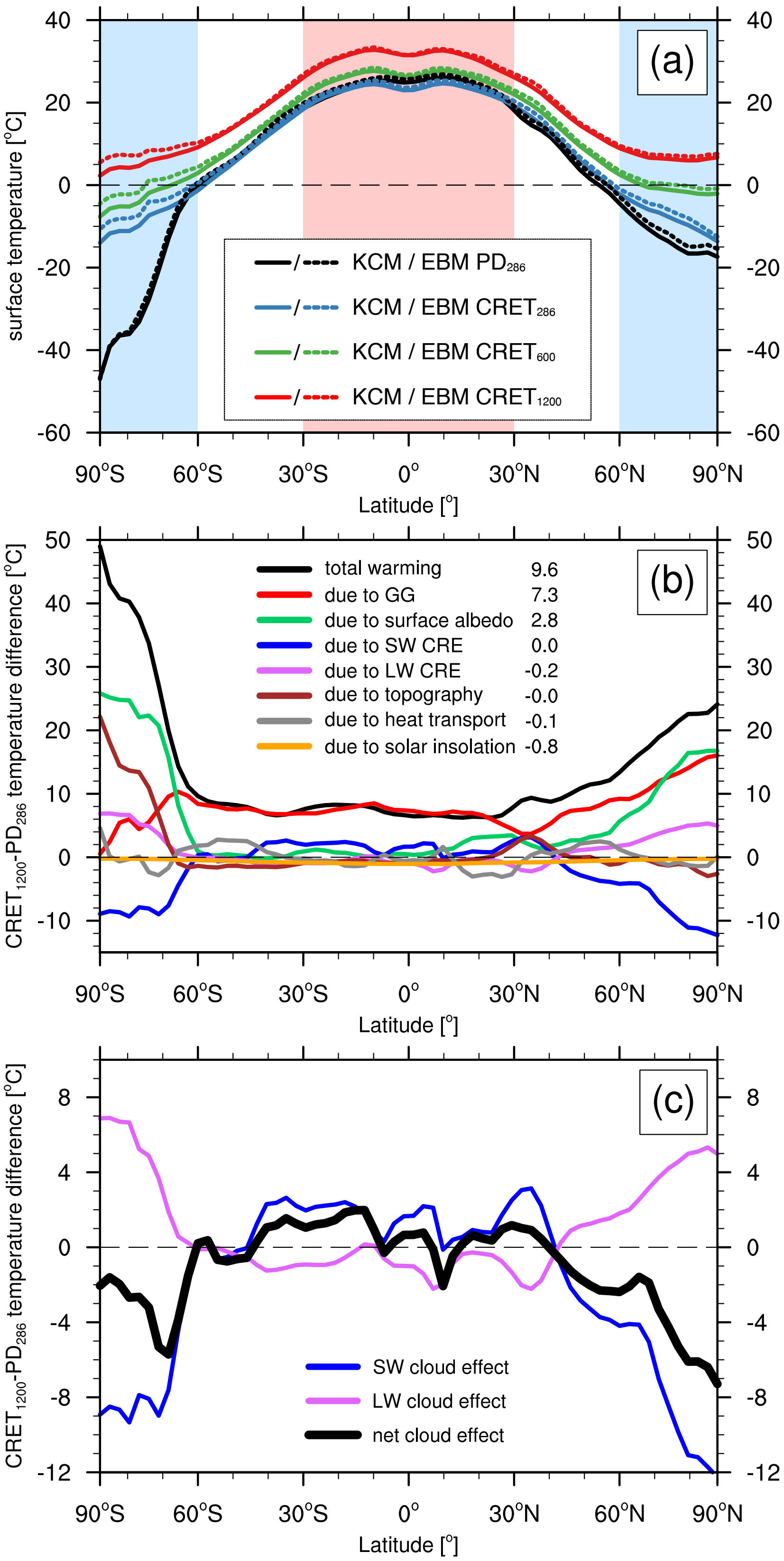

**Figure 2.6:** Simulated zonal mean surface temperatures for the Cretaceous and present-day configurations. Panels show (a) zonal mean 2 m temperatures as simulated by the KCM and approximated by the EBM, (b) the difference in zonal mean temperatures between CRET$_{1200}$ and PD$_{286}$ split into the individual contributions described in Section 2.3.2 and (c) the temperature changes due to clouds. Shading in (a) represent the (red) low-latitude and (blue) high-latitude areas used to define the MTG. Numbers in (b) indicate the global mean temperature change in °C caused by individual processes.

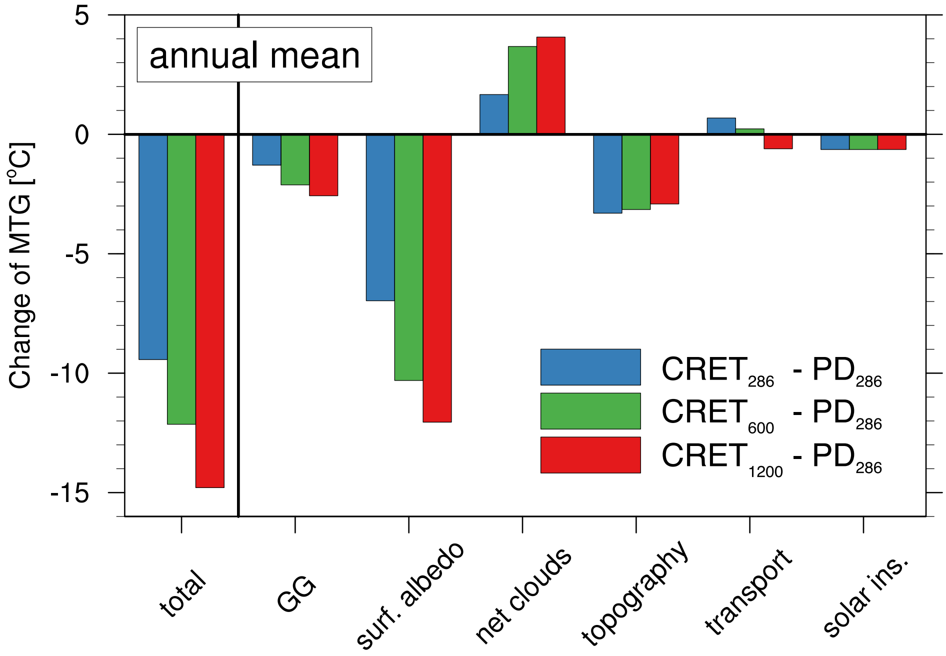

**Figure 2.7:** Changes of the Early Cretaceous annual mean MTG with respect to $PD_{286}$. The total difference is split into the individual processes described in Section 2.3.2. The net cloud effect is the sum of the shortwave and longwave CRE. The MTG is defined as the difference between surface temperatures averaged between 30°S and 30°N and those poleward of 60°S and 60°N.

elevation in the Cretaceous experiments does not change the global mean temperature (Heinemann et al., 2009), local temperatures are increased by up to 20 °C over Antarctica and by 4 °C over the present-day Himalaya. The predominant high-latitude influence reduces the Cretaceous MTG by 3 °C, independent of the $CO_2$ level. The overall largest decrease of the MTG is caused by surface albedo changes. More than half of the 12 °C change of the MTG in $CRET_{1200}$ is already simulated for $CRET_{286}$, highlighting the influence of the prescribed absence of polar ice caps. We attribute the remaining $CO_2$-sensitive ∼5°C reduction to the stronger snow and ice-albedo feedbacks. Globally, the reduced surface albedo during the Early Aptian increased the surface temperature by 2.8 °C. Changes of the atmospheric and oceanic meridional heat transport have only a minor influence on MTG changes. While the effect is positive for $CRET_{286}$, .i.e. a reduced heat transport compared to $PD_{286}$, enhanced deep water formation and associated oceanic heat advection in the Arctic Ocean in $CRET_{1200}$ slightly decrease the resulting MTG. The reduced solar constant during the Early Cretaceous leads to a global mean cooling of 0.8 °C. As the effect scales with the amount of the annual mean insolation, the change at low latitudes is larger than in polar regions. Consequently, the MTG is slightly reduced for all Cretaceous experiments. Cloud radiative effects (CREs) show only a very small influence on the global mean temperature that is dominated by a weak cooling of 0.2 °C due to changes in the simulated longwave radiation. Nevertheless, the pronounced latitudinal differences introduce an important modulation of the MTG (Fig. 2.6c). In general, cloud cover changes influence both the longwave and shortwave radiative fluxes, but their respective height and optical depth determine the relative ratio between both terms. The net cloud effect in $CRET_{1200}$ is dominated by the shortwave CRE leading to small net warming at low latitudes and strong cooling

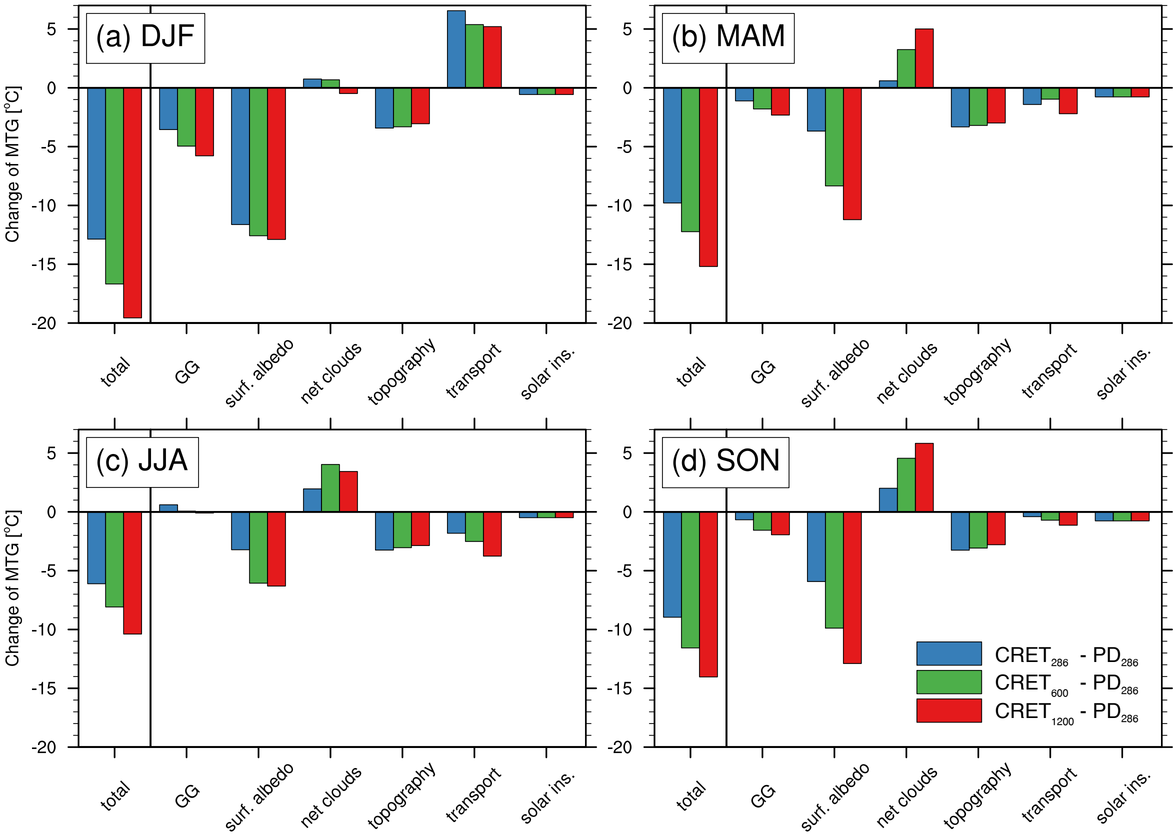

**Figure 2.8:** As in Fig. 2.7, but calculated for the respective seasonal mean temperatures. Panels show months (a) December to February, (b) March to May, (c) June to August and (d) September to November.

at high latitudes. Therefore, the net cloud-induced temperature change is the only process that acts to strengthen the MTG by up to 4 °C. CREs also partly compensate the geographically induced high-latitude warming in $\mathrm{CRET}_{286}$.

The change of the simulated MTG shows pronounced seasonal differences (Fig. 2.8). The MTG reduction in $\mathrm{CRET}_{1200}$ varies between a minimum of 10 °C in the boreal summer months June to August (Fig. 2.8c) and a maximum of nearly 20 °C in the winter months December to February (Fig. 2.8a). The large MTG reduction during the DJF season is mainly caused by surface albedo changes. Maximum solar insolation in the austral summer combined with the reduced albedo of the ice-free Antarctic continent strongly increases polar temperatures, even in $\mathrm{CRET}_{286}$. The stabilising influence of the net cloud effect, visible for all other seasons, diminishes and even slightly contributes to the MTG reduction in $\mathrm{CRET}_{1200}$. High local temperatures reduce the poleward atmospheric heat transport, forming the only stabilising influence on the MTG. The situation reverses of the JJA season. The Southern Hemisphere polar night eliminates the surface albedo influence of Antarctica. The smaller reduction of the MTG is rather caused by the $CO_2$-sensitive ice-albedo feedback in the Arctic Ocean and increased oceanic heat transport. The net cloud effects counteract the high-latitude warming. Overall strength and individual contributions from the individual processes are very similar for the seasons March to May (Fig. 2.8b) and September to November (Fig. 2.8d) and closely resemble the annual mean pattern (Fig. 2.7).

### 2.4.3 Cloud radiative changes

The previous results indicate an important role of CREs in modulating the MTG response to the surface albedo changes. Cloud cover changes are intimately tied to the adjustments of the large-scale atmospheric circulation. We will therefore now turn to the physical causes that drive the Cretaceous atmospheric circulation changes and ultimately control the cloud cover distribution. We separate the geographically forced changes ($\Delta$GEO) from the $CO_2$ effect ($\Delta$RAD) in Fig. 2.9. The results are discussed with focus on three fundamental pathways over which clouds can influence surface temperatures, which are changes in the amount of clouds, their height and their optical thickness. A higher cloud cover will both increase the amount of reflected solar radiation and reduce the outgoing longwave radiation. The shortwave CRE is mainly sensitive to an increase in the optical thickness of low-level ($>$ 680 hPa) clouds, while the longwave CRE increases primarily with the height of the clouds (e.g., Zelinka et al., 2013; Ceppi et al., 2017).

Changes in cloud cover and thickness (expressed as their liquid water content) for $\Delta$GEO are mainly confined to the high latitudes of both hemispheres (Fig. 2.9a,e) and are expressed as an increase of low-level, optically thick clouds that lead to a strong shortwave cooling poleward of 60°S and 60°N (Fig. 2.9g). The cloud cover increase is caused by a drastic reduction of the polar subsidence normally associated with the present-day polar high pressure system, indicated by the positive contours in the reference climatology in Fig. 2.9c. The strongly reduced surface albedo, especially over the ice-free Antarctic continent, increases local surface temperatures during summer and leads to the absence of the polar cell in all Cretaceous simulations. The effect is smaller in the polar regions of the Northern Hemisphere, but also driven by the lower surface albedo resulting from reduced sea-ice cover in $CRET_{286}$ compared to $PD_{286}$. Low latitude changes of vertical atmospheric motions (Fig. 2.9c) are related to the different land-sea distribution and expressed as poleward displacements of the ascending branches of the Hadley cells in both hemispheres. Resulting cloud cover changes and net CRE are overall small.

The $CO_2$ increase in $CRET_{1200}$ leads to a global upward shift of upper tropospheric clouds (Fig. 2.9b) consistent with the vertical displacement of the tropopause in the warmer system. There is an overall tendency of reduced tropical and mid-latitude cloud cover, especially pronounced around the weakened upward branches of the Hadley and Ferrel cell (positive anomalies at negative mean climatology). The reduced, thinner clouds (Fig. 2.9f) lead to a net positive CRE in the low- and mid-latitudes (Fig. 2.9h). The higher latitudes show a different sign of CRE in response to the $CO_2$ increase. The negative shortwave effect due to thicker low-level clouds over the now completely ice-free Arctic leads to a strong net cooling polewards of 50°N. Additionally, the reduction in near-surface clouds and increase at the 800 hPa level indicates an upward displacement of clouds over the Northern Hemisphere polar regions. Even though the temperature-driven increase of liquid cloud water content is also simulated for the higher latitudes of the Southern Hemisphere, the strong negative shortwave CRE is missing over Antarctica, leading to a net cloud induced warming

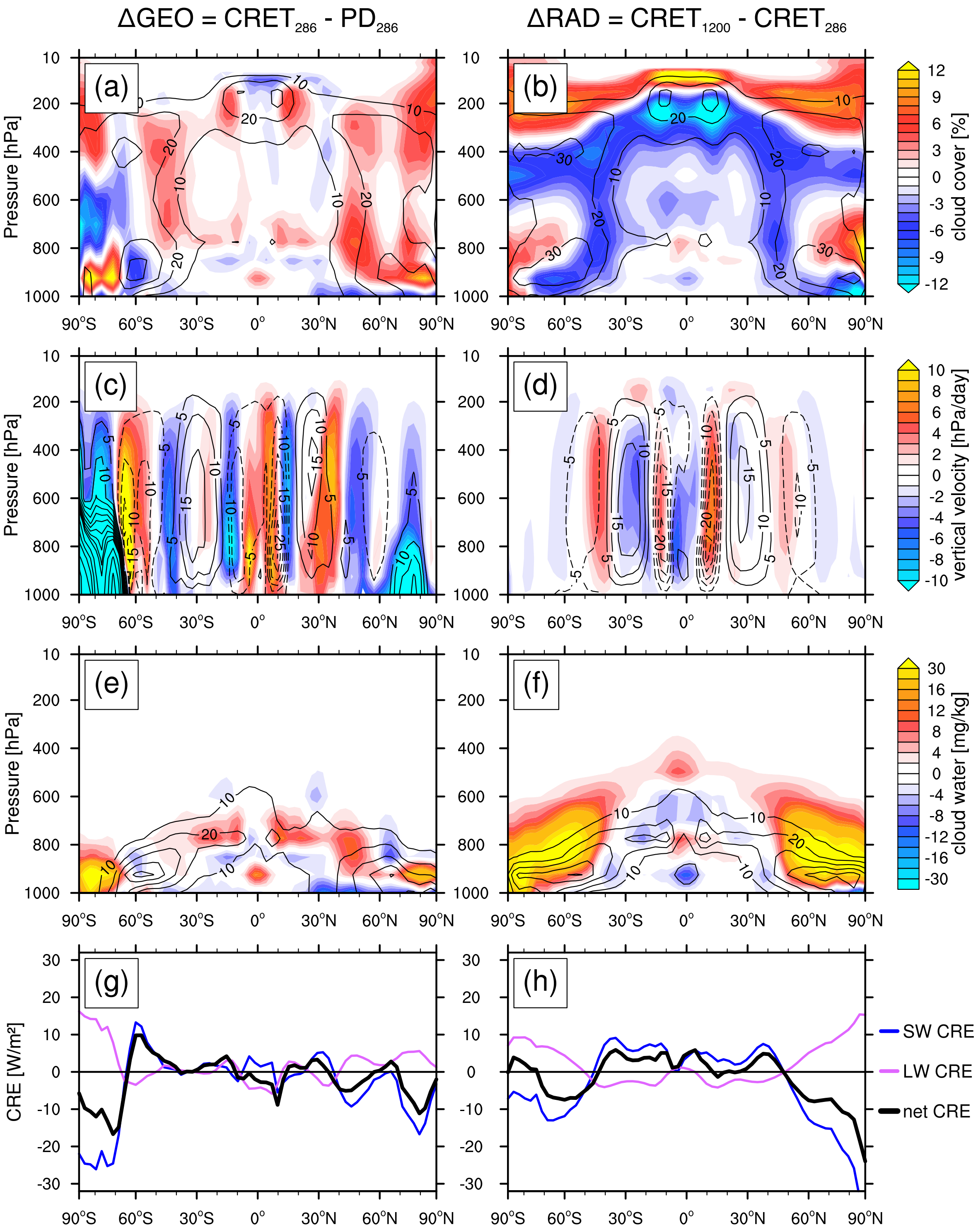

**Figure 2.9:** Atmospheric adjustment to Early Cretaceous geographical and radiative forcing. Panels show zonal mean differences for atmospheric variables for (left) CRET$_{286}$-PD$_{286}$ and (right) CRET$_{1200}$-CRET$_{286}$. Black contour lines show mean climatological fields for (left) PD$_{286}$ and (right) CRET$_{286}$ with dashed contours indicating negative values. Variables shown are (a-b) cloud cover in% of the grid cell, (c-d) vertical pressure velocity in hPa/day, where negative values indicate rising motion, (e-f) cloud liquid water content in mg/kg and (g-h) cloud radiative effects (CRE) for shortwave (SW), longwave (LW) and the net effect of SW+LW in W/m$^2$.

of the polar surface.

The net CRE for $\Delta$RAD changes its sign at around 75°S. This latitude coincides with the transition from the Southern Ocean to the Antarctic continent (Fig. 2.2a) and implies a sensitivity of the cloud response to the surface conditions. The difference in the seasonal cycle of the CREs for the continental Southern Hemisphere and the predominantly marine Northern Hemisphere is shown in Fig. 2.10. The net CRE warms the surface of both poles during the respective polar winter months (Fig. 2.10i-j) due to the missing shortwave radiation and associated CREs (Fig. 2.10g-h). This effect is also simulated for the present-day configuration, but its strength increases for the Early Cretaceous and in response to elevated $CO_2$ due to higher upper-level cloud cover (Fig. 2.10a-b and Fig. 2.9a-b). The cooling shortwave CRE starts with the onset of solar insolation in the respective spring months and quickly outweighs the longwave effects. Low-level cloud cover over both poles during these months is very similar for all 4 simulations (Fig. 2.10c-d). The simultaneous drop in low-level cloud cover and increase at higher altitudes over Antarctica changes the relative influence of shortwave and longwave CREs and decreases the net cloud cooling effect during the peak summer months. In contrast, low-level cloud cover over the Arctic is constant throughout the year and upper-level cloud cover even reduces during boreal spring and summer. The resulting large negative net CRE severely limits the Arctic surface warming during summer (Fig. 2.10l). Together with the longwave-induced winter warming. the simulated surface temperatures in $\mathrm{CRET}_{1200}$ are very constant throughout the year (2-11 °C). On the other hand, the reduced cloud influence over Antarctica allows summer temperatures to rise to nearly 30 °C in $\mathrm{CRET}_{1200}$ (Fig. 2.10l). Respective cold month mean temperatures do not fall below -9 °C. It is noteworthy that $\mathrm{PD}_{286}$ simulates a very similar amplitude of the seasonal temperature cycle of ~25 °C for both polar regions. The combined effect of the Cretaceous surface albedo and cloud changes therefore enhance the seasonal cycle over Antarctica and reduce it over the Arctic.

### 2.4.4 Comparison to CMIP5 models

Our results imply that clouds played a vital role in modulating the Early Cretaceous surface temperature distribution, both for the adaption to changes in the paleogeography as well as to higher greenhouse gas concentrations. On the other hand, cloud-related processes are still the main cause for the large intermodel spread in future warming simulations (Ceppi et al., 2017). We therefore apply the same EBM analysis to the output of 22 CMIP5 climate models forced with an abrupt quadrupling of the atmospheric $CO_2$. Our factorisation of the simulated Early Cretaceous surface warming allows us to directly compare the results for $\Delta$RAD with the CMIP5 ensemble to assess the robustness for our results. We note that the CMIP5 experiments are only integrated for 150 model years and therefore only capture the fast response of the climate system. Therefore, the usefulness of a direct comparison of the magnitude of the simulated global mean warming between KCM and the CMIP5 models is very limited. To still assess the relative sensitivity of our results,

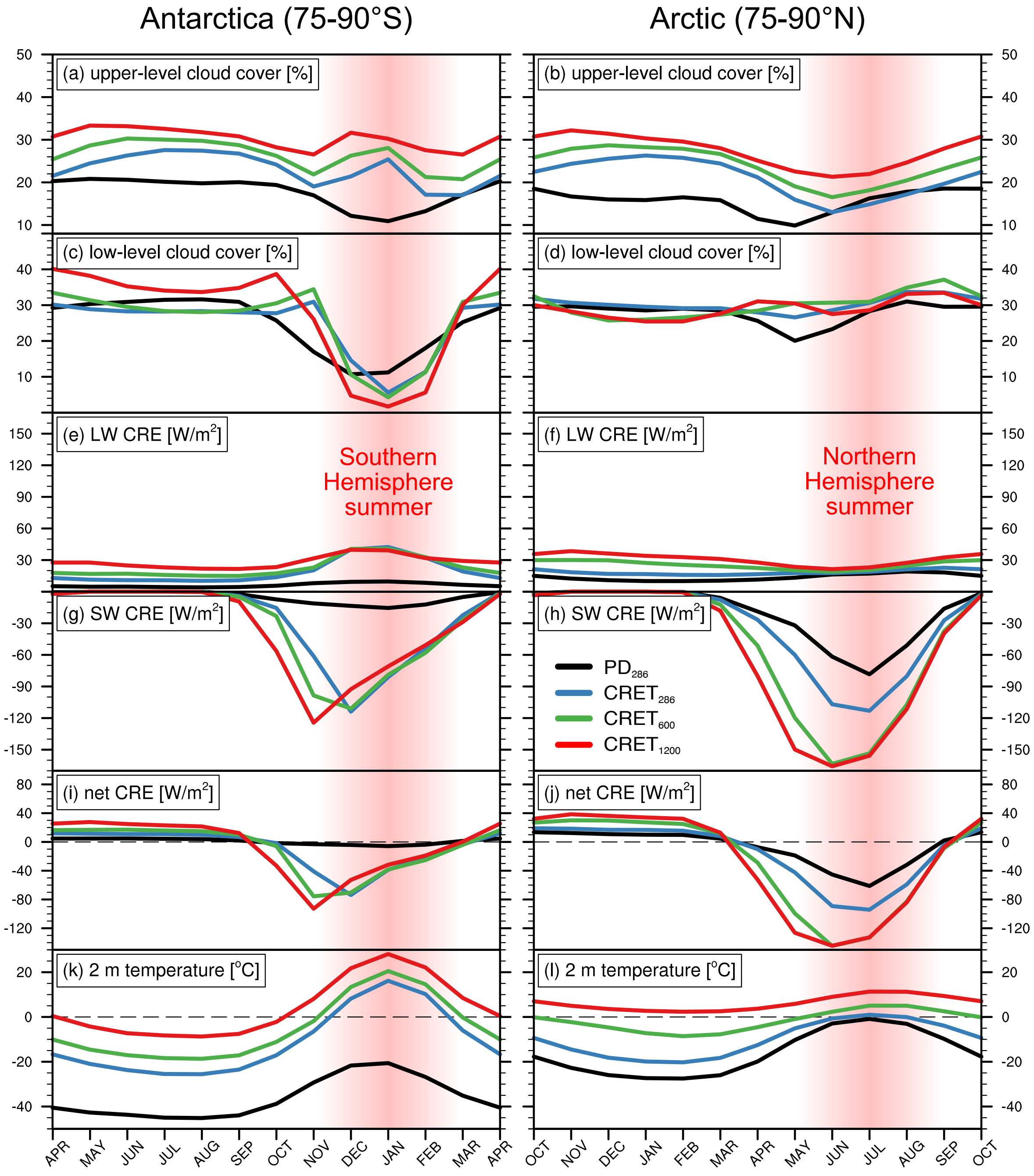

**Figure 2.10:** Seasonal cycle of polar cloud radiative effects for the present day and the Cretaceous. Monthly means are averaged for (left) 75-90°S and (right) 75-90°N. Panels show (a-b) upper-level, i.e. 350-225 hPa, cloud cover, (c-d) low-level, i.e. > 700 hPa, cloud cover, (e-f) shortwave CRE, (g-h) longwave CRE, (i-j) net CRE and (k-l) 2 m surface air temperature.

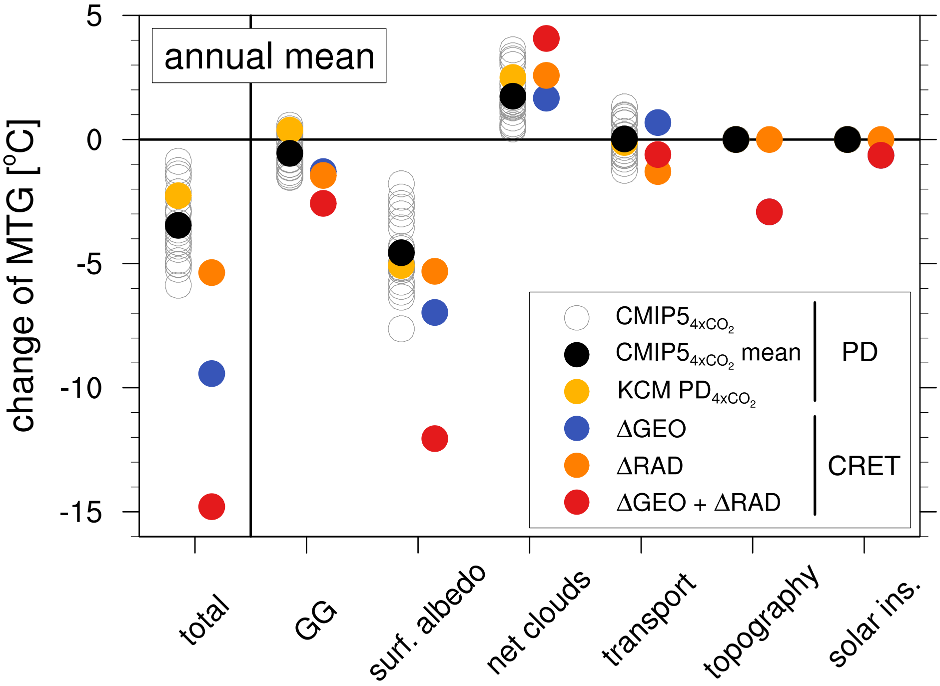

**Figure 2.11:** Changes of the modern and Early Cretaceous annual mean MTG. The total difference is split into the individual processes described in Section 2.3.2. CMIP5 changes are defined as the difference of years 121-140 of the "abrupt4xCO$_2$" experiment to the long-term pre-industrial reference climatology. For comparison, a KCM simulation following the CMIP5 "abrupt4xCO$_2$" protocol is also included. Changes caused by the geographical forcing are defined as ΔGEO = CRET$_{286}$ - PD$_{286}$, while the radiative effect is calculated as ΔRAD = CRET$_{1200}$ - CRET$_{286}$.

we calculate the equilibrium climate sensitivity (ECS) following the method proposed in Andrews et al. (2012). This analysis assumes a linear relation between the top of the atmosphere radiative imbalance caused by a sudden CO$_2$ increase and the resulting global mean surface temperature change. A simple linear regression yields the equilibrium temperature response. We apply this method to the CMIP5 models and comparable CO$_2$ quadrupling experiments for the KCM with present-day and Early Cretaceous geography (see Appendix Fig. 2.A1). The approximated surface warming caused by a doubling of the atmospheric CO$_2$ ranges between 2-4.6 °C for the CMIP5 models (see Appendix Fig. 2.A2). The equivalent present-day KCM simulation yields an ECS of 4.1 °C. This demonstrates that the ECS for the KCM is comparable to other CMIP5 models, but also implies that the simulated total surface warming of 9.6 °C for the Early Cretaceous should be treated as an upper end estimate of the global mean temperature at 1200 ppmv CO$_2$. The resulting ECS for the Early Cretaceous geography is lower by about 0.5 °C. We attribute this mainly to the different sea-ice cover mean states in the reference simulations CRET$_{286}$ and PD$_{286}$. Annual mean sea-ice cover for the Arctic Ocean north of 60°N is reduced from 67% in PD$_{286}$ to 44% in CRET$_{286}$ due to changes in the high-latitude ocean circulation. This in turn reduces the contribution of the ice-albedo feedback to the global mean warming and resulting ECS for the Early Cretaceous.

In contrast to the simulated absolute warming, we assume that a direct comparison of the MTG changes between the KCM and CMIP5 results is possible due to the potentially compensating effect of remaining model drifts in the shorter CMIP5 simulations. The equivalent KCM PD$_{4xCO_2}$

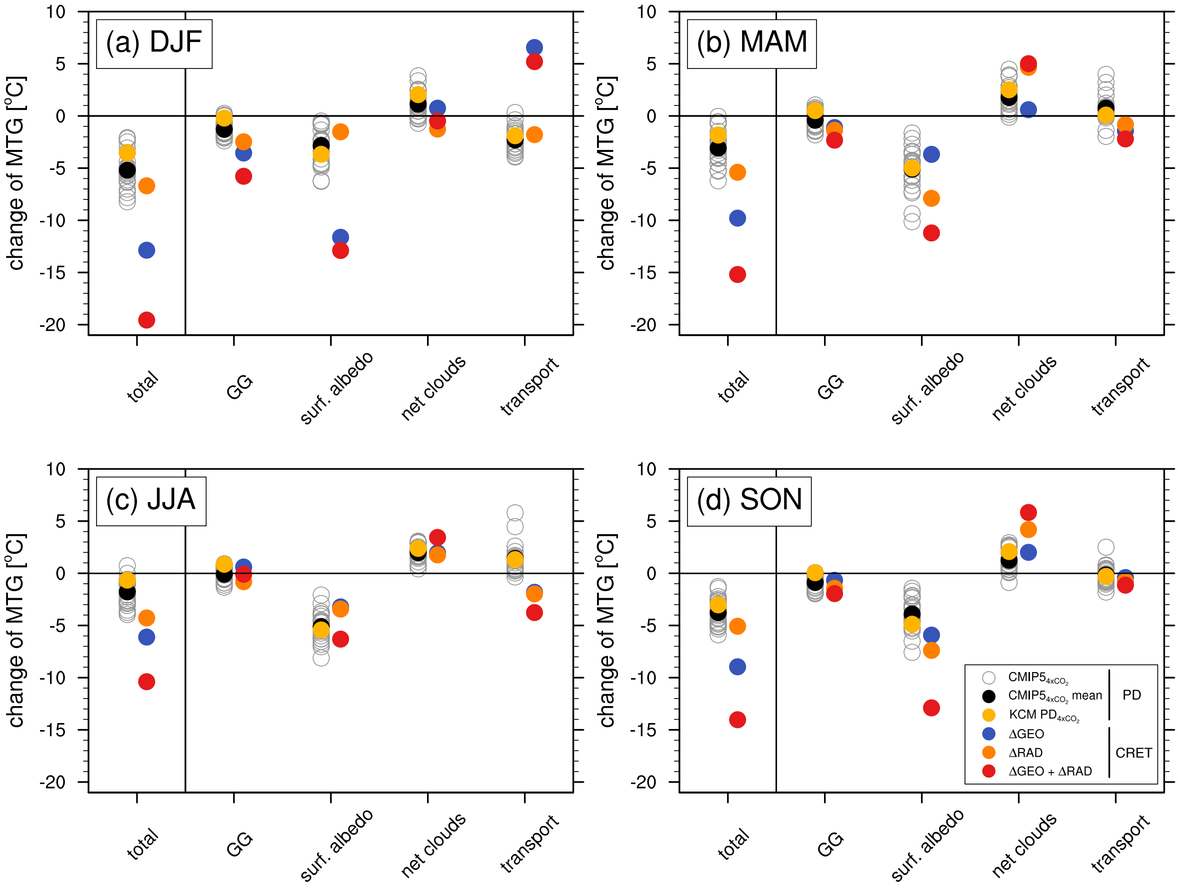

**Figure 2.12:** As in Fig. 2.11, but calculated for the respective seasonal mean temperatures. Panels show months (a) December to February, (b) March to May, (c) June to August and (d) September to November. For simplicity, differences due to topography and solar insolation changes are not shown as they do not vary between individual Cretaceous simulations and do not, by definition, influence the present-day simulations. Nevertheless, they are still included in the sum of the total Cretaceous changes.

experiment simulates MTG changes very similar to the CMIP5 ensemble mean (Fig. 2.11). The overall MTG reduction in the CMIP5 ensemble mean of 3.5 °C is considerably lower than the 14.8 °C change in CRET$_{1200}$. As shown before, 2/3 of the reduction in CRET$_{1200}$ is already caused by ΔGEO. The remaining ΔRAD response is within the range of the CMIP5 ensemble. Differences in the radiative response between the present-day and Early Cretaceous KCM are limited to the greenhouse gas and heat transport changes. The stronger reduction of the MTG due to the Cretaceous greenhouse effect can be explained by an enhanced lapse-rate feedback over the low-elevation Antarctic continent. The increased meridional heat transport in CRET$_{1200}$ is associated with enhanced deep water formation in the ice-free Arctic Ocean. The contribution of surface albedo changes, i.e. the snow and ice-albedo feedback, is close to 5 °C for both time slices. Importantly, the CMIP5 models support the MTG strengthening due to cloud feedbacks. Even though the absolute magnitude varies between individual ensemble members, all models agree on the sign of the net cloud influence. The strength of the cloud change in ΔRAD is close the CMIP5 ensemble mean, the overall large change in CRET$_{1200}$ is caused by the additional contribution by ΔGEO.

The seasonal changes of the MTG controls are shown in Fig. 2.12. The topography and solar insolation changes are constant for all KCM simulations and zero for the CMIP5 simulations. They are therefore excluded from Fig. 2.12 but still accounted for in the total KCM changes. Both KCM and CMIP5 models simulate the largest MTG changes during the months December to January (Fig. 2.12a) and the smallest influence for June to August (Fig. 2.12c). Again, the amplitude of the seasonal cycle is enhanced for the Cretaceous simulations. The discussed seasonality of the net cloud influence in $\Delta$RAD, mainly expressed as change of sign during the December to January season, is not visible for the present-day geography. The CMIP5 models and KCM $\mathrm{PD}_{4xCO_2}$ simulate a constant strengthening of the MTG throughout the year. The strong reduction of meridional heat transport during December to January in $\mathrm{CRET}_{1200}$ is entirely controlled by the removal of the land ice in $\Delta$GEO, the $\Delta$RAD signal is similar to the present day. For the months June to August, the radiative response differs in the sign between the present-day and Cretaceous geography. While the elevated $CO_2$ levels increase the poleward heat transport for the Cretaceous, it is decreased for the present-day simulations.

### 2.4.5 Shifts of the large-scale atmospheric circulation

Changes of the tropospheric temperature gradient are inevitably linked to adjustments of the large-scale atmospheric circulation that will ultimately influence the regional-scale response to the global warming signal. The change in several key circulation metrics, split in the relative contributions from $\Delta$GEO and $\Delta$RAD, is shown for the KCM and CMIP5 results in Fig. 2.13 and Table 2.2. The circulation metrics are defined following Ceppi and Hartmann (2016) and quantify the latitudinal positions of the edges of the Hadley cell (first zero-crossing of the atmospheric mass streamfunction (Fig. 2.14) poleward of the maximum), the subtropical dry zones (precipitation equals evaporation) and the jet stream (maximum zonal-mean zonal surface wind) as well as the strength of the Hadley cell (maximum of the mass streamfunction). In accordance to numerous previous studies, the CMIP5 results indicate a poleward expansion of the atmospheric circulation and, at least for the Northern Hemisphere, a weakening of the Hadley cell strength (e.g.; Lu et al., 2007; Bony et al., 2013; Ceppi and Hartmann, 2016; Hu et al., 2018). While the latitudinal shift is somewhat weaker in the Northern Hemisphere, the CMIP5 ensemble mean edges of the Hadley cell, the dry zone and the jet latitude in the Southern Hemisphere are shifted poleward by about 2°. Again, the poleward expansion will likely scale with a further increase of the global mean temperature change and should therefore only be interpreted as the fast atmospheric response for the shorter CIP5 integrations. Nevertheless, the KCM also shows a consistent poleward displacement of all three metrics for $\Delta$RAD that is within the CMIP5 ensemble range. The response to $\Delta$GEO differs significantly between individual metrics and both hemispheres. While the Northern Hemisphere is mainly characterised by a slight northward shift of the Hadley cell and dry zone edge that is comparable to $\Delta$RAD, the geographically induced changes in the Southern Hemisphere balance or even outweigh the radiative influence. A similar observation can be made for the Northern Hemisphere maximum surface wind.

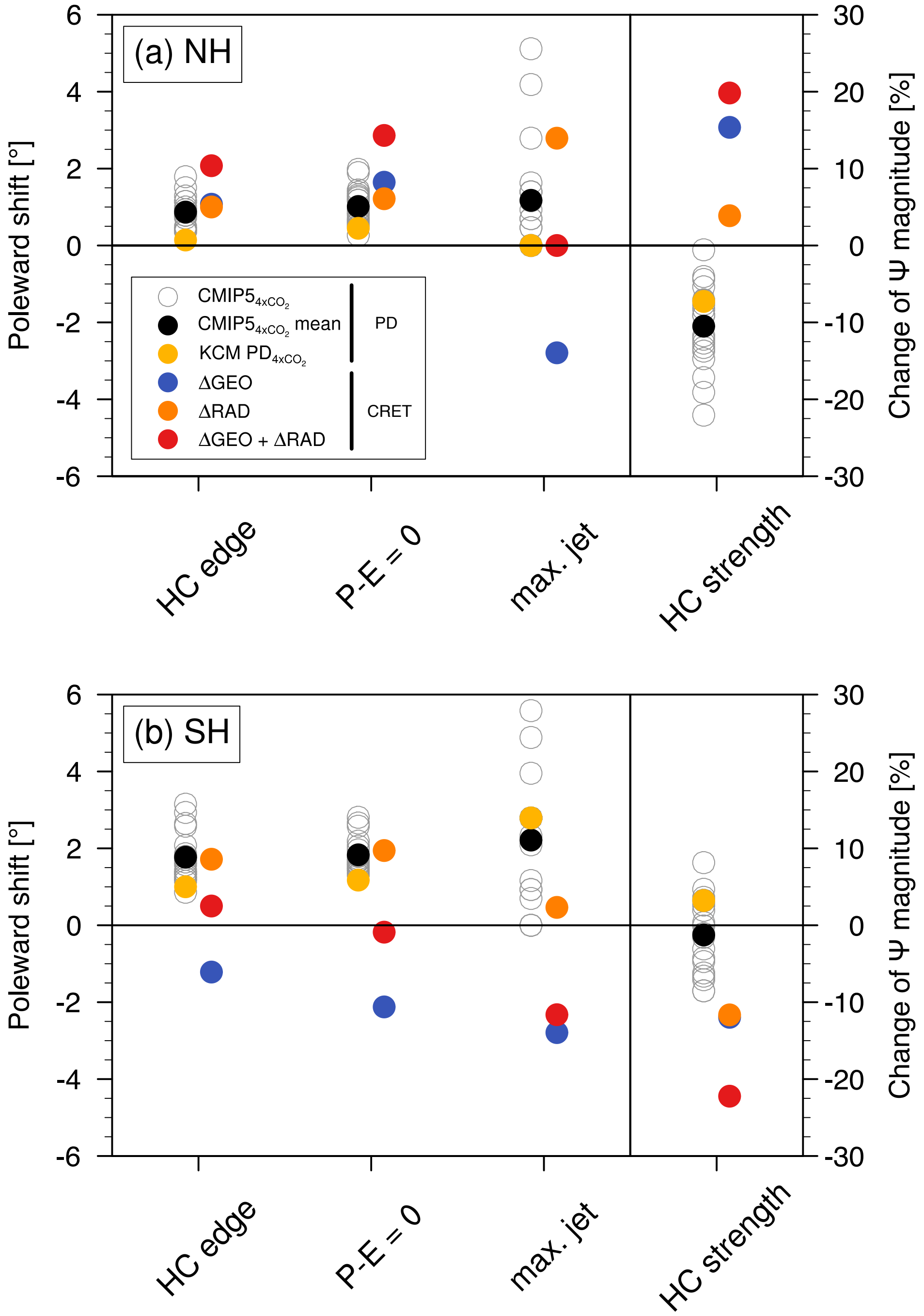

**Figure 2.13:** Changes of the modern and Early Cretaceous large-scale atmospheric circulation. Circulation metrics are calculated for the (a) Northern and (b) Southern Hemisphere and expressed as anomalies to the respective control simulation, i.e. compared to CRET$_{286}$ for $\Delta$RAD and compared to the pre-industrial run for all other data points. Positive values indicate a poleward shift. The definition of circulation metrics follows Ceppi and Hartmann (2016). The Hadley cell (HC) edge is the latitude of the first zero crossing of the atmospheric mass streamfunction $\Psi$ at the 500 hPa level (Fig. 2.14). The edge of the subtropical dry zone is the latitude where precipitation equals evaporation (P - E = 0). The latitude of maximum zonal-mean zonal surface wind is used as an approximation of the surface representation of the jet latitude. The HC strength is the maximum (minimum) of $\Psi$ in the Northern (Southern) Hemisphere and expressed as the change of the absolute magnitude in %. A positive value therefore represents an increased mass transport. All metrics are calculated on the basis of annual mean data. Absolute values for the KCM simulations are shown in Table 2.2.

**Table 2.2:** Overview of atmospheric circulation metrics for the KCM simulations. Definitions for the metrics are given in Fig. 2.13. Values in brackets indicate the difference to the pre-industrial experiment $PD_{286}$ with positive values defined as a poleward shift or increase of the absolute mass transport.

| | HC edge [°] | | P-E = 0 [°] | | max. jet [°] | | HC strength [$10^{10}$kg/s] | |
|---|---|---|---|---|---|---|---|---|
| | NH | SH | NH | SH | NH | SH | NH | SH |
| $PD_{286}$ | 30.4 | -31.7 | 39.4 | -40.4 | 51.6 | -48.8 | 7.4 | -10.8 |
| $CRET_{286}$ | 31.4 (+1.0) | -30.4 (-1.3) | 41.0 (+1.6) | -38.3 (-2.1) | 48.8 (+2.8) | -46.0 (-2.8) | 8.5 (+15%) | -9.5 (-12%) |
| $CRET_{600}$ | 31.9 (+1.5) | -31.1 (-0.6) | 41.6 (+2.2) | -38.9 (-1.5) | 50.7 (+0.9) | -46.0 (-2.8) | 8.6 (+16%) | -9.1 (-16%) |
| $CRET_{1200}$ | 32.4 (+2.0) | -32.2 (+0.5) | 42.2 (+2.8) | -40.3 (-0.1) | 51.6 (+0.0) | -46.5 (-2.3) | 8.9 (+20%) | -8.4 (-22%) |

The contrast between both hemispheres is even greater for the changes in the Hadley cell strength. $\Delta$RAD and $\Delta$GEO both contribute equally to an overall mass transport reduction of 22% in the Southern Hemisphere (Table 2.2), while the Northern Hemisphere cell strengthens by about 20%. No CMIP5 model simulates a strengthening of the Northern Hemisphere Hadley cell, thereby indicating not only a direct adjustment of the atmospheric circulation to the different geography, but also a modulation of the radiative response. While the results in Fig. 2.13 are annual mean changes, the atmospheric mass streamfunction shows a pronounced seasonal cycle with largest transport rates in the respective winter hemisphere (Fig. 2.14). The seasonal split reveals that the increase in the annual mean Northern Hemisphere streamfunction in $CRET_{1200}$ (Fig. 2.14d) is associated with a decrease of the Hadley cell strength during the winter months (Fig. 2.14h), but a strengthening and poleward expansion during boreal spring (Fig. 2.14l). This shift is already visible in $CRET_{286}$ (Fig. 2.14f,j). Furthermore, the maximum of the Cretaceous Northern Hemisphere streamfunction shifts to a more northern position during December to March and leads to the increase in the annual mean climatology. In contrast, the reduction of the austral winter mass transport in the Southern Hemisphere (Fig. 2.14p) is also visible for the respective spring months (Fig. 2.14t) and leads to the general slowdown of the annual mean transport rates (Table 2.2). Overall, the removal of the continental ice masses and the increased interhemispheric symmetry in the land-sea distribution (Fig. 2.2) diminishes the overall contrast in the Hadley cell strength between both hemisphere that is evident for the present-day geography. Furthermore, the seasonal cycle of the Hadley cell mass transport is significantly reduced for the Early Cretaceous.

## 2.5 Discussion

We present a suite of new climate model simulations for the Early Cretaceous. The boundary conditions are designed to represent an Early Aptian (~125 Ma) time slice without continental ice sheets. Experiments are performed at a range of atmospheric $CO_2$ concentrations and compared to a pre-industrial reference simulation to explicitly distinguish between geographically and radiatively forced changes of the climate system. The applied maximum atmospheric $CO_2$ concentration of 1200 ppmv represents reconstructed peak conditions during OAE 1a (Heimhofer et

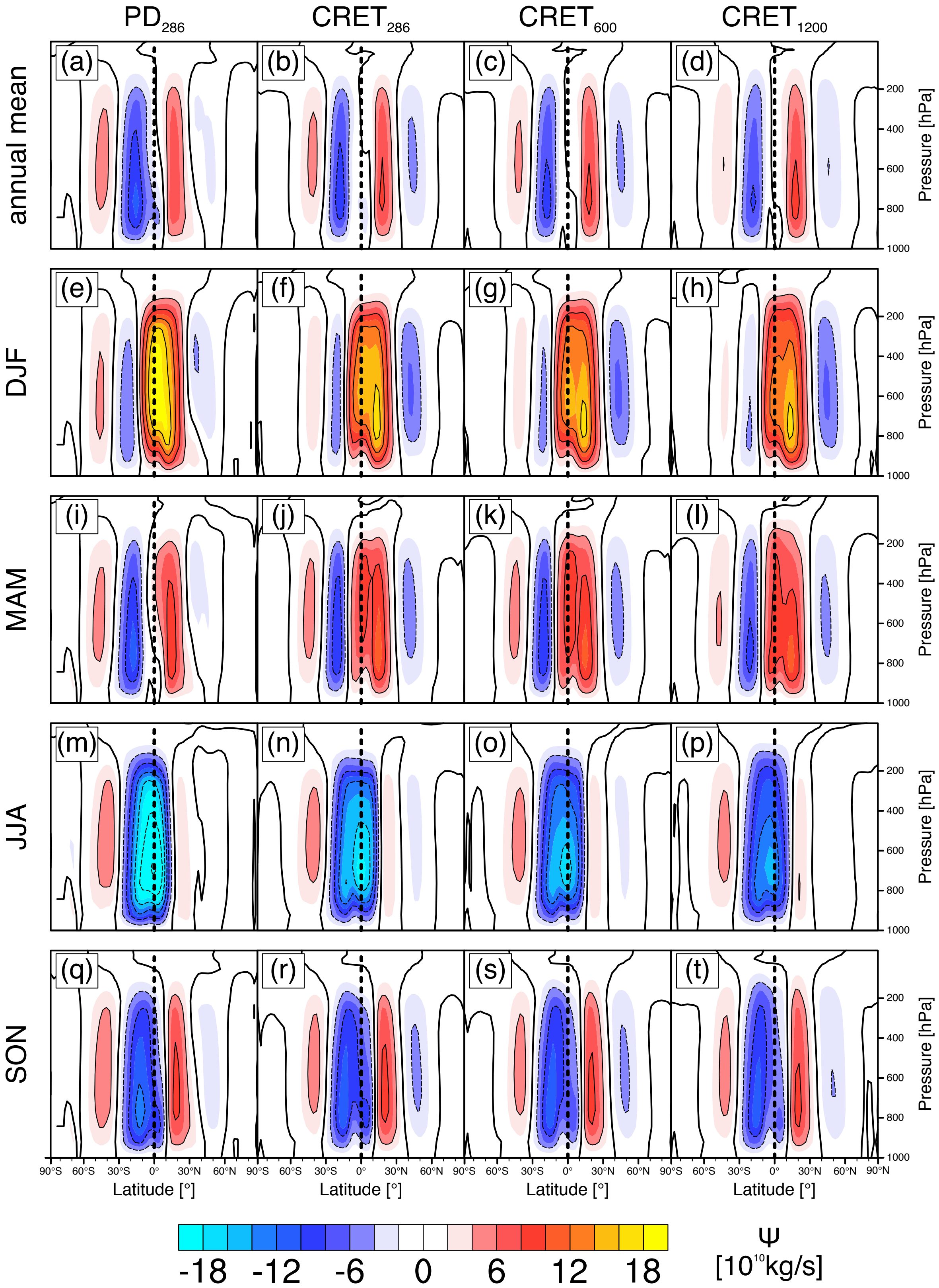

**Figure 2.14:** Atmospheric meridional mass streamfunction for the pre-industrial and Early Cretaceous KCM experiments. Positive values indicate clockwise circulation. Fields are shown for the (a-d) annual mean and (e-t) respective 3-month seasonal means. Shading interval is 2x$10^{10}$kg/s with the black contour line every 4x$10^{10}$kg/s. The black line indicates the zero contour.

al., 2004; Passalia, 2009; Sun et al., 2016). The simulated temperature distribution therefore provides valuable constraints on the atmospheric and oceanic dynamics that might have influenced the global-scale carbon cycle perturbations. Annual mean surface temperatures in $CRET_{1200}$ reach 22.9 °C and are 9.6 °C higher than for pre-industrial conditions. The warming is amplified at high latitudes leading to above-freezing annual mean surface temperatures across the globe. A direct comparison to derived proxy temperatures is limited by the sparse availability of quantitative estimates of surface temperatures for the Early Cretaceous (O'Brien et al., 2017). This is particularly evident in the lack of robust planktonic foraminiferal oxygen isotope data in consequence of the overall low abundance and enhanced dissolution of foraminiferal calcite (O'Brien et al., 2017). Available $TEX_{86}$-derived ocean temperatures for the Early Aptian tropical Pacific range between 30 to 36 °C (Dumitrescu et al., 2006) and agree with maximum SSTs of ~34 °C in $CRET_{1200}$. On the other hand, $TEX_{86}$ samples form the mid-latitude proto-North Atlantic (Naafs and Pancost, 2014) and higher mid-latitude Falkland Plateau (Jenkyns et al., 2012) already exceed the simulated SSTs by ~8 and more than 15 °C, respectively, and indicate a much flatter MTG in both hemispheres than even in $CRET_{1200}$. Sub-Arctic Berriasian to late Valanginian (~145-135 Ma) marine temperatures estimated by belemnite clumped isotope thermometry range between 10-20 °C (Price and Passey, 2013). Equivalent maximum $CRET_{1200}$ temperatures at the approximate paleolatitude of 60-65°N do not exceed 10 °C. Given that mean $CO_2$ concentrations were not significantly different than during the Early Aptian (Wang et al., 2014) and belemnite-derived temperatures from the Vocontian Basin also indicate comparable subtropical temperatures for both periods (Bodin et al., 2015), this further highlights the apparent lower reconstructed than simulated MTG during the Early Cretaceous.

The still existing discrepancies between models and proxies on the fundamental characteristics of the Early Cretaceous greenhouse climate call for a profound analysis of the processes that govern the simulated large-scale temperature distribution and how they differ between individual models. In contrast to other past greenhouse periods like the Early Eocene (Lunt et al., 2012) or the mid-Pliocene (Haywood et al., 2010), there is no coordinated model intercomparison for the Cretaceous. As an intermediate step to enhance the comparability to other modelling results we applied an EBM flux analysis to quantify the influence of individual processes on the simulated warming and to assess how they shape the MTG. By this we can compare the magnitude of the Early Cretaceous warming with the results of a similar analysis of four Early Eocene models that were forced with four times the pre-industrial $CO_2$ concentrations (HadCM3L, GISS, CCSM_W and CCSM_H; Lunt et al., 2012). Changes in the atmospheric greenhouse gas concentrations and the surface albedo are the two only processes that contributed to the 9.6 °C global mean surface warming in $CRET_{1200}$. The overall magnitude is comparable to the Early Eocene results that range between 7.9 to 11.0 °C. In the KCM, the reduced atmospheric emissivity in consequence of the enhanced atmospheric $CO_2$, amplified by a stronger water vapour feedback, leads to a global mean warming of 7.3 °C, which accounts for more than 70% of the total temperature change. The strength of the greenhouse gas warming in the Early Eocene models ranges between 5.9 and 8.3 °C, representing a relative contribution to the overall warming between 69 to 76%. Even though our analysis revealed a relatively high ECS for the KCM, the direct $CO_2$ induced global warming for the Early Cretaceous is therefore very similar to the Early Eocene results. The lower surface albedo, i.e. reduced land and sea ice cover, in $\mathrm{CRET}_{1200}$ causes a further warming of 2.8 °C. Three of the four Eocene models support the changes in the surface albedo as the second most important influence on surface temperatures (warming range between 1.8 and 4.3 °C). In contrast, the GISS model (Roberts et al., 2011) shows a very weak warming of 0.1 °C due to surface albedo changes, but instead a strong warming contribution of 2.4 °C due to cloud feedbacks.

Surface albedo changes represent the dominant influence on the MTG for all Cretaceous and CMIP5 simulations. The removed land ice and the radiative ice-albedo feedback both contribute equally to the overall 12 °C change of the MTG in $\mathrm{CRET}_{1200}$. The strength of the ice-albedo influence matches the CMIP5 ensemble mean. While cloud-related processes do not significantly change the global mean temperature in $\mathrm{CRET}_{1200}$, our analysis reveals an important role of CRE in stabilising the Early Cretaceous MTG. Cloud feedbacks in response to global warming primarily influence the radiation balance by three fundamental mechanisms (see review in Ceppi et al., 2017):

- Rising free tropospheric clouds decrease the cloud emission temperature and therefore emit less longwave radiation to space.
- A decreasing low-level cloud cover at tropical and subtropical latitudes increases the shortwave radiation reaching the surface.
- The increased temperatures enhance the occurrence of liquid water relative to ice in mixed-phase clouds and in turn increase the optical depth and reflectivity of high-latitude low clouds.

While the strength and physical mechanisms of the individual feedbacks have been extensively discussed for the present-day and future warming projections (e.g., Wetherald and Manabe, 1986; Zelinka and Hartmann, 2010; Zelinka et al., 2013; Emory et al., 2014; McCoy et al., 2015; Ceppi et al., 2017), our analysis reveals three important results for the Early Aptian. First, all three described feedbacks are also simulated for the high-$CO_2$ Cretaceous simulation. Their distinct spatial structure lead to a net cloud-induced warming at lower latitudes and cooling in polar regions and thereby to a strengthening of the MTG. Second, the magnitude of the simulated cloud influence on the MTG is comparable to the present-day CMIP5 results and all models agree on the sign of this feedback. We are therefore confident that the discussed large-scale cloud changes for the Cretaceous represent a robust feature across the current generation of climate models. Third, the reduced polar subsidence and increased low-level cloud cover also partly compensate the polar amplification caused by the reduced surface albedo of the Cretaceous geography. Importantly, we show that the

Cretaceous ice-free surface enhances the regional and seasonal variability of the CRE and consequently the seasonal cycle of surface temperatures. The total cloud response to the geographical and radiative changes leads to a strengthening of the MTG of more than 4 °C and is therefore stronger than any changes caused by the lapse-rate feedback or the meridional heat transport.

Our analysis supports previous modelling studies showing that changes of the meridional heat transport in the ocean and atmosphere were not the dominant controls on the global MTG reduction (Heinemann et al., 2009; Lunt et al., 2012). On regional scales, on the other hand, we find important differences between the present-day and the Cretaceous poleward heat advection. The Hadley cell, the meridional component of the tropical atmospheric circulation, shows a distinctly reduced seasonality for the Early Cretaceous geography. Furthermore, the annual mean mass transport response to an increase of atmospheric $CO_2$ even differs on the sign of the change between both hemispheres. This questions the straightforward applicability of concepts of the present-day Hadley cell dynamics for deep-time periods. Given the potential importance of the Hadley cell dynamics on regional depositional environments during the Cretaceous (Wagner et al., 2013), we argue that further work needs to explicitly account for this the time-slice dependence of the mean state.

Changes in the meridional heat transport are also simulated for the restricted Arctic Ocean. Compared to the pre-industrial simulation, the enhanced high-latitude Northern Hemisphere contribution to the global deep water formation increases the oceanic heat transport in the North Pacific and zonal mean temperatures at ∼60°N by 3 °C. This process is only active in the higher-$CO_2$, sea-ice-free simulations and therefore provides a slight positive feedback between increasing $CO_2$ and a reduction of the MTG. Additionally, we show that the onset of the high-latitude Arctic convection critically depends the choice of initial conditions for the model and the applied integration time. In one of our simulations, the initial strong vertical water column stratification in the Arctic Ocean, caused by large surface fresh water inputs, was only slightly reduced over the course of the first 6000 model years. Intriguingly, the global mean temperature trends, the metric commonly used to define a model equilibrium, were very low over the spin-up period. The sudden onset of deep convection in the Arctic Ocean increased surface temperatures over the whole mid and high latitudes by several degrees. A similar slow adjustment of the restricted basin is reported in Heinemann et al. (2009). We therefore propose that defining model equilibria by means of remaining temperature trends alone may not be sufficient for deep-time paleo simulations. A comprehensive understanding of simulated temperature evolution in combination with dynamic variables, e.g. MOC strength, may help identifying intermodel differences of simulated ocean stratification and/or surface temperatures partly caused by insufficient model spin-ups. Particular attention should be paid to remaining model drifts in high-latitude restricted basins.

Uncertainties in available boundary conditions and unavoidable subjective choices in the model setup likely influence the presented results. One apparent shortcoming of most deep-time paleomodelling studies is the focus on $CO_2$ as the only trace gas that influenced past warming. Other greenhouse gas concentrations are generally assumed at their pre-industrial concentrations due to a lack of available reconstructions. Especially elevated methane concentrations have been proposed as a mechanism to intensify global warmth during past greenhouse climates (Pancost et al., 2007; Williscroft et al., 2017) and to particularly promote high-latitude warming (Sloan et al., 1992). Furthermore, the prescribed land surface and vegetation cover in our simulations limits the dynamical response of the Cretaceous surface climate and potentially underestimates high-latitude warming due to missing vegetation feedbacks (Upchurch et al., 1998; Levis et al., 2000; DeConto et al., 2000). We further note that our factorisation in geographical and radiative changes is idealised. Even though the reduced surface elevation of Antarctica would potentially support ice-free conditions at lower $CO_2$ concentrations during the Cretaceous, an absence of land ice in $CRET_{286}$ at the pre-industrial $CO_2$ level is rather unlikely. Modelling studies indicate a threshold for perennial ice accumulation for the Aptian Antarctica between 750 to 840 ppmv $CO_2$ (Ladant and Donnadieu, 2016), even though the fidelity of these results is ultimately limited by the large uncertainties about the elevation history of Antarctica. We therefore conclude that the overall change from an ice-covered Antarctica in $PD_{286}$ to an ice-free state in $CRET_{1200}$ is reasonable, but the individual influence of $\Delta$GEO compared to $\Delta$RAD might be overestimated.

## 2.6 Summary and Conclusions

We use new climate model experiments to quantify the Early Aptian (∼125 Ma) surface warming in response to elevated atmospheric $CO_2$ concentrations and changes of the paleogeography. Based on an EBM flux analysis and constrained by CMIP5 ensemble data we conclude that:

- Peak $CO_2$ concentrations of 1200 ppmv resulted in a global mean surface temperature of 22.9 °C. The overall warming of 9.6 °C, compared to pre-industrial conditions, was caused by an enhanced greenhouse effect (∼70%) and a reduced surface albedo (∼30%).
- The reduction of the respective meridional surface temperature gradient of 14.8 °C (38%) was primarily driven by a reduced high-latitude surface albedo and topography, i.e. the prescribed non-$CO_2$ boundary conditions. Resulting annual mean temperatures were above freezing globally, but still below available mid- and high-latitude proxy data.
- Cloud feedbacks warmed the low-latitudes and cooled the polar regions and therefore partly compensated the polar amplification caused by geographical and radiative changes.
- The strength and sign of the cloud influence on the meridional temperature gradient is consistent with CMIP5 warming experiments applying a present-day geography.
- Our study demonstrates that, on a global scale, the separation of individual warming mechanisms can both improve our understanding of the time-slice-dependent controls on the sur-

face temperature as well as facilitate the intercomparison with other models. This is a vital step in identifying similarities between past greenhouse intervals and in revealing potential differences between individual models that can guide future model development.

- On the regional scale, however, the radiative response can be modulated by the paleogeography. This limits the direct applicability of dynamical frameworks derived from present-day geography. Our results from the restricted Arctic Ocean and the interhemispheric differences in the Hadley cell response demonstrate the need for dedicated time-slice experiments to enable a meaningful comparison to the proxy record.

This chapter quantified the simulated surface warming during the Early Aptian. The direct comparison to other climate models forced with enhanced greenhouse gas concentrations under different paleogeographic conditions revealed a high intermodel consistency in the strength of the predicted overall warming and the mechanisms that controlled the MTG. Nevertheless, the comparison to the available proxy-derived temperatures still shows an underestimation of mid- and high-latitude warming in the models. The next chapter will directly address this longstanding problem in paleoclimatology and show that the presented model simulations can help to identify systematic biases in the available proxy techniques. By the close integration of our simulations with a large compilation of Cretaceous $TEX_{86}$ data we are therefore able to significantly decrease the model-data temperature misfit for the Early Aptian and to re-evaluate the Cretaceous temperature evolution.

## Acknowledgements

Model integrations were conducted at the Computing Center of Kiel University. We thank Janine Blöhdorn for generating most of the Cretaceous boundary conditions for the model and Stefan Hagemann for constructing the parameters for the hydrological discharge model. We acknowledge the World Climate Research Program's Working Group on Coupled Modelling, which is responsible for CMIP, and we thank the climate modelling groups for producing and making available their model output. For CMIP the U.S. Department of Energy's Program for Climate Model Diagnosis and Intercomparison provides coordinating support and led development of software infrastructure in partnership with the Global Organization for Earth System Science Portals.

## References

Abbot, D. S. and Eli Tziperman (2008). "Sea ice, high-latitude convection, and equable climates". In: *Geophysical Research Letters* 35.3, pp. 1–5. DOI: `10.1029/2007GL032286`.

Alley, N. F. and L. A. Frakes (2003). “First known Cretaceous glaciation: Livingston tillite member of the Cadna-owie Formation, South Australia”. In: *Australian Journal of Earth Sciences* 50.2, pp. 139–144. DOI: `10.1046/j.1440-0952.2003.00984.x`.

Alley, N. F., S. B. Hore, and L. A. Frakes (2019). “Glaciations at high-latitude Southern Australia during the Early Cretaceous”. In: *Australian Journal of Earth Sciences*, pp. 1–51. DOI: `10.1080/08120099.2019.1590457`.

Amiot, Romain, Christophe Lécuyer, Eric Buffetaut, Frédéric Fluteau, Serge Legendre, and François Martineau (2004). “Latitudinal temperature gradient during the Cretaceous Upper Campanian-Middle Maastrichtian: $\delta$18O record of continental vertebrates”. In: *Earth and Planetary Science Letters* 226.1-2, pp. 255–272. DOI: `10.1016/j.epsl.2004.07.015`.

Ando, Atsushi, Brian T. Huber, Kenneth G. MacLeod, Tomoko Ohta, and Boo Keun Khim (2009). “Blake Nose stable isotopic evidence against the mid-Cenomanian glaciation hypothesis”. In: *Geology* 37.5, pp. 451–454. DOI: `10.1130/G25580A.1`.

Andrews, Timothy, Jonathan M. Gregory, Mark J. Webb, and Karl E. Taylor (2012). “Forcing, feedbacks and climate sensitivity in CMIP5 coupled atmosphere-ocean climate models”. In: *Geophysical Research Letters* 39.9. DOI: `10.1029/2012GL051607`.

Arthur, M. A., W. E. Dean, and S. O. Schlanger (1985). “Variations in the Global Carbon Cycle During the Cretaceous Related to Climate, Volcanism, and Changes in Atmospheric CO 2”. In: *Geophysical Monograph Series*. Vol. 32, pp. 504–529. DOI: `10.1029/GM032p0504`.

Barron, E. J. and William H. Peterson (1989). “Model Simulation of the Cretaceous Ocean Circulation”. In: *Science* 244.4905, pp. 684–686. DOI: `10.1126/science.244.4905.684`.

Barron, E. J., S. L. Thompson, and S. H. Schneider (1981). “An Ice-Free Cretaceous? Results from Climate Model Simulations”. In: *Science* 212.4494, pp. 501–508. DOI: `10.1126/science.212.4494.501`.

Barron, E. J. and W. M. Washington (1984). “The role of geographic variables in explaining paleoclimates: results from Cretaceous climate model sensitivity studies.” In: *Journal of Geophysical Research* 89.D1, pp. 1267–1279. DOI: `10.1029/JD089iD01p01267`.

Barron, Eric J. (1983). “A warm, equable Cretaceous: The nature of the problem”. In: *Earth-Science Reviews* 19.4, pp. 305–338. DOI: `10.1016/0012-8252(83)90001-6`.

Barron, Eric J., Peter J. Fawcett, David Pollard, and Starley L Thompson (1993). “Model simulations of Cretaceous climates: the role of geography and carbon dioxide”. In: *Philosophical Transactions of the Royal Society of London. Series B: Biological Sciences*. DOI: `10.1098/rstb.1993.0116`.

Barron, Eric J. and Warren M. Washington (1985). “Warm Cretaceous Climates: High Atmospheric CO2 as a Plausible Mechanism”. In: *The Carbon Cycle and Atmospheric CO2: Natural Variations Archaen to Present*. Ed. by E.T. Sundquist and W.S: Broecker. Vol. 32. American Geophysical Union, pp. 546–553. DOI: `10.1029/GM032p0546`.

Barron, Eric J, Peter J Fawcett, William H Peterson, David Pollard, and Starley L Thompson (1995). “A “simulation” of Mid-Cretaceous climate”. In: *Paleoceanography* 10.5, pp. 953–962. DOI: `10.1029/95PA01624`.

Behrooz, L., B. D.A. Naafs, A. J. Dickson, G. D. Love, S. J. Batenburg, and R. D. Pancost (2018). "Astronomically Driven Variations in Depositional Environments in the South Atlantic During the Early Cretaceous". In: *Paleoceanography and Paleoclimatology* 33.8, pp. 894–912. DOI: `10.1029/2018PA003338`.

Bentum, Elisabeth C. van, Almut Hetzel, Hans-J. Brumsack, Astrid Forster, Gert-Jan Reichart, and Jaap S. Sinninghe Damsté (2009). "Reconstruction of water column anoxia in the equatorial Atlantic during the Cenomanian–Turonian oceanic anoxic event using biomarker and trace metal proxies". In: *Palaeogeography, Palaeoclimatology, Palaeoecology* 280.3-4, pp. 489–498. DOI: `10.1016/j.palaeo.2009.07.003`.

Blakey, Ronald C (2008). "Gondwana paleogeography from assembly to breakup—A 500 m.y. odyssey". In: *Special Paper 441: Resolving the Late Paleozoic Ice Age in Time and Space*. Vol. 441. 01. Geological Society of America, pp. 1–28. DOI: `10.1130/2008.2441(01)`.

Blöhdorn, Janine (2013). "Klima und Ozeanzirkulation der Frühen Kreide im Kiel Climate Model". PhD thesis. Christian-Albrechts-Universität Kiel, p. 121.

Bodin, Stéphane, Philipp Meissner, Nico M.M. Janssen, Thomas Steuber, and Jörg Mutterlose (2015). "Large igneous provinces and organic carbon burial: Controls on global temperature and continental weathering during the Early Cretaceous". In: *Global and Planetary Change* 133, pp. 238–253. DOI: `10.1016/j.gloplacha.2015.09.001`.

Bony, Sandrine, Gilles Bellon, Daniel Klocke, Steven Sherwood, Solange Fermepin, and Sébastien Denvil (2013). "Robust direct effect of carbon dioxide on tropical circulation and regional precipitation". In: *Nature Geoscience* 6.6, pp. 447–451. DOI: `10.1038/ngeo1799`.

Bowman, Vanessa C., Jane E. Francis, and James B. Riding (2013). "Late Cretaceous winter sea ice in Antarctica?" In: *Geology* 41.12, pp. 1227–1230. DOI: `10.1130/G34891.1`.

Bralower, Timothy J. (2008). "Volcanic cause of catastrophe". In: *Nature* 454.7202, pp. 285–287. DOI: `10.1038/454285a`.

Caldeira, Ken and James F Kasting (1992). "The life span of biosphere revisited, (Caldeira et Kasting Nature 1992.pdf". In: *Nature* 360, pp. 721–723.

Ceppi, Paulo, Florent Brient, Mark D. Zelinka, and Dennis L. Hartmann (2017). "Cloud feedback mechanisms and their representation in global climate models". In: *Wiley Interdisciplinary Reviews: Climate Change* 8.4. DOI: `10.1002/wcc.465`.

Ceppi, Paulo and Dennis L. Hartmann (2016). "Clouds and the atmospheric circulation response to warming". In: *Journal of Climate* 29.2, pp. 783–799. DOI: `10.1175/JCLI-D-15-0394.1`.

DeConto, Robert M., Esther C. Brady, Jon Bergengren, and William W. Hay (2000). "Late Cretaceous climate, vegetation, and ocean interactions". In: *Warm Climates in Earth History*. Ed. by Brian T. Huber, Kenneth G. Macleod, and Scott L. Wing. Cambridge: Cambridge University Press, pp. 275–296. DOI: `10.1017/CBO9780511564512.010`.

Donnadieu, Y., R. Pierrehumbert, R. Jacob, and F. Fluteau (2006). "Modelling the primary control of paleogeography on Cretaceous climate". In: *Earth and Planetary Science Letters* 248.1-2, pp. 426–437. DOI: `10.1016/j.epsl.2006.06.007`.

Donnadieu, Yannick, Emmanuelle Pucéat, Mathieu Moiroud, François Guillocheau, and Jean-François Deconinck (2016). “A better-ventilated ocean triggered by Late Cretaceous changes in continental configuration”. In: *Nature Communications* 7.1. DOI: `10.1038/ncomms10316`.

Dumitrescu, Mirela, Simon C. Brassell, Stefan Schouten, Ellen C. Hopmans, and Jaap S. Sinninghe Damsté (2006). “Instability in tropical Pacific sea-surface temperatures during the early Aptian”. In: *Geology* 34.10, pp. 833–836. DOI: `10.1130/G22882.1`.

Emory, Amber E, Belay Demoz, Kevin Vermeesch, and Micheal Hicks (2014). “Weakening and strengthening structures in the Hadley Circulation change under global warming and implications for cloud response and climate sensitivity”. In: *Journal of Geophysical Research: Atmosphere* 119.13, pp. 8201–8211. DOI: `10.1002/2013JD020063.Received`.

Fletcher, Benjamin J., Stuart J. Brentnall, Clive W. Anderson, Robert A. Berner, and David J. Beerling (2008). “Atmospheric carbon dioxide linked with Mesozoic and early Cenozoic climate change”. In: *Nature Geoscience* 1.1, pp. 43–48. DOI: `10.1038/ngeo.2007.29`.

Flögel, S., B. Beckmann, P. Hofmann, A. Bornemann, T. Westerhold, R. D. Norris, C. Dullo, and T. Wagner (2008). “Evolution of tropical watersheds and continental hydrology during the Late Cretaceous greenhouse; impact on marine carbon burial and possible implications for the future”. In: *Earth and Planetary Science Letters* 274.1-2, pp. 1–13. DOI: `10.1016/j.epsl.2008.06.011`.

Fluteau, F., Gilles Ramstein, Jean Besse, R. Guiraud, and J. P. Masse (2007). “Impacts of palaeogeography and sea level changes on Mid-Cretaceous climate”. In: *Palaeogeography, Palaeoclimatology, Palaeoecology* 247.3-4, pp. 357–381. DOI: `10.1016/j.palaeo.2006.11.016`.

Gough, D.O. (1981). “Solar interior structure and luminosity variations”. In: *Solar Physics* 74.1, pp. 21–34.

Hagemann, Stefan and Lydia Dümenil (1998). “A parametrization of the lateral waterflow for the global scale”. In: *Climate Dynamics* 14.1, pp. 17–31. DOI: `10.1007/s003820050205`.

Haq, B U, J Hardenbol, and P R Vail (1987). “Chronology of Fluctuating Sea Levels since the Triassic”. In: *Science* 235.4793, pp. 1156–1167. DOI: `10.1126/science.235.4793.1156`.

Hasegawa, H., R. Tada, X. Jiang, Y. Suganuma, S. Imsamut, P. Charusiri, N. Ichinnorov, and Y. Khand (2012). “Drastic shrinking of the Hadley circulation during the mid-Cretaceous Supergreenhouse”. In: *Climate of the Past* 8.4, pp. 1323–1337. DOI: `10.5194/cp-8-1323-2012`.

Haywood, A. M., H. J. Dowsett, B. Otto-Bliesner, M. A. Chandler, A. M. Dolan, D. J. Hill, D. J. Lunt, M. M. Robinson, N. Rosenbloom, U. Salzmann, and L. E. Sohl (2010). “Pliocene model intercomparison project (PlioMIP): Experimental design and boundary conditions (Experiment 1)”. In: *Geoscientific Model Development* 3.1, pp. 227–242. DOI: `10.5194/gmd-3-227-2010`.

Heimhofer, Ulrich, Peter A. Hochuli, Jens O. Herrle, Nils Andersen, and Helmut Weissert (2004). “Absence of major vegetation and palaeoatmospheric pCO2 changes associated with oceanic anoxic event 1a (Early Aptian, SE France)”. In: *Earth and Planetary Science Letters* 223.3-4, pp. 303–318. DOI: `10.1016/j.epsl.2004.04.037`.

Heinemann, M, J H Jungclaus, and J Marotzke (2009). “Warm Paleocene/Eocene climate as simulated in ECHAM5/MPI-OM”. In: *Clim. Past* 5.1987, pp. 785–802. DOI: `10.5194/cp-5-785-2009`.

Hofmann, P. and T. Wagner (2011). "ITCZ controls on Late Cretaceous black shale sedimentation in the tropical Atlantic Ocean". In: *Paleoceanography* 26.4, pp. 1–11. DOI: `10.1029/2011PA002154`.

Hong, Sung Kyung and Yong Il Lee (2012). "Evaluation of atmospheric carbon dioxide concentrations during the Cretaceous". In: *Earth and Planetary Science Letters* 327-328, pp. 23–28. DOI: `10.1016/j.epsl.2012.01.014`.

Hu, Yongyun, Han Huang, and Chen Zhou (2018). "Widening and weakening of the Hadley circulation under global warming". In: *Science Bulletin* 63.10, pp. 640–644. DOI: `10.1016/j.scib.2018.04.020`.

Huber, Brian T., Richard D. Norris, and Kenneth G. MacLeod (2002). "Deep-sea paleotemperature record of extreme warmth during the Cretaceous". In: *Geology* 30.2, pp. 123–126. DOI: `10.1130/0091-7613(2002)030<0123:DSPROE>2.0.CO;2`.

Huber, M. and E. Thomas (2010). "Paleoceanography: The Greenhouse World". In: *Encyclopedia of Ocean Sciences* 86, pp. 319–329. DOI: `10.1016/B978-012374473-9.00701-3`.

Jenkyns, H. C., L. Schouten-Huibers, S. Schouten, and J. S. Sinninghe Damsté (2012). "Warm Middle Jurassic-Early Cretaceous high-latitude sea-surface temperatures from the Southern Ocean". In: *Climate of the Past* 8.1, pp. 215–225. DOI: `10.5194/cp-8-215-2012`.

Jenkyns, Hugh C. (2010). "Geochemistry of oceanic anoxic events". In: *Geochemistry, Geophysics, Geosystems* 11.3, pp. 1–30. DOI: `10.1029/2009GC002788`.

Jing, Dai and Sun Bainian (2018). "Early Cretaceous atmospheric CO2 estimates based on stomatal index of Pseudofrenelopsis papillosa (Cheirolepidiaceae) from southeast China". In: *Cretaceous Research* 85, pp. 232–242. DOI: `10.1016/j.cretres.2017.08.011`.

Kump, Lee R. and David Pollard (2008). "Amplification of Cretaceous Warmth by Biological Cloud Feedbacks". In: *Science* 320.5873, pp. 195–195. DOI: `10.1126/science.1153883`.

Kushner, P. J., I. M. Held, and T. L. Delworth (2001). "Southern Hemisphere atmospheric circulation response to global warming". In: *Journal of Climate* 14.10, pp. 2238–2249. DOI: `10.1175/1520-0442(2001)014<0001:SHACRT>2.0.CO;2`.

Kutzbach, J. E. and R. G. Gallimore (1989). "Pangaean climates: megamonsoons of the megacontinent". In: *Journal of Geophysical Research* 94.D3, pp. 3341–3357. DOI: `10.1029/JD094iD03p03341`.

Ladant, Jean Baptiste and Yannick Donnadieu (2016). "Palaeogeographic regulation of glacial events during the Cretaceous supergreenhouse". In: *Nature Communications* 7, pp. 1–9. DOI: `10.1038/ncomms12771`.

Larson, R. L. (1991). "Latest pulse of Earth: Evidence for a mid-Cretaceous superplume". In: *Geology* 19.6, p. 547. DOI: `10.1130/0091-7613(1991)019<0547:LPOEEF>2.3.CO;2`.

Levis, Samuel, Jonathan A. Foley, and David Pollard (2000). "Large-Scale Vegetation Feedbacks on a Doubled CO2 Climate". In: *Journal of Climate* 13.7, pp. 1313–1325. DOI: `10.1175/1520-0442(2000)013<1313:LSVFOA>2.0.CO;2`.

Littler, Kate, Stuart A. Robinson, Paul R. Bown, Alexandra J. Nederbragt, and Richard D. Pancost (2011). "High sea-surface temperatures during the Early Cretaceous Epoch". In: *Nature Geoscience* 4.3, pp. 169–172. DOI: `10.1038/ngeo1081`.

Lu, Jian, Gabriel A. Vecchi, and Thomas Reichler (2007). “Expansion of the Hadley cell under global warming”. In: *Geophysical Research Letters* 34.6, pp. 2–6. DOI: `10.1029/2006GL028443`.

Lunt, D. J., T. Dunkley Jones, M. Heinemann, M. Huber, A. LeGrande, A. Winguth, C. Loptson, J. Marotzke, C. D. Roberts, J. Tindall, P. Valdes, and C. Winguth (2012). “A model-data comparison for a multi-model ensemble of early Eocene atmosphere-ocean simulations: EoMIP”. In: *Climate of the Past* 8.5, pp. 1717–1736. DOI: `10.5194/cp-8-1717-2012`.

MacLeod, Kenneth G., Brian T. Huber, Álvaro Jiménez Berrocoso, and Ines Wendler (2013). “A stable and hot Turonian without glacial $\delta$18O excursions is indicated by exquisitely preserved Tanzanian foraminifera”. In: *Geology* 41.10, pp. 1083–1086. DOI: `10.1130/G34510.1`.

Madec, Gurvan (2008). “NEMO Ocean engine”. In: *Note du Pôle de modélisation 27*. Institut Pierre-Simon Laplace (IPSL), France.

McCoy, Daniel T, Dennis L Hartmann, Mark D Zelinka, Paulo Ceppi, and Daniel P Grosvenor (2015). “Mixed-phase cloud physics and Southern Ocean cloud feedback in climate models”. In: *Journal of Geophysical Research: Atmospheres* 120.18, pp. 9539–9554. DOI: `10.1002/2015JD023603`.

Miller, Kenneth G, Kenneth G Miller, Michelle A Kominz, James V Browning, James D Wright, Gregory S Mountain, Miriam E Katz, Peter J Sugarman, Benjamin S Cramer, Nicholas Christie-blick, and Stephen F Pekar (2005). “The Phanerozoic Record of Global Sea-Level Change”. In: *Science* 310, pp. 1293–1298. DOI: `10.1126/science.1116412`.

Moriya, Kazuyoshi, Paul A. Wilson, Oliver Friedrich, Jochen Erbacher, and Hodaka Kawahata (2007). “Testing for ice sheets during the mid-Cretaceous greenhouse using glassy foraminiferal calcite from the mid-Cenomanian tropics on Demerara Rise”. In: *Geology* 35.7, p. 615. DOI: `10.1130/G23589A.1`.

Müller, R. Dietmar, Maria Sdrolias, Carmen Gaina, Bernhard Steinberger, and Christian Heine (2008). “Long-term sea-level fluctuations driven by ocean basin dynamics”. In: *Science* 319.5868, pp. 1357–1362. DOI: `10.1126/science.1151540`.

Naafs, B. D A and R. D. Pancost (2014). “Environmental conditions in the South Atlantic (Angola Basin) during the Early Cretaceous”. In: *Organic Geochemistry* 76, pp. 184–193. DOI: `10.1016/j.orggeochem.2014.08.005`.

O’Brien, Charlotte L., Stuart A. Robinson, Richard D. Pancost, Jaap S. Sinninghe Damsté, Stefan Schouten, Daniel J. Lunt, Heiko Alsenz, André Bornemann, Cinzia Bottini, Simon C. Brassell, Alexander Farnsworth, Astrid Forster, Brian T. Huber, Gordon N. Inglis, Hugh C. Jenkyns, Christian Linnert, Kate Littler, Paul Markwick, Alison McAnena, Jörg Mutterlose, B. David A. Naafs, Wilhelm Püttmann, Appy Sluijs, Niels A.G.M. van Helmond, Johan Vellekoop, Thomas Wagner, and Neil E. Wrobel (2017). “Cretaceous sea-surface temperature evolution: Constraints from TEX86 and planktonic foraminiferal oxygen isotopes”. In: *Earth-Science Reviews* 172, pp. 224–247. DOI: `10.1016/j.earscirev.2017.07.012`.

Ohba, Masamichi and Hiroaki Ueda (2010). “A GCM Study on Effects of Continental Drift on Tropical Climate at the Early and Late Cretaceous”. In: *Journal of the Meteorological Society of Japan. Ser. II* 88.6, pp. 869–881. DOI: `10.2151/jmsj.2010-601`.

Otto-Bliesner, Bette L (2002). “Late Cretaceous ocean: Coupled simulations with the National Center for Atmospheric Research Climate System Model”. In: *Journal of Geophysical Research* 107.D2, p. 4019. DOI: `10.1029/2001JD000821`.

Otto-Bliesner, Bette L. and Garland R. Upchurch (1997). “Vegetation-induced warming of high-latitude regions during the late Cretaceous period”. In: *Nature* 385.6619, pp. 804–807. DOI: `10.1038/385804a0`.

Pancost, Richard D., David S. Steart, Luke Handley, Margaret E. Collinson, Jerry J. Hooker, Andrew C. Scott, Nathalie V. Grassineau, and Ian J. Glasspool (2007). “Increased terrestrial methane cycling at the Palaeocene-Eocene thermal maximum”. In: *Nature* 449.7160, pp. 332–335. DOI: `10.1038/nature06012`.

Park, W., N. Keenlyside, M. Latif, A. Ströh, R. Redler, E. Roeckner, and G. Madec (2009). “Tropical Pacific Climate and Its Response to Global Warming in the Kiel Climate Model”. In: *Journal of Climate* 22.1, pp. 71–92. DOI: `10.1175/2008JCLI2261.1`.

Park, W. and M. Latif (2019). “Ensemble global warming simulations with idealized Antarctic meltwater input”. In: *Climate Dynamics* 52.5-6, pp. 3223–3239. DOI: `10.1007/s00382-018-4319-8`.

Passalia, Mauro Gabriel (2009). “Cretaceous pCO2 estimation from stomatal frequency analysis of gymnosperm leaves of Patagonia, Argentina”. In: *Palaeogeography, Palaeoclimatology, Palaeoecology* 273.1-2, pp. 17–24. DOI: `10.1016/j.palaeo.2008.11.010`.

Poulsen, Chris J., Eric J. Barron, Claudia C. Johnson, and Peter Fawcett (1999). “Links between major climatic factors and regional oceanic circulation in the Mid-Cretaceous”. In: *Special Paper 332: Evolution of the Cretaceous Ocean-Climate System*. Geological Society of America, pp. 73–89. DOI: `10.1130/0-8137-2332-9.73`.

Poulsen, Christopher J., Eric J. Barron, Michael A. Arthur, and William H. Peterson (2001). “Response of the Mid-Cretaceous global oceanic circulation to tectonic and CO2 forcings”. In: *Paleoceanography* 16.6, pp. 576–592. DOI: `10.1029/2000PA000579`.

Poulsen, Christopher J., Andrew S. Gendaszek, and Robert L. Jacob (2003). “Did the rifting of the Atlantic Ocean cause the Cretaceous thermal maximum?” In: *Geology* 31.2, pp. 115–118. DOI: `10.1130/0091-7613(2003)031<0115:DTROTA>2.0.CO;2`.

Price, Gregory D. and Benjamin H. Passey (2013). “Dynamic polar climates in a greenhouse world: Evidence from clumped isotope thermometry of early cretaceous belemnites”. In: *Geology* 41.8, pp. 923–926. DOI: `10.1130/G34484.1`.

Price, Gregory D., Richard J. Twitchett, James R. Wheeley, and Giuseppe Buono (2013). “Isotopic evidence for long term warmth in the Mesozoic”. In: *Scientific Reports* 3, pp. 1–5. DOI: `10.1038/srep01438`.

Pucéat, Emmanuelle, Christopher Lécuyer, Yannick Donnadieu, Philippe Naveau, Henri Cappetta, Gilles Ramstein, Brian T. Huber, and Juergen Kriwet (2007). “Fish tooth $\delta$18O revising Late Cretaceous meridional upper ocean water temperature gradients”. In: *Geology* 35.2, pp. 107–110. DOI: `10.1130/G23103A.1`.

Roberts, Christopher D., Allegra N. Legrande, and Aradhna K. Tripati (2011). “Sensitivity of seawater oxygen isotopes to climatic and tectonic boundary conditions in an early Paleogene simulation with GISS ModelE-R”. In: *Paleoceanography* 26.4, pp. 1–16. DOI: `10.1029/2010PA002025`.

Roeckner, E, G Bäuml, Luca Bonaventura, R Brokopf, M Esch, Marco Giorgetta, Stefan Hagemann, Ingo Kirchner, Luis Kornblueh, Elisa Manzini, A Rhodin, U Schlese, Uwe Schulzweida, and Adrian Tompkins (2003). "The atmospheric general circulation model ECHAM 5. PART I: Model description". In: *Max Planck Institute for Meteorology Report* 349.

Royer, Dana L. (2006). "CO2-forced climate thresholds during the Phanerozoic". In: *Geochimica et Cosmochimica Acta* 70.23 SPEC. ISS. Pp. 5665–5675. DOI: `10.1016/j.gca.2005.11.031`.

Schlanger, S. O. and H. C. Jenkyns (1976). "Createaceous oceanic anoxic events: causes and consequences". In: *Geologie en mijbouw* 55.3-4, pp. 179–184.

Sloan, L. Cirbus and D. Pollard (1998). "Polar stratospheric clouds: a high latitude warming mechanism in an ancient greenhouse world". In: *Geophysical Research Letters* 25.18, pp. 3517–3520. DOI: `10.1029/98GL02492`.

Sloan, L. Cirbus, James C. G. Walker, T. C. Moore, David K. Rea, and James C. Zachos (1992). "Possible methane-induced polar warming in the early Eocene". In: *Nature* 357.6376, pp. 320–322. DOI: `10.1038/357320a0`. arXiv: `arXiv:1011.1669v3`.

Son, Seok Woo, Seo Yeon Kim, and Seung Ki Min (2018). "Widening of the Hadley Cell from Last Glacial Maximum to future climate". In: *Journal of Climate* 31.1, pp. 267–281. DOI: `10.1175/JCLI-D-17-0328.1`.

Song, Haijun, Paul B. Wignall, Huyue Song, Xu Dai, and Daoliang Chu (2019). "Seawater Temperature and Dissolved Oxygen over the Past 500 Million Years". In: *Journal of Earth Science* 30.2, pp. 236–243. DOI: `10.1007/s12583-018-1002-2`.

Spicer, Robert A. and Alexei B. Herman (2010). "The Late Cretaceous environment of the Arctic: A quantitative reassessment based on plant fossils". In: *Palaeogeography, Palaeoclimatology, Palaeoecology* 295.3-4, pp. 423–442. DOI: `10.1016/j.palaeo.2010.02.025`.

Sun, Yuewu, Xiang Li, Guowei Zhao, Huan Liu, and Yanlong Zhang (2016). "Aptian and Albian atmospheric CO2 changes during oceanic anoxic events: Evidence from fossil Ginkgo cuticles in Jilin Province, Northeast China". In: *Cretaceous Research* 62.April, pp. 130–141. DOI: `10.1016/j.cretres.2015.12.007`.

Tarduno, J. A., D. B. Brinkman, P. R. Renne, R. D. Cottrell, H. Scher, and P. Castillo (1998). "Evidence for Extreme Climatic Warmth from Late Cretaceous Arctic Vertebrates". In: *Science* 282.5397, pp. 2241–2243. DOI: `10.1126/science.282.5397.2241`.

Taylor, Karl E., Ronald J. Stouffer, and Gerald A. Meehl (2012). "An overview of CMIP5 and the experiment design". In: *Bulletin of the American Meteorological Society* 93.4, pp. 485–498. DOI: `10.1175/BAMS-D-11-00094.1`. arXiv: `arXiv:1011.1669v3`.

Upchurch, Garland R., Bette L. Otto-Bliesner, and Christopher Scotese (1998). "Vegetation–atmosphere interactions and their role in global warming during the latest Cretaceous". In: *Philosophical Transactions of the Royal Society of London. Series B: Biological Sciences* 353.1365. Ed. by D. J. Beerling, W. G. Chaloner, and F. I. Woodward, pp. 97–112. DOI: `10.1098/rstb.1998.0194`.

Van Der Meer, D. G., R. E. Zeebe, D. J. J. van Hinsbergen, A. Sluijs, W. Spakman, and T. H. Torsvik (2014). "Plate tectonic controls on atmospheric CO2 levels since the Triassic". In: *Pro-*

*ceedings of the National Academy of Sciences* 111.12, pp. 4380–4385. DOI: `10.1073/pnas.1315657111`.

Veizer, Ján, Yves Godderis, and Louis M. François (2000). "Evidence for decoupling of atmospheric CO2 and global climate during the Phanerozoic eon". In: *Nature* 408.6813, pp. 698–701. DOI: `10.1038/35047044`.

Wagner, T., P. Hofmann, and S. Flögel (2013). "Marine black shale deposition and Hadley Cell dynamics: A conceptual framework for the Cretaceous Atlantic Ocean". In: *Marine and Petroleum Geology* 43, pp. 222–238. DOI: `10.1016/j.marpetgeo.2013.02.005`.

Wang, Yongdong, Chengmin Huang, Bainian Sun, Cheng Quan, Jingyu Wu, and Zhicheng Lin (2014). "Paleo-CO2 variation trends and the Cretaceous greenhouse climate". In: *Earth-Science Reviews* 129, pp. 136–147. DOI: `10.1016/j.earscirev.2013.11.001`.

Wetherald, RT T and S. Manabe (1986). "An investigation of cloud cover change in response to thermal forcing". In: *Climatic Change* 8.1, pp. 5–23.

Williscroft, Krista, Stephen E. Grasby, Benoit Beauchamp, Crispin T.S. Little, Keith Dewing, Daniel Birgel, Terry Poulton, and Krzysztof Hryniewicz (2017). "Extensive Early Cretaceous (Albian) methane seepage on Ellef Ringnes Island, Canadian High Arctic". In: *Bulletin of the Geological Society of America* 129.7, pp. 788–805. DOI: `10.1130/B31601.1`.

Zelinka, Mark D. and Dennis L. Hartmann (2010). "Why is longwave cloud feedback positive?" In: *Journal of Geophysical Research Atmospheres* 115.16, pp. 1–16. DOI: `10.1029/2010JD013817`.

Zelinka, Mark D., Stephen A. Klein, Karl E. Taylor, Timothy Andrews, Mark J. Webb, Jonathan M. Gregory, and Piers M. Forster (2013). "Contributions of different cloud types to feedbacks and rapid adjustments in CMIP5". In: *Journal of Climate* 26.14, pp. 5007–5027. DOI: `10.1175/JCLI-D-12-00555.1`.

## Appendix: Supplementary Figures

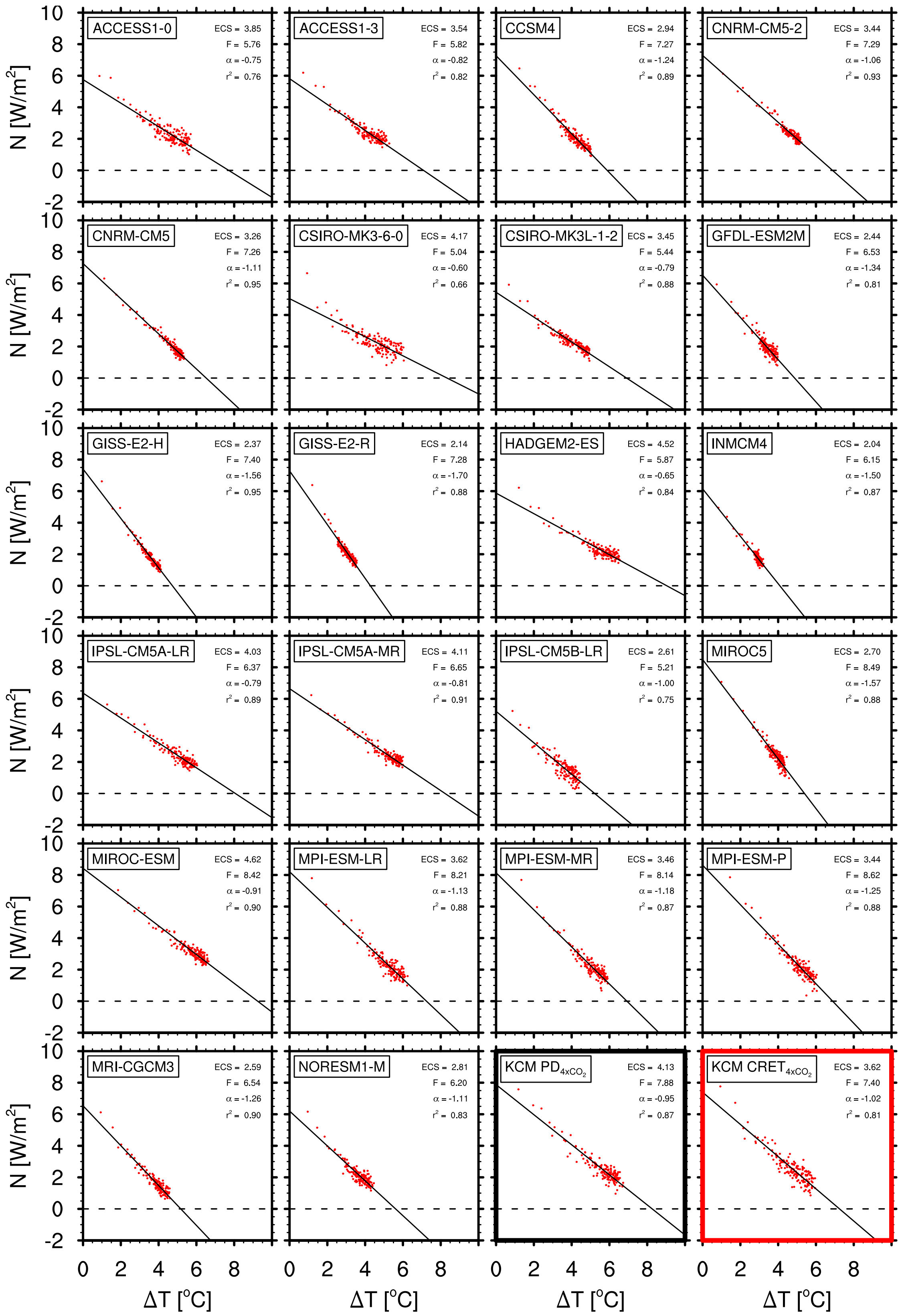

**Figure 2.A1:** Relation between the annual mean radiative imbalance at the top of the atmosphere (N) and the global mean surface air temperature change ΔT. Methodology is described in detail in (Andrews et al., 2012). Results are shown for the first 150 years of CMIP5 and KCM experiments after an instantaneous quadrupling of atmospheric $CO_2$ and calculated as the difference to the respective pre-industrial control climatology. Black line represents a simple linear regression of all 150 years. The intercept at N = 0 is an approximation of the equilibrium climate sensitivity (ECS), while the intercept at ΔT = 0 relates to the adjusted radiative forcing. The slope of the regression line $\alpha$ is interpreted as the feedback strength of the climate system.

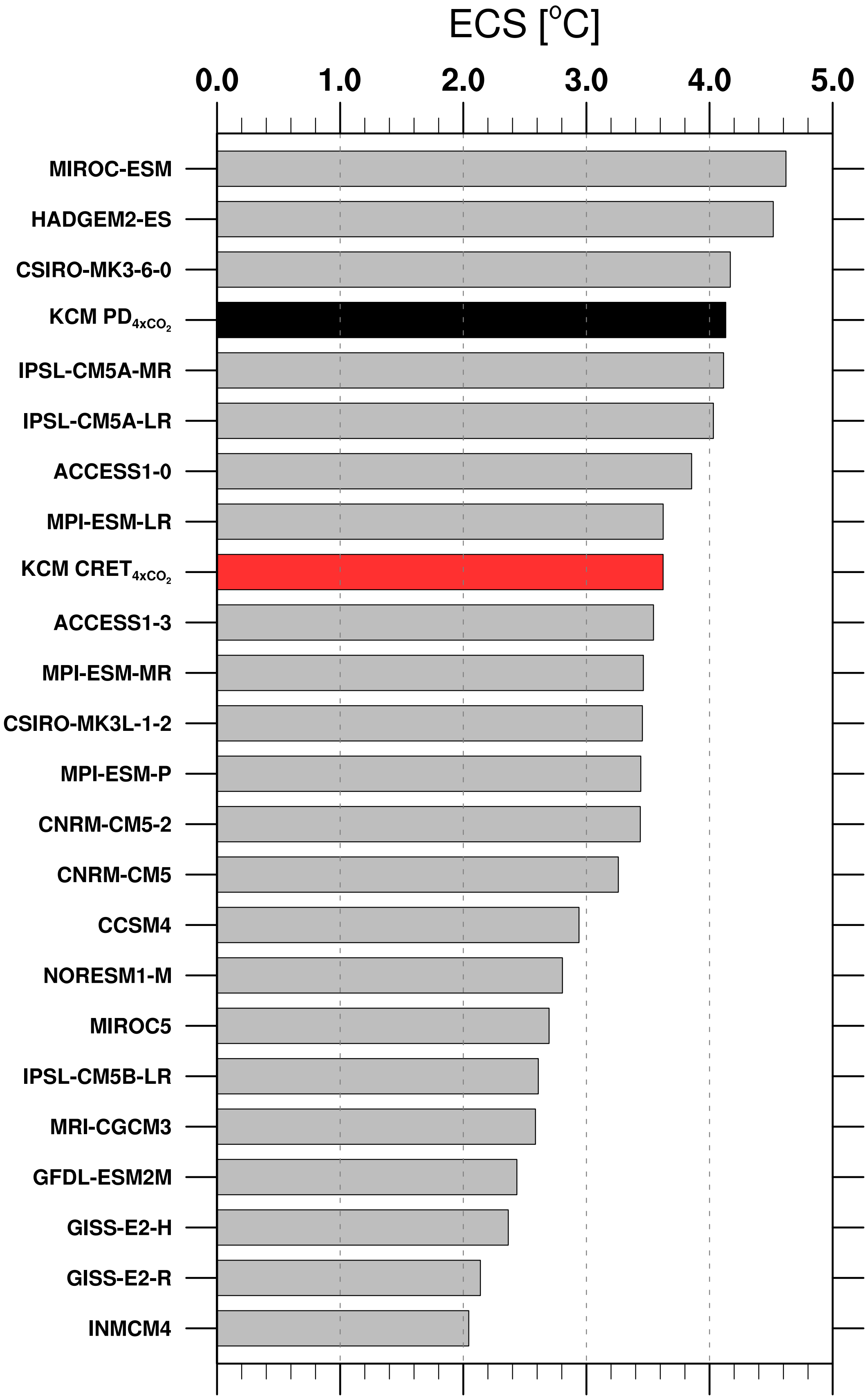

**Figure 2.A2:** Overview of the estimated equilibrium climate sensitivity (ECS) as shown in Figure 2.A1. The ECS represents the simulated global mean temperature increase due to a doubling of atmospheric $CO_2$.

# 3 Evidence for a regional warm bias in the Early Cretaceous $TEX_{86}$ record

Sebastian Steinig, Wolf Dummann, Wonsun Park, Mojib Latif, Stephanie Kusch, Peter Hofmann and Sascha Flögel

**Declaration:** *This chapter is submitted to Earth and Planetary Science Letters (04/2019). I designed the study with support from Sascha Flögel. I carried out all Cretaceous model experiments. Wonsun Park provided the pre-industrial reference simulation. Wolf Dummann, Peter Hofmann and Stephanie Kusch generated the new* $TEX_{86}$ *data. I made the analysis, produced all figures and wrote the manuscript. All co-authors helped improving the manuscript.*

## 3.1 Abstract

The Cretaceous Period (145-66 Ma) provides an opportunity to obtain insights into the adaptation of the climate system to increased atmospheric greenhouse gas concentrations. The organic paleothermometer TEX$_{86}$ is one of the few proxies available for reconstructing quantitative estimates of upper ocean temperatures of this time period. Here we show that the sedimentary TEX$_{86}$ signal in the Early Cretaceous North and South Atlantic shows systematic differences to other Cretaceous samples. In particular, the relative increase in the fractional abundances of the crenarchaeol isomer exhibits similarities with surface sediments from the modern Mediterranean and Red Sea. Dedicated climate model simulations suggest that the formation of warm and saline deep waters in the restricted North and South Atlantic may have influenced TEX$_{86}$ export dynamics leading to a warm bias in reconstructed upper ocean temperatures. Applying a regional calibration from the modern Mediterranean and Red Sea to corresponding TEX$_{86}$ data significantly improves the model-data fit for the Aptian Oceanic Anoxic Event 1a and the overall comparison with other temperature proxies for the Early Cretaceous. Our results demonstrate the need to consider regional and temporal changes of the TEX$_{86}$-temperature relation for the reconstruction of deep-time ocean temperatures.

## 3.2 Introduction

The Cretaceous Period between 145 and 66 Ma is commonly considered a predominantly warm and equable greenhouse climate (Barron, 1983; O'Brien et al., 2017) with elevated levels of atmospheric $CO_2$ caused by enhanced volcanic activity (Van Der Meer et al., 2014). In combination with the ongoing breakup of Pangea (Blakey, 2008) and the simultaneous emergence of young and restricted ocean basins (Fig. 3.1), this period experienced multiple phases of dys- to anoxic conditions in the water column and deposition of marine organic-rich sediments (Jenkyns, 2010). These so-called Oceanic Anoxic Events (OAEs) reveal valuable insights into the response of the climate system to changes in marine ecosystems and the global carbon cycle. OAE 1a in the Early Aptian (∼125 Ma) and OAE 2 at the Cenomanian–Turonian boundary (∼94 Ma) are the two most pronounced events throughout the Cretaceous and are characterised by long-term maxima in surface temperatures (O'Brien et al., 2017).

Quantitative estimates of upper ocean temperatures are necessary for estimating the magnitude of these past climate variations and to better validate paleoclimate model simulations. Reduced abundances of planktonic foraminifera and increased sedimentary calcite dissolution during the Early Cretaceous limit the application of the classic oxygen-isotope $\delta^{18}$O SST proxy (O'Brien et al., 2017). The additional lack of alkenones makes the organic paleothermometer $\text{TEX}_{86}$ (TetraEther indeX of tetraethers consisting of 86 carbons; Schouten et al., 2002) the only other commonly used proxy for Early Cretaceous marine temperatures. The $\text{TEX}_{86}$ proxy is based on the observation that the relative cyclization of isoprenoidal glycerol dialkyl glycerol tetraethers (isoGDGTs) in membrane lipids of marine archaea increases with temperature (Wuchter et al., 2004). Correlation of the isoGDGT distribution in modern core-top sediments with ambient water temperatures allows the reconstruction of past seawater temperatures. A variety of calibrations exist to convert measured $\text{TEX}_{86}$ ratios (see Section 3.3.2; Schouten et al., 2002) to upper ocean temperatures. These partly arise from uncertainties in the actual export depth of the $\text{TEX}_{86}$ signal ranging from the surface (Kim et al., 2010; Tierney and Tingley, 2014) down to 1000 m (Ho and Laepple, 2016). A recent comparison of the meridional gradients of ocean temperatures and core-top $\text{TEX}_{86}$ values concludes that the global signal is most probably formed within the upper 200 m of the water column (Zhang and Liu, 2018).

Comparison of $\text{TEX}_{86}$-derived core-top temperatures with satellite measurements reveal systematic bias patterns of overestimated high-latitude and underestimated low-latitude temperatures (Tierney and Tingley, 2014). Specific areas known to have a $\text{TEX}_{86}$-SST relation different from the global open-ocean calibration are the modern Mediterranean (Kim et al., 2015) and Red Sea (Trommer et al., 2009). Surface sediments in these restricted basins show a strong increase in the fractional abundances of the crenarchaeol isomer and GDGT-2 with water depth for the upper 1000 m (Kim et al., 2015). The resulting warm bias in $\text{TEX}_{86}^{H}$-derived temperatures in deep-water

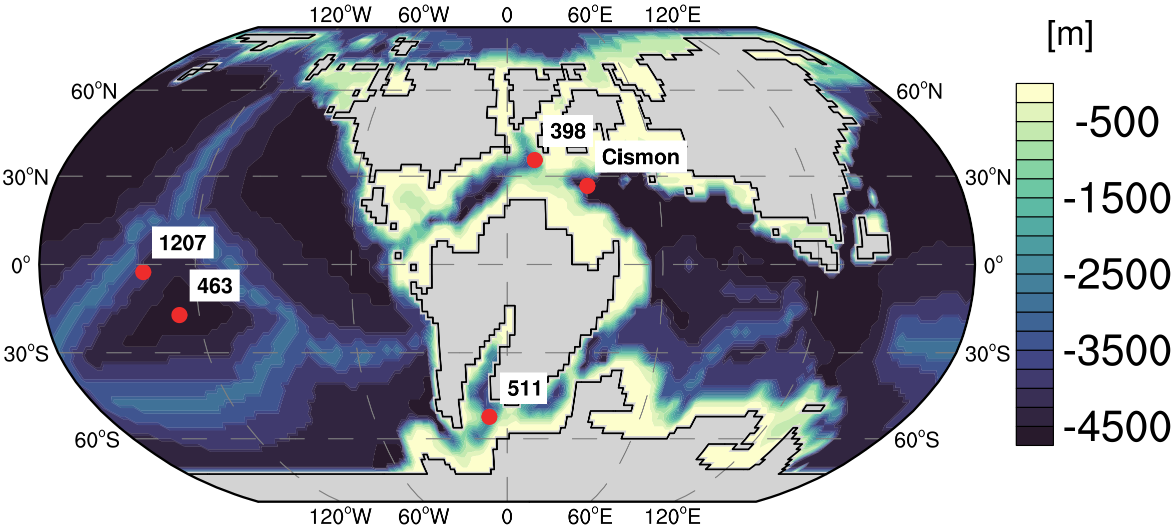

**Figure 3.1:** Model bathymetry and study sites. Model geography and paleolocations (O'Brien et al., 2017) represent an Early Aptian (~125 Ma) time slice. Contour interval is 250 m.

sediments reaches up to 8 °C (Kim et al., 2015) and is also visible in the warm and saline Mediterranean Outflow Water along the Portuguese continental margin (Kim et al., 2016). Similar changes with water depth are observed for suspended particulate matter (SPM) samples from these regions (Kim et al., 2015; Kim et al., 2016) and imply an increased contribution of deep-dwelling Thaumarchaeota that have a different isoGDGT distribution (Taylor et al., 2013; Kim et al., 2015), possibly due to genetic controls (Villanueva et al., 2015; Kim et al., 2016). Paleorecords from the Mediterranean Sea also show a past warm bias in TEX$_{86}^{H}$-derived temperatures that was apparently modulated by changing populations of Thaumarchaeota during the Pliocene-Pleistocene (Polik et al., 2018). A systematic offset between TEX$_{86}^{H}$-derived temperatures and other proxy methods has also been found for the Early Paleogene Southwest Pacific Ocean (Hollis et al., 2012) with an important influence of water depth on GDGT-2/GDGT-3 ratios (Taylor et al., 2013).

Most of the Cretaceous TEX$_{86}$ values, particularly those of the OAE 1a period, exceed the range of recorded present-day core-top data (O'Brien et al., 2017). In combination with the observed regional variability of TEX$_{86}$ export dynamics, the applicability of modern global temperature calibrations for past greenhouse climates is questionable. To assess regional bias and calibration problems for the Cretaceous, we use a recently published quality-controlled compilation (O'Brien et al., 2017) and newly generated Cretaceous TEX$_{86}$ data to identify systematic differences in the isoGDGT distributions. We compare TEX$_{86}$-derived SST and upper ocean temperatures from different calibrations with temperatures derived from a fully coupled atmosphere-ocean general circulation model, the Kiel Climate Model (Park et al., 2009). The model boundary conditions represent an Early Aptian time slice to validate the internal consistency of the OAE 1a TEX$_{86}$ record (Table 3.1), evaluate the local oceanographic setting for individual core locations and test the sensitivity of the results to the applied greenhouse gas forcing.

**Table 3.1:** Overview of study sites. We combine new data from DSDP site 511 with all locations from a Cretaceous compilation (O'Brien et al., 2017) that provide $TEX_{86}$ data with individual isoGDGT fractional abundances around the Early Aptian OAE 1a (∼125 Ma; see Section 3.3.5). Paleolatitude ranges derive from the spread in different reconstruction methods (see Appendix Table 3.A1).

| Site | Reference | Location | Paleowater depth | Paleolatitude |
|---|---|---|---|---|
| DSDP 398 | Naafs and Pancost (2016) | proto-North Atlantic | 500-2000 m[a,b] | 22-36°N |
| DSDP 463 | Schouten et al. (2003) | Mid-Pacific Mountains | 500 - 1000 m[c] | 7-35°S |
| DSDP 511 | this study; Jenkyns et al. (2012) | Falkland Plateau | ∼750 m[a] | 43-56°S |
| ODP 1207 | Dumitrescu et al. (2006) | Shatsky Rise | ∼1300 m[d] | 10°N-21°S |
| Cismon | Bottini et al. (2015) | Italian Southern Alps | 1000-1500 m[e] | 17-25°N |

[a] Holbourn et al. (2001)
[b] Sibuet and Ryan (1979)
[c] Roth (1981)
[d] Bralower et al. (2002)
[e] Bottini et al. (2015)

# 3.3 Methods

## 3.3.1 Model description

Climate model integrations were performed with the Kiel Climate Model (KCM, Park et al., 2009), a fully coupled atmosphere-ocean-sea ice general circulation model. The atmospheric component consists of the ECHAM5 spectral model (Roeckner et al., 2003) configured at a T42 horizontal resolution (∼2.8°× 2.8°) with 19 vertical levels. The ocean-sea ice component NEMO uses a tripolar grid with a nominal horizontal resolution of 2° and 31 vertical levels (Madec, 2008). Existing model boundary conditions (Blöhdorn, 2013) represent an Early Aptian (i.e. ∼125 Ma) time slice based on global paleobathymetry reconstructions (Müller et al., 2008) complemented by information about shelf areas, coastlines and land topography (Blakey, 2008). Routing of river runoff to the ocean is calculated from the land orography (Hagemann and Dümenil, 1998). Simplified zonal mean vegetation properties were used for the land surface (Blöhdorn, 2013). No permanent land ice is assumed for the simulations, although seasonal snowfall and sea ice formation is permitted. Aptian-Albian $CO_2$ reconstructions based on stomatal indices of fossil conifers range from 500 to 1300 ppmv (Jing and Bainian, 2018). We therefore performed two integrations with 600 ($CRET_{600}$) and 1200 ($CRET_{1200}$) ppmv atmospheric $CO_2$ and a reduced solar constant of 1350 $W/m^2$. An additional simulation with pre-industrial levels of $CO_2$ ($CRET_{286}$) is performed to evaluate changes due to the different paleogeography and solar constant alone. Other greenhouse gases are held constant at their pre-industrial values due to a lack of available reconstructions. Experiment $CRET_{1200}$ was initialised with a homogeneous ocean temperature of 10 °C and salinity of 35 and integrated for 6000 model years. Experiments $CRET_{600}$ and $CRET_{286}$ were branched off from $CRET_{1200}$ at year 1000 and also integrated for an additional 5000 years. The change in the globally depth-integrated ocean temperature for the last 1000 model years is below 0.15 °C for all experiments. All results are averaged over the last 500 years of integration.

### 3.3.2 TEX$_{86}$ paleothermometer

Different isoGDGT lipids biosynthesized by marine Thaumarchaeota are named according to their respective number of cyclopentane moieties, i.e. GDGT-0 through GDGT-3, with the exception of Crenarchaeol (Cren) and its isomer (Cren'), which contain 4 cyclopentane moieties and a cyclohexane ring. Highest correlation between different GDGT ratios and annual mean SST was initially reported for the TEX$_{86}$ index (Schouten et al., 2002) defined as:

$$TEX_{86} = \frac{[GDGT-2]+[GDGT-3]+[Cren']}{[GDGT-1]+[GDGT-2]+[GDGT-3]+[Cren']} \qquad (3.1)$$

To account for uncertainties in the actual expoth depth of the sedimentary TEX$_{86}$ signal (Zhang and Liu, 2018), we use several different calibrations to convert measured TEX$_{86}$ values to upper ocean temperatures. The widely applied TEX$^{H}_{86}$ (Kim et al., 2010) calibration uses a logarithmic relationship for an improved correlation with SSTs > 5 °C and is defined as:

$$SST = 68.4 \,\mathrm{x}\, TEX^{H}_{86} + 38.6 \qquad (3.2)$$

with TEX$^{H}_{86}$ = log(TEX$_{86}$). Similarly, a calibration of TEX$^{H}_{86}$ with temperatures integrated over the upper 200 m of the water column was proposed (Kim et al., 2012) as:

$$T_{0-200m} = 54.7 \,\mathrm{x}\, TEX^{H}_{86} + 30.7 \qquad (3.3)$$

An analysis of sediments from the Mediterranean and northern Red Sea deposited at water depths larger than 1000 m also revealed a strong correlation between TEX$^{H}_{86}$ and SST, but with a significantly different slope and intercept of the calibration line (Kim et al., 2015). This suggests that in both basins a deep-water community of Thaumarchaeota with a different isoGDGT distribution influences the TEX$_{86}$ ratio, while the dominant influence of the upper ocean temperature is still preserved. Resulting calibrations are:

$$SST = 56.3 \,\mathrm{x}\, TEX^{H}_{86} + 30.2 \qquad (3.4)$$

and:

$$T_{0-200m} = 57.6 \,\mathrm{x}\, TEX^{H}_{86} + 27.1 \qquad (3.5)$$

A recent study (Ho and Laepple, 2016) suggests an influence of the deep subsurface up to 1000 m water depth on the TEX$_{86}$ signal. We calculate the respective proxy and model temperatures for the subsurface calibration ensemble with the "R" package "subcal" provided by the corresponding authors (Ho and Laepple, 2016). We further compare the results with SSTs computed with the Bayesian model approach BAYSPAR (Tierney and Tingley, 2014; Tierney and Tingley, 2015) inputting all samples from the OAE 1a sites to derive a common calibration. The deep-time analogue prediction uses a prior mean of 30 °C, a prior standard deviation of 20 °C and a search tolerance of 0.21 ($2\sigma$ of $\mathrm{TEX}_{86}$ input data).

### 3.3.3 New $\mathrm{TEX}_{86}$ measurements at DSDP 511 Falkland Plateau

We generated 69 new $\mathrm{TEX}_{86}$ samples from Deep-Sea Drilling Project site 511 to complement existing Lower Cretaceous data from the same location (13 samples with available isoGDGT distributions, Jenkyns et al. 2012). Dried and ground sediments were successively extracted with methanol, dichloromethane:methanol (1:1, v:v), and dichloromethane using ultrasonication. The extracts were combined, dried under mild vacuum, and reacted with acid-activated copper clippings to remove elemental sulphur. The sulphur-free extracts were then partitioned over a self-packed silica column (deactivated with 1% ultrapure $H_2O$) using hexane, hexane:dichloromethane (2:1, v:v), and dichloromethane:methanol (1:1, v:v) successively. The final fraction containing the GDGTs was dissolved in a hexane:isopropanol mixture (95:5, v:v) and passed through a 0.45 mm polytetrafluoroethylene filter and C46 GDGT was added as internal standard. GDGTs were analysed using an Agilent 1290 UHPLC coupled to an Agilent 6460 QQQ mass spectrometer equipped with an APCI ion source. Published chromatographic conditions (Hopmans et al., 2016) were applied and the mass spectrometer was operated in selected ion monitoring mode. Resulting data is shown in Appendix 3.B1.

### 3.3.4 $\mathrm{TEX}_{86}$ compilations and GDGT screening

Besides our new measurements we use published compilations of present-day core-top (Tierney and Tingley, 2015) and Cretaceous (O'Brien et al., 2017) $\mathrm{TEX}_{86}$ samples. A particular advantage of the large Cretaceous compilation is the stringent application of several GDGT distribution parameters to screen for potential secondary, non-thermal effects on the $\mathrm{TEX}_{86}$ signal. The GDGT parameters and exclusion criteria used are the Branched and Isoprenoid Tetraether (BIT) Index > 0.3 (Hopmans et al., 2004), %GDGT-0 > 67% (Sinninghe Damsté et al., 2012), Methane Index (MI) > 0.5 (Zhang et al., 2011), $f_{Cren':Cren'+Cren} > 0.25$ (O'Brien et al., 2017) and $\Delta$Ring Index $|\Delta RI| > 0.3$ (Zhang et al., 2016).

150 samples from the Cretaceous compilation are excluded based on the above criteria (O'Brien et al., 2017). 80 out of the 105 data points from PAMA quarry are identified as potentially influenced by secondary processes and the rest of the data should be interpreted with caution (O'Brien et al., 2017). We therefore decided to exclude all samples from this site from the analysis. [GDGT-0] is not provided for many samples from DSDP site 545. This by definition increases the frac-

tional abundances of other individual isoGDGTs, but does not influence the ratios of multiple isoGDGTs discussed in this work (e.g. [Cren']/[Cren] or [GDGT-2]/[GDGT-3]). We therefore included all samples from DSDP site 545 in the analysis. Together with our new data from DSDP site 511 (n=69, all data points pass the GDGT screening described above), this results in 704 Cretaceous samples that provide individual isoGDGT distributions. We use two modern $\mathrm{TEX}_{86}$ core-top compilations as reference data. For comparability to the Cretaceous data, we only use data providing individual isoGDGT distributions and also exclude samples with $|\Delta \mathrm{RI}| > 0.3$. We further remove samples from the Mediterranean and Red Sea from the global core-top data set (Tierney and Tingley, 2015) resulting in 611 remaining data points. A combined Mediterranean and Red Sea data set (n=195) is based on published compilations from the Mediterranean Sea (Kim et al., 2015) (n=172), the Red Sea (Trommer et al., 2009) (n=20, between 15-28°N) and three Red Sea samples from a global data set (Kim et al., 2008).

### 3.3.5 Age models and definition of OAE 1a

Absolute ages for all $\mathrm{TEX}_{86}$ samples were obtained from the published Cretaceous compilation (O'Brien et al., 2017) and are based on GTS2012 (Ogg et al., 2012). The isoGDGT analysis is performed on all available samples passing the GDGT screening, while the model-proxy temperature comparison (see Fig. 3.2 and Fig. 3.7) is restricted to OAE 1a $\mathrm{TEX}_{86}$ samples. OAE 1a is defined as carbon isotope segments C3-C6 with corresponding depth intervals as reported in the original publications (Table 3.1). At DSDP site 511, the section between 540 and 516 mbsf has been interpreted as the local expression of OAE 1a (Jenkyns et al., 2012). However, a revised foraminiferal biostratigraphy (Huber and Leckie, 2011) suggests a Late Aptian age for the depth interval above 515 mbsf comprising the positive carbon isotope excursion tentatively interpreted as C4-C6, putting the presence of OAE 1a at DSDP Site 511 into question. Given that calcareous nannofossil biostratigraphy indicates a Late Barremian to Early Aptian age of the section between 534.25 and 515 mbsf (Bralower et al., 1994), it most likely predates OAE 1a. As the average $\mathrm{TEX}_{86}^{H}$-derived SST for OAE 1a (C3-C6) at DSDP site 398 is only about 1 °C higher than during pre-OAE 1a conditions (Naafs and Pancost, 2016), we include the corresponding interval (534.25 to 515 mbsf) at DSDP site 511 in our analysis and interpret the associated temperatures as the lower end estimate of OAE 1a.

## 3.4 Results

### 3.4.1 OAE 1a ocean temperatures

The simulated global annual mean SST for the Early Aptian with an atmospheric $\mathrm{CO}_2$ of 1200 ppmv ($\mathrm{CRET}_{1200}$) reaches 24.2 °C (Table 3.2), which is about 7 °C warmer than the pre-industrial reference simulation ($\mathrm{PI}_{286}$). High-latitude warming is amplified and reduces the meridional tem-

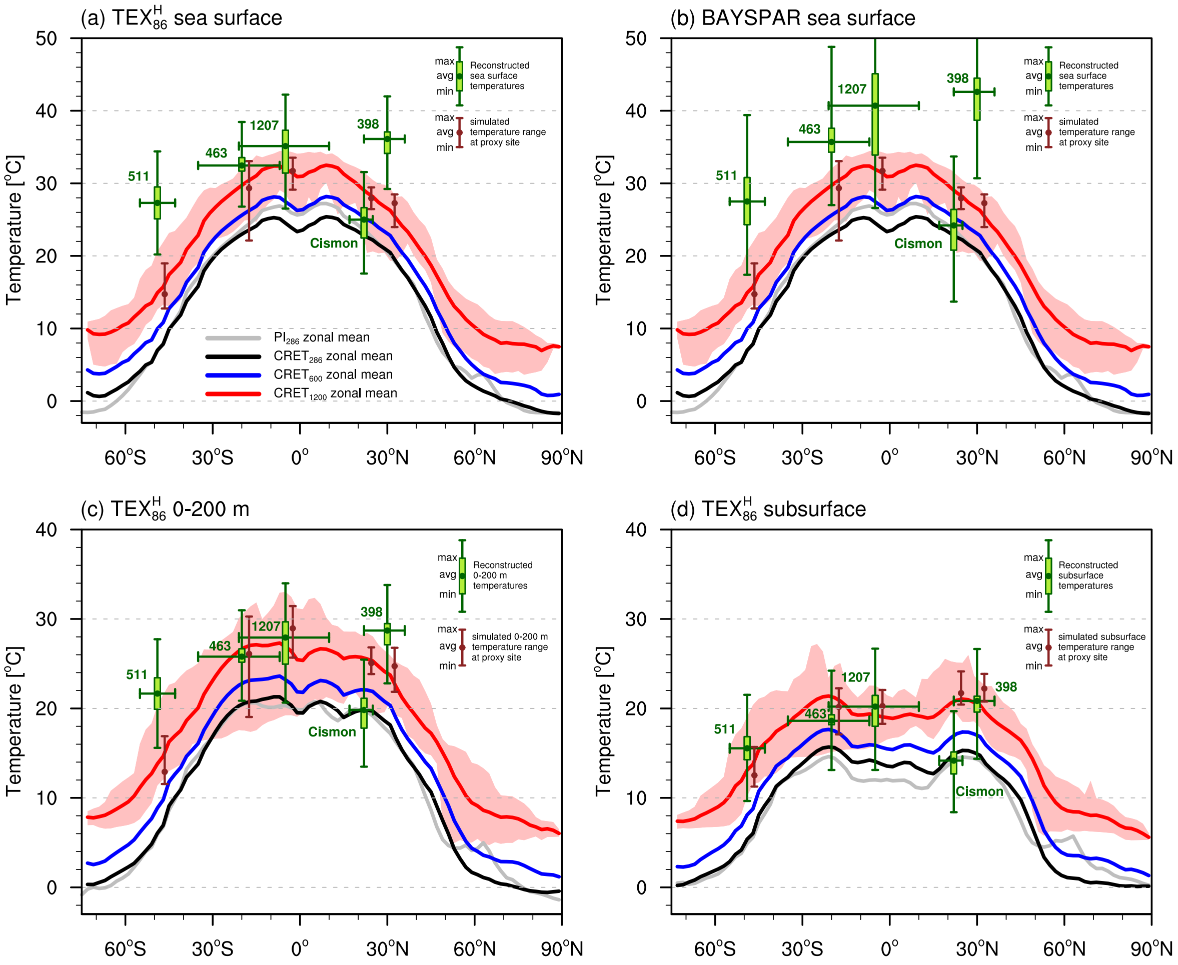

**Figure 3.2:** Model-proxy comparison of upper ocean temperatures for OAE 1a. Calibrations used to convert TEX$_{86}$ values to temperatures are (a) TEX$^H_{86}$ SST (Eq. (3.2), Kim et al. 2010), (b) BAYSPAR (see Section 3.3.2, Tierney and Tingley 2014; Tierney and Tingley 2015), (c) TEX$^H_{86}$ 0-200 m depth-integrated (Eq. (3.3), Kim et al. 2012) and (d) a deep subsurface ensemble calibration (see Section 3.3.2, Ho and Laepple 2016). Corresponding simulated annual mean ocean temperatures are zonally averaged and shown for (a-b) sea surface, (c) 0-200 m depth-integrated and (d) integrated over the deep subsurface (see Section 3.3.2). Shading represents the range of simulated temperatures at each latitude for experiment CRET$_{1200}$. Horizontal lines indicate the range of available paleolatitude estimates for each site (see Table 3.1). Vertical bars reflect the (green) 95% confidence interval for TEX$_{86}$-derived temperatures and the (red) range of simulated temperatures around the approximate paleolocation (uncertainty in latitude and ± 10° in longitude) for experiment CRET$_{1200}$.

**Table 3.2:** Simulated annual mean sea surface temperatures. Results are shown for the pre-industrial (PI) and Cretaceous (CRET) experiments and reported in °C. Subscripts indicate atmospheric CO$_2$ for the respective simulation.

| Experiment | Global mean SST | low-latitude SST $\|\phi\|<30°$ | high-latitude SST $\|\phi\|>60°$ | meridional gradient $\|\phi\|<30°$-$\|\phi\|>60°$ |
|---|---|---|---|---|
| PI$_{286}$ | 17.4 | 24.9 | -0.4 | 25.3 |
| CRET$_{286}$ | 17.1 | 23.5 | 0.4 | 23.1 |
| CRET$_{600}$ | 19.8 | 26.2 | 3.2 | 23.0 |
| CRET$_{1200}$ | 24.2 | 30.3 | 8.7 | 21.6 |

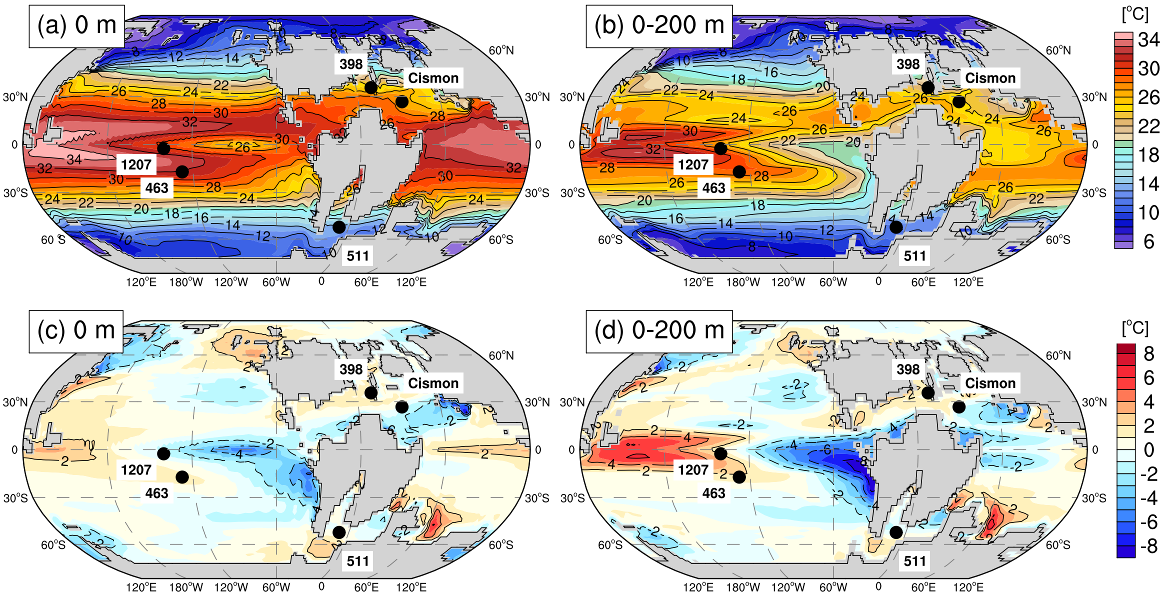

**Figure 3.3:** Maps of simulated ocean temperatures. Temperatures are shown for experiment $Cret_{1200}$ for (a) the surface and (b) the upper 200 m, as well as their (c-d) deviations from the respective zonal mean value at each latitude. Values are in °C. Study sites are shown at their approximate Early Aptian paleopositions (O'Brien et al., 2017).

perature gradient between low and high latitudes from 25.3 °C in $PI_{286}$ to 21.6 °C in $CRET_{1200}$. The Cretaceous continental configuration and the reduced solar constant in a simulation under pre-industrial $CO_2$ forcing ($CRET_{286}$) already reduce the temperature gradient by over 2 °C compared to $PI_{286}$. This change is even larger than the radiatively induced reduction by quadrupling atmospheric $CO_2$.

$TEX_{86}$-derived SSTs for OAE 1a (see Section 3.3.5 for a definition of OAE 1a) are higher than the simulated zonal mean temperatures, both for the $TEX_{86}^{H}$ (Fig. 3.2a, Eq. (3.2)) and the BAYSPAR calibration (Fig. 3.2b). The BAYSPAR calibration yields a higher SST sensitivity at higher $TEX_{86}$ values and maximum SSTs above 40 °C for sites ODP 1207 and DSDP 398. Cismon is the only location with reconstructed SSTs close to simulations $CRET_{600}$ and $CRET_{1200}$, but the offset of over 10 °C (15 °C) for $TEX_{86}^{H}$ (BAYSPAR) to the nearby DSDP site 398 is striking. The overall misfit between model- and $TEX_{86}$-based temperatures decreases distinctly by applying a subsurface calibration (Fig. 3.2c-d). Shallow subsurface temperatures (integrated from 0-200 m, Eq. (3.3)) in the central equatorial Pacific at sites ODP 1207 and DSDP 463 range between 25-30 °C and agree with simulation $CRET_{1200}$. DSDP sites 511 (Falkland Plateau) and 398 (North Atlantic) show higher reconstructed than simulated temperatures. The mean offset varies between 4 °C for the North Atlantic and about 10 °C for the southern South Atlantic. Inclusion of the deeper subsurface (see Section 3.3.2) further reduces the simulated and reconstructed meridional temperature gradient and results in the overall best model-proxy agreement (Fig. 3.2d). $TEX_{86}$ values from Cismon translate into the coolest deep subsurface temperatures at values incompatible with our simulations at higher $CO_2$ levels.

Figure 3.3 illustrates a strong increase in the zonal differences in simulated low-latitude temper-

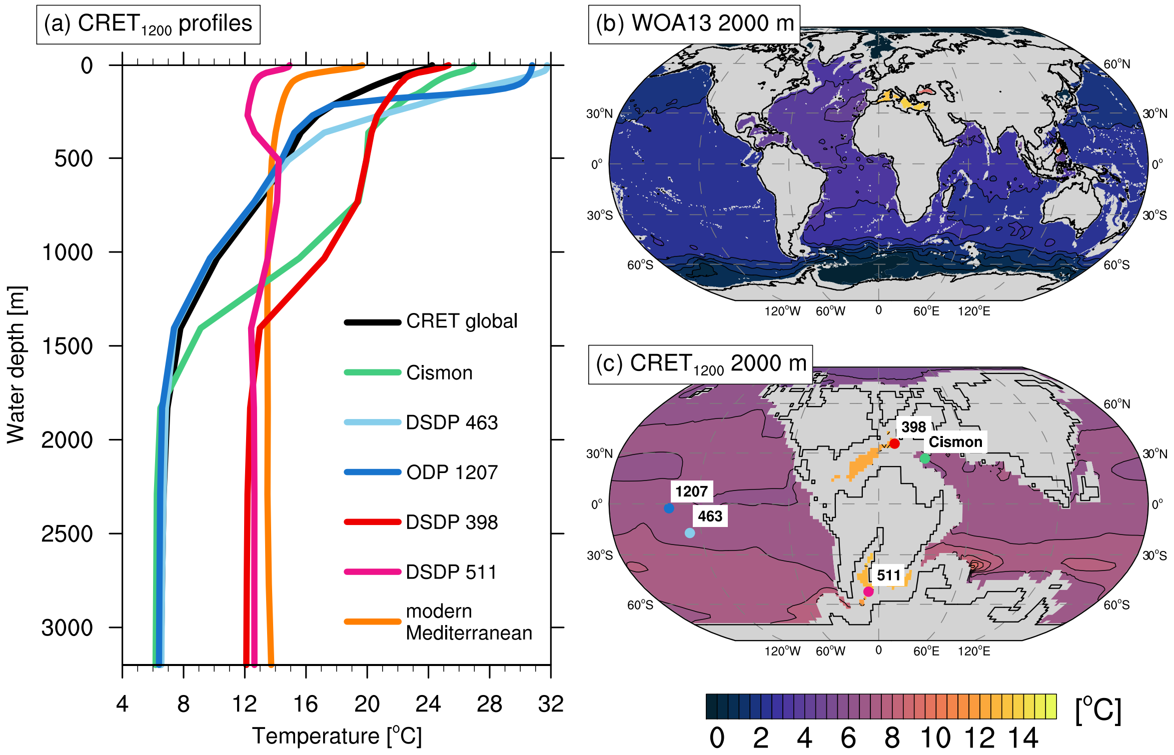

**Figure 3.4:** Comparison of present-day and Cretaceous ocean temperatures. (a) Simulated and observed ocean profiles for annual mean temperature around study sites in CRET$_{1200}$ and the modern Mediterranean Sea, as well as maps of 2000 m ocean temperatures for (b) present day and (c) Cret$_{1200}$. Profiles are averaged over an area of ± 5° in longitude and latitude to account for uncertainty in paleolocation and model bathymetry . Therefore, water depth for the profiles represent maximum depth in the region used for averaging. Black contour line interval is 0.5 °C. Present-day data from the World Ocean Atlas 2013 (Locarnini et al., 2013).

atures when comparing sea surface (Fig. 3.3a) and upper ocean temperatures (Fig. 3.3b). These enhanced longitudinal variations are caused by an increased influence of subsurface ocean dynamics on the otherwise radiatively controlled surface temperatures. The most pronounced features of zonal heterogeneity are the Western Pacific Warm Pool and eastern Pacific upwelling region (Fig. 3.3c-d) caused by westward near-surface winds associated with the Pacific Walker Circulation. This east-west gradient makes the simulated temperatures at the respective core locations highly sensitive to the reconstructed paleoposition, especially with a stronger subsurface contribution to the TEX$_{86}$ signal (Fig. 3.3d). In fact, the difference between the lowest and highest integrated temperature for the upper 200 m across the equatorial Pacific in CRET$_{1200}$ is up to 14 °C, nearly as large as the global meridional temperature gradient between low latitudes ( $|\phi| < 30°$) and high latitudes ( $|\phi| > 60°$) of 18 °C.

There are also clear differences in the ocean temperature profiles at individual study sites (Fig. 3.4a). While the central Pacific closely resembles the temperature profile of the global mean Cretaceous ocean, DSDP sites 398 and 511 are influenced by warmer waters at intermediate and deeper water depths. Simulated deep-water temperatures are about 6 °C warmer than the global mean and close to the 14 °C observed for the present-day Mediterranean Sea. The warm, saline deep waters result from excessive evaporation in low-latitude shallow shelf areas of the young North and South

Atlantic (Fig. 3.1) and fill the deep, silled basins due to the lack of lateral deep-water exchange (Fig. 3.4c). This situation is comparable to the modern Mediterranean Sea where water mass exchange is severely limited by a shallow sill at ∼300 m water depth near the narrow Strait of Gibraltar (Fig. 3.4b).

### 3.4.2 Comparison of Cretaceous and modern isoGDGT distribution patterns

Present-day core-top data (Fig. 3.5a) show a general increase in the fractional abundance of the crenarchaeol isomer ([Cren']) with increasing fractional abundances of crenarchaeol ([Cren]). Cretaceous OAE 1a sites with high $TEX_{86}$ values (>0.8) show fractional abundances of [Cren'] exceeding the range of present-day data (see Appendix Fig. 3.C2). Despite having similar $TEX_{86}$ values, samples from DSDP site 398 are generally enriched in the proportion of [Cren'] compared to samples from ODP site 1207. A similar trend is visible for DSDP site 511 compared to the Cismon samples. A comparable increase in [Cren'] abundance occurs also for surface sediments from the Mediterranean and Red Sea with increasing water depth of the sample location. OAE 1a samples from the North Atlantic and Falkland Plateau match or exceed the regression of deeper sediments from the Mediterranean and Red Sea, while Cismon and most of the ODP site 1207 samples show reduced fractional abundances of [Cren']. Despite the considerable spread in the data, the general tendency of higher fractional abundances of [Cren'] in samples from the restricted Early Cretaceous North and South Atlantic can also be seen in the rest of the Cretaceous data set (Fig. 3.5b) and especially in relation to samples from the Late Cretaceous North Atlantic. This systematic enrichment of [Cren'] indicates a different temperature-isoGDGT relationship or an additional non-temperature influence on these samples that is not detected by the commonly applied GDGT screening criteria (see Section 3.3.4).

Ratios of the fractional abundances of GDGT-2 and GDGT-3 ([GDGT-2]/[GDGT-3]) in the Cretaceous are predominantly lower than for the modern core tops (Fig. 3.5d) due to a decrease in [GDGT-2] and an increase in [GDGT-3] at higher $TEX_{86}$ values (>0.7, see Appendix Fig. 3.C2). Samples from the Atlantic Ocean show increased fractional abundances of [GDGT-2] during the Early Cretaceous compared to the Late Cretaceous. Again, DSDP sites 398 and 511 show overall higher [GDGT-2]/[GDGT-3] ratios than the respective samples from ODP site 1207 and Cismon. Ratios for the Falkland Plateau range between 4 to 12, similar to deeper sediments from the Mediterranean Sea.

The systematic differences in isoGDGT distributions can also be identified in relation to derived $TEX_{86}$ ratios. We combine the previous results in the ratio of fractional abundances of [Cren'] and [GDGT-2] compared to [Cren] in eq. (3.6):

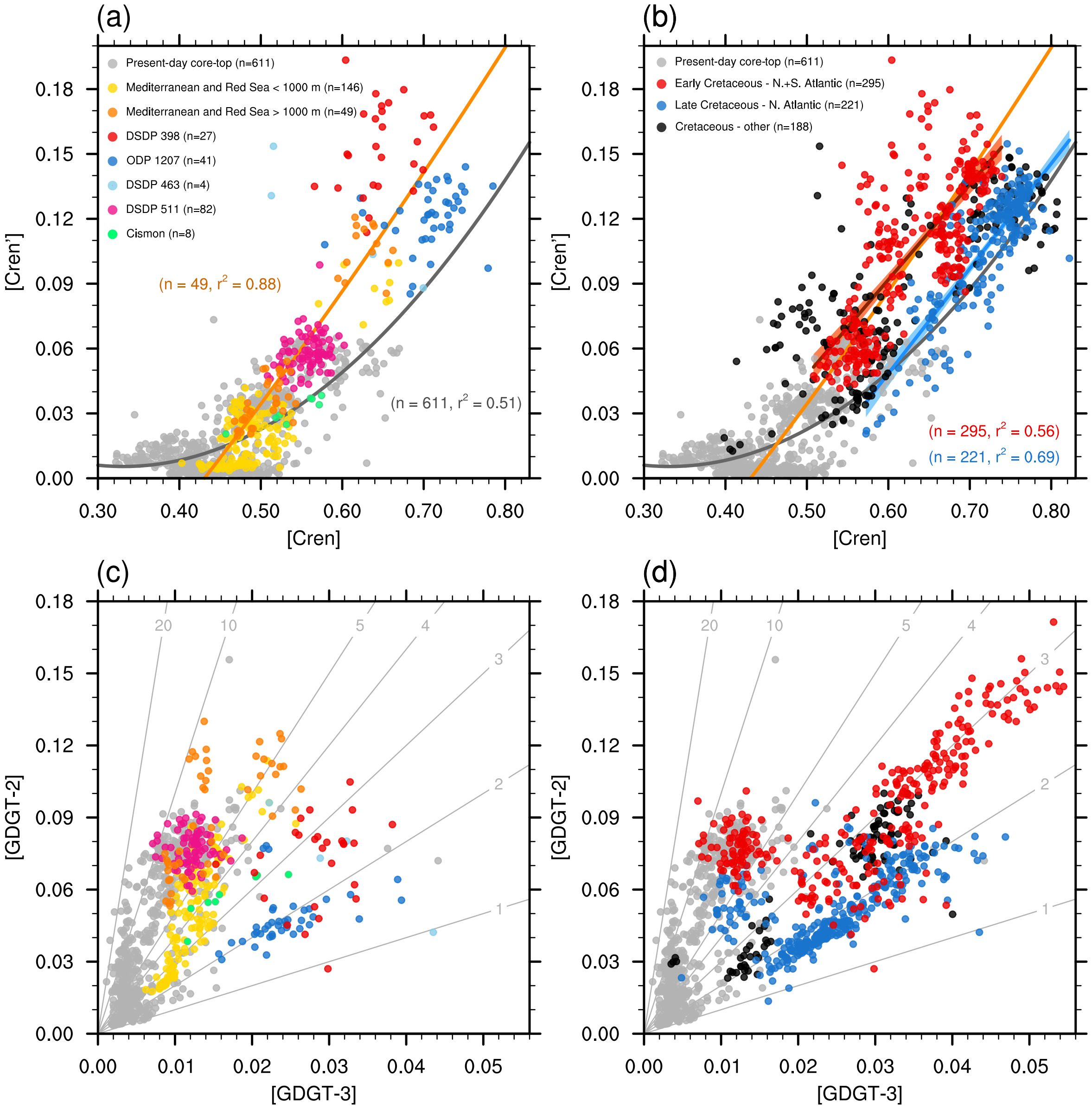

**Figure 3.5:** Fractional abundances of isoGDGTs for modern and Cretaceous samples. Cross-plots are shown for fractional abundances of (a-b) crenarchaeol against the crenarchaeol isomer and (c-d) GDGT-2 against GDGT-3. Colours represent samples from (a,c) sites covering OAE 1a as well as from the present-day Mediterranean and Red Sea and (b,d) the complete Cretaceous compilation. Results for individual sites are shown in Appendix Fig. 3.C3 with respective references listed in Appendix Table 3.A2. Paleolocations of the Early Cretaceous North and South Atlantic sites (DSDP 603, DSDP 534, DSDP 398, ODP 1049, DSDP 545 and DSDP 511) and the Late Cretaceous North Atlantic sites (ODP 1258, ODP 1259, DSDP 367, Bass River, Meirs Farm, Brazos River and Shuqualak) are shown in Appendix Fig. 3.C1. Regression lines represent the quadratic polynomial regression for (gray) present-day and the (orange) combined Mediterranean and Red Sea core-top data for sites deeper than 1000 m. Linear regressions and its 95% confidence intervals are shown for the respective (red) Early Cretaceous North and South Atlantic and the (blue) Late Cretaceous North Atlantic groups. Lines in (c-d) represent contours of constant [GDGT-2]/[GDGT-3] ratios.

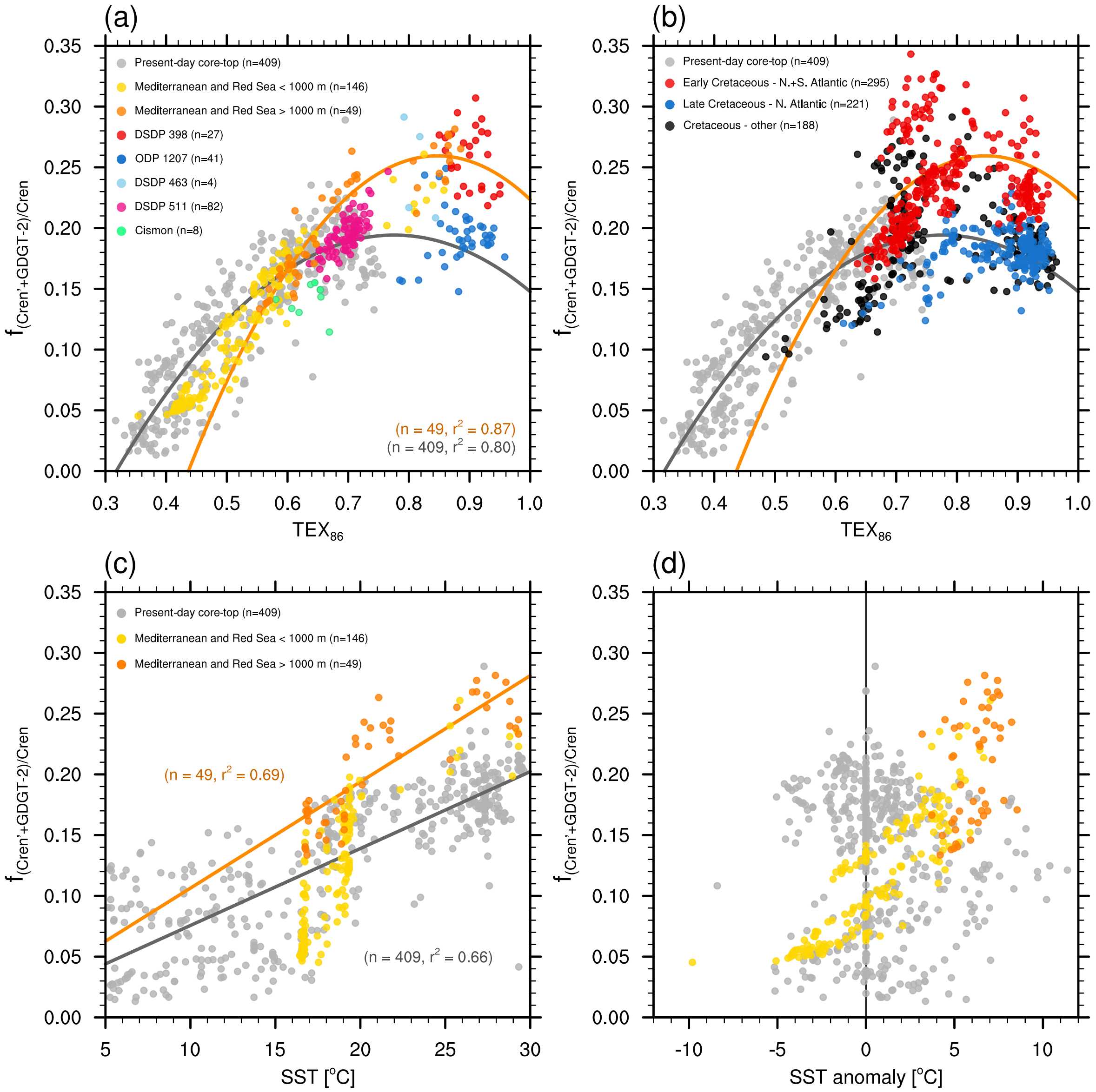

**Figure 3.6:** New isoGDGT ratio compared to $\mathrm{TEX}_{86}$ and SST. Shown are cross-plots of the $f_{(Cren'+GDGT-2)/Cren}$ ratio (Eq. (3.6)) against (a-b) $\mathrm{TEX}_{86}$, (c) satellite derived annual mean SST and (d) the difference between $\mathrm{TEX}_{86}^{H}$-derived and satellite measured temperatures. Data is shown for the present-day and Cretaceous compilations. Following the definition of $\mathrm{TEX}_{86}^{H}$, we exclude modern samples from regions with SST < 5 °C. Colours represent samples from (a) sites covering OAE 1a as well as from the present-day Mediterranean and Red Sea, (b) the whole Cretaceous compilation and (c-d) the present-day Mediterranean and Red Sea. Results for individual sites are shown in Appendix Fig. 3.C3 with respective references listed in Appendix Table 3.A2. Lines show (a-b) the quadratic polynomial and (c) linear regression for the present-day as well as the combined deep Mediterranean and Red Sea core-top data for sites deeper than 1000 m.

$$f_{(Cren'+GDGT-2)/Cren} = \frac{[Cren'] + [GDGT-2]}{[Cren] + [Cren'] + [GDGT-2]} \tag{3.6}$$

Values for $f_{(Cren'+GDGT-2)/Cren}$ show a strong increase with $TEX_{86}$ for samples from DSDP sites 511 and 398 (Fig. 3.6a) and the rest of the Early Cretaceous North and South Atlantic (Fig. 3.6b) that follows or exceeds the deep Mediterranean and Red Sea regression. ODP site 1207 and Cismon and the rest of the available Cretaceous data plot closely to the extrapolated global present-day core-top regression. The clear separation between the Early and Late Cretaceous Atlantic Ocean samples is a striking result. Absolute values of $f_{(Cren'+GDGT-2)/Cren}$ for DSDP site 511 are comparable to sediments from the deep Mediterranean, but indistinguishable from the global core-top data at the respective $TEX_{86}$ range. Nevertheless, we note that the increase in $f_{(Cren'+GDGT-2)/Cren}$ with $TEX_{86}$ for samples from the Falkland Plateau is closer to the deep Mediterranean and Red Sea than the global regression. Besides the observed increase in [Cren'] with temperature, samples from the Mediterranean and Red Sea show an additional enrichment of [Cren'] with water depth that is not present in global core-top data (see Appendix Fig. 3.C4). The higher relative abundances of [Cren'] and [GDGT-2] lead to a relative decrease in [GDGT-1] and [GDGT-3] in the $TEX_{86}$ ratio in eq. (3.1) (see Section 3.3.2). Since [GDGT-1] only influences the denominator in eq. (3.1) these systematic changes in the isoGDGT distribution lead to higher $TEX_{86}$ values in deeper sediments (Kim et al., 2015), despite similar surface temperatures (Fig. 3.6c). As previously reported (Kim et al., 2015), the resulting warm bias for $TEX_{86}^{H}$-derived SSTs amounts to up to 8 °C (Fig. 3.6d).

### 3.4.3 Implications for Early Cretaceous ocean temperatures

In summary, simulated local hydrographic parameters and the measured isoGDGT distributions at DSDP sites 398 and 511 indicate environmental conditions for the $TEX_{86}$ signal that are more comparable to the present-day Mediterranean and Red Sea than global core-top data. Regional calibrations have been developed for both basins for sediments deposited below 1000 m (Kim et al., 2015). In the modern data set for the Mediterranean and the Red Sea high correlations between $TEX_{86}^{H}$ and SST or 0-200 m temperatures are already observed for samples from water depths > 250 m (see Appendix Fig. 3.C5). Shallow sediments from the upper 250 m show markedly different ring indices indicating additional non-temperature influences on the isoGDGT distribution (see Appendix Fig. 3.C6). Temperature calibrations omitting samples from the upper 500 m or 1000 m are very similar and significantly different to the global regression (see Appendix Fig. 3.C5). The paleowater depth estimates for the Cretaceous OAE 1a sites start at $\sim$500 m (see Table 3.1) and hence the published regional calibrations from the deep Mediterranean and Red Sea (see Section 3.3.2) can be applied to the OAE 1a data. As a result, reconstructed upper ocean temperatures are significantly lower than for the respective global calibrations (Fig. 3.7). Mean SSTs are reduced from 36

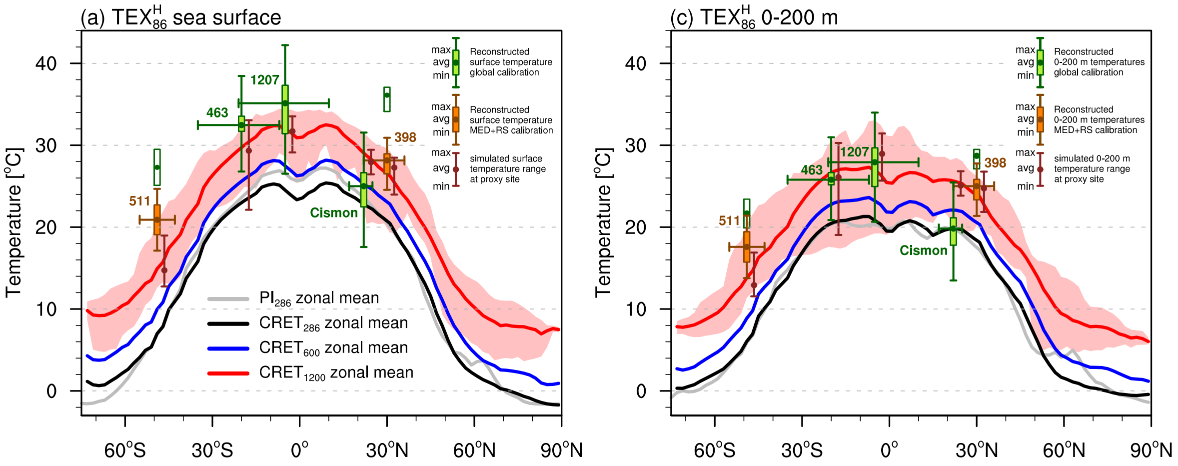

**Figure 3.7:** Model-proxy comparison of upper ocean temperatures for OAE 1a. As in Fig. 3.2, but applying regionally different temperature calibrations for the TEX$_{86}$ samples. These are the global TEX$_{86}^{H}$ sea surface temperature and subsurface calibrations, i.e. Eq. (3.2) and (3.3) for sites 463, 1207 and Cismon, as well as the Mediterranean and Red Sea SST and subsurface calibrations, i.e. Eq. (3.4) and (3.5) for sites 511 and 398.

to 28 °C and from 27.5 to 21 °C for sites 398 and 511 respectively (Fig. 3.7a). Respective 0-200 m integrated temperatures are lower by about 4 °C for both sites (Fig. 3.7b). This brings the upper ocean temperatures for the North and South Atlantic within the upper end of the CRET$_{1200}$ simulation and substantially reduces the misfit between the mid-latitude sites Cismon and DSDP 398.

Independent validation of the proposed lower temperatures for the North and South Atlantic is challenging because of the sparse availability of additional quantitative temperature proxies. Available low- and mid-latitude TEX$_{86}$ and oxygen isotope data uniformly show highest upper ocean temperatures around the Cenomanian-Turonian boundary and subsequent long-term cooling (Fig. 3.8). TEX$_{86}^{H}$-derived temperatures during the Cretaceous Thermal Optimum reach up to 37 °C for the surface (Fig. 3.8a) and 30 °C for the upper 200 m (Fig. 3.8c), with the latter comparable to the warmest values found in fish teeth from the western Tethys (Fig. 3.8e; Pucéat et al., 2003). The magnitude of peak TEX$_{86}^{H}$-derived SSTs agrees with those from planktonic foraminifera (Fig. 3.8d; O'Brien et al., 2017). High $\delta^{18}$O values of belemnites (Fig. 3.8d; Bodin et al., 2015) and fish teeth during the earliest Cretaceous show overall lower mean temperatures comparable to the Campanian-Maastrichtian interval. Similarly, TEX$_{86}$ samples from the Boreal realm show lowest temperatures during the Early Hauterivian and a gradual increase towards OAE 1a (Fig. 3.8a). In contrast, TEX$_{86}^{H}$-derived temperatures from two sites in the North Atlantic (DSDP sites 603 and 534; Littler et al., 2011) record very warm and stable conditions over a period of about 14 million years during the Berriasian–Barremian (see Appendix Fig. 3.C7). Surface (0-200 m) temperatures average at around 36 °C (28 °C) which is on par with peak OAE 1a and OAE 2 conditions and above the CRET$_{1200}$ simulation. The equivalent mean temperature change between the Valanginian minimum and OAE 2 maximum recorded in the fish teeth is significantly larger and amounts to about 10 °C, assuming no changes in the seawater fractionation. A similar decrease in $\delta^{18}$O of 2-

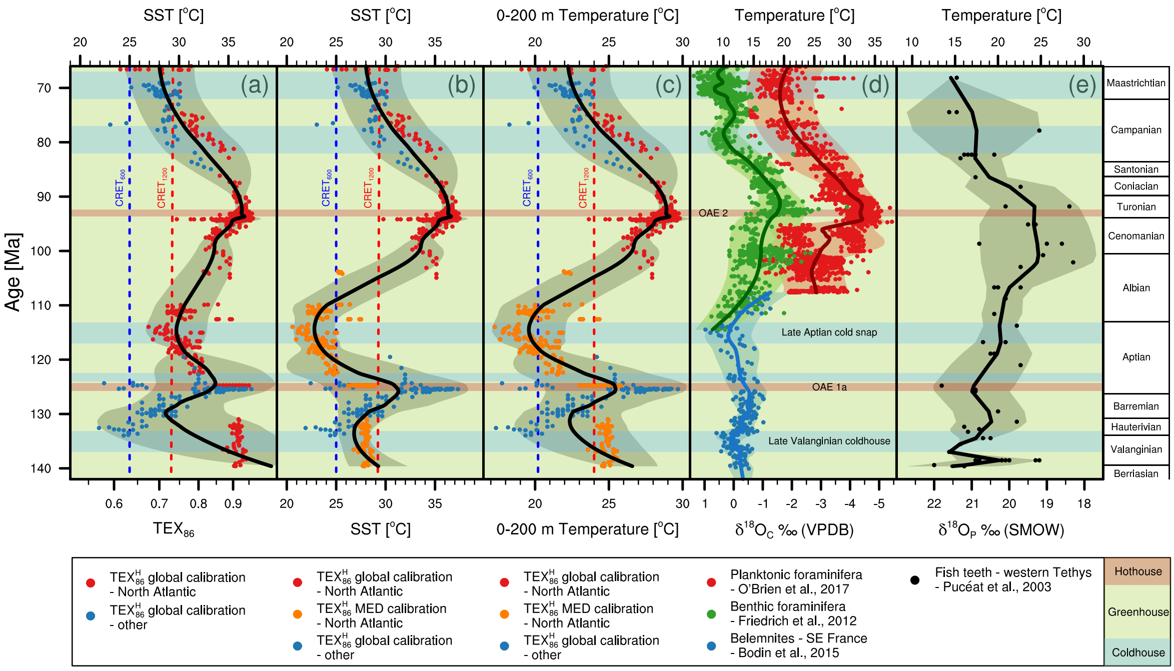

**Figure 3.8:** Cretaceous ocean temperature evolution for different proxy archives. Panels show data for (a-c) TEX$_{86}$ (O'Brien et al., 2017), (d) $\delta^{18}O_{carb}$ of a planktonic (O'Brien et al., 2017) and benthic compilation (Friedrich et al., 2012) as well as for belemnites from the Vocontian Basin (Bodin et al., 2015) and (e) $\delta^{18}O_{PO_4}$ of fish teeth from the western Tethyan platform (Pucéat et al., 2003). TEX$_{86}$ and planktonic foraminiferal data are only shown for paleolatitudes between 41°S-41°N (O'Brien et al., 2017). TEX$_{86}$ data also includes samples where no individual isoGDGT distributions are available. An overview of all study sites is shown in Appendix Table 3.A2. Temperature conversion follows (a-b) the TEX$_{86}^{H}$ SST calibrations based on either global or deep Mediterranean and Red Sea core-top data, i.e. Eq. (3.2) and (3.4), (c) as in (b) but for 0-200 m integrated temperatures, i.e. Eq. (3.3) and (3.5), and (d-e) the temperature equations (Hut, 1987; Kolodny et al., 1983) with a $\delta^{18}O_{seawater}$ of -1‰ (VSMOW) for a non-glacial world. Following the previous results, the respective regional Mediterranean and Red Sea calibrations have only been applied to the Early Cretaceous North Atlantic sites (DSDP 603, DSDP 534, DSDP 398, ODP 1049 and DSDP 545). Solid lines show a LOESS fit (span = 0.25) with the 95% prediction interval indicated by the shading around it. Vertical dashed lines represent simulated Early Aptian (a-b) SSTs and (c) 0-200 m mean temperatures averaged between 40°S-40°N. Background shading indicates published climatic state based on compiled sedimentological, paleontological and geochemical data (Bodin et al., 2015). Ages for fish teeth data are adjusted to GTS2012 (Ogg et al., 2012).

3 ‰ is also visible between Albian and Turonian values in a compilation of benthic foraminifera (Friedrich et al., 2012). Applying the Mediterranean and Red Sea calibration to Early Cretaceous TEX$_{86}$ samples from the North Atlantic (Fig. 3.8b-c) reduces the observed spread during the earliest Cretaceous and increases the amplitude of the Late Aptian cold snap. In agreement to the belemnite record, resulting minimum values for the Late Aptian cold snap and Late Valanginian coldhouse are similar and around low- to mid-latitude CRET$_{600}$ temperatures (40°S-40°N).

## 3.5 Discussion

### 3.5.1 Consistency of the OAE 1a TEX$_{86}$ record

Our simulations reveal an improved model-data fit for the Early Aptian OAE 1a by applying the 0-200 m depth-integrated calibrations, compared to the sea surface calibrations. Except for the

Cismon site, the reconstructed temperatures based on the deep subsurface calibration are also close to $CRET_{1200}$. This enhanced model-proxy congruence has also been shown for the early Eocene (Ho and Laepple, 2016) but the ecological justification of this statistical approach remains under debate (Tierney et al., 2017; Ho and Laepple, 2017). Based on modern core-top data, a recent study concluded that the $TEX_{86}$ signal is generated within the upper 200 m (Zhang and Liu, 2018). We show that the $CRET_{1200}$ simulation is only consistent with the OAE 1a $TEX_{86}$ record when we apply regionally varying temperature calibrations for the upper 200 m water depth.

The inter-site comparison of available proxy data with regard to results from the physical ocean model allows an approach to test the $TEX_{86}$ records irrespective of a temperature calibration. During the Early Cretaceous, paleogeographic reconstructions place ODP site 1207 and DSDP site 463 into the equatorial central to western Pacific (Dumitrescu et al., 2006; O'Brien et al., 2017), a region that forms the Western Pacific Warm Pool both in modern observations and the Cretaceous simulations. The Warm Pool is mainly caused by the westward blowing trade winds piling up the warm surface waters in the central and western part of the basin. The resulting shoaling of the thermocline in the east leads to upwelling of cooler waters off the coast of South America and produces a strong zonal gradient of upper ocean temperatures along the equator (Clement et al., 2005). Based on this reasoning, $TEX_{86}$ values from the Warm Pool region should also be the highest globally for OAE 1a. It is therefore surprising that $TEX_{86}$ values at site 398 in the North Atlantic are on average even slightly higher than those in the Pacific Warm Pool. Under the assumption that both records cover the same time interval and therefore atmospheric $CO_2$ levels we interpret this misfit as a sign for an additional non-temperature influence on the $TEX_{86}$ signal in the North Atlantic.

### 3.5.2 Reasons for the systematic isoGDGT differences

The comparison of the isoGDGT distributions reveals a general increase in the relative proportions of [Cren'] and [GDGT-2] in samples from the Early Cretaceous North and South Atlantic compared to other Cretaceous data, even after applying a strict GDGT screening for potential secondary influences (see Section 3.3.4). The magnitude of enrichment of [Cren'] relative to [Cren] is remarkably similar to the difference observed between shallow and deep-water sediments from the modern Mediterranean and Red Sea. The exact reasons for this water-depth control on the $TEX_{86}$ signal in these marine settings are still not clear (Villanueva et al., 2015; Kim et al., 2015; Kim et al., 2016). One hypothesis put forward (Kim et al., 2015) is that the warm intermediate and bottom water temperatures in these restricted basins lead to higher ammonium generation rates due to increased organic matter mineralisation. This might increase the abundance of the nitrifying Thaumarchaeota in deeper waters and therefore enhance their contribution to the sedimentary $TEX_{86}$ signal. It is also possible that the warm and saline bottom waters promote the preservation and export of membrane lipids of the deep-water Thaumarchaeota (Kim et al., 2016). In accordance, our simulations reveal that the oceanographic setting of the Early Cretaceous North and

South Atlantic was more similar to the modern Mediterranean Sea than to open-ocean conditions. Mean evaporation exceeded precipitation and formed warm and saline intermediate and bottom waters that filled the silled basins.

### 3.5.3 Ocean circulation in the Early Cretaceous North and South Atlantic

Water mass exchange in the opening South Atlantic was severely restricted by the Falkland Plateau (Pérez-Díaz and Eagles, 2017) and the shallow depth of the proto-Drake Passage (Donnadieu et al., 2016). Simulated water masses at DSDP site 511 were dominated by surface inflow of cool and fresh Southern Ocean waters and a southward subsurface return flow of warm and saline South Atlantic Intermediate Water. This anti-estuarine circulation bears a resemblance to the modern Strait of Gibraltar and the Portuguese continental margin where a strong warm bias in $\mathrm{TEX}_{86}^{H}$-derived temperatures has been attributed to the presence of the warm and saline Mediterranean Outflow Water (Kim et al., 2016).

In contrast, the North Atlantic was characterised by an estuarine circulation with a wind-driven zonal surface water export to the Pacific Ocean and intermediate water inflow via the Central American Seaway (Trabucho-Alexandre et al., 2012). The narrow proto-Caribbean ocean, small island arcs between North and South America (Ross and Scotese 1988) and the still closed equatorial Atlantic passage (Sewall et al., 2007) severely limited intermediate water exchange with the Pacific during the Early Cretaceous. In our simulations and in accordance with other available reconstructions for the Early Aptian (Sewall et al., 2007), the North Atlantic was effectively isolated from the global deep-water circulation below 1200 m. This geographical restriction favoured the local formation of warm and saline deep waters.

While quantitative reconstructions of the circulation in the young Atlantic Ocean are complicated by the still limited knowledge about paleogeographic boundary conditions, previous studies support the idea of limited connectivity to surrounding basins. Conspicuously cool Aptian-Albian surface temperatures derived from oxygen isotopes of planktonic foraminifera from the subtropical North Atlantic have been interpreted to reflect a high-evaporative fractionation factor influencing local seawater composition (Huber et al., 2011). Absolute water mass exchange of the North Atlantic with adjacent basins, diagnosed from corresponding anomalous strontium isotopic values, might have been even lower than the modern day transport between the Mediterranean Sea and the Atlantic Ocean (Huber et al., 2011). While this might be a rather extreme estimate, other climate model simulations also show locally formed warm and saline intermediate and deep waters (Barron and Peterson, 1990), primarily driven by the local geographic confinement (Poulsen et al., 2001). The resulting low vertical temperature gradient is also evident in the South Atlantic in the form of virtually identical oxygen isotope values for planktonic and benthic foraminifera at the Falkland

Plateau during the Aptian/Albian boundary interval (Huber et al., 2018). $\delta^{18}$O-derived benthic temperatures for the Albian range between 8-12 °C (Huber et al., 2018) and therefore lie between $CRET_{600}$ and $CRET_{1200}$ bottom water temperatures. In addition, sub-thermocline Barremian-Aptian temperatures of 10-16 °C, based on oxygen-isotope ratios of belemnites from the Falkland Plateau (Price and Gröcke, 2002) are also very similar to deep-water temperatures in $CRET_{1200}$ and the modern Mediterranean Sea (Locarnini et al., 2013).

### 3.5.4 Differences between Early and Late Cretaceous isoGDGTs

The reduced fractional abundances of [Cren'] and [GDGT-2] and increases in [Cren] in Late Cretaceous samples from the North Atlantic allow for two possible explanations. First, temporal changes might simply arise by chance due to different sampling locations. This would imply that the processes leading to the enhanced subsurface influence are limited only to certain regions of the North Atlantic or Late Cretaceous sites are situated at too shallow water depths to record any contribution of deep-dwelling Thaumarchaeota. Indeed, we note that the Early Cretaceous sites are rather clustered towards the probably more restricted (Arthur and Natland, 1979) northern and eastern parts of the North Atlantic, while most younger records are situated closer to the equator or western part of the basin (O'Brien et al., 2017). The overall reduced [GDGT-2]/[GDGT-3] ratios of the Late Cretaceous samples could also indicate shallower paleowater depths (Taylor et al., 2013). While Late Cretaceous sites with very shallow water depths (e.g. Bass River, Meirs Farm or Brazos River; see Appendix Table 3.A2) exclude per se any influence of deeper living archaeal communities, we also find no suspicious isoGDGT distributions at deep-water site DSDP 367 (Schouten et al., 2003; Forster et al., 2007). The relative large number and random selection of the locations forming the Early and Late Cretaceous groups in this analysis could also indicate a common underlying mechanism that led to a temporal change of the large-scale oceanographic setting. We hypothesise that enhanced intermediate and deep-water exchange with adjacent basins and the gradual shift from a highly restricted to a more ventilated Atlantic Ocean led to a progressive decline of the subsurface influence (up to 1000 m in the modern Mediterranean Sea (Kim et al., 2015)) on the sedimentary $TEX_{86}$ signal. The opening of the equatorial Atlantic gateway during the mid-Cretaceous (Pérez-Díaz and Eagles, 2017) allowed for enhanced water mass flow between the North and South Atlantic and might explain the observed transient changes in isoGDGT distributions. While a full deep water passage was probably not established before the Campanian (Friedrich and Erbacher, 2006), a shallow and maybe even intermediate water connection might have been present since 100 Ma (Pérez-Díaz and Eagles, 2017). Model simulations show a drop of the North Atlantic intermediate water temperature (salinity) at 1500 m depth of about 7 °C (0.5) between the Albian and Turonian times solely because of changes in the paleogeography (Poulsen et al., 2001) and enhanced inflow of Southern Ocean sourced waters (Donnadieu et al., 2016). The gradual widening of the proto-Caribbean ocean throughout the Early Cretaceous (Ross and Scotese, 1988) might have additionally increased the advection of cooler Pacific intermediate water into the North Atlantic (Topper et al., 2011). The resulting decrease in intermediate water temperatures and salinities potentially reduced the unusually high influence of the deep-dwelling Thaumarchaeota observed during the Early Cretaceous.

### 3.5.5 Implications for the meridional temperature gradient

We find an improved model-data congruence for OAE 1a when applying the Mediterranean and Red Sea calibration to the respective Cretaceous data. Proxy and model results show a meridional temperature gradient that is weaker than in the pre-industrial simulation but significantly stronger than the one derived from the global $\mathrm{TEX}_{86}^{H}$ calibration. This challenges previous studies indicating a minimal equator-to-pole temperature gradient during the Aptian (O'Brien et al., 2017) and OAE 1a (Jenkyns et al., 2012), but supports results from the BAYSPAR deep-time model (Naafs and Pancost, 2016). Our simulations reveal that the currently available $\mathrm{TEX}_{86}$ record for OAE 1a is not suitable to derive global temperature gradients. The interpretation of estimated equatorial Pacific temperatures is limited by strong zonal gradients in upper ocean temperatures and therefore rely on uncertain paleolocation reconstructions. DSDP site 511, being the only higher mid-latitude site is located on the subsiding Falkland Plateau where local hydrography was governed by the ongoing widening of the South Atlantic and uncertain connectivity to adjacent basins (Pérez-Díaz and Eagles, 2017).

Clearly, our approach of applying the modern Mediterranean and Red Sea calibration to parts of the Cretaceous data can only be considered a first approximation under the assumption that $\mathrm{TEX}_{86}$ export dynamics are comparable. But it would also mean that the warm bias for Early Cretaceous sites varies with the respective paleowater depth. Given the large uncertainty in these estimates for deep-time periods (Table 3.1), this further complicates the reconstruction of absolute temperatures. Areas outside of the restricted North and South Atlantic are therefore probably more suitable for assessing the mean ocean temperature evolution and could reveal valuable information about the strength and transient nature of any regional $\mathrm{TEX}_{86}$ warm bias. This becomes even more important as the vast majority of Cretaceous $\mathrm{TEX}_{86}$ data are derived from the North Atlantic (O'Brien et al., 2017). In contrast, less than 5% of the samples were collected from the Pacific Ocean even though it covered most of the Cretaceous world ocean.

## 3.6 Summary and Conclusions

Based on two independent lines of evidence resulting from physical circulation modelling and the systematic comparison of Cretaceous and modern isoGDGT distributions we conclude that:

1. Early Cretaceous North and South Atlantic isoGDGT samples show a systematic increase

in the relative abundance of [Cren'] and [GDGT-2] with a simultaneous decrease in [Cren] compared to other Cretaceous data. As the derived $TEX_{86}$ ratio does not include [Cren], this potentially influences resulting Early Cretaceous $TEX_{86}$ values and the regional $TEX_{86}$-temperature relation.

2. We expect that this offset is caused by an enhanced contribution of deep-water archaeal communities with a different isoGDGT distribution influencing the sedimentary $TEX_{86}$ signal that is similar to observations from the modern Mediterranean and Red Sea.
3. General circulation modelling shows the local formation of warm and saline intermediate and deep waters in the restricted North and South Atlantic Ocean that may have provided ideal environmental conditions for deep-water dwelling Thaumarchaeota.
4. Applying a regional temperature calibration from the modern Mediterranean and Red Sea to the respective Cretaceous data reduces reconstructed upper ocean temperatures by 4-8 °C.
5. Resulting OAE 1a upper ocean temperatures agree with model simulations at atmospheric $CO_2$ levels of 1200 ppmv.
6. Potential regional and temporal changes of the $TEX_{86}$-temperature relation should be considered when interpreting the $TEX_{86}$ paleorecord of restricted basins.

Whatever the exact reasons for the observed systematic differences in the isoGDGT distributions might be, its existence indicates the need to apply regionally varying temperature calibrations that reflect the differences in the $TEX_{86}$ signal. The next step to find these present-day analogue environments will be to better understand spatial differences in the $TEX_{86}$ export dynamics and what secondary processes besides temperature influence the isoGDGT distributions in modern core-top data, especially in deep restricted basins.

## Acknowledgements

We thank the International Ocean Discovery Program (IODP), which provided the samples for the new $TEX_{86}$ measurements. We further thank the German Research Foundation (DFG) for funding this research within the project "Evolving carbon sinks in the young South Atlantic: Drivers of global climate in the early Cretaceous greenhouse?". S.F. has been additionally supported by the German Research Foundation through the collaborative research project SFB 754 (sub-project A7). This is a contribution to PalMod. Model integrations were conducted at the Computing Center of Kiel University. We thank Janine Blöhdorn for generating most of the Cretaceous boundary conditions for the model and Stefan Hagemann for constructing the parameters for the hydrological discharge model. We are also grateful to Oliver Friedrich for providing the compilation of benthic foraminifera oxygen isotopic data.

## References

Arthur, Michael A. and James H. Natland (1979). "Carbonaceous sediments in the North and South Atlantic: The role of salinity in stable stratification of early Cretaceous basins". In: *Deep drilling results in the Atlantic Ocean: Continental Margins and Paleoenvironment.* Vol. 3, pp. 375–401. DOI: `10.1029/ME003p0375`.

Barron, Eric J. (1983). "A warm, equable Cretaceous: The nature of the problem". In: *Earth-Science Reviews* 19.4, pp. 305–338. DOI: `10.1016/0012-8252(83)90001-6`.

Barron, Eric J. and William H. Peterson (1990). "Mid-Cretaceous ocean circulation: Results from model sensitivity studies". In: *Paleoceanography* 5.3, pp. 319–337. DOI: `10.1029/PA005i003p00319`.

Blakey, Ronald C (2008). "Gondwana paleogeography from assembly to breakup—A 500 m.y. odyssey". In: *Special Paper 441: Resolving the Late Paleozoic Ice Age in Time and Space*. Vol. 441. 01. Geological Society of America, pp. 1–28. DOI: `10.1130/2008.2441(01)`.

Blöhdorn, Janine (2013). "Klima und Ozeanzirkulation der Frühen Kreide im Kiel Climate Model". PhD thesis. Christian-Albrechts-Universität Kiel, p. 121.

Bodin, Stéphane, Philipp Meissner, Nico M.M. Janssen, Thomas Steuber, and Jörg Mutterlose (2015). "Large igneous provinces and organic carbon burial: Controls on global temperature and continental weathering during the Early Cretaceous". In: *Global and Planetary Change* 133, pp. 238–253. DOI: `10.1016/j.gloplacha.2015.09.001`.

Bottini, C., E. Erba, D. Tiraboschi, H. C. Jenkyns, S. Schouten, and J. S. Sinninghe Damsté (2015). "Climate variability and ocean fertility during the Aptian Stage". In: *Climate of the Past* 11.3, pp. 383–402. DOI: `10.5194/cp-11-383-2015`.

Bralower, Timothy J., Seymour O. Schlanger, William V. Sliter, David J. Allard, R. Mark Leckie, and Michael A. Arthur (1994). "Timing and Paleoceanography of Oceanic Dysoxia/Anoxia in the Late Barremian to Early Aptian (Early Cretaceous)". In: *Palaios* 9.4, pp. 335–369. DOI: `10.2307/3515055`.

Bralower, Timothy J., Isabella Premoli Silva, and Mitchell J. Malone (2002). "New evidence for abrupt climate change in the Cretaceous and Paleogene: An Ocean Drlling Program expedition to Shatsky Rise, northwest Pacific". In: *GSA Today* 12.11, pp. 4–10. DOI: `10.1130/1052-5173(2002)012<0004:NEFACC>2.0.CO;2`.

Clement, Amy C., Richard Seager, and Raghu Murtugudde (2005). "Why are there tropical warm pools?" In: *Journal of Climate* 18.24, pp. 5294–5311. DOI: `10.1175/JCLI3582.1`.

Donnadieu, Yannick, Emmanuelle Pucéat, Mathieu Moiroud, François Guillocheau, and Jean-François Deconinck (2016). "A better-ventilated ocean triggered by Late Cretaceous changes in continental configuration". In: *Nature Communications* 7.1. DOI: `10.1038/ncomms10316`.

Dumitrescu, Mirela, Simon C. Brassell, Stefan Schouten, Ellen C. Hopmans, and Jaap S. Sinninghe Damsté (2006). "Instability in tropical Pacific sea-surface temperatures during the early Aptian". In: *Geology* 34.10, pp. 833–836. DOI: `10.1130/G22882.1`.

Forster, Astrid, Stefan Schouten, Kazuyoshi Moriya, Paul A. Wilson, and Jaap S. Sinninghe Damsté (2007). "Tropical warming and intermittent cooling during the Cenomanian/Turonian oceanic anoxic event 2: Sea surface temperature records from the equatorial Atlantic". In: *Paleoceanography* 22.1. DOI: `10.1029/2006PA001349`.

Friedrich, Oliver and Jochen Erbacher (2006). "Benthic foraminiferal assemblages from Demerara Rise (ODP Leg 207, western tropical Atlantic): possible evidence for a progressive opening of the Equatorial Atlantic Gateway". In: *Cretaceous Research* 27.3, pp. 377–397. DOI: `10.1016/j.cretres.2005.07.006`.

Friedrich, Oliver, Richard D. Norris, and Jochen Erbacher (2012). "Evolution of middle to late Cretaceous oceans-A 55 m.y. Record of Earth's temperature and carbon cycle". In: *Geology* 40.2, pp. 107–110. DOI: `10.1130/G32701.1`.

Hagemann, Stefan and Lydia Dümenil (1998). "A parametrization of the lateral waterflow for the global scale". In: *Climate Dynamics* 14.1, pp. 17–31. DOI: `10.1007/s003820050205`.

Ho, Sze Ling and Thomas Laepple (2016). "Flat meridional temperature gradient in the early Eocene in the subsurface rather than surface ocean". In: *Nature Geoscience* 9.8, pp. 606–610. DOI: `10.1038/ngeo2763`.

— (2017). "Reply to 'Eocene temperature gradients". In: *Nature Geoscience* 10.8, pp. 539–540. DOI: `10.1038/ngeo2998`.

Holbourn, Ann, Wolfgang Kuhnt, and Emanuel Soeding (2001). "Atlantic paleobathymetry, paleoproductivity and paleocirculation in the late Albian: The benthic foraminiferal record". In: *Palaeogeography, Palaeoclimatology, Palaeoecology* 170.3-4, pp. 171–196. DOI: `10.1016/S0031-0182(01)00223-1`.

Hollis, Christopher J., Kyle W.R. Taylor, Luke Handley, Richard D. Pancost, Matthew Huber, John B. Creech, Benjamin R. Hines, Erica M. Crouch, Hugh E.G. Morgans, James S. Crampton, Samantha Gibbs, Paul N. Pearson, and James C. Zachos (2012). "Early Paleogene temperature history of the Southwest Pacific Ocean: Reconciling proxies and models". In: *Earth and Planetary Science Letters* 349-350, pp. 53–66. DOI: `10.1016/j.epsl.2012.06.024`.

Hopmans, Ellen C., Stefan Schouten, and Jaap S. Sinninghe Damsté (2016). "The effect of improved chromatography on GDGT-based palaeoproxies". In: *Organic Geochemistry* 93, pp. 1–6. DOI: `10.1016/j.orggeochem.2015.12.006`.

Hopmans, Ellen C, Johan W.H. Weijers, Enno Schefuß, Lydie Herfort, Jaap S. Sinninghe Damsté, and Stefan Schouten (2004). "A novel proxy for terrestrial organic matter in sediments based on branched and isoprenoid tetraether lipids". In: *Earth and Planetary Science Letters* 224.1-2, pp. 107–116. DOI: `10.1016/j.epsl.2004.05.012`.

Huber, B. T. and R. M. Leckie (2011). "Planktic foraminiferal species turnover across deep-sea Aptian/Albian boundary sections". In: *The Journal of Foraminiferal Research* 41.1, pp. 53–95. DOI: `10.2113/gsjfr.41.1.53`.

Huber, Brian T., Kenneth G. MacLeod, Darren R. Gröcke, and Michal Kucera (2011). "Paleotemperature and paleosalinity inferences and chemostratigraphy across the Aptian/Albian boundary in the subtropical North Atlantic". In: *Paleoceanography* 26.4. DOI: `10.1029/2011PA002178`.

Huber, Brian T., Kenneth G. MacLeod, David K. Watkins, and Millard F. Coffin (2018). "The rise and fall of the Cretaceous Hot Greenhouse climate". In: *Global and Planetary Change* 167, pp. 1–23. DOI: `10.1016/j.gloplacha.2018.04.004`.

Hut, G (1987). *Consultants' group meeting on stable isotope reference samples for geochemical and hydrological investigations.* Tech. rep. International Atomic Energy Agency.

Jenkyns, H. C., L. Schouten-Huibers, S. Schouten, and J. S. Sinninghe Damsté (2012). "Warm Middle Jurassic-Early Cretaceous high-latitude sea-surface temperatures from the Southern Ocean". In: *Climate of the Past* 8.1, pp. 215–225. DOI: `10.5194/cp-8-215-2012`.

Jenkyns, Hugh C. (2010). "Geochemistry of oceanic anoxic events". In: *Geochemistry, Geophysics, Geosystems* 11.3, pp. 1–30. DOI: `10.1029/2009GC002788`.

Jing, Dai and Sun Bainian (2018). "Early Cretaceous atmospheric CO2 estimates based on stomatal index of Pseudofrenelopsis papillosa (Cheirolepidiaceae) from southeast China". In: *Cretaceous Research* 85, pp. 232–242. DOI: `10.1016/j.cretres.2017.08.011`.

Kim, Jung Hyun, Jaap van der Meer, Stefan Schouten, Peer Helmke, Veronica Willmott, Francesca Sangiorgi, Nalân Koç, Ellen C. Hopmans, and Jaap S Sinninghe Damsté (2010). "New indices and calibrations derived from the distribution of crenarchaeal isoprenoid tetraether lipids: Implications for past sea surface temperature reconstructions". In: *Geochimica et Cosmochimica Acta* 74.16, pp. 4639–4654. DOI: `10.1016/j.gca.2010.05.027`.

Kim, Jung Hyun, Oscar E. Romero, Gerrit Lohmann, Barbara Donner, Thomas Laepple, Eddie Haam, and Jaap S. Sinninghe Damsté (2012). "Pronounced subsurface cooling of North Atlantic waters off Northwest Africa during Dansgaard-Oeschger interstadials". In: *Earth and Planetary Science Letters* 339-340, pp. 95–102. DOI: `10.1016/j.epsl.2012.05.018`.

Kim, Jung Hyun, Stefan Schouten, Ellen C. Hopmans, Barbara Donner, and Jaap S. Sinninghe Damsté (2008). "Global sediment core-top calibration of the TEX86 paleothermometer in the ocean". In: *Geochimica et Cosmochimica Acta* 72.4, pp. 1154–1173. DOI: `10.1016/j.gca.2007.12.010`.

Kim, Jung Hyun, Stefan Schouten, Marta Rodrigo-Gámiz, Sebastiaan Rampen, Gianluca Marino, Carme Huguet, Peer Helmke, Roselyne Buscail, Ellen C. Hopmans, Jörg Pross, Francesca Sangiorgi, Jack B M Middelburg, and Jaap S. Sinninghe Damsté (2015). "Influence of deep-water derived isoprenoid tetraether lipids on the TEX86H paleothermometer in the Mediterranean Sea". In: *Geochimica et Cosmochimica Acta* 150, pp. 125–141. DOI: `10.1016/j.gca.2014.11.017`.

Kim, Jung Hyun, Laura Villanueva, Claudia Zell, and Jaap S. Sinninghe Damsté (2016). "Biological source and provenance of deep-water derived isoprenoid tetraether lipids along the Portuguese continental margin". In: *Geochimica et Cosmochimica Acta* 172, pp. 177–204. DOI: `10.1016/j.gca.2015.09.010`.

Kolodny, Yehoshua, Boaz Luz, and Oded Navon (1983). "Oxygen isotope variations in phosphate of biogenic apatites, I. Fish bone apatite-rechecking the rules of the game". In: *Earth and Planetary Science Letters* 64.3, pp. 398–404. DOI: `10.1016/0012-821X(83)90100-0`.

Littler, Kate, Stuart A. Robinson, Paul R. Bown, Alexandra J. Nederbragt, and Richard D. Pancost (2011). “High sea-surface temperatures during the Early Cretaceous Epoch”. In: *Nature Geoscience* 4.3, pp. 169–172. DOI: `10.1038/ngeo1081`.

Locarnini, R. A., A. V. Mishonov, J. I. Antonov, T. P. Boyer, H. E. Garcia, O. K. Baranova, M. M. Zweng, C. R. Paver, J. R. Reagan, D. R. Johnson, M. Hamilton, and D. Seidov (2013). “World Ocean Atlas 2013. Vol. 1: Temperature.” In: *NOAA Atlas NESDIS* 73.September, p. 40.

Madec, Gurvan (2008). “NEMO Ocean engine”. In: *Note du Pôle de modélisation 27*. Institut Pierre-Simon Laplace (IPSL), France.

Müller, R. Dietmar, Maria Sdrolias, Carmen Gaina, Bernhard Steinberger, and Christian Heine (2008). “Long-term sea-level fluctuations driven by ocean basin dynamics”. In: *Science* 319.5868, pp. 1357–1362. DOI: `10.1126/science.1151540`.

Naafs, B.D.A. and R.D. Pancost (2016). “Sea-surface temperature evolution across Aptian Oceanic Anoxic Event 1a”. In: *Geology* 44.11, pp. 959–962. DOI: `10.1130/G38575.1`.

O’Brien, Charlotte L., Stuart A. Robinson, Richard D. Pancost, Jaap S. Sinninghe Damsté, Stefan Schouten, Daniel J. Lunt, Heiko Alsenz, André Bornemann, Cinzia Bottini, Simon C. Brassell, Alexander Farnsworth, Astrid Forster, Brian T. Huber, Gordon N. Inglis, Hugh C. Jenkyns, Christian Linnert, Kate Littler, Paul Markwick, Alison McAnena, Jörg Mutterlose, B. David A. Naafs, Wilhelm Püttmann, Appy Sluijs, Niels A.G.M. van Helmond, Johan Vellekoop, Thomas Wagner, and Neil E. Wrobel (2017). “Cretaceous sea-surface temperature evolution: Constraints from TEX86 and planktonic foraminiferal oxygen isotopes”. In: *Earth-Science Reviews* 172, pp. 224–247. DOI: `10.1016/j.earscirev.2017.07.012`.

Ogg, J.G., L.A. Hinnov, and Chunju Huang (2012). “Cretaceous”. In: *The Geologic Time Scale*. Vol. 1-2. Elsevier, pp. 793–853. DOI: `10.1016/B978-0-444-59425-9.00027-5`.

Park, W., N. Keenlyside, M. Latif, A. Ströh, R. Redler, E. Roeckner, and G. Madec (2009). “Tropical Pacific Climate and Its Response to Global Warming in the Kiel Climate Model”. In: *Journal of Climate* 22.1, pp. 71–92. DOI: `10.1175/2008JCLI2261.1`.

Pérez-Díaz, Lucía and Graeme Eagles (2017). “South Atlantic paleobathymetry since early Cretaceous”. In: *Scientific Reports* 7.1. DOI: `10.1038/s41598-017-11959-7`.

Polik, Catherine A., Felix J. Elling, and Ann Pearson (2018). “Impacts of Paleoecology on the TEX86 Sea Surface Temperature Proxy in the Pliocene-Pleistocene Mediterranean Sea”. In: *Paleoceanography and Paleoclimatology* 33.12, pp. 1472–1489. DOI: `10.1029/2018PA003494`.

Poulsen, Christopher J., Eric J. Barron, Michael A. Arthur, and William H. Peterson (2001). “Response of the Mid-Cretaceous global oceanic circulation to tectonic and CO2 forcings”. In: *Paleoceanography* 16.6, pp. 576–592. DOI: `10.1029/2000PA000579`.

Price, Gregory D. and Darren R. Gröcke (2002). “Strontium-isotope stratigraphy and oxygen- and carbon-isotope variation during the Middle Jurassic-Early Cretaceous of the Falkland Plateau, South Atlantic”. In: *Palaeogeography, Palaeoclimatology, Palaeoecology* 183.3-4, pp. 209–222. DOI: `10.1016/S0031-0182(01)00486-2`.

Pucéat, Emmanuelle, Christophe Lécuyer, Simon M. F. Sheppard, Gilles Dromart, Stéphane Reboulet, and Patricia Grandjean (2003). “Thermal evolution of Cretaceous Tethyan marine waters inferred from oxygen isotope composition of fish tooth enamels”. In: *Paleoceanography* 18.2. DOI: `10.1029/2002PA000823`.

Roeckner, E, G Bäuml, Luca Bonaventura, R Brokopf, M Esch, Marco Giorgetta, Stefan Hagemann, Ingo Kirchner, Luis Kornblueh, Elisa Manzini, A Rhodin, U Schlese, Uwe Schulzweida, and Adrian Tompkins (2003). "The atmospheric general circulation model ECHAM 5. PART I: Model description". In: *Max Planck Institute for Meteorology Report* 349.

Ross, Malcolm I. and Christopher R. Scotese (1988). "A hierarchical tectonic model of the Gulf of Mexico and Caribbean region". In: *Tectonophysics* 155.1-4, pp. 139–168. DOI: `10.1016/0040-1951(88)90263-6`.

Roth, P.H (1981). "Mid-Cretaceous Calcareous Nannoplankton from the Central Pacific: Implications for Paleoceanography". In: *Initial Reports of the Deep Sea Drilling Project, 62*. Vol. 75. U.S. Government Printing Office, pp. 471–489. DOI: `10.2973/dsdp.proc.62.113.1981`.

Schouten, Stefan, Ellen C. Hopmans, Astrid Forster, Yvonne van Breugel, Marcel M.M. Kuypers, and Jaap S. Sinninghe Damsté (2003). "Extremely high sea-surface temperatures at low latitudes during the middle Cretaceous as revealed by archaeal membrane lipids". In: *Geology* 31.12, p. 1069. DOI: `10.1130/G19876.1`.

Schouten, Stefan, Ellen C. Hopmans, Enno Schefuß, and Jaap S. Sinninghe Damsté (2002). "Distributional variations in marine crenarchaeotal membrane lipids: A new tool for reconstructing ancient sea water temperatures?" In: *Earth and Planetary Science Letters* 204.1-2, pp. 265–274. DOI: `10.1016/S0012-821X(02)00979-2`.

Sewall, J O, R S W van de Wal, K van der Zwan, C van Oosterhout, H A Dijkstra, and C R Scotese (2007). "Climate model boundary conditions for four Cretaceous time slices". In: *Climate of the Past* 3.4, pp. 647–657. DOI: `10.5194/cpd-3-791-2007`.

Sibuet, J.-C. and W.B.F. Ryan (1979). "Site 398: Evolution of the West Iberian Passive Continental Margin in the Framework of the Early Evolution of the North Atlantic Ocean". In: *Initial Reports of the Deep Sea Drilling Project, 47 Pt. 2*. U.S. Government Printing Office. DOI: `10.2973/dsdp.proc.47-2.138.1979`.

Sinninghe Damsté, Jaap S., Jort Ossebaar, Stefan Schouten, and Dirk Verschuren (2012). "Distribution of tetraether lipids in the 25-ka sedimentary record of Lake Challa: extracting reliable TEX86 and MBT/CBT palaeotemperatures from an equatorial African lake". In: *Quaternary Science Reviews* 50, pp. 43–54. DOI: `10.1016/j.quascirev.2012.07.001`.

Taylor, Kyle W.R., Matthew Huber, Christopher J. Hollis, Maria T. Hernandez-Sanchez, and Richard D. Pancost (2013). "Re-evaluating modern and Palaeogene GDGT distributions: Implications for SST reconstructions". In: *Global and Planetary Change* 108, pp. 158–174. DOI: `10.1016/j.gloplacha.2013.06.011`.

Tierney, Jessica E., Jaap S. Sinninghe Damsté, Richard D. Pancost, Appy Sluijs, and James C. Zachos (2017). "Eocene temperature gradients". In: *Nature Geoscience* 10.8, pp. 538–539. DOI: `10.1038/ngeo2997`.

Tierney, Jessica E. and Martin P. Tingley (2014). "A Bayesian, spatially-varying calibration model for the TEX86 proxy". In: *Geochimica et Cosmochimica Acta* 127, pp. 83–106. DOI: `10.1016/j.gca.2013.11.026`.

— (2015). "A TEX86 surface sediment database and extended Bayesian calibration". In: *Scientific Data* 2, pp. 1–10. DOI: `10.1038/sdata.2015.29`.

Topper, R. P.M., J. Trabucho Alexandre, E. Tuenter, and P. Th Meijer (2011). “A regional ocean circulation model for the mid-Cretaceous North Atlantic Basin: Implications for black shale formation”. In: *Climate of the Past* 7.1, pp. 277–297. DOI: `10.5194/cp-7-277-2011`.

Trabucho-Alexandre, J., W. W. Hay, and P. L. De Boer (2012). “Phanerozoic environments of black shale deposition and the Wilson Cycle”. In: *Solid Earth* 3.1, pp. 29–42. DOI: `10.5194/se-3-29-2012`.

Trommer, Gabriele, Michael Siccha, Marcel T.J. van der Meer, Stefan Schouten, Jaap S. Sinninghe Damsté, Hartmut Schulz, Christoph Hemleben, and Michal Kucera (2009). “Distribution of Crenarchaeota tetraether membrane lipids in surface sediments from the Red Sea”. In: *Organic Geochemistry* 40.6, pp. 724–731. DOI: `10.1016/j.orggeochem.2009.03.001`.

Van Der Meer, D. G., R. E. Zeebe, D. J. J. van Hinsbergen, A. Sluijs, W. Spakman, and T. H. Torsvik (2014). “Plate tectonic controls on atmospheric CO2 levels since the Triassic”. In: *Proceedings of the National Academy of Sciences* 111.12, pp. 4380–4385. DOI: `10.1073/pnas.1315657111`.

Villanueva, Laura, Stefan Schouten, and Jaap S. Sinninghe Damsté (2015). “Depth-related distribution of a key gene of the tetraether lipid biosynthetic pathway in marine Thaumarchaeota”. In: *Environmental microbiology* 17.10, pp. 3527–3539. DOI: `10.1111/1462-2920.12508`.

Wuchter, Cornelia, Stefan Schouten, Marco J L Coolen, and Jaap S. Sinninghe Damsté (2004). “Temperature-dependent variation in the distribution of tetraether membrane lipids of marine Crenarchaeota: Implications for TEX86 paleothermometry”. In: *Paleoceanography* 19.4, pp. 1–10. DOI: `10.1029/2004PA001041`.

Zhang, Yi Ge and Xiaoqing Liu (2018). “Export Depth of the TEX86 Signal”. In: *Paleoceanography and Paleoclimatology* 33.7, pp. 666–671. DOI: `10.1029/2018PA003337`.

Zhang, Yi Ge, Mark Pagani, and Zhengrong Wang (2016). “Ring Index: A new strategy to evaluate the integrity of TEX86 paleothermometry”. In: *Paleoceanography* 31.2, pp. 220–232. DOI: `10.1002/2015PA002848`.

Zhang, Yi Ge, Chuanlun L. Zhang, Xiao-Lei Liu, Li Li, Kai-Uwe Hinrichs, and John E. Noakes (2011). “Methane Index: A tetraether archaeal lipid biomarker indicator for detecting the instability of marine gas hydrates”. In: *Earth and Planetary Science Letters* 307.3-4, pp. 525–534. DOI: `10.1016/j.epsl.2011.05.031`.

# Appendix A: Supplementary Tables

**Table 3.A1:** Paleolatitude estimates for OAE 1a sites. Reconstructions are based on a rotational model by Getech Plc as reported in the original Cretaceous TEX$_{86}$ compilation (O'Brien et al., 2017), GPlates (`https://gws.gplates.org`; Matthews et al., 2016), the Ocean Drilling Stratigraphic Network (`http://www.odsn.de`; Hay et al., 1999) and an online paleolatitude calculator (`http://www.paleolatitude.org`; Hinsbergen et al., 2015) applying different paleomagnetic reference frames (Torsvik et al., 2012; Besse and Courtillot, 2002; Kent and Irving, 2010). Time slices are chosen closest to OAE 1a and depend on respective time scale and temporal resolution.

| Site | Location | Getech Plc Aptian | GPlates 125 Ma | ODSN 120 Ma | paleolatitudes.org Torsvik et al. (2012) 120 Ma min/mean/max | paleolatitudes.org Besse and Courtillot (2002) 120 Ma min/mean/max | paleolatitudes.org Kent and Irving (2010) 120 Ma min/mean/max | **mean** (min-max) |
|---|---|---|---|---|---|---|---|---|
| DSDP 398 | proto-North Atlantic | 34°N | 32°N | 26°N | 31°N/33°N/36°N | 22°N/24°N/27°N | 30°N/33°N/36°N | **30°N** (22-36°N) |
| Cismon | Italian Southern Alps | 25°N | 25°N | 17°N | no data | no data | no data | **22°N** (17-25°N) |
| ODP 1207 | Shatsky Rise | -3°S | 10°N | 21°S | no data | no data | no data | **5°S** (10°N-21°S) |
| DSDP 463 | Mid-Pacific Mountains | 17°S | 7°S | 35°S | no data | no data | no data | **20°S** (7-35°S) |
| DSDP 511 | Falkland Plateau | 49°S | 53°S | 56°S | 46°S/48°S/51°S | 46°S/49°S/51°S | 43°S/46°S/48°S | **50°S** (43-56°S) |

**Table 3.A2:** Overview of study sites. All sites from the Cretaceous compilation (O'Brien et al., 2017) that provide individual isoGDGT distributions are included, while those that provide only derived TEX$_{86}$ values are limited to lower paleolatitudes (41°S-41°N) as listed in the original Cretaceous compilation (O'Brien et al., 2017). All sites marked with a low paleolatitude are included in Fig. 8 of the main text. NA = North Atlantic, SA = South Atlantic, O = Other.

| Site | Location | Region | Latitude | Age (Ma) | GDGTs | Reference |
|---|---|---|---|---|---|---|
| Shuqualak-Evans borehole | Mississippi, USA | NA | Low | 66 - 83 | Yes | Linnert et al. (2014) |
| Brazos River 1 section | Texas, USA | NA | Low | 67 | Yes | Vellekoop et al. (2014) |
| Meirs Farm 1 | New Jersey, USA | NA | Low | 67 | Yes | Vellekoop et al. (2016) |
| Aderet borehole 1 | Israel | O | Low | 69 - 85 | Yes | Alsenz et al. (2013) |
| FL533 | Arctic Ocean | O | High | 71 ± 1 | Yes | Jenkyns et al. (2004) |
| ODP 1259 | Demerara Rise | NA | Low | 86 - 94 | Yes | Forster et al. (2007a)<br>Bornemann et al. (2008) |
| ODP 1258 | Demerara Rise | NA | Low | 92 - 105 | Yes | Forster et al. (2007a) |
| ODP 1260 | Demerara Rise | NA | Low | 93 - 97 | No | Forster et al. (2007b) |
| Bass River borehole | New Jersey Shelf, USA | NA | Low | 93 - 94 | Yes | Helmond et al. (2014) |
| DSDP 367 | Cape Verde Basin | NA | Low | 94 | No | Schouten et al. (2003)<br>Forster et al. (2007b) |
| ODP 1276 | Newfoundland Basin | NA | Low | 94 | No | Sinninghe Damsté et al. (2010) |
| Wunstorf core | Lower Saxony Basin | O | High | 94 | Yes | Van Helmond et al. (2015) |
| DSDP 545 | Mazagan Plateau | NA | Low | 104 - 123 | Yes | Hofmann et al. (2008)<br>Wagner et al. (2008)<br>McAnena et al. (2013) |
| ODP 1049 | Blake Nose Plateau | NA | Low | 113 | Yes | Schouten et al. (2003)<br>Wagner et al. (2008) |
| DSDP 511 | Falkland Plateau | SA | High | 117 - 126 | Yes | Jenkyns et al. (2012) |
| Alstätte 1 outcrop | Northwest Germany | O | Low | 120 - 130 | No | Mutterlose et al. (2014) |
| DSDP 463 | Mid-Pacific Mountains | O | Low | 124 - 125 | Yes | Schouten et al. (2003) |
| Cismon core | Italian Southern Alps | O | Low | 124 - 125 | Yes | Bottini et al. (2015) |
| ODP 1207 | Shatsky Rise | O | Low | 125 - 126 | Yes | Dumitrescu et al. (2006) |
| DSDP 398 | proto-North Atlantic | NA | Low | 125 ±2 | Yes | Naafs and Pancost (2016) |
| A39 outcrop | Northwest Germany | O | Low | 126 - 130 | No | Mutterlose et al. (2010) |
| Gott outcrop | Northwest Germany | O | Low | 129 - 130 | No | Mutterlose et al. (2010) |
| Moorberg outcrop | Northwest Germany | O | Low | 129 - 130 | No | Mutterlose et al. (2012) |
| ODP 766 | Exmouth Plateau | O | High | 130 - 136 | Yes | Littler et al. (2011) |
| DSDP 534 | Blake-Bahama Basin | NA | Low | 131 - 140 | Yes | Littler et al. (2011) |
| Speeton outcrop | Northeast England | O | Low | 132 - 133 | No | Mutterlose et al. (2012) |
| DSDP 603 | Eastern North America | NA | Low | 132- 137 | Yes | Littler et al. (2011) |
| ODP 692 | Weddell Sea | O | High | 138 ± 7 | Yes | Littler et al. (2011) |
| DSDP 249 | Mozambique Ridge | O | High | 138 ± 7 | Yes | Littler et al. (2011) |

## References for Appendix A

Alsenz, Heiko, Julia Regnery, Sarit Ashckenazi-Polivoda, Aaron Meilijson, Libby Ron-Yankovich, Sigal Abramovich, Peter Illner, Ahuva Almogi-Labin, Shimon Feinstein, Zsolt Berner, and Wilhelm Püttmann (2013). “Sea surface temperature record of a Late Cretaceous tropical Southern Tethys upwelling system”. In: *Palaeogeography, Palaeoclimatology, Palaeoecology* 392, pp. 350–358. DOI: `10.1016/j.palaeo.2013.09.013`.

Besse, Jean and Vincent Courtillot (2002). “Apparent and true polar wander and the geometry of the geomagnetic field over the last 200 Myr”. In: *Journal of Geophysical Research: Solid Earth* 107.B11, EPM 6–1–EPM 6–31. DOI: `10.1029/2000JB000050`.

Bornemann, André, Richard D. Norris, Oliver Friedrich, Britta Beckmann, Stefan Schouten, Jaap S Sinninghe Damsté, Jennifer Vogel, Peter Hofmann, and Thomas Wagner (2008). “Isotopic evidence for glaciation during the Cretaceous supergreenhouse.” In: *Science* 319.5860, pp. 189–92. DOI: `10.1126/science.1148777`.

Bottini, C., E. Erba, D. Tiraboschi, H. C. Jenkyns, S. Schouten, and J. S. Sinninghe Damsté (2015). “Climate variability and ocean fertility during the Aptian Stage”. In: *Climate of the Past* 11.3, pp. 383–402. DOI: `10.5194/cp-11-383-2015`.

Dumitrescu, Mirela, Simon C. Brassell, Stefan Schouten, Ellen C. Hopmans, and Jaap S. Sinninghe Damsté (2006). “Instability in tropical Pacific sea-surface temperatures during the early Aptian”. In: *Geology* 34.10, pp. 833–836. DOI: `10.1130/G22882.1`.

Forster, Astrid, Stefan Schouten, Marianne Baas, and Jaap S. Sinninghe Damsté (2007a). “Mid-Cretaceous (Albian–Santonian) sea surface temperature record of the tropical Atlantic Ocean”. In: *Geology* 35.10, p. 919. DOI: `10.1130/G23874A.1`.

Forster, Astrid, Stefan Schouten, Kazuyoshi Moriya, Paul A. Wilson, and Jaap S. Sinninghe Damsté (2007b). “Tropical warming and intermittent cooling during the Cenomanian/Turonian oceanic anoxic event 2: Sea surface temperature records from the equatorial Atlantic”. In: *Paleoceanography* 22.1. DOI: `10.1029/2006PA001349`.

Hay, William W., Robert M. DeConto, Christopher N. Wold, Kevin M. Wilson, Silke Voigt, Michael Schulz, Adrienne Rossby Wold, Wolf-Christian Dullo, Alexander B. Ronov, Alexander N. Balukhovsky, and Emanuel Söding (1999). “Alternative global Cretaceous paleogeography”. In: *Special Paper 332: Evolution of the Cretaceous Ocean-Climate System*, pp. 1–47. DOI: `10.1130/0-8137-2332-9.1`.

Helmond, Niels A. G. M. van, Itzel Ruvalcaba Baroni, Appy Sluijs, Jaap S. Sinninghe Damsté, and Caroline P. Slomp (2014). “Spatial extent and degree of oxygen depletion in the deep proto-North Atlantic basin during Oceanic Anoxic Event 2”. In: *Geochemistry, Geophysics, Geosystems* 15.11, pp. 4254–4266. DOI: `10.1002/2014GC005528`.

Hinsbergen, Douwe J. J. van, Lennart V. de Groot, Sebastiaan J. van Schaik, Wim Spakman, Peter K. Bijl, Appy Sluijs, Cor G. Langereis, and Henk Brinkhuis (2015). “A Paleolatitude Calculator for Paleoclimate Studies”. In: *PLOS ONE* 10.6. Ed. by Dana L. Royer, e0126946. DOI: `10.1371/journal.pone.0126946`.

Hofmann, Peter, Isabel Stüsser, Thomas Wagner, Stefan Schouten, and Jaap S. Sinninghe Damsté (2008). “Climate-ocean coupling off North-West Africa during the Lower Albian: The Oceanic

Anoxic Event 1b". In: *Palaeogeography, Palaeoclimatology, Palaeoecology* 262.3-4, pp. 157–165. DOI: `10.1016/j.palaeo.2008.02.014`.

Jenkyns, H. C., L. Schouten-Huibers, S. Schouten, and J. S. Sinninghe Damsté (2012). "Warm Middle Jurassic-Early Cretaceous high-latitude sea-surface temperatures from the Southern Ocean". In: *Climate of the Past* 8.1, pp. 215–225. DOI: `10.5194/cp-8-215-2012`.

Jenkyns, Hugh C., Astrid Forster, Stefan Schouten, and Jaap S. Sinninghe Damsté (2004). "High temperatures in the Late Cretaceous Arctic Ocean". In: *Nature* 432.7019, pp. 888–892. DOI: `10.1038/nature03143`.

Kent, Dennis V. and Edward Irving (2010). "Influence of inclination error in sedimentary rocks on the Triassic and Jurassic apparent pole wander path for North America and implications for Cordilleran tectonics". In: *Journal of Geophysical Research: Solid Earth* 115.10, pp. 1–25. DOI: `10.1029/2009JB007205`.

Linnert, Christian, Stuart A. Robinson, Jackie A. Lees, Paul R. Bown, Irene Pérez-Rodríguez, Maria Rose Petrizzo, Francesca Falzoni, Kate Littler, José Antonio Arz, and Ernest E. Russell (2014). "Evidence for global cooling in the Late Cretaceous". In: *Nature Communications* 5.May. DOI: `10.1038/ncomms5194`.

Littler, Kate, Stuart A. Robinson, Paul R. Bown, Alexandra J. Nederbragt, and Richard D. Pancost (2011). "High sea-surface temperatures during the Early Cretaceous Epoch". In: *Nature Geoscience* 4.3, pp. 169–172. DOI: `10.1038/ngeo1081`.

Matthews, Kara J., Kayla T. Maloney, Sabin Zahirovic, Simon E. Williams, Maria Seton, and R. Dietmar Müller (2016). "Global plate boundary evolution and kinematics since the late Paleozoic". In: *Global and Planetary Change* 146, pp. 226–250. DOI: `10.1016/j.gloplacha.2016.10.002`.

McAnena, A., S. Flögel, P. Hofmann, J. O. Herrle, A. Griesand, J. Pross, H. M. Talbot, J. Rethemeyer, K. Wallmann, and T. Wagner (2013). "Atlantic cooling associated with a marine biotic crisis during the mid-Cretaceous period". In: *Nature Geoscience* 6.7, pp. 558–561. DOI: `10.1038/ngeo1850`.

Mutterlose, Jörg, Cinzia Bottini, Stefan Schouten, and Jaap S. Sinninghe Damsté (2014). "High sea-surface temperatures during the early Aptian Oceanic Anoxic event 1a in the Boreal Realm". In: *Geology* 42.5, pp. 439–442. DOI: `10.1130/G35394.1`.

Mutterlose, Jörg, Matthias Malkoc, Stefan Schouten, and Jaap S. Sinninghe Damsté (2012). "Reconstruction of vertical temperature gradients in past oceans - Proxy data from the Hauterivian-early Barremian (Early Cretaceous) of the Boreal Realm". In: *Palaeogeography, Palaeoclimatology, Palaeoecology* 363-364, pp. 135–143. DOI: `10.1016/j.palaeo.2012.09.006`.

Mutterlose, Jörg, Matthias Malkoc, Stefan Schouten, Jaap S. Sinninghe Damsté, and Astrid Forster (2010). "TEX86 and stable $\delta$18O paleothermometry of early Cretaceous sediments: Implications for belemnite ecology and paleotemperature proxy application". In: *Earth and Planetary Science Letters* 298.3-4, pp. 286–298. DOI: `10.1016/j.epsl.2010.07.043`.

Naafs, B.D.A. and R.D. Pancost (2016). "Sea-surface temperature evolution across Aptian Oceanic Anoxic Event 1a". In: *Geology* 44.11, pp. 959–962. DOI: `10.1130/G38575.1`.

O'Brien, Charlotte L., Stuart A. Robinson, Richard D. Pancost, Jaap S. Sinninghe Damsté, Stefan Schouten, Daniel J. Lunt, Heiko Alsenz, André Bornemann, Cinzia Bottini, Simon C. Brassell, Alexander Farnsworth, Astrid Forster, Brian T. Huber, Gordon N. Inglis, Hugh C. Jenkyns, Christian Linnert, Kate Littler, Paul Markwick, Alison McAnena, Jörg Mutterlose, B. David A. Naafs, Wilhelm Püttmann, Appy Sluijs, Niels A.G.M. van Helmond, Johan Vellekoop, Thomas Wagner, and Neil E. Wrobel (2017). "Cretaceous sea-surface temperature evolution: Constraints from TEX86 and planktonic foraminiferal oxygen isotopes". In: *Earth-Science Reviews* 172, pp. 224–247. DOI: `10.1016/j.earscirev.2017.07.012`.

Schouten, Stefan, Ellen C. Hopmans, Astrid Forster, Yvonne van Breugel, Marcel M.M. Kuypers, and Jaap S. Sinninghe Damsté (2003). "Extremely high sea-surface temperatures at low latitudes during the middle Cretaceous as revealed by archaeal membrane lipids". In: *Geology* 31.12, p. 1069. DOI: `10.1130/G19876.1`.

Sinninghe Damsté, Jaap S., Elisabeth C. van Bentum, Gert Jan Reichart, Jörg Pross, and Stefan Schouten (2010). "A CO2 decrease-driven cooling and increased latitudinal temperature gradient during the mid-Cretaceous Oceanic Anoxic Event 2". In: *Earth and Planetary Science Letters* 293.1-2, pp. 97–103. DOI: `10.1016/j.epsl.2010.02.027`.

Torsvik, Trond H., Rob Van der Voo, Ulla Preeden, Conall Mac Niocaill, Bernhard Steinberger, Pavel V. Doubrovine, Douwe J.J. van Hinsbergen, Mathew Domeier, Carmen Gaina, Eric Tohver, Joseph G. Meert, Phil J.A. McCausland, and L. Robin M. Cocks (2012). "Phanerozoic Polar Wander, Palaeogeography and Dynamics". In: *Earth-Science Reviews* 114.3-4, pp. 325–368. DOI: `10.1016/j.earscirev.2012.06.007`.

Van Helmond, N. A.G.M., A. Sluijs, J. S. Sinninghe Damsté, G. J. Reichart, S. Voigt, J. Erbacher, J. Pross, and H. Brinkhuis (2015). "Freshwater discharge controlled deposition of Cenomanian-Turonian black shales on the NW European epicontinental shelf (Wunstorf, northern Germany)". In: *Climate of the Past* 11.3, pp. 495–508. DOI: `10.5194/cp-11-495-2015`.

Vellekoop, J., A. Sluijs, J. Smit, S. Schouten, J. W. H. Weijers, J. S. Sinninghe Damste, and H. Brinkhuis (2014). "Rapid short-term cooling following the Chicxulub impact at the Cretaceous-Paleogene boundary". In: *Proceedings of the National Academy of Sciences* 111.21, pp. 7537–7541. DOI: `10.1073/pnas.1319253111`.

Vellekoop, Johan, Selen Esmeray-Senlet, Kenneth G. Miller, James V. Browning, Appy Sluijs, Bas van de Schootbrugge, Jaap S. Sinninghe Damsté, and Henk Brinkhuis (2016). "Evidence for Cretaceous-Paleogene boundary bolide "impact winter" conditions from New Jersey, USA". In: *Geology* 44.8, pp. 619–622. DOI: `10.1130/G37961.1`.

Wagner, Thomas, Jens O. Herrle, Jaap S.Sinninghe Damsté, Stefan Schouten, Isabel Stüsser, and Peter Hofmann (2008). "Rapid warming and salinity changes of Cretaceous surface waters in the subtropical north Atlantic". In: *Geology* 36.3, pp. 203–206. DOI: `10.1130/G24523A.1`.

# Appendix B: New TEX$_{86}$ data for DSDP Site 511

**Table 3.B1:** Raw isoGDGT data and derived TEX$_{86}$ values for 69 samples from DSDP Site 511, Falkland Plateau

| sample name | MCD [m] | GDGT-0 | GDGT-1 | GDGT-2 | GDGT-3 | Cren | Cren' | TEX$_{86}$ | TEX$_{86}^{H}$-SST |
|---|---|---|---|---|---|---|---|---|---|
| 511-55-2 3-6cm | 481.53 | 1504.7 | 428.86 | 565.87 | 129.94 | 3976.52 | 341.67 | 0.70753031 | 28.3225615 |
| 511-56-4 63-64cm | 494.63 | 34402.85 | 8040.44 | 10044.92 | 902.54 | 66376.74 | 7163.43 | 0.69254183 | 27.6865072 |
| 511-56-5 138-140cm | 496.88 | 20320.34 | 4267.58 | 6277.25 | 585.5 | 40039.21 | 4455.75 | 0.72619286 | 29.095955 |
| 511-57-1 75-77cm | 499.75 | 24025.55 | 5435.05 | 7129.43 | 870.27 | 49102.1 | 5411.11 | 0.7116051 | 28.4931509 |
| 511-57-1 134-135cm | 500.34 | 127647.92 | 28694.31 | 37248.8 | 3566.52 | 246401.42 | 20757.44 | 0.68211763 | 27.2359745 |
| 511-57-2 20-23cm | 500.7 | 32976.2 | 6664.73 | 8030.41 | 817.33 | 55453.55 | 5168.67 | 0.67773875 | 27.0446625 |
| 511-57-2 103-104cm | 501.53 | 187969.26 | 43099.23 | 57150.21 | 6434.61 | 404327.65 | 37697.47 | 0.70149068 | 28.0678982 |
| 511-57-3 94-96cm | 502.94 | 9827.99 | 2946.37 | 4205.25 | 586.03 | 25135.44 | 3342.81 | 0.73409317 | 29.4173809 |
| 511-57-4 66-69cm | 504.16 | 138589.79 | 29094.71 | 31335.09 | 4586.51 | 235306.48 | 21162.23 | 0.66239031 | 26.3641957 |
| 511-57-4 100-101cm | 504.5 | 112177.55 | 29788.05 | 39818.83 | 4118.52 | 241287.06 | 28312.34 | 0.70806831 | 28.3451407 |
| 511-57-6 34-35cm | 506.84 | 49752.57 | 13225.07 | 18376.95 | 2240.22 | 118525.52 | 14627.52 | 0.72714802 | 29.1350013 |
| 511-58-2 120-125cm | 511.2 | 11761.36 | 4345.87 | 6276.62 | 937.54 | 40566.23 | 6994.06 | 0.76577294 | 30.672441 |
| 511-58-4 34-36cm | 513.05 | 12994.8 | 3779.15 | 4666.04 | 714.18 | 29693.49 | 3511.49 | 0.70174479 | 28.0786571 |
| 511-58-4 47-49cm | 513.18 | 8636.09 | 2417.42 | 2690.32 | 484.87 | 18445.2 | 2240.59 | 0.69138794 | 27.6369711 |
| 511-58-4 94-95cm | 513.65 | 199638.45 | 54652.16 | 63106.4 | 10362.54 | 515910.41 | 51317.86 | 0.69542757 | 27.8100302 |
| 511-58-4 117-118cm | 513.88 | 1155721.15 | 315625.43 | 361406.81 | 55815.31 | 2710338.37 | 236811.02 | 0.67449839 | 26.9022946 |
| 511-58-4 132-134cm | 514.03 | 415463.62 | 119804.75 | 149767.32 | 23171.92 | 992180.82 | 99749.08 | 0.69475958 | 27.7814828 |
| 511-58-cc 7-9cm | 514.28 | 381834.52 | 124584.34 | 169758.91 | 23818.78 | 1254540.28 | 128065.75 | 0.7208055 | 28.8747576 |
| 511-59-1 1-2cm | 518.01 | 247913.2 | 75365.04 | 100706.06 | 11960.58 | 630040.34 | 63600.25 | 0.70049493 | 28.0257015 |
| 511-59-1 20-21cm | 518.2 | 397986.31 | 117565.75 | 144989.84 | 21917.88 | 1112403.42 | 109334.28 | 0.7014641 | 28.0667729 |
| 511-59-1 43-45cm | 518.43 | 706772.38 | 209014.03 | 306721.64 | 37978.6 | 2020227.48 | 236943.34 | 0.73564533 | 29.4801243 |
| 511-59-1 62-64cm | 518.62 | 1238595.31 | 342334.64 | 456287.75 | 62528.06 | 3197986.11 | 306986.58 | 0.70693966 | 28.2977523 |
| 511-59-1 98-100cm | 518.98 | 1471352.55 | 418918.76 | 603542.75 | 76628.61 | 3954957.92 | 362148.39 | 0.71331254 | 28.5643423 |
| 511-59-1 116-117cm | 519.16 | 1380472.98 | 369701.84 | 489941.73 | 68594.02 | 3528037.53 | 336915.74 | 0.707781 | 28.3330848 |
| 511-59-1 130-132cm | 519.3 | 473203.12 | 129589.47 | 151513.62 | 27103.44 | 1233570.56 | 103164.49 | 0.68498153 | 27.360434 |
| 511-59-2 1-2cm | 519.51 | 696707.26 | 189654.33 | 201864.24 | 32169.99 | 1564611.88 | 153309.75 | 0.67130869 | 26.7614833 |
| 511-59-2 22-23cm | 519.72 | 744616.62 | 215967.4 | 258234.31 | 35679.24 | 2015317.46 | 167397.08 | 0.68112446 | 27.1926908 |
| 511-59-2 58-60cm | 520.08 | 478977.28 | 115135.01 | 141907.16 | 16155.24 | 1089929.06 | 101108.87 | 0.69240428 | 27.6806064 |
| 511-59-2 107-108cm | 520.57 | 658586.4 | 179341.07 | 218924.61 | 35816.7 | 1799920.75 | 171312.3 | 0.70376173 | 28.1639144 |
| 511-59-3 5-8cm | 521.05 | 157230.06 | 42574.81 | 42513.6 | 7662.02 | 325495.34 | 29644.98 | 0.65215354 | 25.9015302 |
| 511-59-3 50-52cm | 521.5 | 704966.02 | 190737.32 | 199521.36 | 35155.93 | 1634455.33 | 149940.7 | 0.66848777 | 26.6363932 |
| 511-59-3 116-118cm | 522.16 | 199130.43 | 52463.62 | 50708.29 | 8871.34 | 402866.03 | 39065.73 | 0.65280938 | 25.9313889 |
| 511-59-4 2-3cm | 522.52 | 624427.04 | 138225.58 | 144758.24 | 27177.87 | 1311535.52 | 102108.24 | 0.66472068 | 26.4685208 |
| 511-59-4 36-37cm | 522.86 | 184640.68 | 48041.77 | 51685.72 | 7851.09 | 429673.64 | 40242.64 | 0.67500086 | 26.9244157 |
| 511-59-4 118-120cm | 523.68 | 75863.77 | 21318.7 | 25890.63 | 3909.52 | 171839.62 | 18633.11 | 0.69436414 | 27.7645704 |
| 511-60-1 9-10cm | 527.59 | 162595.82 | 46174.17 | 55849.36 | 8752.73 | 385065.66 | 39808.05 | 0.69336666 | 27.7218661 |
| 511-60-1 41-43cm | 527.91 | 357851.05 | 88967.69 | 108591.57 | 15621.2 | 832944.18 | 88558.3 | 0.70514995 | 28.222453 |
| 511-60-1 128-130cm | 528.78 | 148035.35 | 39074.07 | 41010.45 | 6216.15 | 318285.21 | 26500.71 | 0.65360291 | 25.9674759 |
| 511-60-2 66-69cm | 529.66 | 241499.25 | 54861.56 | 56379.38 | 9808.51 | 433286.35 | 43975.6 | 0.66755617 | 26.5949664 |
| 511-60-2 118-120cm | 530.18 | 319301.43 | 77828.19 | 78890.26 | 14692.05 | 662171.52 | 53059.46 | 0.65328015 | 25.9528034 |
| 511-60-3 8-10cm | 530.58 | 175835.49 | 42004.97 | 44762.63 | 6238.58 | 330367.32 | 32717.46 | 0.66589442 | 26.5209276 |
| 511-60-3 30-33cm | 530.8 | 178402.97 | 45574.97 | 45422.57 | 9106.36 | 368946.66 | 36271.89 | 0.66581334 | 26.5173104 |
| 511-60-3 105-108cm | 531.55 | 287174.41 | 67853.07 | 74940.74 | 11361.91 | 570808.77 | 43907.89 | 0.65741779 | 26.1403551 |
| 511-60-4 28-29cm | 532.28 | 145137.74 | 35246.12 | 31573.4 | 6062.06 | 269806.84 | 23933.23 | 0.63594289 | 25.1537991 |
| 511-60-5 33-36cm | 533.71 | 191002.74 | 43909.87 | 39478.54 | 8139.01 | 348741.55 | 34173 | 0.65067842 | 25.8342618 |
| 511-60-5 94-96cm | 534.32 | 127806.69 | 37829.88 | 54486.41 | 6914.48 | 335066.45 | 44743.63 | 0.73724579 | 29.5446813 |
| 511-60-6 9-11cm | 534.68 | 768444.88 | 213962.02 | 295098.02 | 46584.21 | 2009294.9 | 204819.44 | 0.71864269 | 28.78549 |
| 511-60-6 26-28cm | 534.85 | 1213884.04 | 341840.98 | 422051.24 | 68736.03 | 3010266.92 | 287458.06 | 0.69480836 | 27.7835683 |
| 511-60-cc 1-2cm | 535.18 | 969093.01 | 293804.59 | 371243.71 | 57951.05 | 2591713.34 | 256194.17 | 0.69995248 | 28.0026891 |
| 511-61-1 7-9cm | 537.07 | 424044.66 | 122890.46 | 175761.9 | 27174.66 | 1244462.31 | 136556.26 | 0.73422382 | 29.4226675 |
| 511-61-1 101-104cm | 538.01 | 554512.79 | 166139.56 | 234503.59 | 32939.91 | 1643375.97 | 170825.22 | 0.72512031 | 29.0520488 |
| 511-61-2 20-22cm | 538.7 | 359136.15 | 104519.19 | 122029.26 | 21117.69 | 964137.79 | 95425.13 | 0.69536039 | 27.8071605 |
| 511-61-2 67-68cm | 539.17 | 254832.92 | 81247.43 | 101349.63 | 16032.64 | 723628.4 | 86531.73 | 0.71508268 | 28.6379682 |
| 511-61-2 144-145cm | 539.94 | 536972.37 | 155450.78 | 201461.78 | 30829.64 | 1434158.26 | 151715.5 | 0.7118388 | 28.5029052 |
| 511-61-3 38-40cm | 540.38 | 294904.3 | 85655.23 | 102255.29 | 15814.03 | 715237.48 | 85166.05 | 0.70350288 | 28.1529863 |
| 511-61-3 120-121cm | 541.2 | 170962.97 | 52620.88 | 63893.39 | 10783.52 | 451910.4 | 49183.8 | 0.7018336 | 28.0824164 |
| 511-61-4 34-37cm | 541.84 | 391145.33 | 113667.35 | 129757.1 | 24736.03 | 1083483.44 | 109959.34 | 0.69938801 | 27.9787239 |
| 511-61-4 130-132cm | 542.8 | 64619.44 | 21768.17 | 30569.2 | 4821.67 | 214583.35 | 23707.78 | 0.73081457 | 29.2844121 |
| 511-61-cc 5-7cm | 544.24 | 50507.24 | 15099.46 | 18403.13 | 3081.21 | 141123.88 | 16463.66 | 0.71535942 | 28.649462 |
| 511-62-1 67-68cm | 547.17 | 24397.1 | 7673.68 | 8292.28 | 1384.61 | 61328.25 | 6394.13 | 0.67682557 | 27.00461 |
| 511-62-1 118-120cm | 547.68 | 280593.07 | 71427.87 | 88562.89 | 15302.3 | 699574.23 | 71388.32 | 0.71044483 | 28.4446763 |
| 511-62-2 7-8cm | 548.07 | 289087.18 | 80374.47 | 93104.93 | 19743.8 | 695527.43 | 68178.42 | 0.69252497 | 27.6857841 |
| 511-62-2 83-86cm | 548.83 | 293164 | 87257.94 | 109264.7 | 17626.35 | 796892.63 | 80497.27 | 0.70385526 | 28.1678619 |
| 511-62-3 5-6cm | 549.55 | 236512.9 | 71334.43 | 93026.52 | 16458.58 | 637609.97 | 72687.85 | 0.71861005 | 28.7841406 |
| 511-62-3 40-42cm | 549.9 | 121843.88 | 37794.81 | 41796.36 | 7105.53 | 299007.27 | 31931.63 | 0.68140148 | 27.2047703 |
| 511-62-3 148-149cm | 550.98 | 197715.44 | 57191.86 | 66616.35 | 13454.27 | 503609.43 | 50964.1 | 0.69615418 | 27.8410517 |
| 511-62-4 81-82cm | 551.81 | 62808.97 | 18587.35 | 23320.61 | 3709.31 | 168965.78 | 18480.02 | 0.71001348 | 28.4266351 |
| 511-62-4 125-126cm | 552.25 | 454514.29 | 153726.86 | 210969.56 | 31594.15 | 1360309.98 | 132675.93 | 0.70938262 | 28.4002291 |
| 511-62-5 69-70cm | 553.19 | 24704.78 | 7219.09 | 9231.85 | 1689.93 | 65615.44 | 7465.54 | 0.71807489 | 28.7620102 |

# Appendix C: Supplementary Figures

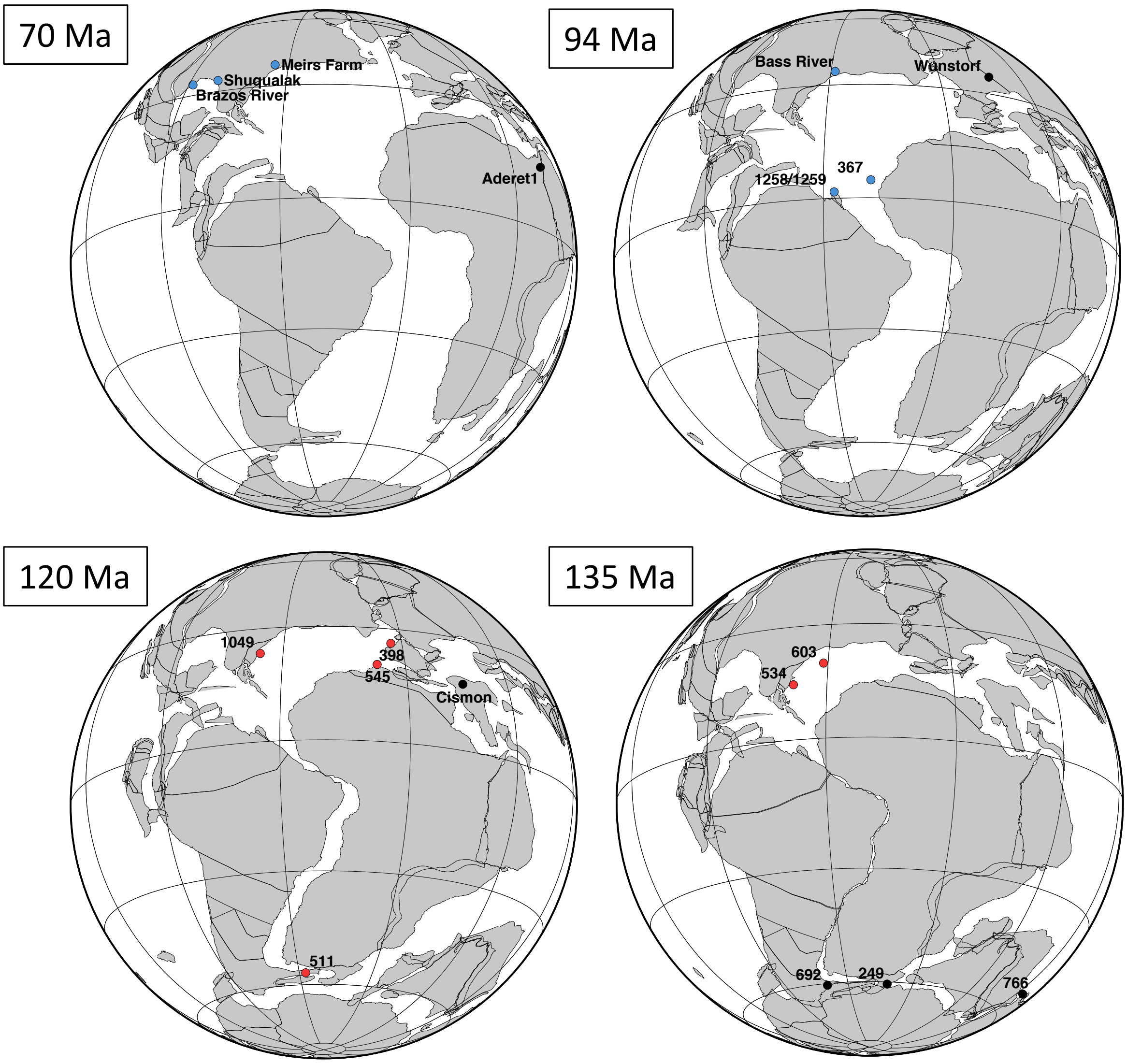

**Figure 3.C1:** Paleogeographic reconstructions for study sites. Shown are all sites from the study region that provide individual isoGDGT fractional abundances (see Appendix Table 3.A2). Color coding represents groups for Early Cretaceous North and South Atlantic, Late Cretaceous Nort Atlantic and other Cretaceous sites as used in Fig. 3.5 and 3.6 of the main text and Appendix Fig. 3.C2. Sites are assigned to the closest available time slice (70 Ma, 94 Ma, 120 Ma or 135 Ma), therefore not all sites provide data for the exact shown age. Reconstructions generated at `http://www.odsn.de/odsn/services/paleomap/adv_map.html`.

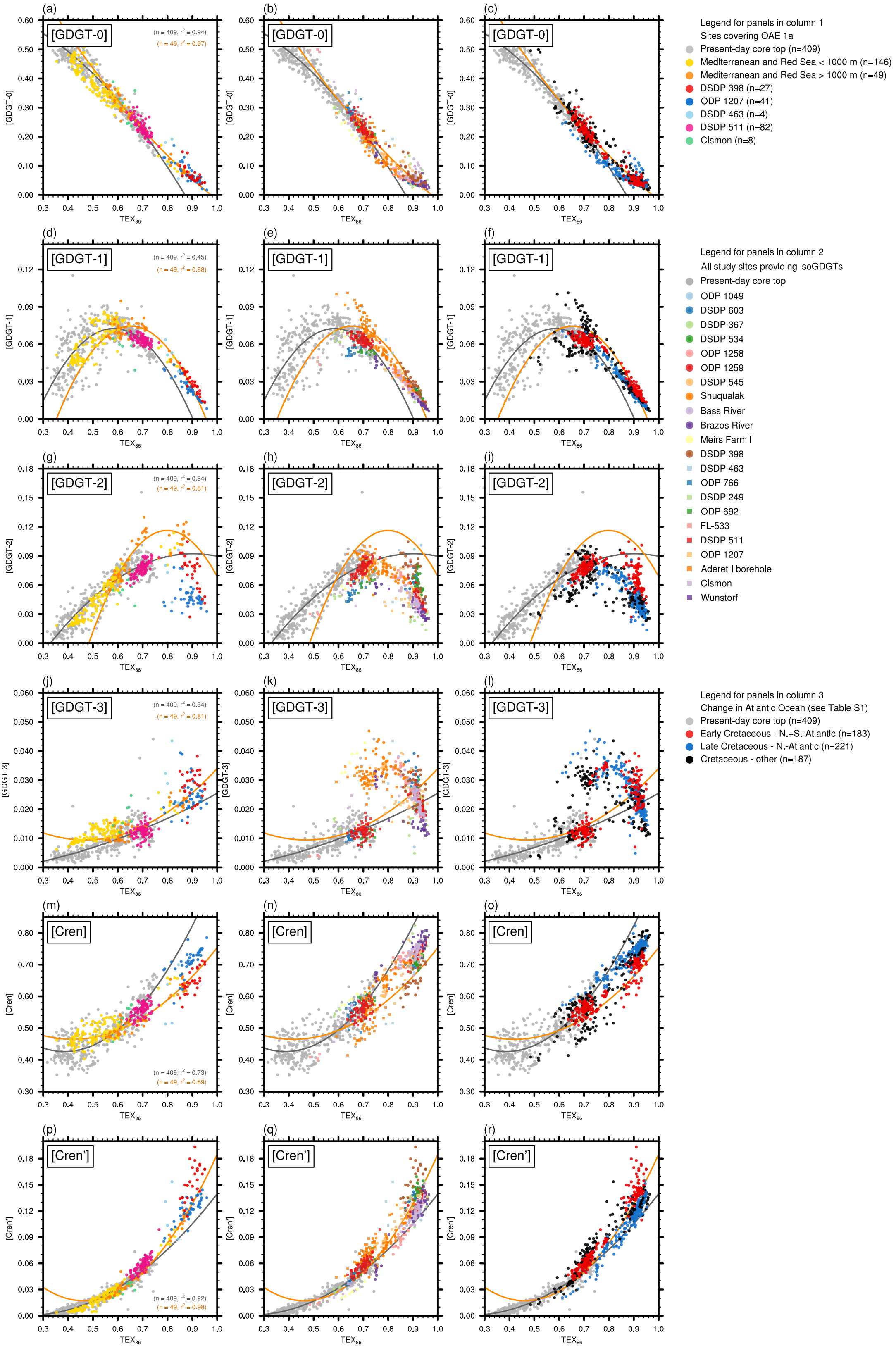

**Figure 3.C2:** Fractional abundances of individual isoGDGTs against derived $TEX_{86}$ ratios. Data include core-tops and surface sediments from a global present-day data set for regions with SST > 5°C (Tierney and Tingley, 2015), the modern Mediterranean and Red Sea (Kim et al., 2015; Trommer et al., 2009), the Cretaceous compilation (O'Brien et al., 2017) and new measurements for DSDP site 511. Columns show data for sites covering OAE 1a, all Cretaceous sites and the temporal change for sites from the Cretaceous Atlantic Ocean respectively. See Appendix Table 3.A2 for an overview of the individual study sites. Fractional abundances of [GDGT-0] are not available for many samples from DSDP site 545 leading to consequently higher abundances of the other isoGDGTs. We therefore excluded these samples from this figure. Quadratic polynomial regressions are shown for (gray) global present-day data and for (orange) deep sites below 1000 m from the modern Mediterranean and Red Sea.

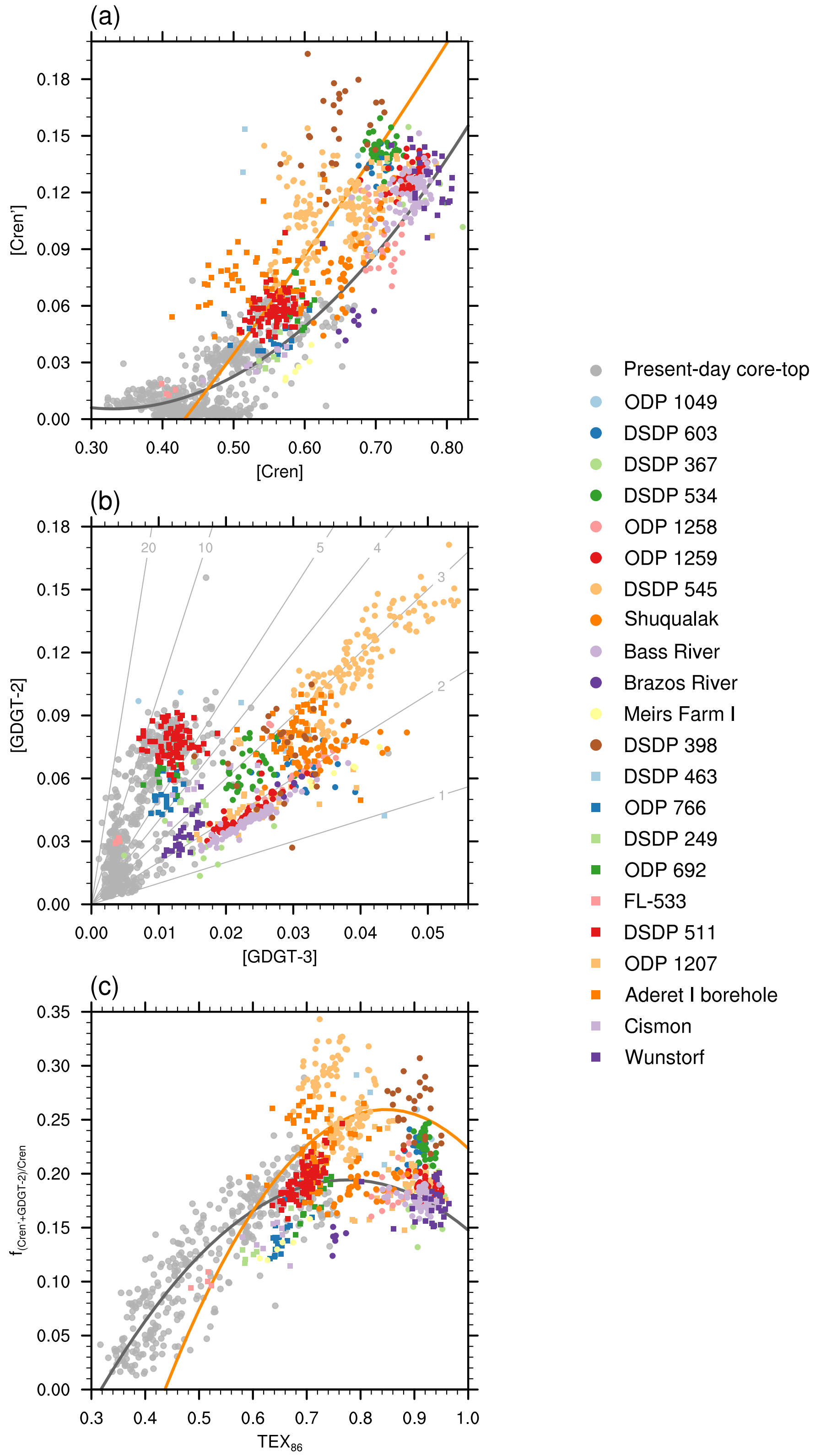

**Figure 3.C3:** Cross-plots of fractional abundances of (a) crenarchaeol against the crenarchaeol isomer, (b) GDGT-2 against GDGT-3 and (c) $f_{(Cren'+GDGT-2)/Cren} = \frac{[Cren']+[GDGT-2]}{[Cren]+[Cren']+[GDGT-2]}$ against TEX$_{86}$. [GDGT-0] is not provided for many samples from DSDP site 545. This by definition increases the fractional abundances of other individual isoGDGTs, but does not influence the ratios of multiple isoGDGTs discussed in this work (e.g. [Cren']/[Cren], [GDGT-2]/[GDGT-3] or $f_{(Cren'+GDGT-2)/Cren}$). We therefore included these samples in this figure. Quadratic polynomial regressions in panel (a) and (c) are shown for global present-day data in gray and for deep sites below 1000 m from the modern Mediterranean and Red Sea in orange. Contours in panel (b) represent lines of constant [GDGT-2]/[GDGT-3] ratios.

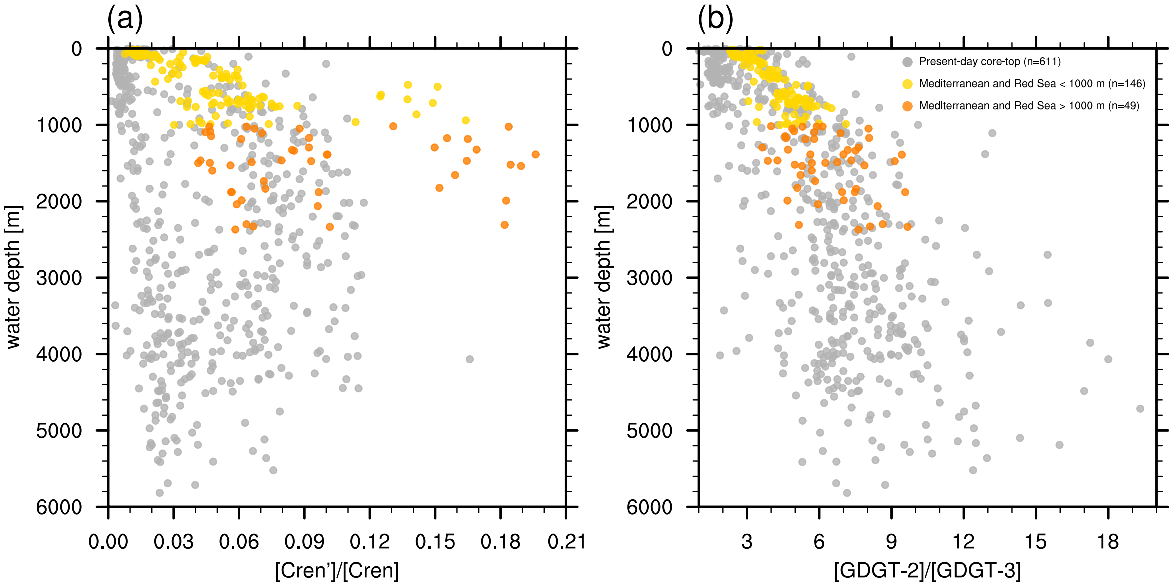

**Figure 3.C4:** Water depth dependence of [Cren']/[Cren] and [GDGT-2]/[GDGT-3] ratios in modern surface sediments.

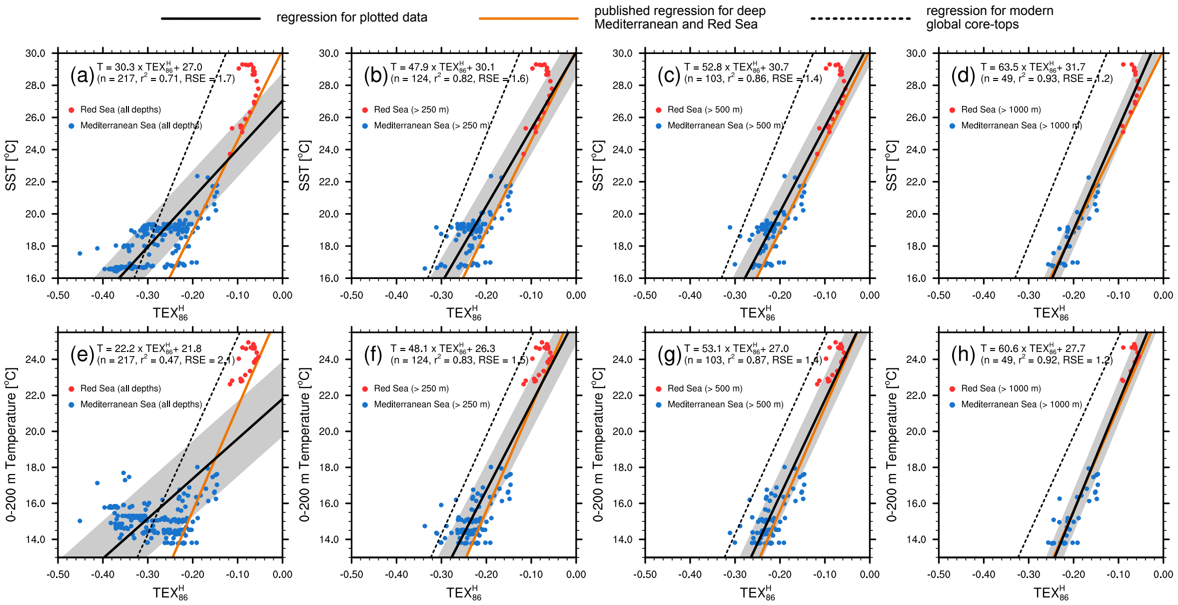

**Figure 3.C5:** TEX$^H_{86}$ correlations with SST and 0-200 m integrated temperatures (Locarnini et al., 2013) for the combined Mediterranean and Red Sea core-top and surface sediment data. The dashed lines represent the respective global calibrations (Kim et al., 2010; Kim et al., 2012) with no water depth restriction applied. Solid black lines show the calculated linear regression after removing samples from the respective depth intervals. Shading indicates ± the residual standard error. Orange lines represent the published regressions for deep sites (> 1000 m) from the modern Mediterranean and northern Red Sea (Kim et al., 2015). The analysis is similar to this previous study (Kim et al., 2015), but the resulting regressions are slightly different due to the inclusion of additional samples from the southern Red Sea (Trommer et al., 2009).

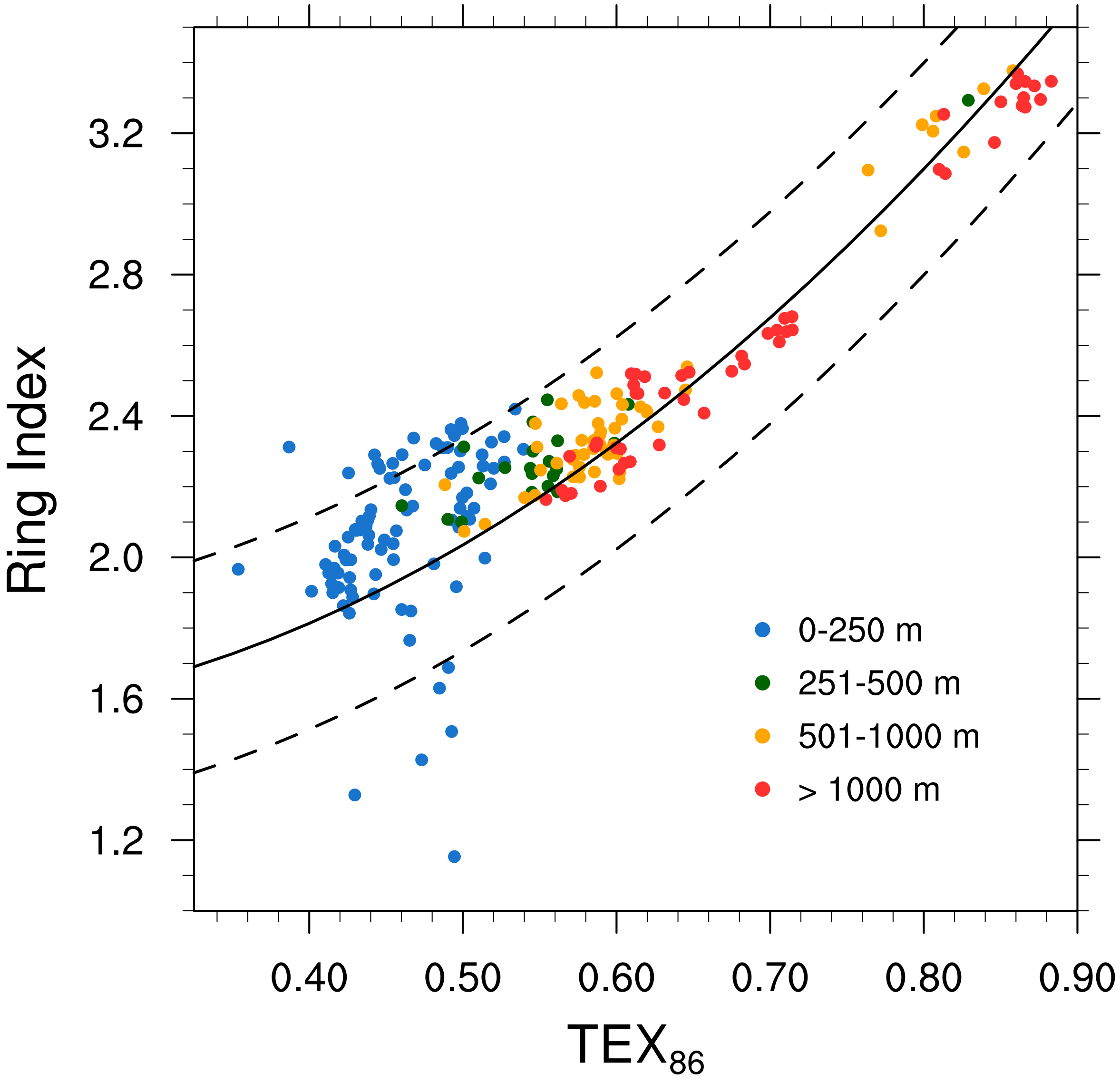

**Figure 3.C6:** Ring index (RI) for $TEX_{86}$ samples from the modern Mediterranean and Red Sea for different depth intervals. With RI = 0 x [GDGT-0] + 1 x [GDGT-1] + 2 x [GDGT-2] + 3 x [GDGT-3] + 4 x [Cren] + 4 x [Cren']. The black lines represent the global modern $TEX_{86}$-RI core-top relationship (Zhang and Liu, 2018) and its $2\sigma$ uncertainty range that is used to exclude data points with different isoGDGT productions. All samples from water depths greater than 250 m fall within the $2\sigma$ range.

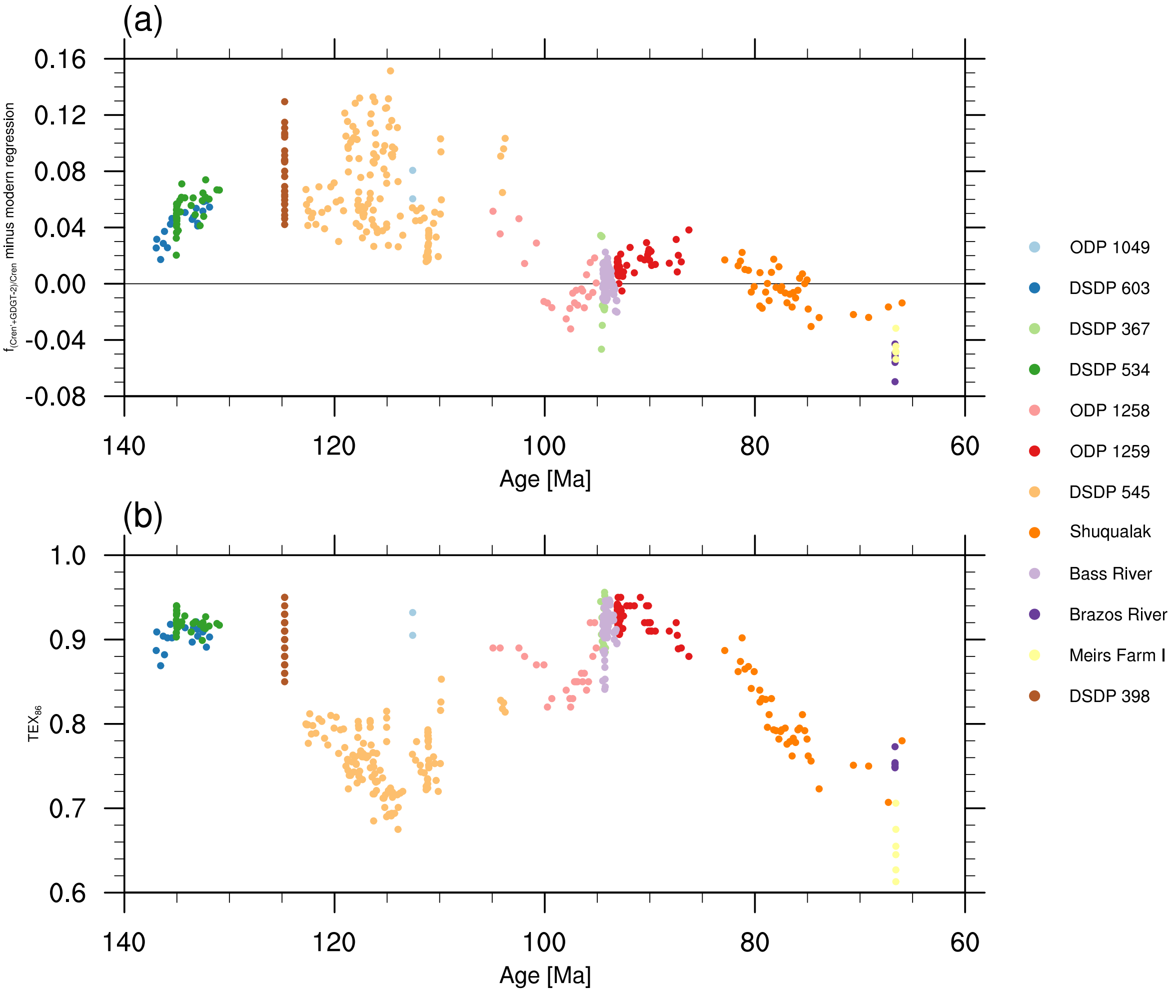

**Figure 3.C7:** Temporal evolution of Cretaceous isoGDGT anomalies. All sites from the North Atlantic that provide individual isoGDGT distributions are included. Shown are (a) the difference of the $f_{(Cren'+GDGT-2)/Cren} = \frac{[Cren']+[GDGT-2]}{[Cren]+[Cren']+[GDGT-2]}$ ratio to the present-day regression at the respective TEX$_{86}$ value shown in Appendix Fig. 3.C3c and (b) corresponding TEX$_{86}$ values.

# 4 Controls on Early Cretaceous South Atlantic Ocean circulation and carbon burial - a climate model-proxy synthesis

Sebastian Steinig, Wolf Dummann, Peter Hofmann, Wonsun Park, Mojib Latif, Martin Frank, Jens O. Herrle, Thomas Wagner and Sascha Flögel

**Declaration:** *This chapter is in preparation for submission. Sascha Flögel and Peter Hofmann proposed the study. I designed and carried out all experiments, made the analysis and wrote the chapter. Wolf Dummann provided the geochemical part of Fig. 4.1. The interpretation of the results benefited greatly from discussions with all project partners.*

## 4.1 Abstract

Black shale sediments from the Barremian to Albian South Atlantic document intense and widespread marine organic carbon burial during the initial stages of seafloor spreading between Africa and South America. The enhanced sequestration of atmospheric $CO_2$ makes these young ocean basins potential drivers of Early Cretaceous carbon cycle and climate perturbations. The opening of marine gateways between initially restricted basins and related circulation and ventilation changes is a commonly invoked explanation for the transient formation and destruction of these regional carbon sinks. Still, large uncertainties in paleogeographic reconstructions limit not only the interpretation of available paleoceanographic data but also prevent any robust model-based quantification of the proposed circulation and carbon burial changes. Here we assess the principal controls on the Early Cretaceous South Atlantic and Southern Ocean circulation changes under full consideration of the uncertainties in available paleogeographic boundary conditions. Specifically, we use a large ensemble of climate model experiments to simulate the Barremian to Albian progressive opening of the Falkland Plateau and Georgia Basin gateways with different configurations of the proto-Drake Passage, the Walvis Ridge and atmospheric $CO_2$ concentrations. The experiments are designed to complement latest geochemical data across the region and to test derived circulation hypotheses. Increased evaporation and intermediate water formation at subtropical latitudes drive a meridional overturning circulation whose vertical extent is mainly determined by the sill depth of the Falkland Plateau. The export of this warm and saline intermediate water leads to bottom water temperatures in the Falkland Basin that reach up to 15 °C and even exceed local surface temperatures. The simulated temperature and salinity range, representing the sensitivity to uncertain boundary conditions, increases with water depth. Temperatures in the deep Cape Basin vary between 3.1 to 17.6 °C. Local overturning and upper ocean stratification in the restricted Angola Basin are particularly sensitive to atmospheric $CO_2$ concentrations due to large-scale changes in the hydrological cycle. Densest water masses are formed in the southern Angola Basin and reach the deep Cape Basin as Walvis Ridge Overflow Water. The neodymium isotope and organic carbon burial record in the Southern Ocean can only be reproduced with a shallow, 200 m deep proto-Drake Passage. Both a closed and a too deep gateway reduce the sensitivity of Weddell Sea circulation and convection to paleogeographic changes of the Falkland Plateau. The close integration of new climate model experiments with multi-proxy paleoceanographic data thereby provides valuable constraints on the configuration of key oceanic gateways during the Early Cretaceous. Finally, the simulated processes are integrated in a recent carbon burial framework to show the principal control of the regional gateway evolution on the progressive shift from prevailing saline and oxygen-depleted subtropical water masses to the dominance of ventilated, high-latitude deep waters.

## 4.2 Introduction

The Early Cretaceous (i.e., Barremian to Albian) South Atlantic Ocean provides a unique possibility of gaining insights into the complex interplay of large-scale tectonics, related ocean circulation and carbon burial changes and the global climate evolution. On the one hand, the young ocean basin emerges in the wake of the ongoing breakup of Gondwana and rifting between South America and Africa that started in Late Jurassic (Torsvik et al., 2009). On the other hand, the general warmth of the Early Cretaceous greenhouse climate (O'Brien et al., 2017) was punctuated with severe perturbations of the global carbon cycle (e.g., Weissert, 1989; Bralower et al., 1994), short-term temperature fluctuations (Bodin et al., 2015; Jenkyns, 2018) and marine biotic crises (McAnena et al., 2013). The large shelf areas and restricted circulation in young ocean basins produce favourable conditions for enhanced biogeochemical turnover rates and organic carbon burial (Trabucho-Alexandre et al., 2012), thereby providing a possible link between regional basin evolution and global carbon cycle perturbations. Sedimentary evidence for periods of enhanced carbon sequestration come from the widespread deposition of organic-rich black shales found throughout the Mesozoic Atlantic Ocean, with an increased occurrence during the Aptian-Albian (Stein et al., 1986). Biogeochemical modelling shows that the restricted environments of the developing South Atlantic and Southern Ocean acted as efficient carbon sinks that played a crucial role in driving global cooling during the Late Aptian (McAnena et al., 2013).

Dummann et al. (submitted) reconstructed the Early Cretaceous gateway opening in the southern South Atlantic and the related formation and destruction of regional carbon sinks. They combine a new stratigraphic framework for several sites across the South Atlantic and Southern Ocean with radiogenic neodymium (Nd) isotope signatures to trace past water mass mixing between both basins (Fig. 4.1c). The neodymium isotopic composition, expressed as $\epsilon_{Nd}$(t), is used as a quasi-conservative tracer of bottom water masses (Frank, 2002). Differences in the $\epsilon_{Nd}$(t) of seawater are mainly caused by spatially heterogeneous lithogenic input in the source region of a water mass and by mixing along its flow path. Dummann et al. (submitted) demonstrate the dominant control of marine gateways on the local ocean circulation and ventilation. Before 124 Ma, the paleogeographic position of the Falkland Plateau severely limited water mass exchange between the South Atlantic and the Southern Ocean (Fig. 4.1d). Limited ventilation of the Cape Basin led to oxygen deficient deep waters and formation of organic-rich black shales (Fig. 4.1b). The detection of a more radiogenic water mass at DSDP Site 511 on the Falkland Plateau at around 119 Ma marks the onset of increased South Atlantic Intermediate Water (SAIW) export due to a progressive westward drift of the Falkland Plateau (Fig. 4.1e). At about 113 Ma to 110 Ma, the Maurice Ewing Bank cleared the southern tip of Africa and allowed the first deep water exchange between the South Atlantic and Southern Ocean (Fig. 4.1f). Less radiogenic $\epsilon_{Nd}$(t) signatures in the South Atlantic indicate the stronger advection of cold, oxygenated Southern Ocean water. As a consequence, the enhanced organic carbon burial ended even in the deep South Atlantic.

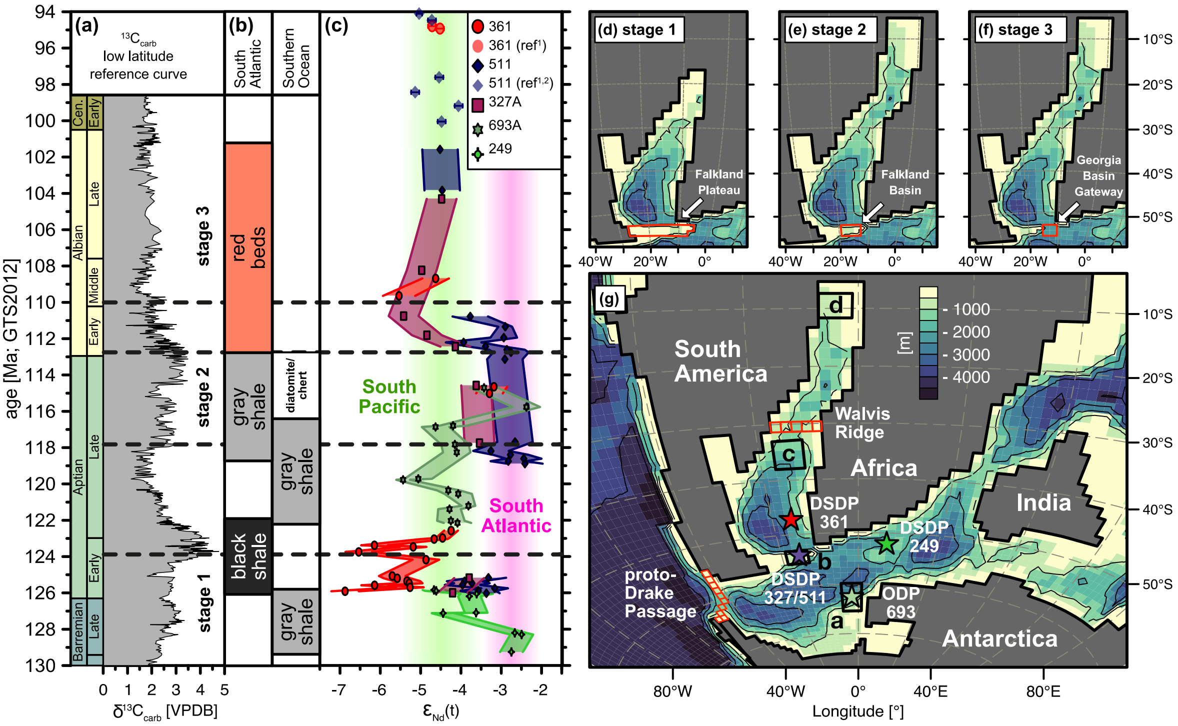

**Figure 4.1:** Reconstructed circulation history (modified from Dummann et al. (submitted)) and model set-up. Panels show the (a) low latitude carbon isotope reference curve compiled by Herrle et al. (2015), (b) dominant lithology for South Atlantic and Southern Ocean sites and (c) evolution of seawater Nd isotope signatures with ±2 SD range. Green and pink shading indicates proposed Nd isotope range of the South Pacific and South Atlantic Intermediate Water end-members. Additional literature $\epsilon_{Nd}$(t) values are taken from Murphy and Thomas (ref[1], 2013) and Robinson et al. (ref[2], 2010). Panels (d-f) show applied model bathymetries for stages 1 to 3 and (g) the approximate paleolocations of the study sites adapted to the stage 2 model bathymetry. Highlighted grid points for the proto-Drake Passage and Walvis Ridge show maximum applied gateway depth. Black rectangles in (g) represent areas used for averaging in Fig. 4.5.

Climate models would be an ideal tool to test these proxy-derived hypotheses and to quantify the associated regional circulation changes. Previous modelling studies support the idea that the large-scale ocean circulation in the young South Atlantic and Southern Ocean was primarily controlled by the applied paleogeography (Chaboureau et al., 2012; Lunt et al., 2016; Uenzelmann-Neben et al., 2017). But this also means that the validity of any simulated mean state and potentially also the predicted response to the proposed gateway changes critically depends on the quality of model boundary conditions. While this poses a problem for all paleomodelling applications in general, it becomes even more important for regional scales of deep-time periods. For the Early Cretaceous South Atlantic opening we identify 3 major uncertainties in available boundary conditions:

1. Stomata-based reconstructions of Barremian-Albian atmospheric $CO_2$ concentrations vary between 400-1500 ppmv (Wang et al., 2014; Jing and Bainian, 2018).
2. Estimates of the proto-Drake Passage (DP, Fig. 4.1g) topography for the Early Cretaceous range from an intermediate depth (Sewall et al., 2007; Eagles, 2010) to shallow marine (Cao et al., 2017) to a complete closure (Hay et al., 1999).

3. The depth of the Walvis Ridge (WR), separating the southern South Atlantic from the Angola Basin (Fig. 4.1g), is poorly constrained (Pérez-Díaz and Eagles, 2017).

All of these uncertainties have the potential to influence the simulated mean state and the response to changes in the paleogeographic position of the Falkland Plateau. To resolve this dilemma, we simulate the first three stages of the proposed gateway history under full consideration of the above-mentioned uncertainties. We follow the concept of ensemble forecasting used for numerical weather prediction, but instead of accounting for imperfect initial conditions, we try to account for uncertainties in the paleogeographic boundary conditions. We generate a large ensemble of 36 model simulations instead of dedicated sensitivity experiments to estimate the full range of results arising from the uncertainties in the boundary conditions and to identify possible nonlinear responses of the regional ocean circulation. We further use the spread between different ensemble members to assess the robustness of our results. Finally, we constrain the range of simulated circulation scenarios with the reconstructed water mass mixing to derive an integrated history of ocean circulation and carbon burial for the Early Cretaceous South Atlantic and Southern Ocean.

## 4.3 Methods

### 4.3.1 Model description

We use the Kiel Climate Model (KCM, Park et al., 2009), a fully coupled atmosphere-ocean-sea ice general circulation model, for all simulations. It consists of the spectral atmospheric general circulation model ECHAM5 (Roeckner et al., 2003), configured at a horizontal resolution of ~2.8° x 2.8° (T42) with 19 vertical levels (Park and Latif, 2019). The ocean-sea ice component NEMO (Madec, 2008) uses a tripolar grid at a horizontal resolution of 2° x 2° (ORCA2) at 31 vertical levels with an equatorial refinement of the meridional resolution to 0.5°. The global land topography and ocean bathymetry (Blöhdorn, 2013) represent an Early Aptian (~125 Ma) time slice and are based on reconstructions from Müller et al. (2008) and Blakey (2008). Freshwater routing from the land surface into the ocean follows the land orography (Hagemann and Dümenil, 1998). Simplified climate-zone dependent vegetation parameters (Blöhdorn, 2013) are applied to the ice-free land surface. Seasonal snowfall and sea ice formation is permitted. Integrations are performed at atmospheric $CO_2$ concentrations of 600 and 1200 ppmv to account for the large spread in available reconstructions for the Early Cretaceous (e.g., Wang et al., 2014; Jing and Bainian, 2018). The solar constant is reduced by ~1% (1350 $W/m^2$), while the orbital parameters and other greenhouse gases besides $CO_2$ are fixed at their pre-industrial values due to a lack of reconstructions.

### 4.3.2 South Atlantic and Southern Ocean paleobathymetry

To increase comparability to previous studies and enhance reproducibility, we replace the regional ocean bathymetry of the study area with published climate model boundary conditions for the Early Cretaceous (Sewall et al., 2007). In order to focus on the gateway related circulation changes during the initial stages of the South Atlantic opening, we keep the large-scale bathymetry of the Southern Ocean and southern South Atlantic fixed throughout all simulations. Sewall et al. (2007) provide paleobathymetries for the two suitable time slices of the Early Aptian and Early Albian. We chose the latter as our base configuration (Fig. 4.1g) due to two reasons. First, it features an initial shallow water connection between India and Antarctica. This proto-Indian Ocean is missing in the Early Aptian time slice, but present in other reconstructions (Golonka, 2007; Gibbons et al., 2013) and newer climate model boundary conditions for the earliest Cretaceous (Lunt et al., 2016). Second, it includes a shallower maximum water depth of the DP of ∼1400 m compared to the ∼2000 m in the Early Aptian time slice (Sewall et al., 2007). This is more in line with the general view of only a shallow or intermediate water connection between the Pacific Ocean and the Weddell Sea during the Cretaceous (e.g., Eagles, 2010; Donnadieu et al., 2016; Cao et al., 2017), while the onset of deep water exchange is associated with the formation of oceanic crust starting around the Oligocene (Lagabrielle et al., 2009). To account for the considerable uncertainty in estimates of the DP depth, ranging from about 1400 m (Sewall et al., 2007) to shallow marine (Cao et al., 2017) to a closed gateway (Hay et al., 1999), we perform the simulations with three different maximum depths of the passage of 1400 m, 200 m and 0 m, respectively (200 m and 0 m depths are applied to all highlighted DP grid points in Fig. 4.1g). Paleobathymetric reconstructions for the Walvis Ridge between the Cape-Argentine and Angola basins (Fig. 4.1g), are similarly uncertain (Pérez-Díaz and Eagles, 2017). We therefore conduct two sets of simulations with a maximum depth of the Walvis Ridge of either ∼1200 m (Sewall et al., 2007) or 200 m (200 m depth is applied to all highlighted WR grid points in Fig. 4.1g). As for the large-scale bathymetry, we use the same land orography for all simulations.

Due to the proposed crucial role of the Falkland Plateau in governing the water mass exchange between the South Atlantic and Southern Ocean we update its representation in the model bathymetry. Shape and position are based on a recent high-resolution regional study (see Appendix Fig. 4.A1, Pérez-Díaz and Eagles, 2017), but the limited model resolution only allows for an idealised geometry (red polygon in Fig. 4.1d). It consists of a shallow (250 m) Malvinas Basin in the west, a deeper Falkland Basin (750 m, Fig. 4.1d) and a shallow (250 m) Maurice Ewing Bank in the east. The chosen Falkland Basin depth is in between a reconstructed Aptian shelf environment (Harris et al., 1977; Basov and Krasheninnikov, 1983) and a Late Albian paleo-water depth of ∼800 m (Holbourn et al., 2001). This estimated subsidence based on assemblages of benthic foraminifers is supported by backtracking methods (Müller et al., 2018). The depth of the Georgia Basin Gateway (Fig. 4.1f) was set to 2500 m (Pérez-Díaz and Eagles, 2017)

### 4.3.3 Ensemble approach and model spin-up

We design model geographies for three consecutive time slices representing the initial stages of the South Atlantic opening (Fig. 4.1d-f). They resemble the proposed characteristics of the first three stages of the reconstructed water mass exchange between the South Atlantic and Southern Ocean (see Section 4.2) associated with a progressive westward drift of the Falkland Plateau. The bathymetry of the Southern Ocean and southern South Atlantic (i.e. the Cape-Argentine Basin) is fixed for all stages due to the large uncertainties in the available reconstructions (Pérez-Díaz and Eagles, 2017). In fact, at the upper end of reconstructions the southern South Atlantic at 120 Ma is as wide and even deeper than the minimum estimate at 110 Ma (see Appendix Fig. 4.A1). For the region north of the WR we apply the Early Aptian bathymetry from Sewall et al. (2007) for stage 1 and the Early Albian time slice for stages 2 and 3 to assess the influence of the changing Angola Basin geometry. As the applied orography around the Angola Basin is fixed to an Early Aptian time slice and does not include the Early Albian equatorial rift valley shown in Sewall et al. (2007), we add a drainage basin to the north of the Angola Basin for stages 2 and 3. These three stages are integrated with all possible combinations of sensitivity parameters discussed above, i.e. variable DP depth (0/200/1400 m), variable WR depth (200/1200 m) and two atmospheric $CO_2$ end-members (600/1200 ppmv). This leads to 12 different ensemble members for each stage and 36 simulations in total.

Throughout the analysis we will focus on the circulation changes associated with four key processes defined as:

1. A doubling of atmospheric $CO_2$, i.e. 1200 minus 600 ppmv (hereafter $\Delta CO_2$)
2. An opening of the proto-Drake Passage, i.e. original maximum depth of 1400 m minus closed gateway (hereafter $\Delta$DP)
3. An opening of a deep water connection between the South Atlantic and Southern Ocean via the Georgia Basin, i.e. stage 3 minus stage 2 (hereafter $\Delta$GBG)
4. A deeper Walvis Ridge, i.e. 1200 m minus 200 m (hereafter $\Delta$WR)

If not stated differently, these changes are averaged over all respective ensemble members, i.e. results for $\Delta CO_2$ represent the average difference between 18 simulations with 1200 ppmv and 18 simulations with 600 ppmv $CO_2$.

The simulations are initialised with the output of two existing 6000-year-long integrations utilising the boundary conditions described in Section 4.3.1 at 600 and 1200 ppmv $CO_2$, respectively. These two simulations are started from a homogeneous ocean with a temperature of 10 °C and a salinity of 35 and reach an equilibrium even in the deeper ocean (see Appendix Fig. 4.A2). From this, 6 experiments for stages 1 to 3 at the two $CO_2$ levels are branched off and integrated for a further 2000 years to allow the regional circulation to adapt to the modified geography described in Section 4.3.2. Ensemble simulations with changes in the depth of the DP (WR) are branched off at model year 2000 (2500) and integrated for a further 1000 (500) years. Ensemble members with a closed DP are integrated for an additional 500 years to account for the larger regional temperature response. Results are averaged over the respective last 100 model years at which the simulations approach an equilibrium even for the deep South Atlantic and Southern Ocean (see Appendix Fig. 4.A3). On the global scale, a small deep ocean temperature drift associated with the changes of the DP is still visible (see Appendix Fig. 4.A2). We therefore extended three simulations with different DP configurations up to model year 5000 to demonstrate the long-term stability of the solutions. The model drift in global mean ocean temperature at 2290 m water depth over these additional 2000 years (1500 years for the closed DP) is below 0.3 °C for all simulations.

### 4.3.4 Study sites and interactive data access

The model results are discussed in the light of organic carbon burial and neodymium isotope records obtained from several drill sites across the South Atlantic and Southern Ocean (Dummann et al., submitted, Fig. 4.1). Sediments from DSDP Site 361, located on the continental margin in the eastern South Atlantic, were deposited at an estimated paleo-water depth of 2000-2500 m (Melguen, 1978, and references therein). DSDP Sites 511 and 327 were drilled in the eastern part of the Falkland Basin with a reconstructed increase in the paleo-water depth from an Aptian shelf environment to $\sim$800 m in the Late Albian (see Section 4.3.2.) The two Southern Ocean sites, ODP Hole 693A and DSDP Site 249, are located in the Weddell Sea and on the Mozambique Ridge with paleo-water depth estimates of 200-500 m (Leckie, 1990) and less than 200 m (Weissert, 1981), respectively.

We present a novel way to interactively access and visualise the climate model experiments used in this study. Global fields of key climatic variables for all 36 simulations are available online at `https://kcm-earth-app.herokuapp.com`. The tool can be used to follow the conclusions derived in this manuscript or could act as a starting point to draft new ideas on Early Cretaceous climate dynamics.

## 4.4 Results

### 4.4.1 Ensemble mean circulation

The ensemble mean fields, i.e. the averages across all 36 simulations, provide the most robust estimate of the main circulation features and are used as a baseline to further test the sensitivity to

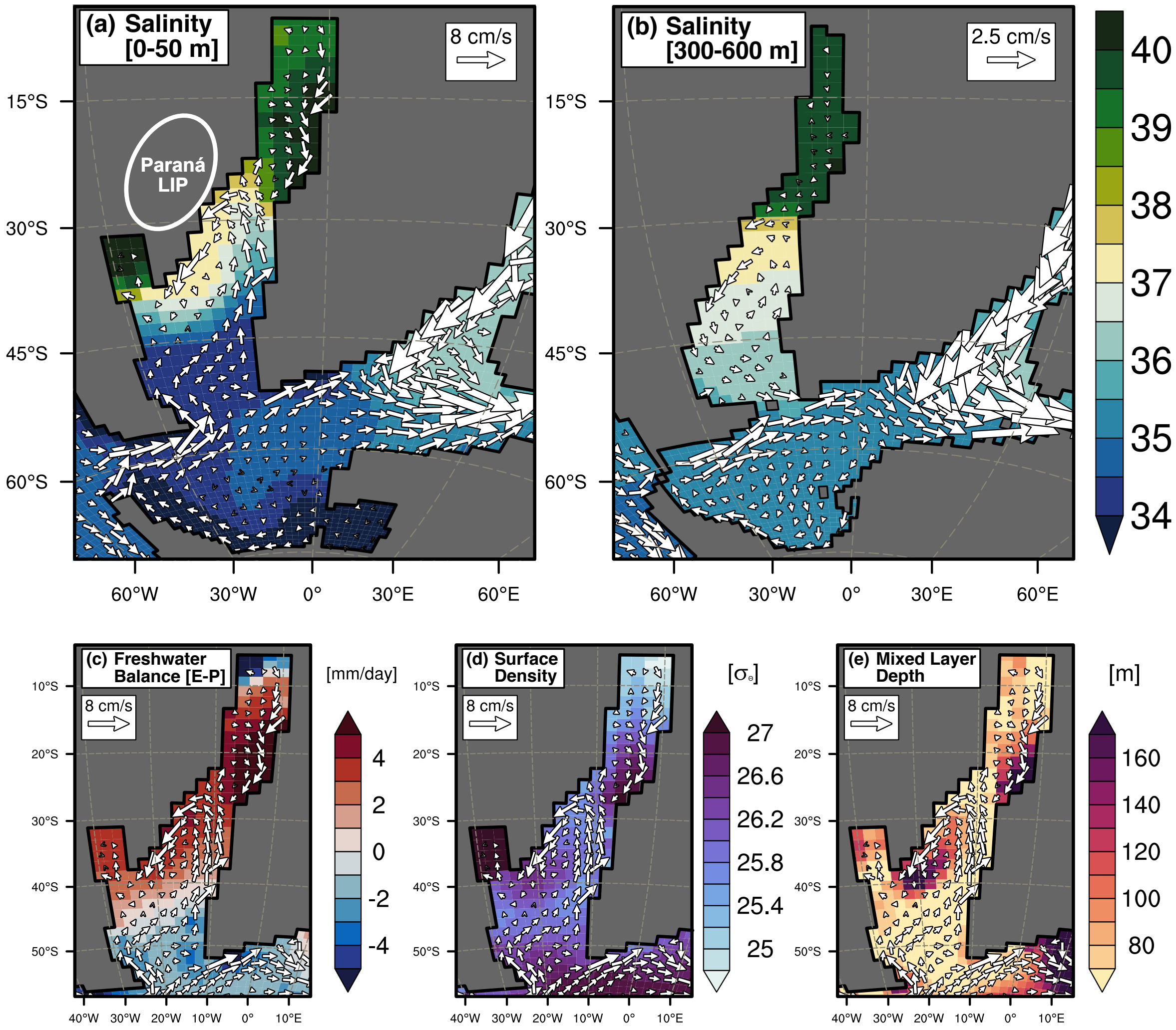

**Figure 4.2:** Simulated mean ocean circulation averaged over all 36 ensemble simulations. Only those grid points are shown that represent ocean values in at least half of the simulations. Panels show annual mean ocean velocity and salinity averaged over (a) 0-50 m and (b) 300-600 m, as well as 0-50 m velocity on top of the (c) net freshwater flux from the ocean to the atmosphere, (d) sea surface density and (e) climatological maximum monthly mean mixed layer depth. Velocity vector length is limited to two times the reference magnitude for figure clarity. The freshwater flux is calculated as evaporation minus precipitation minus river runoff. Positive values indicate a net flux from the ocean to the atmosphere. White oval in (a) represents approximate position of the Paraná large igneous province.

individual boundary conditions. The Southern Ocean circulation is dominated by the prevailing westerly winds that drive a surface water inflow from the South Pacific via the DP (Fig. 4.2a). After passing the southern tip of South America, a surface current of ~5 cm/s enters the southern South Atlantic via the Malvinas Basin and carries fresh southern-sourced surface waters along the eastern boundary northwards. Surface circulation in the narrow South Atlantic is cyclonic in the Angola Basin and anticyclonic south of the WR. Surface salinities increase in the southward return flows of these small scale gyres as a consequence of enhanced rates of evaporation at subtropical latitudes (Fig. 4.2c). The associated larger surface densities (Fig. 4.2d) enhance vertical mixing (Fig. 4.2e) and lead to the formation of South Atlantic Intermediate Water (SAIW). As the WR severely limits lateral intermediate water exchange, the deeper Angola Basin is characterised by a sluggish circulation and is filled with a locally produced highly saline water mass (Fig. 4.2b). SAIW formed in the vicinity of the Paraná large igneous province (Fig. 4.2a) exits the South Atlantic via the Falkland Plateau at flow speeds of 1-2 cm/s, mixes with Southern Ocean Intermediate Water and finally merges with the southern limb of the strong subtropical gyre circulating India.

### 4.4.2 Controls on temperature and salinity

As a result of the salinity-driven intermediate water formation the southern South Atlantic and the Angola Basin both show pronounced subsurface maxima in temperature and salinity at depths between 200-600 m (Fig. 4.3a-b). The deeper parts of the silled basins are filled with relatively warm and saline waters averaging around 10 °C at 3000 m in the Cape Basin and 20 °C at 1400 m in the Angola Basin. In comparison, mean bottom water temperatures in the Southern Ocean are lower at 5.5 °C and as low as 4 °C in the global mean. The deep Cape-Argentine and Angola basins also show the largest spread in simulated temperatures and salinities across individual ensemble members (Fig. 4.3c-d). Zonal mean values differ by as much as 15 °C and a salinity of 5.8. Simulated amplitudes are highest in regions directly affected by the presence of the GBG and WR which control horizontal water mass mixing. Bottom water temperatures drop on average by 5-7 °C in response to the opening of these gateways (Fig. 4.4e-f), while a doubling of the atmospheric $CO_2$ increases temperatures by about 5 °C (Fig. 4.4c). This makes $\Delta$GBG and $\Delta$WR the dominant control on temperature (Fig. 4.3e) and salinity (Fig. 4.3e) for large parts of the deeper South Atlantic. Resulting bottom water temperatures at DSDP Site 361 (Fig. 4.3a) show a remarkably large range from 3.1 to 17.6 °C (Fig. 4.4a-b) with a mean value of 10.4 °C. The most constant temperatures with an inter-model spread below 4 °C are simulated for the upper 200 m just south of the WR. Southern Ocean temperatures are primarily determined by $CO_2$, while enhanced freshwater advection resulting from a DP opening (see Appendix Fig. 4.A4) dominate the regional salinity variability (Fig. 4.3f).

The simulated temperature response to changing boundary conditions shows pronounced horizontal and vertical differences (Fig. 4.5). While $\Delta CO_2$ leads to a homogeneous warming of the upper Weddell Sea of 4-5 °C (Fig 4.5e), the northern Angola Basin shows an enhanced mean subsurface warming of 7.5 °C between 100-200 m (Fig. 4.5h). In contrast, subsurface warming just south of the WR (Fig. 4.5g) is reduced to below 2 °C in the mean with even a slight cooling at some grid points. Changes related to the WR depth are mainly confined to the Angola Basin and increase with depth (Fig. 4.5h). The spread in simulated salinities increases considerably from south to north with values for the northern Angola Basin ranging between 36 and 42 (see Appendix Fig. 4.A5). An open DP reduces the temperature (Fig. 4.5e) and salinity in the Weddell Sea throughout the water column. The sea surface temperature (SST) drop of 4 °C for $\Delta$DP at DSDP Site 693 is of the same order as the $\Delta CO_2$ signal. Surprisingly, all ensembles simulate a subsurface warming of 1-3 °C on the Falkland Plateau (Fig. 4.5f) and throughout the South Atlantic (Fig. 4.4d) in response to a DP opening. This leads to stage 2 bottom water temperatures at DSDP Site 511 that are

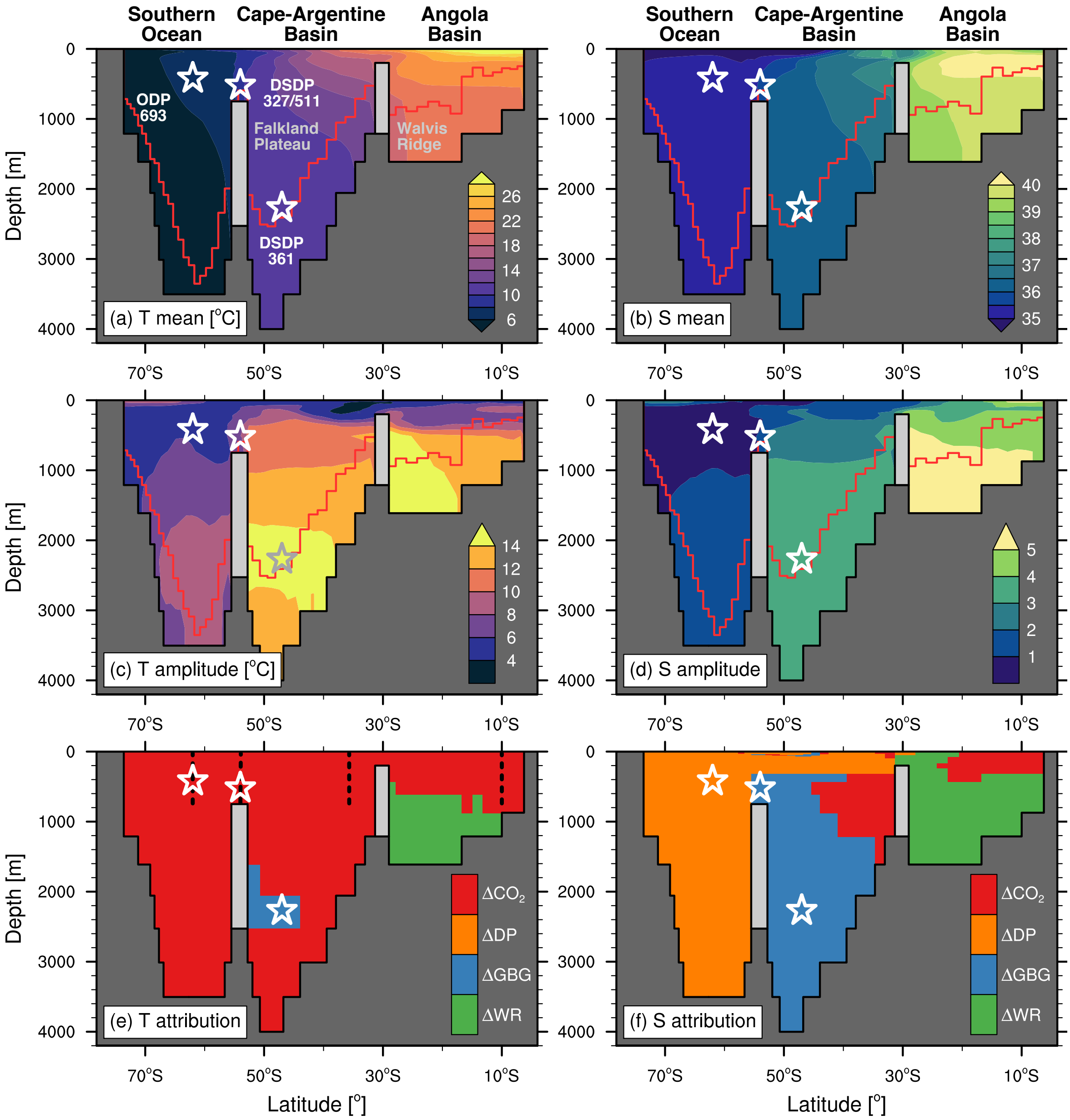

**Figure 4.3:** Zonal mean sections of temperature and salinity for the South Atlantic and Southern Ocean. Values are averaged between 30°W and 10°W at the Falkland Plateau and between 30°W and 0° elsewhere. Black (red) lines indicate maximum (average) water depth at the respective latitude. Panels show the (a-b) ensemble mean, (c-d) the difference between the minimum and maximum simulated value and (e-f) the respective process causing the largest mean change. Individual processes are defined in Section 4.3.3 and shown in Fig. 4.4 and Appendix Fig. 4.A4, respectively. Dotted lines in (e) indicate vertical sections analysed in Fig. 4.5.

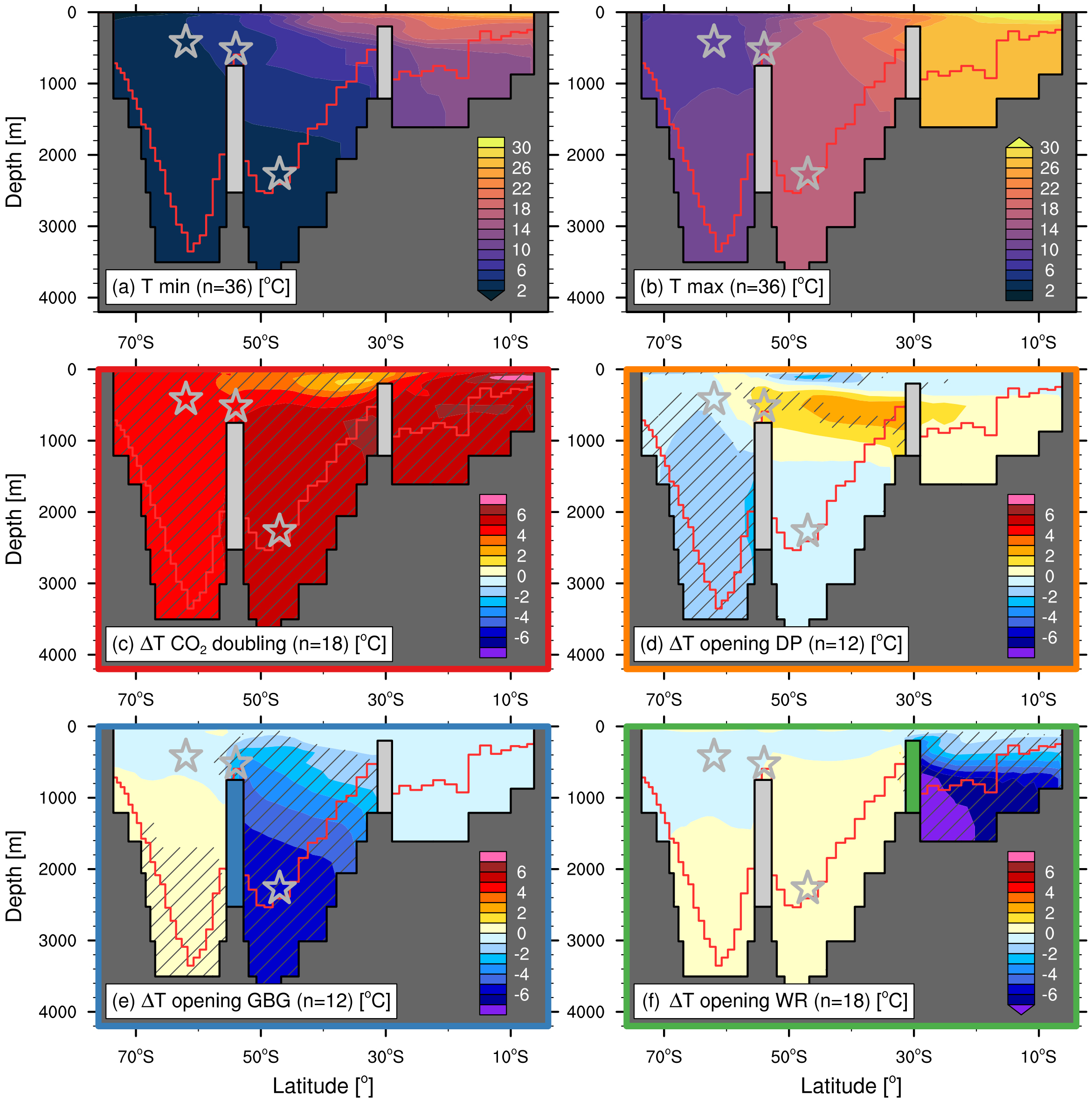

**Figure 4.4:** Zonal mean temperature sections for the South Atlantic and Southern Ocean. Values are averaged between 30°W and 10°W at the Falkland Plateau and between 30°W and 0° elsewhere. Black (red) lines indicate maximum (average) water depth at the respective latitude. Panels show the (a) minimum and (b) maximum simulated value across all 36 ensemble members and (c-e) the mean change associated with the individual processes defined in Section 4.3.3. Hatching indicates areas where all the respective 12 or 18 model responses agree on the sign of the change.

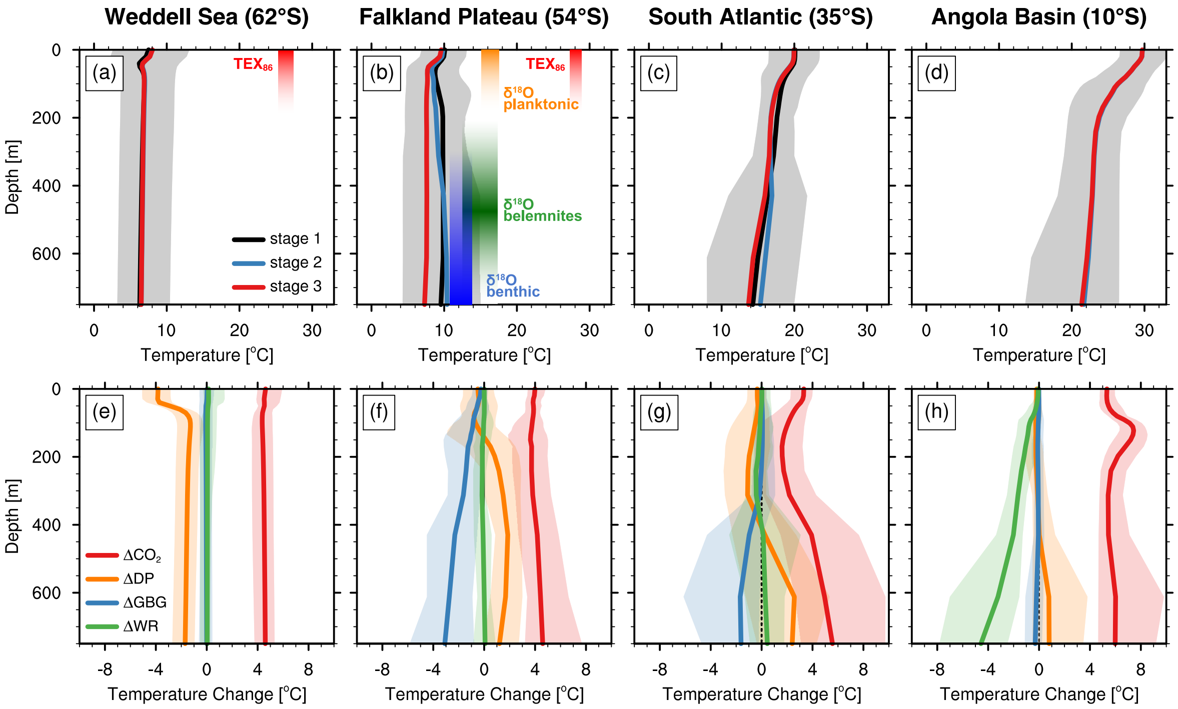

**Figure 4.5:** Simulated and reconstructed ocean temperature profiles across the Southern Ocean and South Atlantic. Solid lines represent regional averages (areas shown in Fig. 4.1g), while the shading indicates the simulated maximum and minimum grid point values of the respective area across all simulations. Upper row represents the temporal changes associated with stages 1 to 3, while the lower row shows the respective temperature changes caused by the individual processes defined in Section 4.3.3. The area used for averaging across the Falkland Plateau Basin in panels (b) and (f) moves westward for each consecutive model stage to allow comparison with the proxy record. Published ocean temperature estimates are based on TEX$_{86}$ (Jenkyns et al., 2012) and oxygen isotope data from foraminifera (Huber et al., 2018) and belemnites (Price and Gröcke, 2002). Temperature conversion follows the logarithmic TEX$_{86}^{H}$ calibration (Kim et al., 2010) and equation (1) of Bemis et al. (1998) with a seawater $\delta^{18}$O of -1‰ respectively. All available Aptian-Albian data are included and shown as ±1 standard deviation around the mean value at the approximate depth of signal formation. Foraminifera isotope data from the Aptian-Albian boundary interval at DSDP Site 511 are excluded due to a potential strong local freshwater influence (Huber et al., 2018).

even slightly higher than those at the surface (Fig. 4.5b). The upper end of simulated bottom water temperatures on the Falkland Plateau coincide with paleotemperature estimates derived from oxygen isotope data from benthic foraminifera and belemnites. Simulated SSTs range between 7-13 °C, while those derived from planktonic foraminifera are higher by about 6 °C. Temperature estimates based on the TEX$_{86}$ paleothermometer exceed the ensemble mean temperatures in the Weddell Sea and the Falkland Plateau by as much as 18 °C.

Vertical differences in the simulated responses of temperature and salinity influence the local water mass stratification (see Appendix Fig. 4.A5). A deeper DP significantly increases Weddell Sea stratification around 50 m water depth, while it is decreased on the Falkland Plateau. On average, $\Delta CO_2$ slightly increases upper ocean stratification in the Weddell Sea and the South Atlantic. In the northern Angola Basin, on the other hand, higher $CO_2$ increases especially the surface salinity and subsurface temperature, leading to a strongly reduced density stratification in the upper 100 m.

### 4.4.3 Controls on meridional overturning circulation

The large spatial differences in the simulated temperature changes, e.g. upper ocean temperatures in the South Atlantic that are insensitive to $CO_2$ changes, indicate a crucial role of regional ocean dynamics in modulating the response to boundary condition changes. We quantify these circulation changes in terms of the meridional overturning circulation (MOC). Individual changes of the respective meridional and vertical velocity components are shown in Appendix Fig. 4.A6-4.A7. The ensemble mean MOC in the Cape-Argentine Basin (Fig. 4.6a) is dominated by the previously described salinity-driven intermediate water formation. The positive values indicate northward flow at the surface, maximum sinking at around 40°S and a subsequent southward return flow of the SAIW. The overall mean volume transport of 1.2 Sv (1 Sv = $10^6$ $m^3/s$) is low due to the limited basin dimensions, and the maximum is reached within the upper 200 m. Despite the large range of applied boundary conditions, all 36 ensemble members agree on the sign of this overturning in the upper 1000 m of the southern South Atlantic (Fig. 4.7a). The vertical extent is limited to the Falkland Plateau sill depth, leading to rather stagnant conditions in the deeper Cape-Argentine Basin.

Further to the north, the WR cuts off the Angola Basin overturning from the SAIW cell. Mean MOC is weak but driven by evaporative formation of dense bottom waters just north of the WR (Fig. 4.2d) and upwelling at the northern end. The circulation in the upper 200 m of the Angola Basin is highly sensitive to $\Delta CO_2$ (Fig. 4.7f). The northern end of the Angola Basin during stages 2 and 3 reaches the tropical regions (Fig. 4.1) leading to locally enhanced rates of precipitation and river runoff (Fig. 4.2c). This net surface freshwater input increases the surface density stratification and limits vertical mixing in the northern part of the basin at 600 ppmv $CO_2$. The doubling of $CO_2$ increases evaporation rates and, surprisingly, also reduces local precipitation (see Appendix Fig. 4.A8). Resulting increased surface salinities lead to denser surface waters and enable a shallow and clockwise MOC (see Appendix Fig. 4.A9) associated with enhanced subsurface temperatures (Fig. 4.5h) and a reduced density stratification. In contrast, the weak MOC in the smaller Angola Basin during stage 1 is rather insensitive to boundary condition changes (Fig. 4.7c).

The saline and dense water filling the restricted Angola Basin eventually spills over the WR into the southern South Atlantic (4.7b). This Walvis Ridge Overflow Water (WROW) is the densest water mass in the South Atlantic and therefore reaches the deepest parts of the Cape-Argentine Basin (see Appendix Fig. 4.A10). Depth-integrated volume transport across the WR is weak and does not exceed 0.7 Sv, but it is always directed southward for the deepest and therefore densest model layer.

As the regional overturning is driven by strong evaporation, the doubling of $CO_2$ leads to an amplification and downward extension of the SAIW cell (Fig. 4.6c). A deeper WR enhances the SAIW cell, while the vertical dipole pattern throughout the South Atlantic (Fig. 4.6f) also indi-

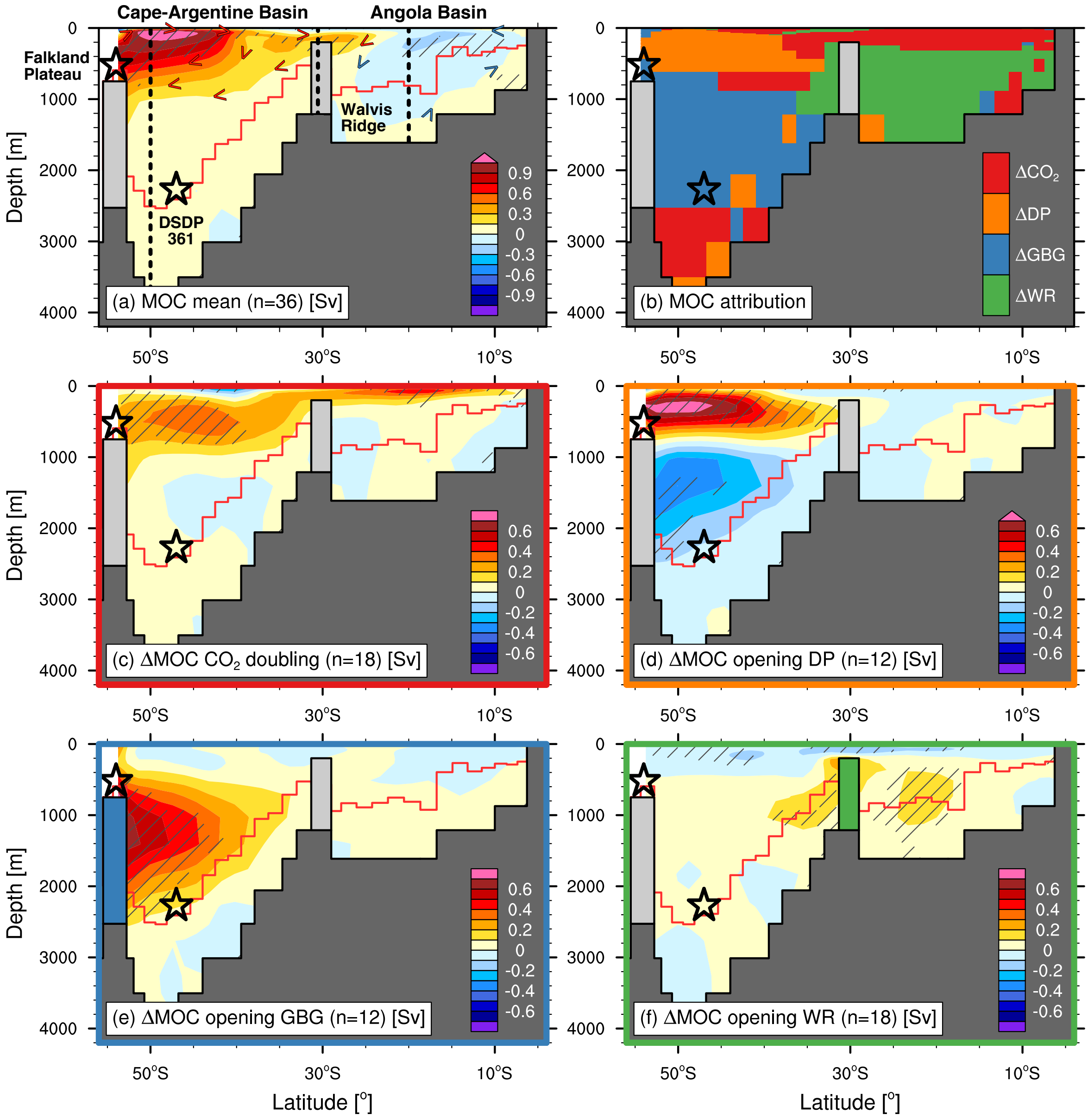

**Figure 4.6:** South Atlantic meridional overturning circulation (MOC). Panels show the (a) ensemble mean, (b) the respective boundary condition resulting in the largest mean MOC change and (c-f) individual MOC changes associated with the processes defined in Section 4.3.3. Values are in Sv with 1 Sv = $10^6$ m$^3$/s. Positive (negative) values represent clockwise (counterclockwise) circulation. Hatching indicates region where all ensemble members agree on the sign of the shown field. Black (red) lines indicate maximum (average) water depth at the respective latitude. Dotted lines in (a) indicate vertical sections analysed in Fig. 4.7.

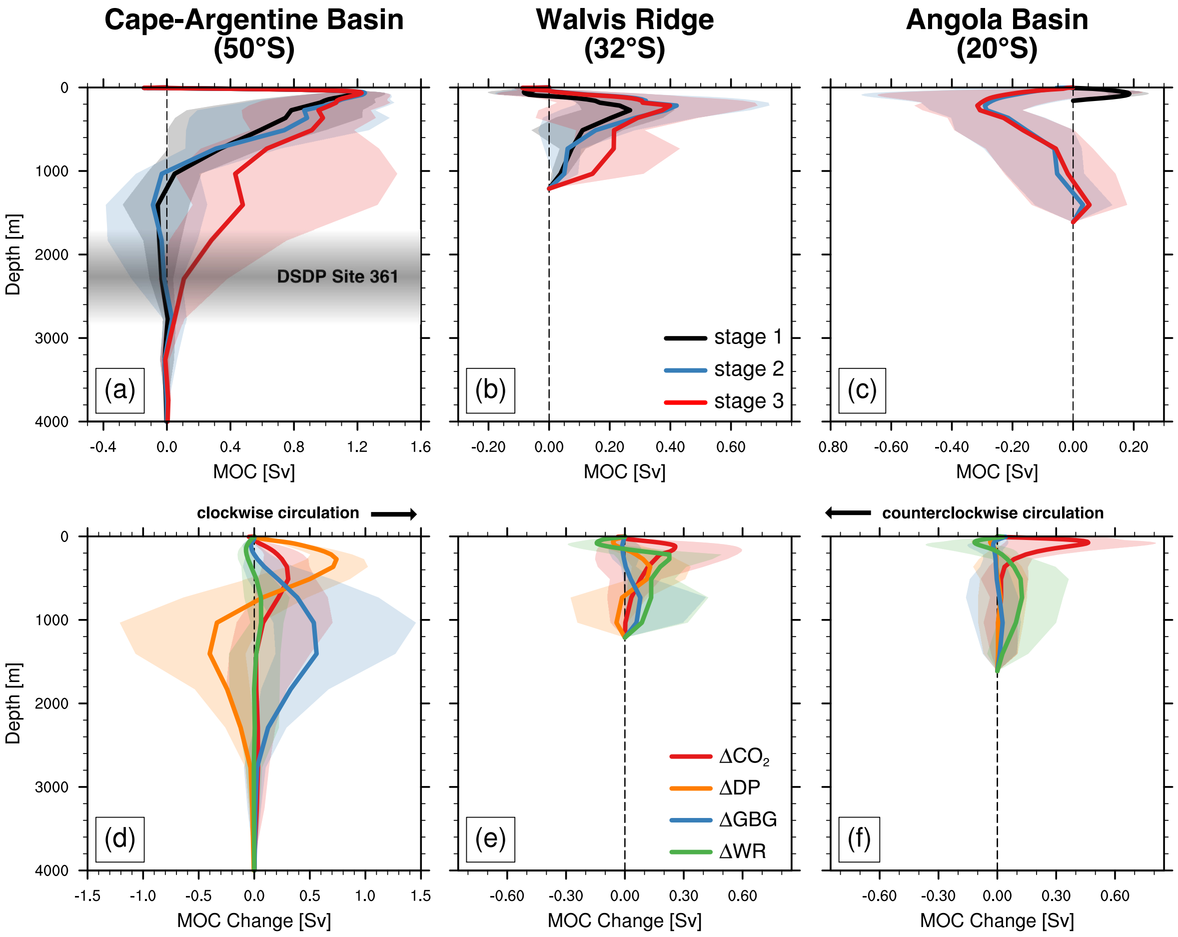

**Figure 4.7:** Profiles of the South Atlantic meridional overturning circulation (MOC). Profiles are shown for (left) 50°S, (middle) 32°S and (right) 20°S (see Fig. 4.6a). Upper row represents the temporal changes associated with stages 1 to 3, while the lower row shows the respective MOC changes caused by the individual processes defined in Section 4.3.3. Shading represents the respective ensemble spread with the ensemble mean indicated by solid lines. Values are in Sv with 1 Sv = $10^6$ $m^3/s$. Positive (negative) values represent clockwise (counterclockwise) circulation.

cates a deepening of the area of maximum overturning. The opening of the DP creates the largest change of the upper ocean MOC (Fig. 4.6b) with a mean increase of 0.7 Sv between 200-400 m (Fig. 4.6d). The strengthened upper cell is also associated with a negative recirculation below the Falkland Plateau depth. Maximum strength of this counterclockwise circulation is below 0.4 Sv for all simulations (Fig. 4.7a). The largest change of the MOC in the deeper Cape-Argentine Basin is simulated for the opening of the GBG (Fig. 4.6b) as the positive SAIW cell during stage 3 extends down to the new sill depth of 2500 m (Fig. 4.6e). The response to ΔGBG is positive for all ensemble members (Fig. 4.7c), but the ensemble spread is large as the resulting deep water mixing also depends on the prevailing Weddell Sea density stratification. The strength of the stage 3 deep cell in the South Atlantic reduces significantly for an open DP (Fig. 4.7d). Overall, total southward volume transport of 0.3 Sv (range from 0.1-0.8 Sv) for depths below 2000 m is very low. WROW export increases for stage 3 (Fig. 4.6b) as the dense water mass contributes to the enhanced deep part of the South Atlantic overturning.

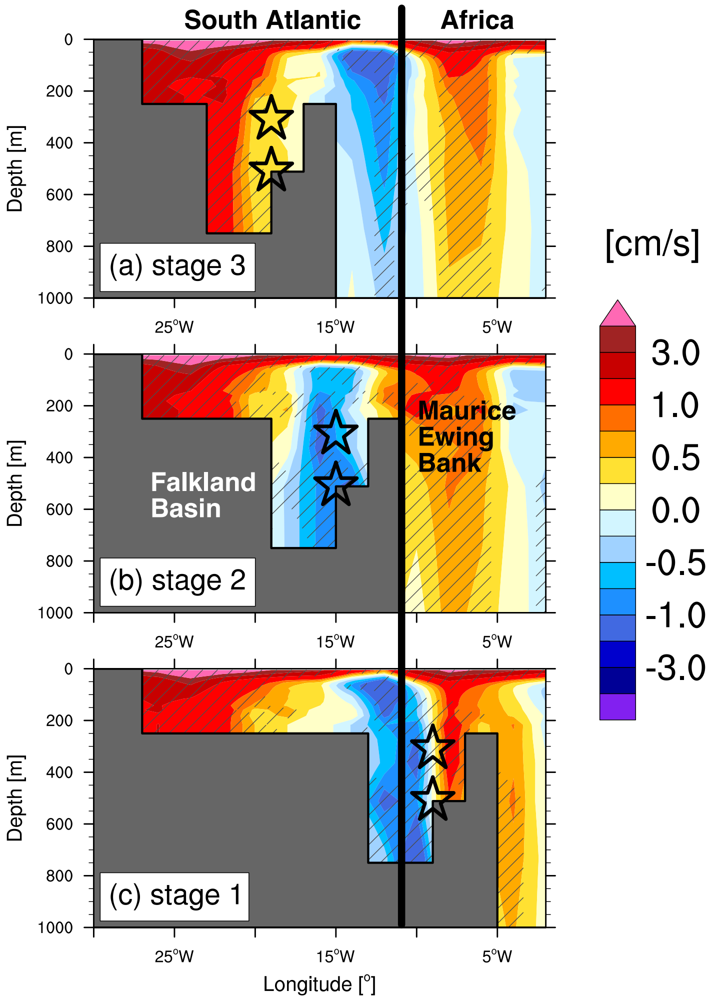

**Figure 4.8:** Temporal changes of SAIW export at the Falkland Plateau. Panels show zonal sections of ensemble mean meridional velocities for stages 1-3 averaged over the area highlighted in Fig. 4.1d. Thick black line indicates the location of the southwesternmost point of the African continent. Hatching highlights areas where all 12 respective ensemble simulations agree on the sign of velocity. Contour interval is 1.0 cm/s and is reduced to 0.25 cm/s between -1.0 and 1.0 cm/s. Positive (negative) values indicate northward (southward) flow.

### 4.4.4 SAIW influence on Southern Ocean circulation

The export of SAIW into the Southern Ocean is primarily controlled by the paleogeographic position of the Falkland Plateau. During stage 1, the eastern end of the Falkland Plateau is situated just south off the African continent, thereby limiting intermediate water exchange via the Falkland Basin (Fig. 4.8c). DSDP Sites 327 and 511, located in the eastern part of the Falkland Basin, are influenced by a mixture of southern-sourced waters in the east and SAIW in the west. All 12 ensemble members agree on the northward advection of Southern Ocean water in the eastern Falkland Basin. At stage 2, the Maurice Ewing Bank has cleared the southern tip of Africa (Fig. 4.8b) and the study sites lie in the core of the outflowing SAIW. During stage 3, the centre of the SAIW remains at the easternmost part of the South Atlantic and now enters the Southern Ocean via the GBG. The Falkland Basin is characterised by the northward advection of colder and fresher Souther Ocean waters over the whole gateway depth.

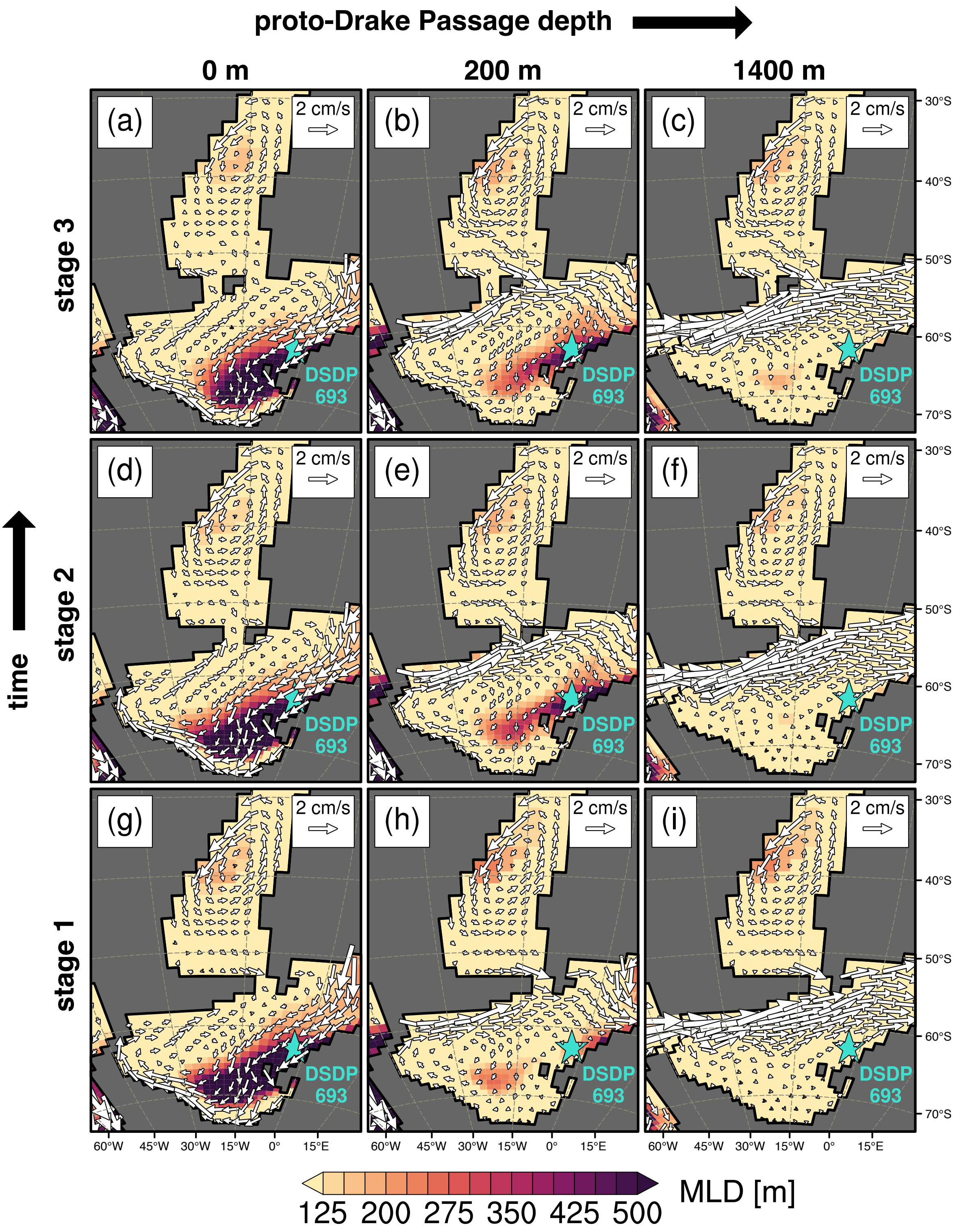

**Figure 4.9:** Southern Ocean circulation and convection. Vectors show ocean velocity in cm/s averaged from 100-600 m on contours of the climatological maximum monthly mixed layer depth in metres. Only grid points with a depth larger than 600 m are shown. Panels depict stages 1 to 3 with different DP depths of (left) 0 m, (middle) 200 m and (right) 1400 m. Each panel is averaged over 4 ensemble simulations with varying $CO_2$ and WR depth.

The temporal changes in SAIW export and associated salinity advection have the potential to influence the Weddell Sea circulation and high-latitude convection. On the other hand, the DP configuration and the resulting inflow from the Pacific Ocean will ultimately define the mean water mass characteristics and circulation patterns in the Weddell Sea. We therefore use our ensemble simulations to first evaluate the mean Southern Ocean circulation for the different DP configurations and then test the regional sensitivity to the progressive opening of the Falkland Plateau Gateway. The respective depth of the DP determines the total volume transport between South Pacific and Southern Ocean. While it is by definition zero for a closed DP, the transport increases to an average of 6.8 Sv (range from 6.0 to 8.2 Sv) for the 200 m configuration. The original maximum depth of 1400 m results in a mean transport rate of 20.7 Sv (range from 19.1 to 22.3 Sv). The associated high zonal subsurface velocities in the Southern Ocean are considerably larger than the outflowing SAIW (Fig. 4.9i) and effectively shield the Antarctic shelf regions from the influence of SAIW. The resulting weak Weddell Sea gyre in combination with the freshwater input from the Antarctic continent create fresh surface waters (Fig. 4.2a) that prevent deeper convection. The situation during stage 2 (Fig. 4.9f) and stage 3 (Fig. 4.9c) is very similar and DSDP Site 693 is influenced by a weak eastward subsurface flow throughout all stages. In the case of a closed DP, the wind-driven eastward surface current can not be balanced by an inflow from the South Pacific, but needs to be replaced by a westward subsurface current from the Mozambique Basin that flows along the Antarctic coastline (Fig. 4.9g). The advection of these more saline waters enables the onset of deep convection along the Antarctic shelf break. Again, this overall circulation is very similar for all three stages, while SAIW export is distinctly lower for the closed DP simulations (Fig. 4.9a,d,g). A shallow DP of 200 m is the only configuration that shows significant changes of the Southern Ocean circulation and ventilation in response to the South Atlantic opening. While the Weddell Sea gyre strength and convection are weak during stage 1 (Fig. 4.9h), both intensify during stage 2 (Fig. 4.9e) and stage 3 (Fig. 4.9b). Once the Falkland Basin advances to a more western position, the reduced DP transport and zonal flow speeds in the Southern Ocean allow the SAIW to reach the Weddell Sea gyre (see Appendix Fig. 4.A11). The previously salinity-limited vertical mixing increases and a clear southwesterly flow marks DSDP Site 693.

Figure 4.9 reveals an overall increase of Southern Ocean convection for a decreasing DP depth. This is caused by enhanced advection of warm and saline waters from the Tethys Ocean in turn increasing salinities in the Mozambique Basin and eastern Weddell Sea. Figure 4.10 shows that while the DP transport decreases with the gateway depth, the volume transport south of India remains nearly constant and above 40 Sv. The reduced DP throughflow is compensated by enhanced velocities between Africa and India (Fig. 4.10b,c). The depth-integrated transport for the 200 m and closed DP configurations increases by more than 40 and 60%, respectively. The enhanced heat advection associated with a closed DP leads to a surface temperature increase in the Mozambique Basin and the Weddell Sea of more than 3 °C (Fig. 4.10c) and between 2-3 °C in the Mozambique Basin for a 200 m DP (Fig. 4.10b). A clear inter-hemispheric dipole pattern in surface temperature

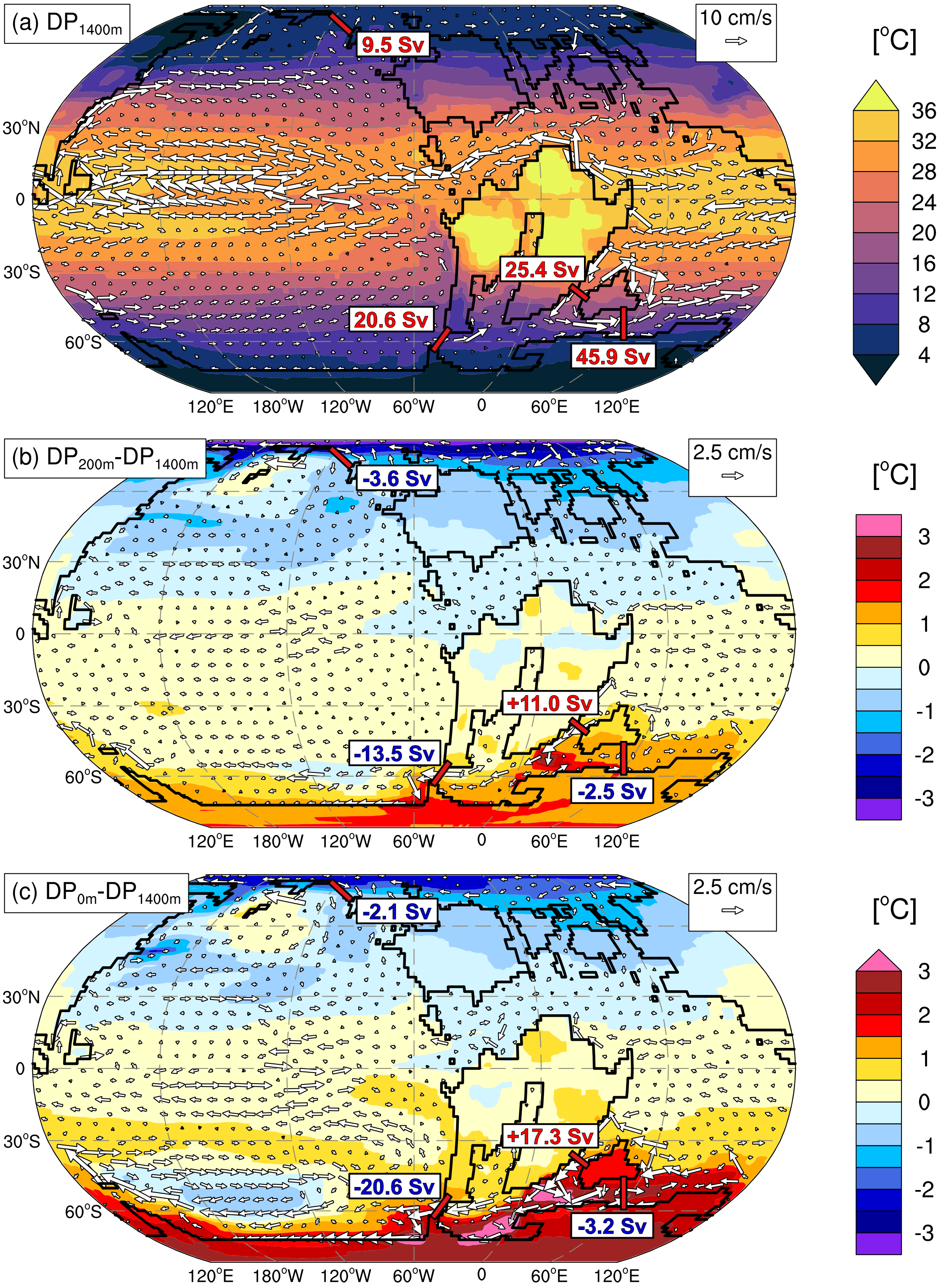

**Figure 4.10:** Surface climate sensitivity to proto-Drake Passage depth. Vectors show ocean velocity in cm/s averaged over the upper 100 m on contours of 2 m temperature in °C. Numbers indicate the depth integrated volume transport across the respective sections. Values are in Sv with 1 Sv = $10^6$ $m^3/s$. Panels show (a) annual mean values for the original DP depth of 1400 m and the respective differences to this for the (b) 200 m and (c) closed DP. Velocity vector length is limited to two times the reference magnitude for figure clarity. Results are shown for three individual ensemble members with an extended spin-up to reach a global equilibrium state (see Section 4.3.3). Values are averaged over model years 4900-4999.

changes is visible due to a reorganization of the simulated global overturning circulation. Bottom water formation in the high-latitude Arctic Ocean is only simulated for the 1400 m DP depth. Consequently, surface heat advection into the restricted basin weakens and Arctic surface temperatures are reduced by up to 3 °C (Fig. 4.10b). Surface warming over Antarctica reaches 1-2 °C for the 200 m DP and 2-3 °C for a closed DP.

## 4.5 Discussion

Our ensemble approach reveals a fundamental control of the applied boundary conditions on the simulated regional circulation, while their relative contributions vary considerably between individual basins. Furthermore, we show that the simulated response to paleogeographic changes can be sensitive to the respective mean state and therefore can itself depend on the choice of other boundary conditions. This nonlinear model behaviour is an important result since most paleoclimate modelling studies usually have to either focus on a single mean state or on the sensitivity to just one parameter due to computational limitations. In the following we will discuss the dominant controls on the simulated circulation in three different regions, from north to south, and assess potential implications for the interpretation of local proxy records. In the end, we implement the analysed physical mechanisms into the proposed gateway opening and carbon burial history presented in Dummann et al. (submitted).

### 4.5.1 Angola Basin sensitivity to atmospheric $CO_2$

Strong evaporation and resulting increased surface densities drive the overturning circulation in the restricted Angola Basin. As the local precipitation gradually increases towards the northern Intertropical Convergence Zone (ITCZ), highest surface densities and intermediate water formation are simulated just north of the Walvis Ridge between 20-25°S. This is consistent throughout all simulations and in agreement to reported Early Albian mixed layer depths in Uenzelmann-Neben et al. (2017). More restricted ensemble members indicate that the whole basin, except for a thin surface layer, was filled with this dense water mass with maximum salinities exceeding 42. This agrees with biomarker reconstructions indicating a hypersaline environment ($S > 40$) for large parts of the water column during the Aptian (Naafs and Pancost, 2014). While the applied WR depth influences absolute temperatures and salinities in the deeper parts of the Angola Basin, we find a dominant control of atmospheric $CO_2$ on the circulation and related water column stratification for the upper 200 m during stages 2 and 3. These two later stages represent a reconstructed Early Albian Angola Basin geometry with a northward extent up to 6°S (Sewall et al., 2007). Local precipitation exceeds evaporation in this part of the basin which leads to locally reduced surface salinities and densities. Enhanced river runoff from tropical Africa amplifies the net surface freshwater gain, leading to an estuarine circulation with a net southward surface flow in the 600 ppmv simulations. A somewhat surprising result is that the doubling of atmospheric $CO_2$ does not only increase evaporation over the ocean but also reduces local precipitation. This is part of a large-scale shift of atmospheric convection from the southern and northern boundaries of the ITCZ to its centre, leading to a reduced width but increased strength of the tropical rain belt. The drier conditions further increase the positive evaporation-precipitation balance over the whole Angola Basin, but particularly in the northern part. The higher surface densities drive a shallow, clockwise overturning in the upper 100-200 m. Resulting increased mixing of heat and fresh water into the subsurface in turn diminishes the vertical density gradient in the northern Angola Basin.

Due to the restricted circulation, the magnitude of these stratification changes critically depends on the strength of local river runoff and resulting surface salinities. While the ensemble mean salinity in the southern Angola Basin exceeds 40, it is reduced to 38-39 at the northern boundary. Chaboureau et al. (2012) show that this north-south gradient can increase sharply for a narrower Late Aptian basin geometry and increased orography or changed freshwater routing, with minimum surface salinities of down to 20. This implies that our simulated river runoff influence on the northernmost basin is a rather conservative estimate. The proposed mechanism and its influence on upper ocean stratification could therefore be even more important in the case of an earlier, narrower basin. Pérez-Díaz and Eagles (2017) show that, within the reported uncertainty ranges, seafloor spreading in the Angola Basin could have reached latitudes of about 10°S already at 120 Ma.

The sensitivity of the local water column stratification to atmospheric changes has the potential to influence the reported Aptian black shale deposition (Stein et al., 1986; Bralower et al., 1994; Naafs and Pancost, 2014). Importantly, the proposed mechanism leads to an increased stratification in the Angola Basin at lower $CO_2$ concentrations, inverse to the results simulated for the other basins. Behrooz et al. (2018) show that organic carbon burial in the Angola Basin exhibits a pronounced cyclicity and conclude that orbitally driven variations in the hydrological cycle caused changes in nutrient availability and upper ocean stratification that ultimately controlled local black shale deposition. In addition, we show that similar changes in environmental conditions can also be caused by variations in atmospheric $CO_2$. Wallmann et al. (2019) demonstrate that oscillations on orbital timescales and of a comparable $CO_2$ amplitude as used in our study could arise internally from a marine redox see-saw and can be simulated for the Cretaceous without any external forcing.

Our results add to the idea of a dominant influence of atmospheric dynamics on Early Cretaceous marine black shale deposition (Wagner et al., 2013). We show that the simulated turnover in upper ocean circulation and stratification can be explained by large-scale shifts of the atmospheric circulation and a northward migration of tropical precipitation driven by atmospheric $CO_2$ changes. We note that due to the prescribed land surface, our simulations potentially underestimate the full response of the hydrological cycle due to missing vegetation-atmosphere feedbacks of greenhouse climates (e.g., Upchurch et al., 1998; Levis et al., 2000; Zhou et al., 2012). Uncertainties in local orography and related changes in precipitating clouds (Houze, 2012) are additional factors with demonstrated effects on the equatorial Aptian climate (Chaboureau et al., 2012). Nevertheless, the simulated narrowing of the ITCZ is a large-scale pattern across the Aptian-Albian South American and African continent. Furthermore, projections for the twenty-first century also show a consistent narrowing and intensification of the ITCZ in response to elevated $CO_2$ (Byrne et al., 2018) that is supported by the extending observational record (Wodzicki and Rapp, 2016). We conclude that the progressive northward opening of the Early Cretaceous Angola Basin did not only change the mean freshwater balance but also enhanced the regional sensitivity to tropical climate variability.

### 4.5.2 Comparison to Falkland Plateau temperature proxies

Independent validation of the simulated temperature distribution is difficult due to sparse availability of quantitative proxy estimates for the study region and interval. To our knowledge, the only suitable Aptian-Albian oxygen isotope or $TEX_{86}$ data come from the higher latitude Weddell Sea and Falkland Plateau (O'Brien et al., 2017). For the latter, absolute $\delta^{18}O$-derived surface temperatures from Aptian-Albian planktonic foraminifera (Huber et al., 2018) average 16 °C, which is 3.0 °C higher than even maximum model SSTs. As the Falkland Plateau SSTs are mainly sensitive to $\Delta CO_2$, an unrealistic further doubling of atmospheric $CO_2$ concentrations would be needed to close the model-proxy misfit. Another possible solution would be an enhanced hydrological cycle with an associated lower $\delta^{18}O$ of local seawater that would reduce reconstructed temperatures (Huber et al., 2018). In accordance to this, our 1200 ppmv $CO_2$ simulations show that the net fresh water gain (precipitation exceeding evaporation) between 50-60°S was on average 24% larger for the Cretaceous than in a comparable present-day simulation. The enhanced freshwater is advected across the Falkland Plateau as part of the surface limb of the described South Atlantic overturning circulation and could potentially influence local carbonate chemistry.

As uncertainties in the local freshwater balance would primarily affect absolute temperature reconstructions for surface-dwelling species, we interpret the model-proxy comparison for subsurface and bottom water temperatures as a more robust test. The warmest bottom water temperatures on the Falkland Plateau are simulated for an increased $CO_2$, an open DP and a closed GBG. Despite the direct radiative warming in response to higher $CO_2$ concentrations, we show that all three factors lead to an enhanced subsurface advection of warm and saline SAIW into the Falkland Basin. This creates a subsurface temperature maximum during stage 2, where bottom water temperatures even exceed SSTs by up to 3 °C. The simulated bottom water temperatures of up to 15 °C agree with oxygen isotope-derived temperatures from Aptian-Albian benthic foraminifera (Huber et al., 2018) and Barremian-Aptian belemnites (Price and Gröcke, 2002). Our analysis shows that the export of SAIW during the early opening phase was confined to the Falkland Basin and the advection of this warm and salty water mass primarily shaped the local vertical temperature gradient. In addition, changes in the Early Cretaceous paleogeography alone can cause substantial temperature variations on the Falkland Plateau (Lunt et al., 2016). Any conclusions from local temperature records to global changes should therefore be drawn with caution.

The model-predicted and $TEX_{86}$-reconstructed (Jenkyns et al., 2012) temperature difference of about 18 °C can not be reconciled, even taking into account the reported large calibration uncertainties (O'Brien et al., 2017). On the other hand, even the modern $TEX_{86}$ core-top record is known to significantly deviate from satellite-measured temperatures on regional scales (Tierney and Tingley, 2014). One of these examples with a $TEX_{86}$-derived warm bias of up to 8 °C is the deeper Mediterranean Sea (Kim et al., 2015). Our analysis shows remarkable similarities between the Aptian-Albian South Atlantic and the present-day Mediterranean Sea, as both are deep and restricted evaporative basins characterised by a salinity driven, anti-estuarine circulation. Even the observed mean temperature around 13 °C and salinity of above 38 (Borghini et al., 2014) are within the simulated Cretaceous ensemble range. Since the $TEX_{86}$ warm bias is also found in the Mediterranean Outflow Water along the Portuguese continental margin (Kim et al., 2016), this setting could be a potential modern analogue to partly explain the high $TEX_{86}$-derived temperatures for the Early Cretaceous Falkland Plateau and Weddell Sea.

### 4.5.3 Constraints on Early Cretaceous Drake Passage depth

The DP depth plays a crucial role in the simulated mean Southern Ocean circulation and how it responds to changes in SAIW export. A comparison with the local geochemical data presented in Dummann et al. (submitted) therefore allows an evaluation of the most likely Early Cretaceous DP configuration. Dummann et al. (submitted) report a relative unradiogenic, Pacific-sourced intermediate water mass for the Weddell Sea site 693 between 122-117 Ma. The neodymium isotopes during the latest Aptian shift towards a radiogenic SAIW signature that was previously only recorded on the Falkland Plateau. The shallow 200 m DP is the only configuration that resembles this transition in response to a westward progression of the Falkland Plateau.

SAIW export for the closed DP is too weak to reach the approximate paleolocation of DSDP Site 693. Our analysis shows that the complete closure of the DP is compensated by enhanced southwestward advection of warm and saline subtropical Tethys waters into the Mozambique Basin and Weddell Sea. The reduced meridional salinity contrast to the South Atlantic results in a weaker and shallower SAIW export. Furthermore, the increased surface salinities reduce upper ocean stratification and enable a vigorous convection cell in the central and eastern Weddell Sea. In consideration of the close proximity to the Antarctic continent and the amplified hydrological cycle, we would expect the seawater neodymium samples to show a locally derived imprint. The clear offset between seawater and detrital samples throughout the record (Dummann et al., submitted) therefore makes the simulated closed DP scenario unlikely. An increase of the DP depth to 1400 m results in a total zonal transport of 20.7 Sv, more than an order of magnitude larger than the SAIW export. The Weddell Sea is therefore isolated from any changes in South Atlantic circulation and the constant advection of Pacific-sourced waters can not explain the reconstructed transition to a more radiogenic signal.

The reduced Southern Ocean velocities for a shallower 200 m DP allow a southward spread of SAIW for stages 2 and 3. The increased advection of the saline SAIW and the accelerated Weddell Sea gyre increase vertical ocean mixing and therefore ventilation. Intriguingly, the previously recorded enhanced organic carbon burial and gray shale deposition at DSDP Site 693 ceased simultaneously with the occurrence of the radiogenic water mass (Dummann et al., submitted). We therefore attribute this transition to the increased oxygenation of high-latitude subsurface waters and resulting decreased preservation of organic matter. As the simulated circulation changes are very similar under low and high radiative forcing, we can exclude a dominant role of atmospheric $CO_2$ changes in driving the reconstructed Weddell Sea turnover. The simultaneous change in multiple geochemical variables combined with a demonstrated physical mechanism provide clear evidence for a causal relation between South Atlantic gateway evolution and Southern Ocean circulation changes during the Late Aptian. Furthermore, the mean-state dependence of the simulated Weddell Sea changes provides a prime example for the benefits of the ensemble approach compared to individual sensitivity experiments.

The close integration of our ensemble modelling with the reconstructed water mass mixing also provides a unique possibility to better constrain the configuration of a key oceanic gateway. Even though the water mass exchange between the South Pacific and Southern Ocean will also depend on the width and orientation of the gateway, we hypothesise that the maximum depth will principally determine the total volume transport across the DP. In a modelling study for the Late Cretaceous, Donnadieu et al. (2016) report a very similar total DP transport of 7 Sv for a reduced gateway depth of 145 m. Importantly, their simulated transport already increases sharply to 16 Sv for a DP depth of 408 m. The volume flux for a sill depth below 1000 m is only marginally higher at 17.6 Sv and is therefore comparable to our 1400 m configuration that does not reproduce the Weddell Sea changes. Combining tectonical and paleobiological evidence (Golonka, 2007; Cao et al., 2017) with our integrated modelling, we conclude that the proto-Drake Passage during the Aptian-Albian most likely represented a shallow marine gateway not significantly deeper than 200 m.

While most previous research on the DP focused on the onset of deep water transport during the Paleogene (e.g., Lawver and Gahagan, 2003; Livermore et al., 2005), our results imply a profound influence of the DP depth on the global Early Cretaceous ocean circulation. A shallow or closed DP weakens the simulated meridional overturning cell in the Northern Hemisphere significantly. Even though our simulated high-latitude convection might be sensitive to the regional bathymetry, other studies with a modern land-sea distribution also show a distinct slowdown or even collapse of the Atlantic Meridional Overturning Circulation for DP sill depths below 1100-1400 m (Sijp and England, 2005; Yang et al., 2014). The changes in the large-scale overturning are intimately tied to the strength of the oceanic poleward heat transport and reduce surface temperatures over the whole Northern Hemisphere, with strongest cooling of 1-3°C over the Arctic Ocean. Southern Hemisphere temperature changes are dominated by the increased heat advection via the strengthened subtropical gyre circulating India. Surface temperature differences compared to the 1400 m DP configuration exceed 3 °C in the Weddell Sea and Mozambique Basin and range between 2-3 °C over Antarctica. We note that the results for the changes in the global overturning circulation should be interpreted with caution. Even though the integration length of 3000 years is comparable to previous studies (Sijp and England, 2005; Donnadieu et al., 2016; Niezgodzki et al., 2017) and the remaining global temperature drift is low, a reorganisation of the simulated deep water formation and a full model equilibration could potentially take even longer (Jansen et al., 2018). Still, our results highlight the benefits of better constraints on the DP configuration to improve model-proxy comparability, especially for high-latitude temperatures.

### 4.5.4 Integrated ocean circulation and carbon burial history

Our results allow to test and to add to the hypotheses of the opening history of the Early Cretaceous South Atlantic presented in Dummann et al. (submitted). The reconstruction of regional water mass circulation and mixing is primarily based on the isotopic differences in seawater $\epsilon_{Nd}$(t) between more radiogenic SAIW ($\epsilon_{Nd}$(t) signatures between -3.2 to -2.5) and less radiogenic Pacific-sourced waters ($\epsilon_{Nd}$(t) signatures between -5.5 to -3.5). Therefore, one of our most important results is that the SAIW formation mechanism and region is consistent throughout all 36 ensemble members and comparable to previous results (Uenzelmann-Neben et al., 2017). As even the deeper WR significantly limits the lateral water mass exchange with the Angola Basin, SAIW is formed in the area of locally highest E-P fluxes in the northwestern Cape-Argentine Basin. The proposed radiogenic isotopic signature of SAIW, potentially derived from erosional input of the Paraná large igneous province, is therefore a suitable end-member to trace regional water mass mixing throughout the Aptian to Albian. Due to the restricted and narrow basin, the overall mean volume transport of 1.2 Sv is rather low compared to the transport estimate of 17.2 Sv for the present-day Atlantic Meridional Overturning Circulation (McCarthy et al., 2015). We use the model-derived temporal changes in regional ocean circulation to complement the new stratigraphic framework and local gateway history (Fig. 4.11).

The common and rather unradiogenic $\epsilon_{Nd}$(t) values in the Weddell Sea (DSDP Site 249) and the Falkland Basin (DSDP Sites 327 and 511) during the latest Barremian to Early Aptian (∼127 to ∼124 Ma) are consistent with the simulated zonal advection of South Pacific water masses via the DP (Fig. 4.11c). The Falkland Basin during this time, shielded by the African continent in the north, formed a restricted, semi-enclosed basin favouring organic-rich black shale deposi-

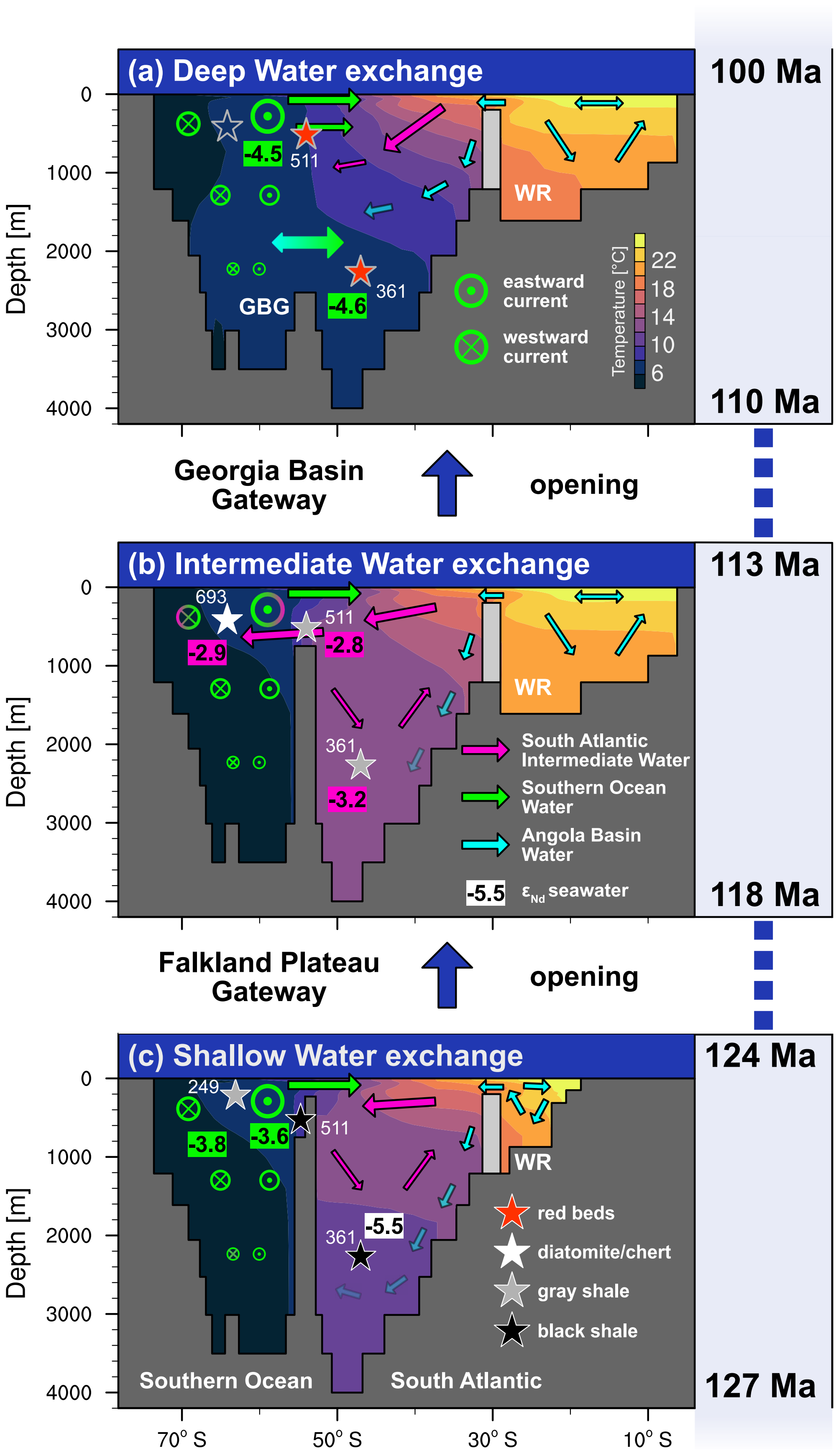

**Figure 4.11:** Schematic diagram of proposed integrated Aptian to Albian circulation evolution of the South Atlantic and Southern Ocean. Contours represent ensemble mean zonal mean (30°W-0°) ocean temperature for (a) stage 3, (b) stage 2 and (c) stage 1. Arrows depict the proposed circulation only qualitatively. Colour code represents main lithology at individual study sites, while the bold numbers show the average $\epsilon_{Nd}$(t) isotope signature for the respective time periods as reported in Dummann et al. (submitted) and shown in Fig. 4.1.

tion (Dummann et al., submitted). Due to the limited grid resolution and uncertain local paleobathymetry, the model is not able to resolve the proposed restricted local circulation on the Falkland Plateau. Nevertheless, the stronger influence of Southern Ocean Water for a more eastward position of the Falkland Plateau is clearly demonstrated. Black shales with total organic carbon (TOC) contents of up to 20% are also found at DSDP Site 361 in the deep Cape Basin. In the model, the deep South Atlantic circulation is sluggish, but influenced by saline Walvis Ridge Overflow Water (WROW) from the north. The combination of the most restricted environment with the highest evaporation and lowest precipitation forms the largest reservoir of dense water masses in the Angola Basin. As this water mass eventually overflows the WR it sinks along the topography into the deepest parts of the Cape-Argentine Basin. Average WROW volume transport of $\sim$0.1 Sv is low and vigorous entrainment of South Atlantic waters reduces density differences on its way down the slope. The model results are in agreement with early hypotheses that anoxic waters from the Angola Basin spilling over the WR increased stratification in the deep South Atlantic and promoted marine organic carbon burial (e.g., Natland, 1978; Arthur and Natland, 1979; Stein et al., 1986). Unradiogenic $\epsilon_{Nd}$(t) signatures at site 361 support a disconnect of the deep basin from the overlying SAIW cell.

TOC values at site 361 decrease during stage 2 (Fig. 4.11b), indicating an enhanced ventilation of the deep Cape Basin between $\sim$118 to $\sim$113 Ma. Our idealised simulations reveal no significant changes in the region between stages 1 and 2, but the applied paleogeographic changes are by design minimal. We therefore provide two hypotheses that could explain the reconstructed shift to a better ventilated, more radiogenic water mass in the deep Cape Basin. First, our simulations show that the depth of the SAIW cell was ultimately controlled by the sill depth of the Falkland Plateau. During the Aptian-Albian, the Falkland Plateau subsided from an initial shelf to an outer shelf to middle bathyal environment (see Section 4.3.2). We speculate that the maximum SAIW depth would have deepened in parallel, thereby increasing the oxygen content and radiogenic $\epsilon_{Nd}$(t) signature of the deeper South Atlantic. Second, due to the large uncertainty in paleobathymetric estimates of the Early Cetaceous South Atlantic (Pérez-Díaz and Eagles, 2017), we used a constant Cape-Argentine Basin geometry for all three stages. In reality, the progressive rifting would have led to a more gradual increase of the basin volume. Assuming that the advection of WROW was relatively constant from the Early to the Late Aptian, the relative influence of locally formed and better ventilated water masses would have increased compared to the anoxic WROW. Either way, we propose that these Late Aptian paleogeographic changes enabled a less restricted circulation in the deep Cape Basin. At the same time, the intermediate water sites on the Falkland Plateau and in the Weddell Sea indicate the advection of more radiogenic SAIW in consequence of the opening of the Falkland Plateau Gateway. The proposed better ventilated waters and in turn reduced TOC contents are consistent with the model-predicted changes (see Section 4.4.4).

The opening of the Georgia Basin Gateway between $\sim$113 to $\sim$110 Ma represents the most profound shift both in the geochemical data as well as in the ensemble simulations. Model results show that the outflowing SAIW is confined to the southwestern tip of Africa for all stages. As the Falkland Plateau moves further to the west during stage 3, subsurface circulation in the whole Falkland Basin switches direction and comes under the influence of cold Southern Ocean water. The $\epsilon_{Nd}$(t) values in the Falkland Basin support a gradual shift in the water mass provenance to a more unradiogenic, Pacific water signature (Fig. 4.11a). Simultaneously, the onset of red bed deposition underlines the enhanced advection of cold, oxygenated high-latitude water masses entering the South Atlantic. Data for DSDP Site 361 indicate the presence of a similarly unradiogenic and oxygenated southern-sourced water mass in the deep Cape Basin during the Albian, even though the low core recovery limits the stratigraphical constraints. In contrast, the simulations are characterised by a weak southward export of South Atlantic waters via the whole GBG depth during stage 3. We identify two processes, that probably acted in concert, as the most probable explanation for this difference. First, our simulated stage 3 marks only the initial opening of the GBG with a width of only two model grid points. An even less restricted deep water exchange at a later time would potentially increase the contribution of northward flowing Southern Ocean deep waters. In accordance to this hypothesis, Donnadieu et al. (2016) show that the deep South Atlantic during the Cenomanian/Turonian boundary at ~94 Ma was already characterised by a net northward transport of 4.2 Sv between 1,200 and 2,750m. Second, the enhanced salinity-driven formation of intermediate and deep waters in the South Atlantic was a direct consequence of the highly restricted circulation in the young basins (this study; Poulsen et al., 2001). The gradual widening and a potential first, shallow equatorial opening towards the North Atlantic between ~110 Ma (Scotese and Wright, 2018) and ~100 Ma (Pérez-Díaz and Eagles, 2017) would have reduced surface salinities and therefore local intermediate and deep water densities. The result would be a shallowing of the SAIW and WROW export depths and a gradual transition from a previously salinity-driven deep water formation at low-latitudes to a temperature-driven convection regime in the high-latitude Weddell Sea (Poulsen et al., 2001).

## 4.6 Summary and Conclusions

We present a large ensemble of climate modelling experiments to assess the fundamental controls on the Early Cretaceous ocean circulation in the evolving South Atlantic. With the close integration of a regional stratigraphic framework and available geochemical data we conclude that:

1. Excessive evaporation and restricted circulation led to the salinity-driven formation of intermediate waters in the subtropical South Atlantic. The southward export of warm and saline intermediate waters was balanced by the wind-driven advection of cold and fresh high-latitude Southern Ocean waters. The vertical extent of the resulting overturning circulation was mainly limited by the sill depth of the Falkland Plateau.

2. Increasing geographical restrictions towards the northern end of the South Atlantic pro-

duced densest water masses in the silled Angola Basin. These saline and presumably anoxic waters entered the South Atlantic via overflow across the Walvis Ridge and promoted the deposition of organic-rich black shales in the deep Cape Basin during the Early Aptian.

3. Progressive northward rifting enhanced the sensitivity of the Angola Basin circulation and stratification to changes in atmospheric $CO_2$ via large-scale shifts in tropical precipitation. Resulting variations in nutrient availability and ocean ventilation had the potential to influence or even drive the observed organic carbon burial variability.
4. Absolute Aptian-Albian ocean temperatures, especially in the deep Cape-Argentine and Angola basins, are highly uncertain and differ by as much as 15 °C for individual ensemble members. Paleogeographic and associated circulation changes represent the largest influence on temperature and salinity for most parts of the restricted South Atlantic and must therefore be taken into account in any reconstruction of the local temperature evolution.
5. The simulated response of the Weddell Sea circulation to South Atlantic gateway changes depends on the strength of the prevailing circumpolar current. Based on the model-proxy comparison we estimate that the proto-Drake Passage during the Early Cretaceous allowed water mass advection from the South Pacific, but its depth was limited to around 200 m.
6. The consecutive opening of the Falkland Plateau and Georgia Basin gateways led to a stepwise transition from the initial influence of warm, oxygen-depleted intermediate and deep waters produced at subtropical latitudes, towards a dominance of high-latitude convection forming cold and oxygenated deep waters in the Weddell Sea. This turnover in regional deep water ventilation ultimately controlled the end of enhanced organic carbon burial during the Early Albian.

The presented simulation results provide the basis for future biogeochemical modelling to quantify the influence of the regional carbon burial changes on the global carbon cycle. Our integrated ensemble approach will allow to directly test the influence of uncertainties in the paleogeography and stratigraphy on the estimated magnitude of local carbon burial and to further evaluate the potential role of the young South Atlantic and Southern Ocean in driving carbon cycle perturbations and climatic changes during the Early Cretaceous.

## References

Arthur, Michael A. and James H. Natland (1979). “Carbonaceous sediments in the North and South Atlantic: The role of salinity in stable stratification of early Cretaceous basins”. In: *Deep drilling results in the Atlantic Ocean: Continental Margins and Paleoenvironment.* Vol. 3, pp. 375–401. DOI: `10.1029/ME003p0375`.

Basov, IA and VA Krasheninnikov (1983). "Benthic Foraminifers in Mesozoic and Cenozoic Sediments of the Southwestern Atlantic As an Indicator of Paleoenvironment, Deep Sea Drilling Project Leg 71". In: *Initial Reports of the Deep Sea Drilling Project, 71*. U.S. Government Printing Office. DOI: `10.2973/dsdp.proc.71.128.1983`.

Behrooz, L., B. D.A. Naafs, A. J. Dickson, G. D. Love, S. J. Batenburg, and R. D. Pancost (2018). "Astronomically Driven Variations in Depositional Environments in the South Atlantic During the Early Cretaceous". In: *Paleoceanography and Paleoclimatology* 33.8, pp. 894–912. DOI: `10.1029/2018PA003338`.

Bemis, Bryan E, Howard J. Spero, Jelle Bijma, and David W Lea (1998). "Reevaluation of the oxygen isotopic composition of planktonic foraminifera: Experimental results and revised paleotemperature equations". In: *Paleoceanography* 13.2, pp. 150–160. DOI: `10.1029/98PA00070`.

Blakey, Ronald C (2008). "Gondwana paleogeography from assembly to breakup—A 500 m.y. odyssey". In: *Special Paper 441: Resolving the Late Paleozoic Ice Age in Time and Space*. Vol. 441. 01. Geological Society of America, pp. 1–28. DOI: `10.1130/2008.2441(01)`.

Blöhdorn, Janine (2013). "Klima und Ozeanzirkulation der Frühen Kreide im Kiel Climate Model". PhD thesis. Christian-Albrechts-Universität Kiel, p. 121.

Bodin, Stéphane, Philipp Meissner, Nico M.M. Janssen, Thomas Steuber, and Jörg Mutterlose (2015). "Large igneous provinces and organic carbon burial: Controls on global temperature and continental weathering during the Early Cretaceous". In: *Global and Planetary Change* 133, pp. 238–253. DOI: `10.1016/j.gloplacha.2015.09.001`.

Borghini, M., H. Bryden, K. Schroeder, S. Sparnocchia, and A. Vetrano (2014). "The Mediterranean is becoming saltier". In: *Ocean Science* 10.4, pp. 693–700. DOI: `10.5194/os-10-693-2014`.

Bralower, Timothy J., Seymour O. Schlanger, William V. Sliter, David J. Allard, R. Mark Leckie, and Michael A. Arthur (1994). "Timing and Paleoceanography of Oceanic Dysoxia/Anoxia in the Late Barremian to Early Aptian (Early Cretaceous)". In: *Palaios* 9.4, pp. 335–369. DOI: `10.2307/3515055`.

Byrne, Michael P., Angeline G. Pendergrass, Anita D. Rapp, and Kyle R. Wodzicki (2018). "Response of the Intertropical Convergence Zone to Climate Change: Location, Width, and Strength". In: *Current Climate Change Reports* 4.4, pp. 355–370. DOI: `10.1007/s40641-018-0110-5`.

Cao, Wenchao, Sabin Zahirovic, Nicolas Flament, Simon Williams, Jan Golonka, and R. Dietmar Müller (2017). "Improving global paleogeography since the late Paleozoic using paleobiology". In: *Biogeosciences* 14.23, pp. 5425–5439. DOI: `10.5194/bg-14-5425-2017`.

Chaboureau, A.-C., Y Donnadieu, P Sepulchre, C Robin, F Guillocheau, and S Rohais (2012). "The Aptian evaporites of the South Atlantic: a climatic paradox?" In: *Climate of the Past* 8.3, pp. 1047–1058. DOI: `10.5194/cp-8-1047-2012`.

Donnadieu, Yannick, Emmanuelle Pucéat, Mathieu Moiroud, François Guillocheau, and Jean-François Deconinck (2016). "A better-ventilated ocean triggered by Late Cretaceous changes in continental configuration". In: *Nature Communications* 7.1. DOI: `10.1038/ncomms10316`.

Dummann, Wolf, Sebastian Steinig, Peter Hofmann, Sascha Flögel, Anne H. Osborne, Martin Frank, Jens O. Herrle, and Thomas Wagner (submitted). "The impact of Early Cretaceous gateway evolution on ocean circulation and organic carbon burial in the emerging South Atlantic and Southern Ocean basins”.

Eagles, Graeme (2010). “The age and origin of the central Scotia Sea”. In: *Geophysical Journal International* 183.2, pp. 587–600. DOI: `10.1111/j.1365-246X.2010.04781.x`.

Frank, Martin (2002). “Radiogenic isotopes: Tracers of past ocean circulation and erosional input”. In: *Reviews of Geophysics* 40.1, p. 1001. DOI: `10.1029/2000RG000094`.

Gibbons, Ana D, Joanne M Whittaker, and R Dietmar Müller (2013). “The breakup of East Gondwana: Assimilating constraints from Cretaceous ocean basins around India into a best-fit tectonic model”. In: *Journal of Geophysical Research: Solid Earth* 118.3, pp. 808–822. DOI: `10.1002/jgrb.50079`.

Golonka, Jan (2007). “Phanerozoic Paleoenvironment and Paleolithofacies Maps. Mesozoic”. In: *Geologia* 33, pp. 211–264.

Hagemann, Stefan and Lydia Dümenil (1998). “A parametrization of the lateral waterflow for the global scale”. In: *Climate Dynamics* 14.1, pp. 17–31. DOI: `10.1007/s003820050205`.

Harris, Wayne K, William V Sliter, U S Geological Survey, and Menlo Park (1977). “Site 327”. In: *Initial Reports of the Deep Sea Drilling Project, 36*. U.S. Government Printing Office. DOI: `10.2973/dsdp.proc.36.103.1977`.

Hay, William W., Robert M. DeConto, Christopher N. Wold, Kevin M. Wilson, Silke Voigt, Michael Schulz, Adrienne Rossby Wold, Wolf-Christian Dullo, Alexander B. Ronov, Alexander N. Balukhovsky, and Emanuel Söding (1999). “Alternative global Cretaceous paleogeography”. In: *Special Paper 332: Evolution of the Cretaceous Ocean-Climate System*, pp. 1–47. DOI: `10.1130/0-8137-2332-9.1`.

Herrle, Jens O., Claudia J. Schröder-Adams, William Davis, Adam T. Pugh, Jennifer M. Galloway, and Jared Fath (2015). “Mid-Cretaceous High Arctic stratigraphy, climate, and Oceanic Anoxic Events”. In: *Geology* 43.5, pp. 403–406. DOI: `10.1130/G36439.1`.

Holbourn, Ann, Wolfgang Kuhnt, and Emanuel Soeding (2001). “Atlantic paleobathymetry, paleoproductivity and paleocirculation in the late Albian: The benthic foraminiferal record”. In: *Palaeogeography, Palaeoclimatology, Palaeoecology* 170.3-4, pp. 171–196. DOI: `10.1016/S0031-0182(01)00223-1`.

Houze, Robert A. (2012). “Orographic effects on precipitating clouds”. In: *Reviews of Geophysics* 50.1. DOI: `10.1029/2011RG000365`.

Huber, Brian T., Kenneth G. MacLeod, David K. Watkins, and Millard F. Coffin (2018). “The rise and fall of the Cretaceous Hot Greenhouse climate”. In: *Global and Planetary Change* 167, pp. 1–23. DOI: `10.1016/j.gloplacha.2018.04.004`.

Jansen, Malte F., Louis Philippe Nadeau, and Timothy M. Merlis (2018). “Transient versus equilibrium response of the ocean’s overturning circulation to warming”. In: *Journal of Climate* 31.13, pp. 5147–5163. DOI: `10.1175/JCLI-D-17-0797.1`.

Jenkyns, H. C., L. Schouten-Huibers, S. Schouten, and J. S. Sinninghe Damsté (2012). “Warm Middle Jurassic-Early Cretaceous high-latitude sea-surface temperatures from the Southern Ocean”. In: *Climate of the Past* 8.1, pp. 215–225. DOI: `10.5194/cp-8-215-2012`.

Jenkyns, Hugh C (2018). “Transient cooling episodes during Cretaceous Oceanic Anoxic Events with special reference to OAE 1a ( Early Aptian )”. In: *Philosophical Transactions of the Royal Society A* 376.20170073, pp. 1–26. DOI: `10.1098/rsta.2017.0073`.

Jing, Dai and Sun Bainian (2018). “Early Cretaceous atmospheric CO2 estimates based on stomatal index of Pseudofrenelopsis papillosa (Cheirolepidiaceae) from southeast China”. In: *Cretaceous Research* 85, pp. 232–242. DOI: `10.1016/j.cretres.2017.08.011`.

Kim, Jung Hyun, Jaap van der Meer, Stefan Schouten, Peer Helmke, Veronica Willmott, Francesca Sangiorgi, Nalân Koç, Ellen C. Hopmans, and Jaap S Sinninghe Damsté (2010). “New indices and calibrations derived from the distribution of crenarchaeal isoprenoid tetraether lipids: Implications for past sea surface temperature reconstructions”. In: *Geochimica et Cosmochimica Acta* 74.16, pp. 4639–4654. DOI: `10.1016/j.gca.2010.05.027`.

Kim, Jung Hyun, Stefan Schouten, Marta Rodrigo-Gámiz, Sebastiaan Rampen, Gianluca Marino, Carme Huguet, Peer Helmke, Roselyne Buscail, Ellen C. Hopmans, Jörg Pross, Francesca Sangiorgi, Jack B M Middelburg, and Jaap S. Sinninghe Damsté (2015). “Influence of deep-water derived isoprenoid tetraether lipids on the TEX86H paleothermometer in the Mediterranean Sea”. In: *Geochimica et Cosmochimica Acta* 150, pp. 125–141. DOI: `10.1016/j.gca.2014.11.017`.

Kim, Jung Hyun, Laura Villanueva, Claudia Zell, and Jaap S. Sinninghe Damsté (2016). “Biological source and provenance of deep-water derived isoprenoid tetraether lipids along the Portuguese continental margin”. In: *Geochimica et Cosmochimica Acta* 172, pp. 177–204. DOI: `10.1016/j.gca.2015.09.010`.

Lagabrielle, Yves, Yves Goddéris, Yannick Donnadieu, Jacques Malavieille, and Manuel Suarez (2009). “The tectonic history of Drake Passage and its possible impacts on global climate”. In: *Earth and Planetary Science Letters* 279.3-4, pp. 197–211. DOI: `10.1016/j.epsl.2008.12.037`.

Lawver, Lawrence A. and Lisa M. Gahagan (2003). “Evolution of Cenozoic seaways in the circum-Antarctic region”. In: *Palaeogeography, Palaeoclimatology, Palaeoecology* 198.1-2, pp. 11–37. DOI: `10.1016/S0031-0182(03)00392-4`.

Leckie, R.M. (1990). “Middle Cretaceous Planktonic Foraminifers of the Antarctic Margin: Hole 693A|ODP Leg 113”. In: *Proceedings of the Ocean Drilling Program, 113 Scientific Reports*. Vol. 113. Ocean Drilling Program, pp. 1–6. DOI: `10.2973/odp.proc.sr.113.122.1990`.

Levis, Samuel, Jonathan A. Foley, and David Pollard (2000). “Large-Scale Vegetation Feedbacks on a Doubled CO2 Climate”. In: *Journal of Climate* 13.7, pp. 1313–1325. DOI: `10.1175/1520-0442(2000)013<1313:LSVFOA>2.0.CO;2`.

Livermore, Roy, Adrian Nankivell, Graeme Eagles, and Peter Morris (2005). “Paleogene opening of Drake Passage”. In: *Earth and Planetary Science Letters* 236.1-2, pp. 459–470. DOI: `10.1016/j.epsl.2005.03.027`.

Lunt, Daniel J., Alex Farnsworth, Claire Loptson, Gavin L. Foster, Paul Markwick, Charlotte L. O&apos;Brien, Richard D. Pancost, Stuart A. Robinson, and Neil Wrobel (2016). “Palaeogeographic controls on climate and proxy interpretation”. In: *Climate of the Past* 12.5, pp. 1181–1198. DOI: `10.5194/cp-12-1181-2016`.

Madec, Gurvan (2008). “NEMO Ocean engine”. In: *Note du Pôle de modélisation 27*. Institut Pierre-Simon Laplace (IPSL), France.

McAnena, A., S. Flögel, P. Hofmann, J. O. Herrle, A. Griesand, J. Pross, H. M. Talbot, J. Rethemeyer, K. Wallmann, and T. Wagner (2013). "Atlantic cooling associated with a marine biotic crisis during the mid-Cretaceous period". In: *Nature Geoscience* 6.7, pp. 558–561. DOI: `10.1038/ngeo1850`.

McCarthy, G.D., D.A. Smeed, W.E. Johns, E. Frajka-Williams, B.I. Moat, D. Rayner, M.O. Baringer, C.S. Meinen, J. Collins, and H.L. Bryden (2015). "Measuring the Atlantic Meridional Overturning Circulation at 26°N". In: *Progress in Oceanography* 130, pp. 91–111. DOI: `10.1016/j.pocean.2014.10.006`.

Melguen, M. (1978). "Facies Evolution, Carbonate Dissolution Cycles in Sediments from the Eastern South Atlantic (DSDP Leg 40) Since the Early Cretaceous". In: *Initial Reports of the Deep Sea Drilling Project, 40*. U.S. Government Printing Office. DOI: `10.2973/dsdp.proc.40.129.1978`.

Müller, R. D., J. Cannon, S. Williams, and A. Dutkiewicz (2018). "PyBacktrack 1.0: A Tool for Reconstructing Paleobathymetry on Oceanic and Continental Crust". In: *Geochemistry, Geophysics, Geosystems* 19.6, pp. 1898–1909. DOI: `10.1029/2017GC007313`.

Müller, R. Dietmar, Maria Sdrolias, Carmen Gaina, Bernhard Steinberger, and Christian Heine (2008). "Long-term sea-level fluctuations driven by ocean basin dynamics". In: *Science* 319.5868, pp. 1357–1362. DOI: `10.1126/science.1151540`.

Murphy, Daniel P. and Deborah J. Thomas (2013). "The evolution of Late Cretaceous deep-ocean circulation in the Atlantic basins: Neodymium isotope evidence from South Atlantic drill sites for tectonic controls". In: *Geochemistry, Geophysics, Geosystems* 14.12, pp. 5323–5340. DOI: `10.1002/2013GC004889`.

Naafs, B. D A and R. D. Pancost (2014). "Environmental conditions in the South Atlantic (Angola Basin) during the Early Cretaceous". In: *Organic Geochemistry* 76, pp. 184–193. DOI: `10.1016/j.orggeochem.2014.08.005`.

Natland, J.H. (1978). "Composition, Provenance, and Diagenesis of Cretaceous Clastic Sediments Drilled on the Atlantic Continental Rise off Southern Africa, DSDP Site 361&#151;Implications for the Early Circulation of the South Atlantic". In: *Initial Reports of the Deep Sea Drilling Project, 40*. U.S. Government Printing Office. DOI: `10.2973/dsdp.proc.40.130.1978`.

Niezgodzki, Igor, Gregor Knorr, Gerrit Lohmann, Jarosław Tyszka, and Paul J. Markwick (2017). "Late Cretaceous climate simulations with different CO2levels and subarctic gateway configurations: A model-data comparison". In: *Paleoceanography* 32.9, pp. 980–998. DOI: `10.1002/2016PA003055`.

O'Brien, Charlotte L., Stuart A. Robinson, Richard D. Pancost, Jaap S. Sinninghe Damsté, Stefan Schouten, Daniel J. Lunt, Heiko Alsenz, André Bornemann, Cinzia Bottini, Simon C. Brassell, Alexander Farnsworth, Astrid Forster, Brian T. Huber, Gordon N. Inglis, Hugh C. Jenkyns, Christian Linnert, Kate Littler, Paul Markwick, Alison McAnena, Jörg Mutterlose, B. David A. Naafs, Wilhelm Püttmann, Appy Sluijs, Niels A.G.M. van Helmond, Johan Vellekoop, Thomas Wagner, and Neil E. Wrobel (2017). "Cretaceous sea-surface temperature evolution: Constraints from TEX86 and planktonic foraminiferal oxygen isotopes". In: *Earth-Science Reviews* 172, pp. 224–247. DOI: `10.1016/j.earscirev.2017.07.012`.

Park, W., N. Keenlyside, M. Latif, A. Ströh, R. Redler, E. Roeckner, and G. Madec (2009). "Tropical Pacific Climate and Its Response to Global Warming in the Kiel Climate Model". In: *Journal of Climate* 22.1, pp. 71–92. DOI: `10.1175/2008JCLI2261.1`.

Park, W. and M. Latif (2019). "Ensemble global warming simulations with idealized Antarctic meltwater input". In: *Climate Dynamics* 52.5-6, pp. 3223–3239. DOI: `10.1007/s00382-018-4319-8`.

Pérez-Díaz, Lucía and Graeme Eagles (2017). "South Atlantic paleobathymetry since early Cretaceous". In: *Scientific Reports* 7.1. DOI: `10.1038/s41598-017-11959-7`.

Poulsen, Christopher J., Eric J. Barron, Michael A. Arthur, and William H. Peterson (2001). "Response of the Mid-Cretaceous global oceanic circulation to tectonic and CO2 forcings". In: *Paleoceanography* 16.6, pp. 576–592. DOI: `10.1029/2000PA000579`.

Price, Gregory D. and Darren R. Gröcke (2002). "Strontium-isotope stratigraphy and oxygen- and carbon-isotope variation during the Middle Jurassic-Early Cretaceous of the Falkland Plateau, South Atlantic". In: *Palaeogeography, Palaeoclimatology, Palaeoecology* 183.3-4, pp. 209–222. DOI: `10.1016/S0031-0182(01)00486-2`.

Robinson, Stuart A., Daniel P. Murphy, Derek Vance, and Deborah J. Thomas (2010). "Formation of "Southern Component Water" in the Late Cretaceous: Evidence from Nd-isotopes". In: *Geology* 38.10, pp. 871–874. DOI: `10.1130/G31165.1`.

Roeckner, E, G Bäuml, Luca Bonaventura, R Brokopf, M Esch, Marco Giorgetta, Stefan Hagemann, Ingo Kirchner, Luis Kornblueh, Elisa Manzini, A Rhodin, U Schlese, Uwe Schulzweida, and Adrian Tompkins (2003). "The atmospheric general circulation model ECHAM 5. PART I: Model description". In: *Max Planck Institute for Meteorology Report* 349.

Scotese, C.R. and N. Wright (2018). "PALEOMAP Paleodigital Elevation Models (PaleoDEMS) for the Phanerozoic PALEOMAP Project, https://www.earthbyte.org/paleodem-resource-scotese-and-wright-2018".

Sewall, J O, R S W van de Wal, K van der Zwan, C van Oosterhout, H A Dijkstra, and C R Scotese (2007). "Climate model boundary conditions for four Cretaceous time slices". In: *Climate of the Past* 3.4, pp. 647–657. DOI: `10.5194/cpd-3-791-2007`.

Sijp, Willem P. and Matthew H. England (2005). "Role of the drake passage in controlling the stability of the ocean's thermohaline circulation". In: *Journal of Climate* 18.12, pp. 1957–1966. DOI: `10.1175/JCLI3376.1`.

Stein, Rüdiger, Jürgen Rullkötter, and Dietrich H. Welte (1986). "Accumulation of organic-carbon-rich sediments in the Late Jurassic and Cretaceous Atlantic Ocean — A synthesis". In: *Chemical Geology* 56.1-2, pp. 1–32. DOI: `10.1016/0009-2541(86)90107-5`.

Tierney, Jessica E. and Martin P. Tingley (2014). "A Bayesian, spatially-varying calibration model for the TEX86 proxy". In: *Geochimica et Cosmochimica Acta* 127, pp. 83–106. DOI: `10.1016/j.gca.2013.11.026`.

Torsvik, Trond H., Sonia Rousse, Cinthia Labails, and Mark A. Smethurst (2009). "A new scheme for the opening of the South Atlantic Ocean and the dissection of an Aptian salt basin". In: *Geophysical Journal International* 177.3, pp. 1315–1333. DOI: `10.1111/j.1365-246X.2009.04137.x`.

Trabucho-Alexandre, J., W. W. Hay, and P. L. De Boer (2012). "Phanerozoic environments of black shale deposition and the Wilson Cycle". In: *Solid Earth* 3.1, pp. 29–42. DOI: `10.5194/se-3-29-2012`.

Uenzelmann-Neben, Gabriele, Tobias Weber, Jens Grützner, and Maik Thomas (2017). "Transition from the Cretaceous ocean to Cenozoic circulation in the western South Atlantic — A twofold reconstruction". In: *Tectonophysics* 716, pp. 225–240. DOI: `10.1016/j.tecto.2016.05.036`.

Upchurch, Garland R., Bette L. Otto-Bliesner, and Christopher Scotese (1998). "Vegetation–atmosphere interactions and their role in global warming during the latest Cretaceous". In: *Philosophical Transactions of the Royal Society of London. Series B: Biological Sciences* 353.1365. Ed. by D. J. Beerling, W. G. Chaloner, and F. I. Woodward, pp. 97–112. DOI: `10.1098/rstb.1998.0194`.

Wagner, T., P. Hofmann, and S. Flögel (2013). "Marine black shale deposition and Hadley Cell dynamics: A conceptual framework for the Cretaceous Atlantic Ocean". In: *Marine and Petroleum Geology* 43, pp. 222–238. DOI: `10.1016/j.marpetgeo.2013.02.005`.

Wallmann, Klaus, Sascha Flögel, Florian Scholz, Andrew W. Dale, Tronje P. Kemena, Sebastian Steinig, and Wolfgang Kuhnt (2019). "Periodic changes in the Cretaceous ocean and climate caused by marine redox see-saw". In: *Nature Geoscience* 12.6, pp. 456–461. DOI: `10.1038/s41561-019-0359-x`.

Wang, Yongdong, Chengmin Huang, Bainian Sun, Cheng Quan, Jingyu Wu, and Zhicheng Lin (2014). "Paleo-CO2 variation trends and the Cretaceous greenhouse climate". In: *Earth-Science Reviews* 129, pp. 136–147. DOI: `10.1016/j.earscirev.2013.11.001`.

Weissert, Helmut (1981). "The environment of deposition of black shales in the Early Cretaceous: an ongoing controversy". In: *The Deep Sea Drilling Project: A Decade of Progress*. January 1981. SEPM (Society for Sedimentary Geology), pp. 547–560. DOI: `10.2110/pec.81.32.0547`.

— (1989). "C-Isotope stratigraphy, a monitor of paleoenvironmental change: A case study from the early cretaceous". In: *Surveys in Geophysics* 10.1, pp. 1–61. DOI: `10.1007/BF01901664`.

Wodzicki, K. R. and A. D. Rapp (2016). "Long-term characterization of the Pacific ITCZ using TRMM, GPCP, and ERA-Interim". In: *Journal of Geophysical Research* 121.7, pp. 3153–3170. DOI: `10.1002/2015JD024458`.

Yang, Simon, Eric Galbraith, and Jaime Palter (2014). "Coupled climate impacts of the Drake Passage and the Panama Seaway". In: *Climate Dynamics* 43.1-2, pp. 37–52. DOI: `10.1007/s00382-013-1809-6`.

Zhou, J., C. J. Poulsen, N. Rosenbloom, C. Shields, and B. Briegleb (2012). "Vegetation-climate interactions in the warm mid-Cretaceous". In: *Climate of the Past* 8.2, pp. 565–576. DOI: `10.5194/cp-8-565-2012`.

# Appendix: Supplementary Figures

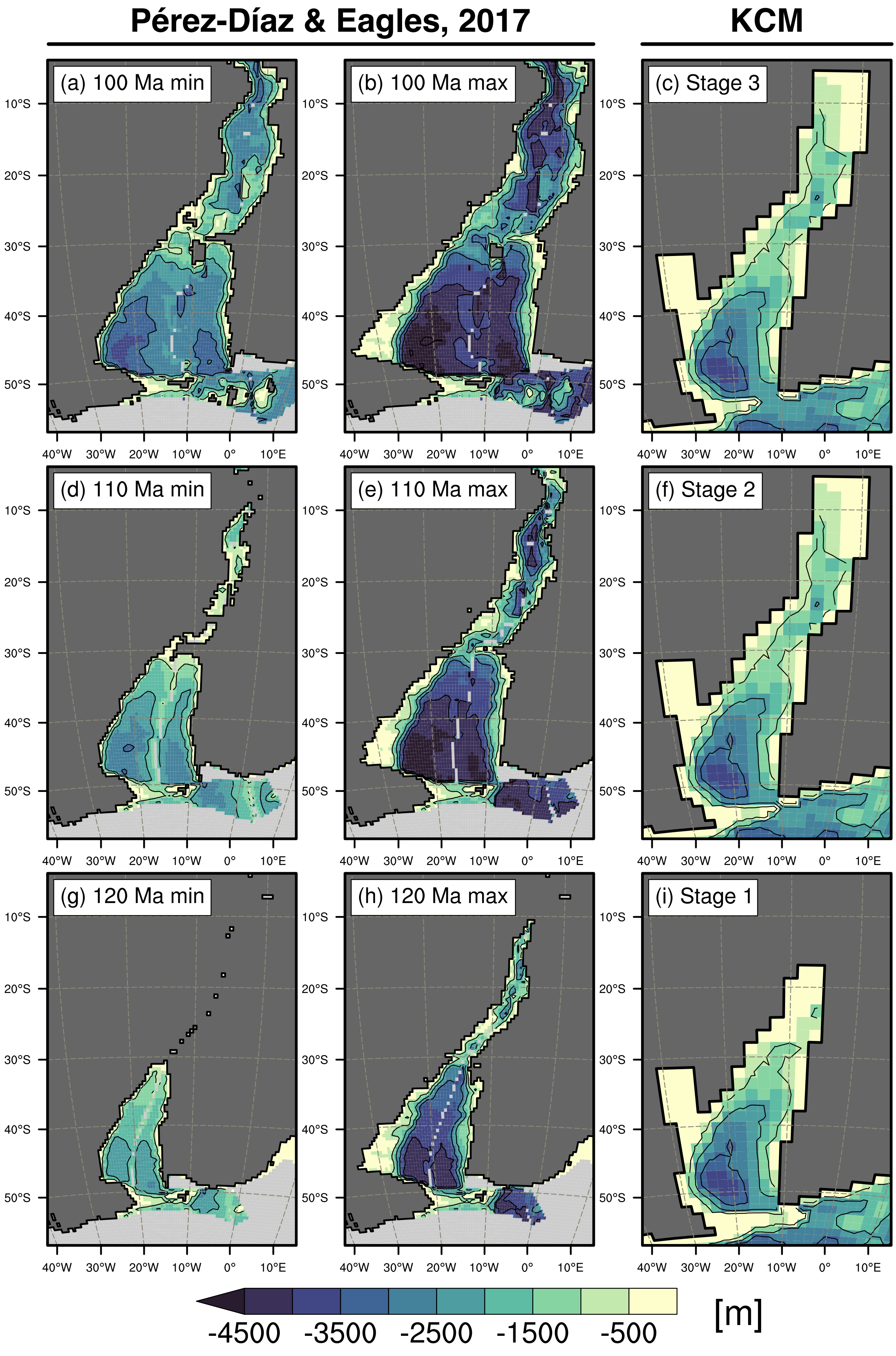

**Figure 4.A1:** Comparison of model bathymetry and available reconstructions for the South Atlantic. Only reported minimum and maximum water depth is shown for each stage and data has been regridded to a 0.5° x 0.5° horizontal grid. Contour line interval is 1000 m.

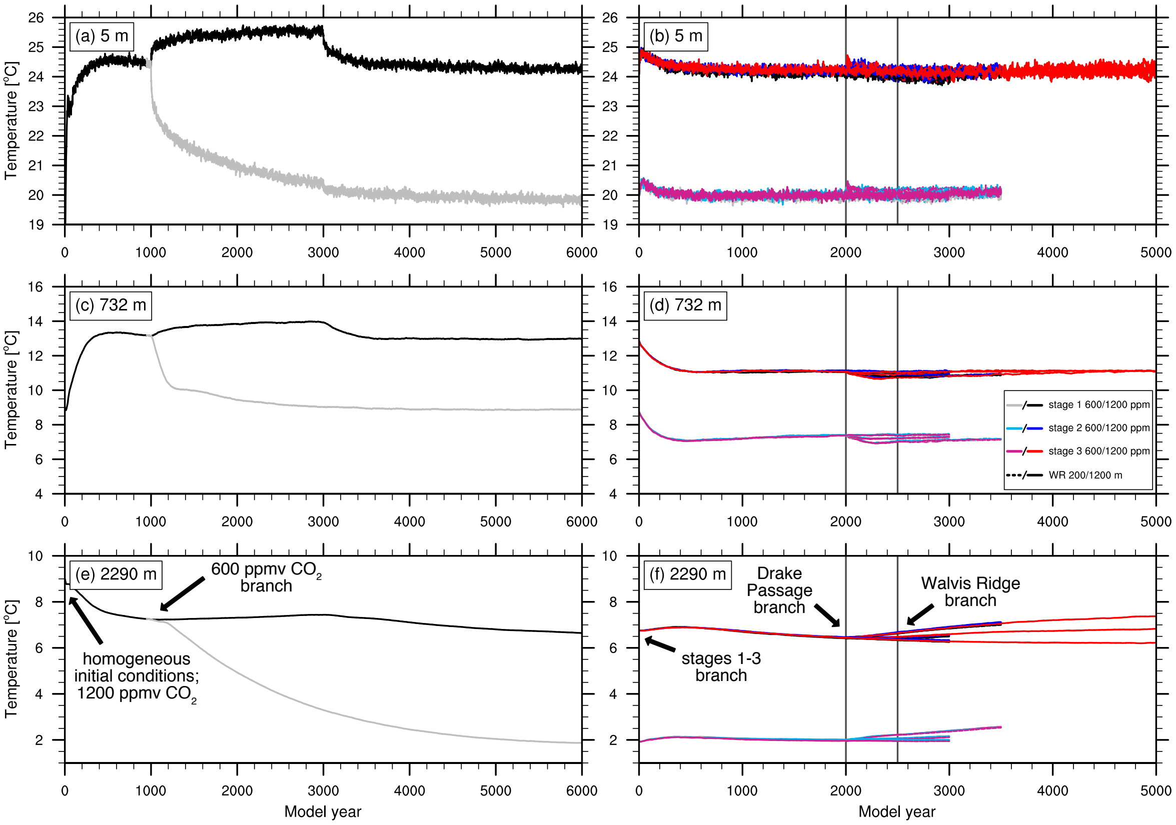

**Figure 4.A2:** Time series of globally averaged annual mean ocean temperatures in °C at 5 m, 732 m and 2290 m. Left column shows spin-up with a slightly different model bathymetry used as initial conditions (see Section 4.3.1) for the simulations discussed in the main text (right column). The sudden shifts in temperature at years 1000 and 3000 of the initial spin-up are related to a temporary increase of the atmospheric time step.

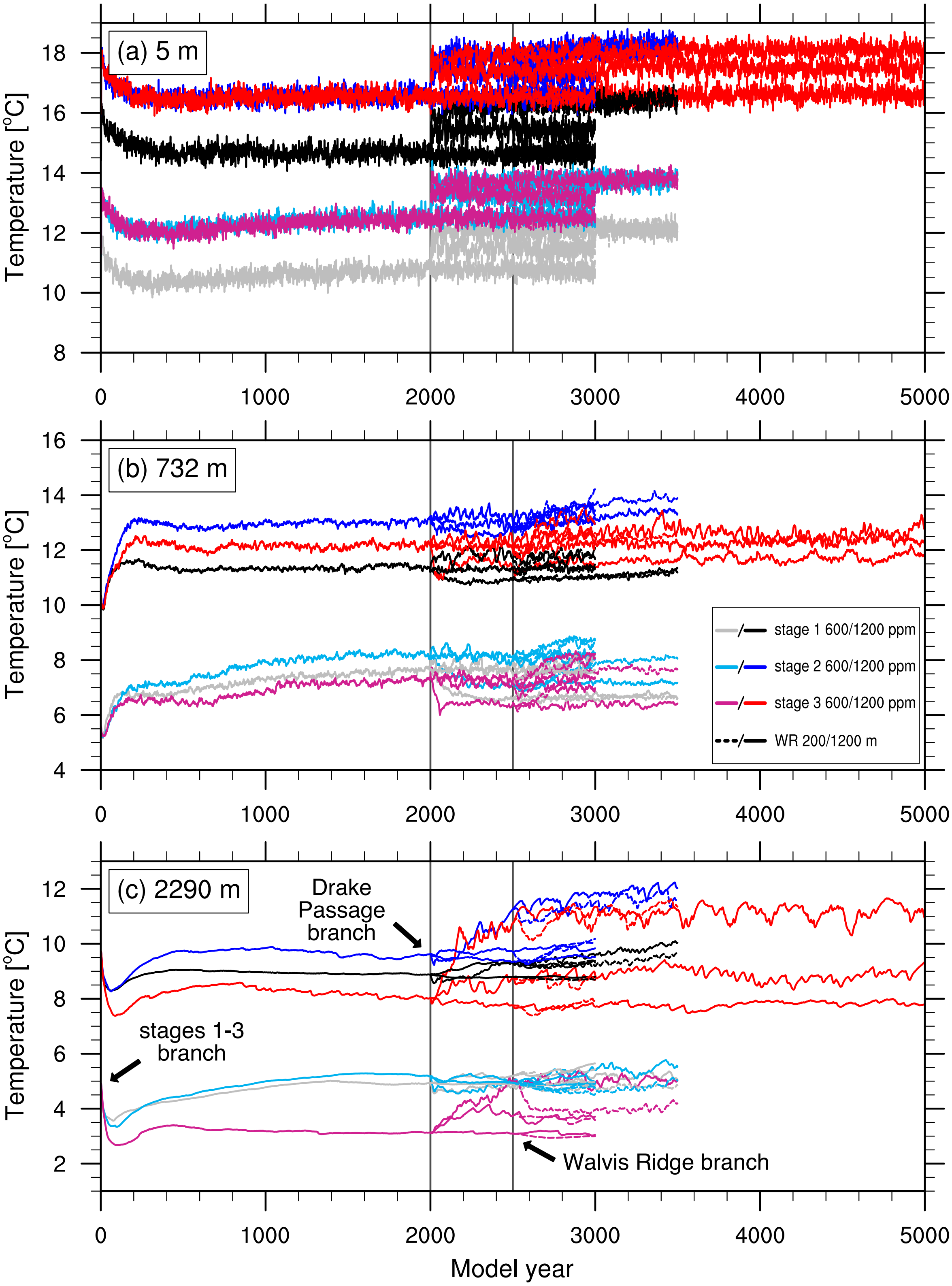

**Figure 4.A3:** Time series of annual mean ocean temperatures in °C averaged over the South Atlantic and Southern Ocean (0°-90°S, 40°W-20°E) at 5 m, 732 m and 2290 m. Color coding represents the different stages defined in the main text and the two levels of atmospheric $CO_2$.

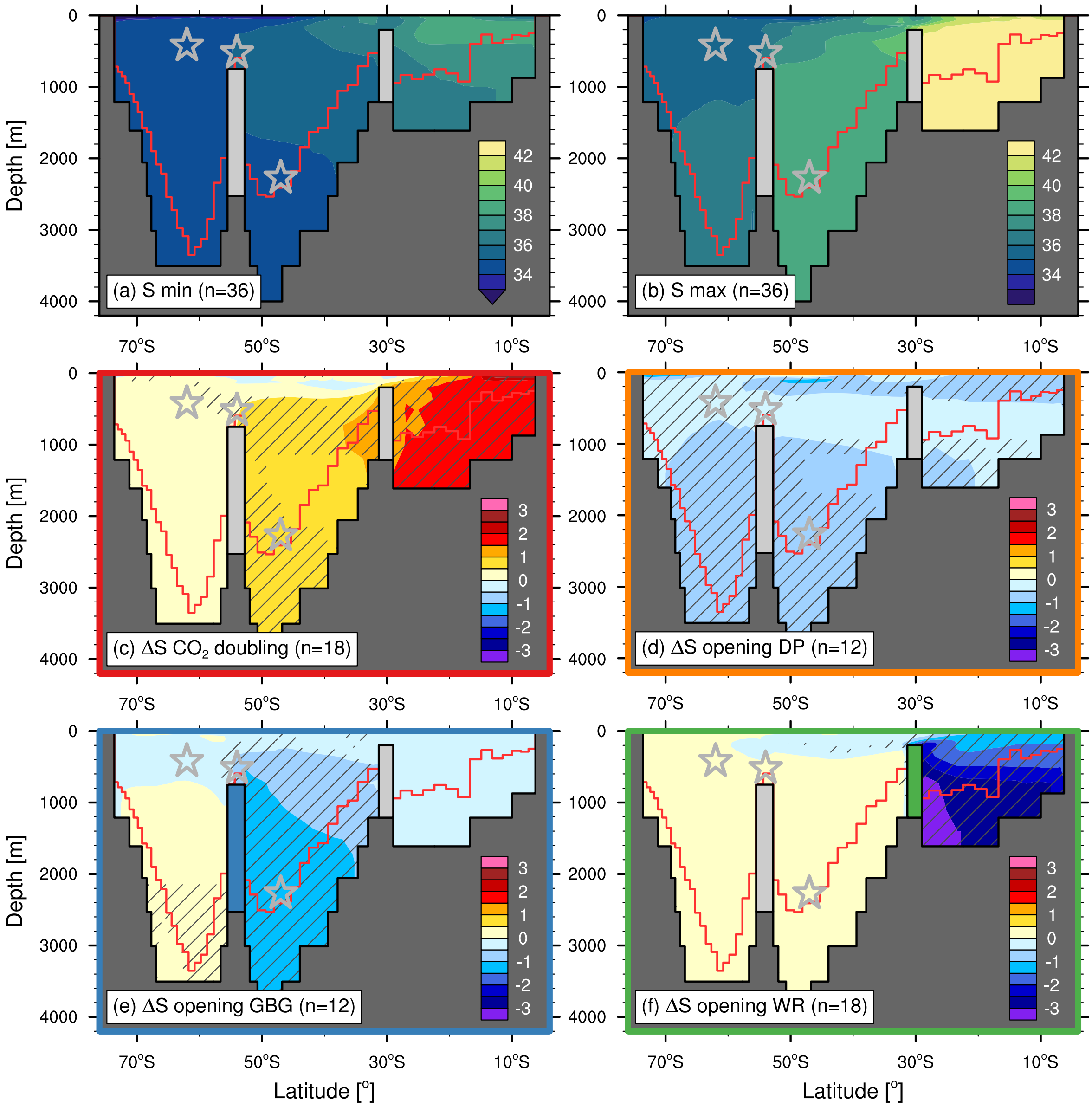

**Figure 4.A4:** Zonal mean salinity sections for the South Atlantic and Southern Ocean. Values are averaged between 30°W and 10°W at the Falkland Plateau and between 30°W and 0° elsewhere. Black (red) lines indicate maximum (average) water depth at the respective latitude. Panels show the (a) minimum and (b) maximum simulated value across all 36 ensemble members and (c-e) the mean change associated with the individual processes defined in Section 4.3.3 of the main text. Hatching indicates areas where all the respective 12 or 18 model responses agree on the sign of the change.

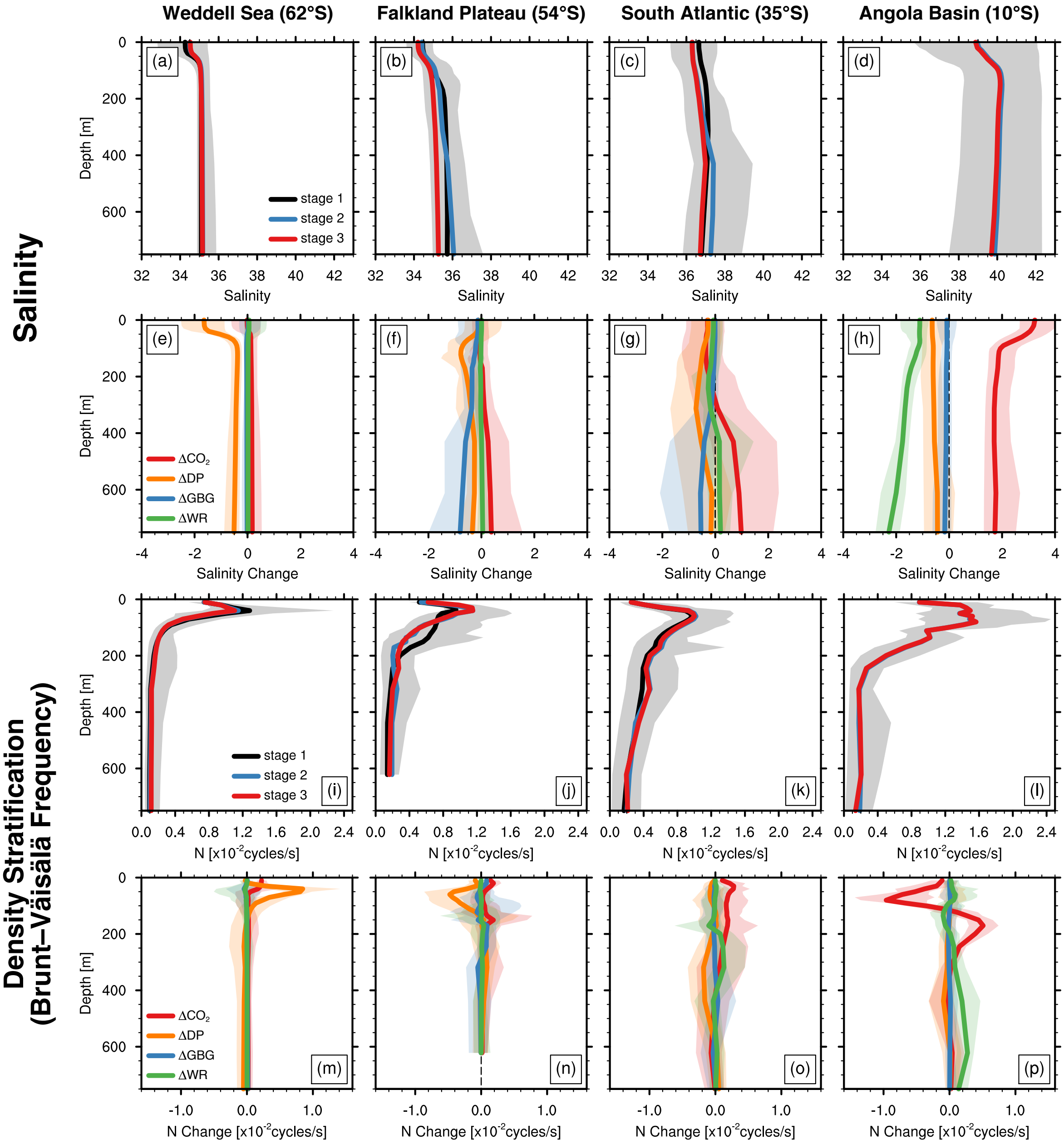

**Figure 4.A5:** Simulated ocean salinity profiles and density stratification across the Southern Ocean and South Atlantic. Density stratification is expressed in terms of the Brunt–Väisälä frequency (buoyancy frequency) defined as: $N = \sqrt{-\frac{g}{\rho_0}\frac{\delta\rho(z)}{\delta z}}$, where $\rho$ is the potential density. Solid lines represent regional averages (areas shown in Fig. 4.1g of the main text), while the shading indicates the simulated maximum and minimum grid point values of the respective area across all simulations. Analysed processes are defined in Section 4.3.3 of the main text. The area used for averaging across the Falkland Plateau Basin in panels (b),(f),(j) and (n) moves westward for each consecutive model stage to allow comparison with the proxy record. N is calculated on model mid depths and therefore only defined to 620 m on the Falkland Plateau. All simulations have a global mean salinity of 35.

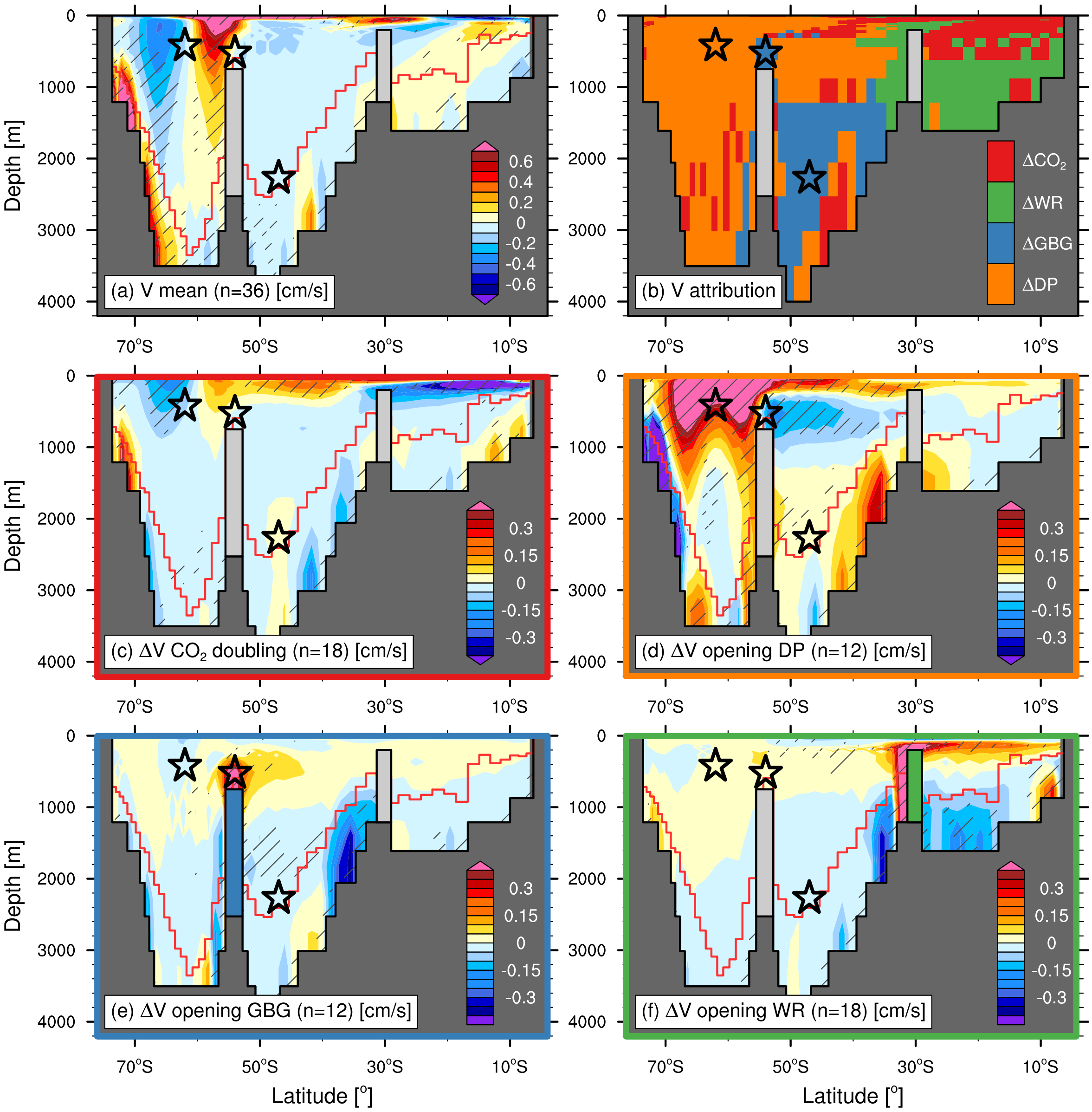

**Figure 4.A6:** Meridional ocean circulation. Panels show the (a) ensemble mean, (b) the respective boundary condition resulting in the largest mean change and (c-f) the mean change associated with the individual processes defined in Section 4.3.3 of the main text. Fields are smoothed with a nine point average for figure clarity and shown in cm/s. Positive (negative) values represent northward (southward) flow. Contour range only shows a subset of the data to focus on changes in the South Atlantic. Hatching indicates region where all ensemble members agree on the sign of the shown field. Black (red) lines indicate maximum (average) water depth at the respective latitude.

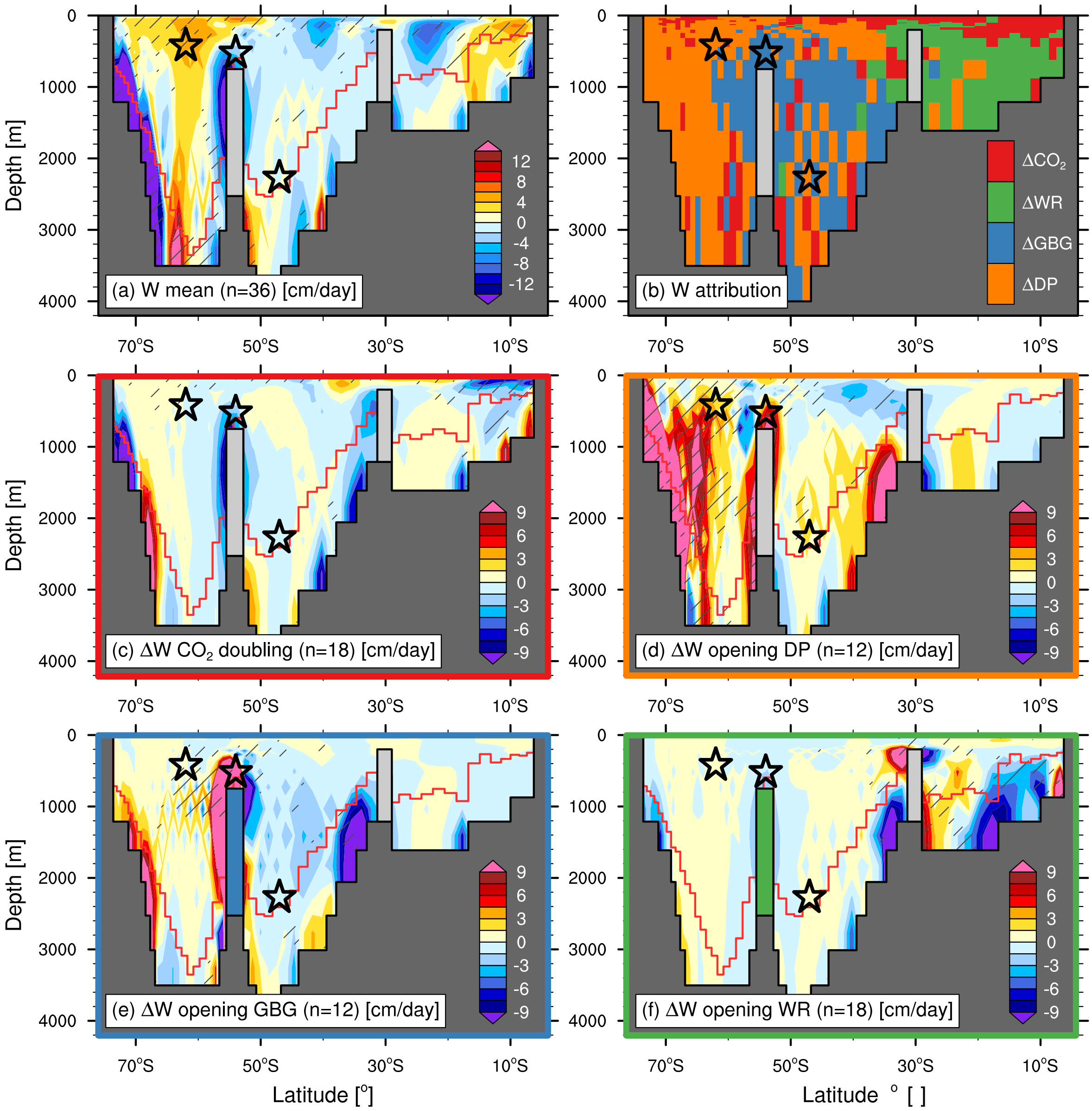

**Figure 4.A7:** Vertical ocean circulation. Panels show the (a) ensemble mean, (b) the respective boundary condition resulting in the largest mean change and (c-f) the mean change associated with the individual processes defined in Section 4.3.3 of the main text. Fields are smoothed with a nine point average for figure clarity and shown in cm/day. Positive (negative) values represent upward (downward) flow. Contour range only shows a subset of the data to focus on changes in the South Atlantic. Hatching indicates region where all ensemble members agree on the sign of the shown field. Black (red) lines indicate maximum (average) water depth at the respective latitude.

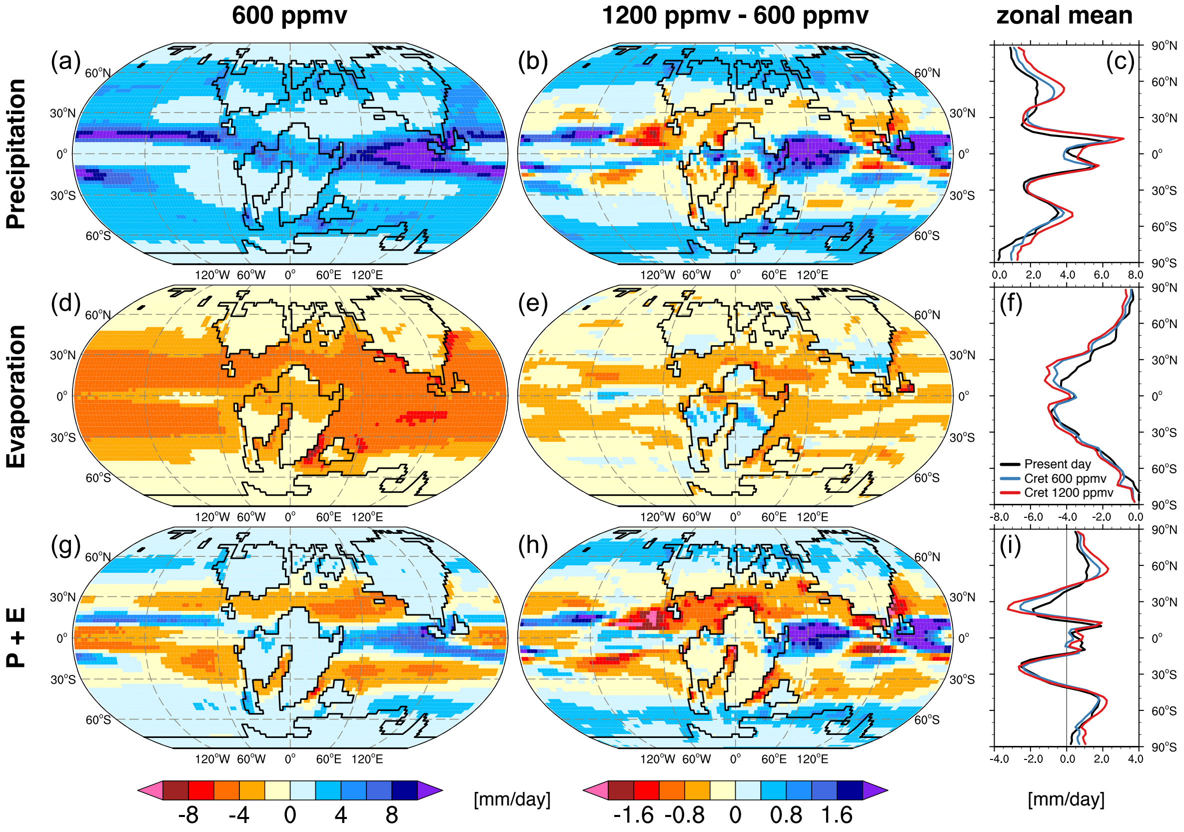

**Figure 4.A8:** $CO_2$ sensitivity of the global hydrological cycle. Panels show ensemble mean (n=18) precipitation, evaporation and the sum of both for (left) 600 ppmv $CO_2$, (middle) the respective change for a doubling of $CO_2$ and (right) the zonal mean values for the 600 and 1200 ppmv ensembles as well as for the same model configuration under present-day boundary conditions. All values are given in mm/day.

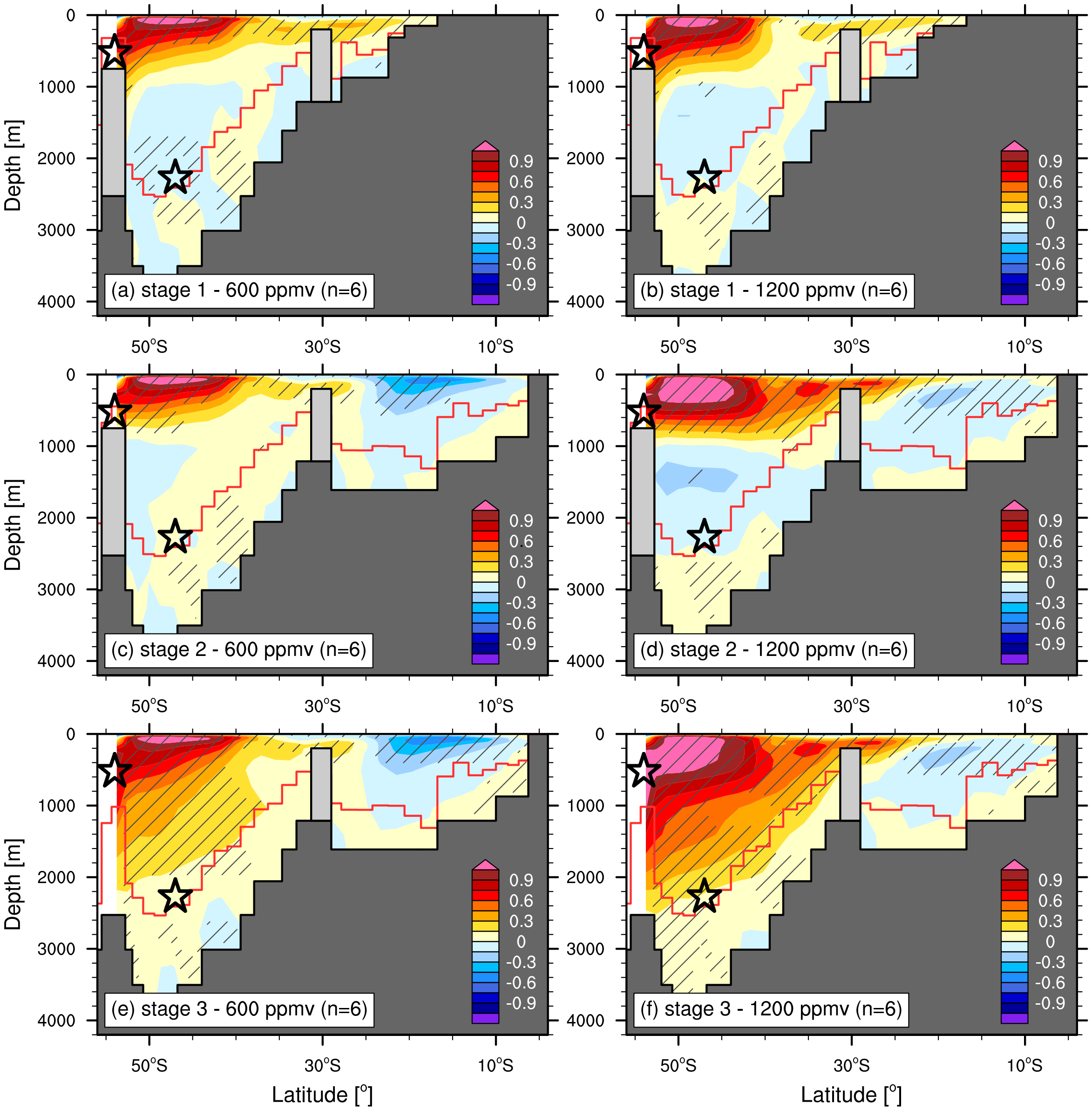

**Figure 4.A9:** South Atlantic meridional overturning circulation (MOC). Panels show the respective ensemble means for stages 1 to 3 integrated at (left) 600 ppmv and (right) 1200 ppmv. Values are in Sv with 1 Sv = $10^6$ $m^3/s$. Positive (negative) values represent clockwise (counterclockwise) circulation. Hatching indicates region where all 6 ensemble members agree on the sign of the MOC. Black (red) lines indicate maximum (average) water depth at the respective latitude.

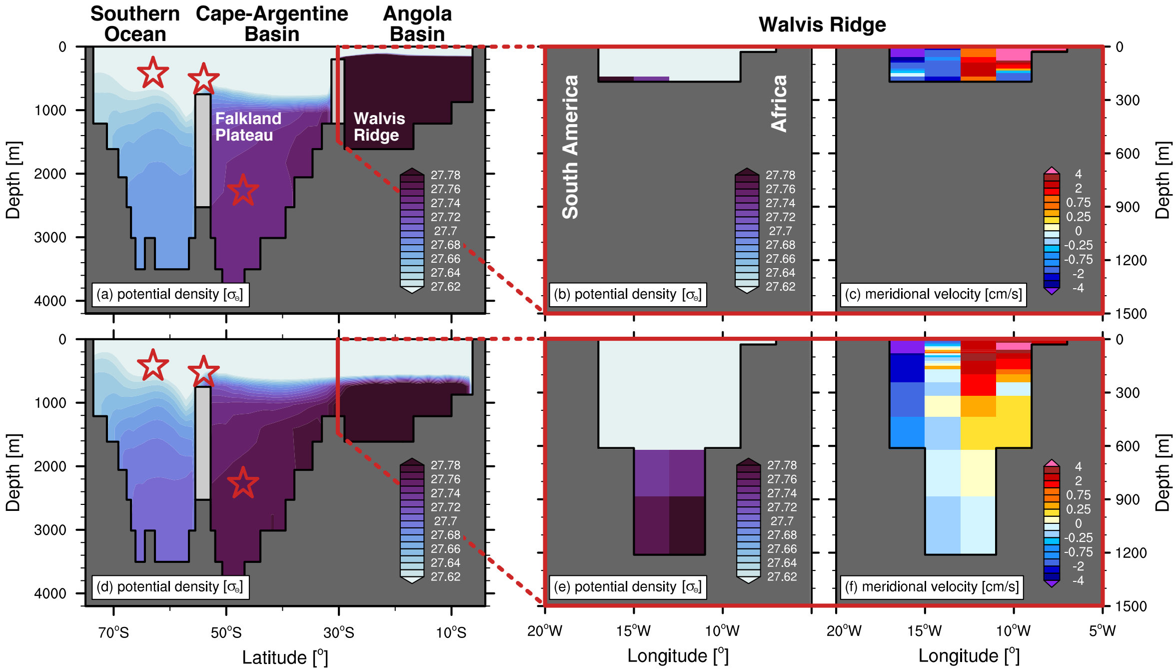

**Figure 4.A10:** Export of Walvis Ridge Overflow Water (WROW). Panels show the stage 2 ensemble mean (a,d) zonal mean potential density as well as the (b,e) potential density and (c,f) meridional velocity across the Walvis Ridge. Upper row is averaged across the 6 ensemble members with a 200 m Walvis Ridge, the lower row shows results for the 6 ensemble members with a 1200 m Walvis Ridge. Zonal mean values are averaged between 30°W and 10°W at the Falkland Plateau and between 30°W and 0° elsewhere. Colormap for potential density only shows a small range of the data to focus on WROW density interval. Contour interval for the meridional velocity is nonlinear.

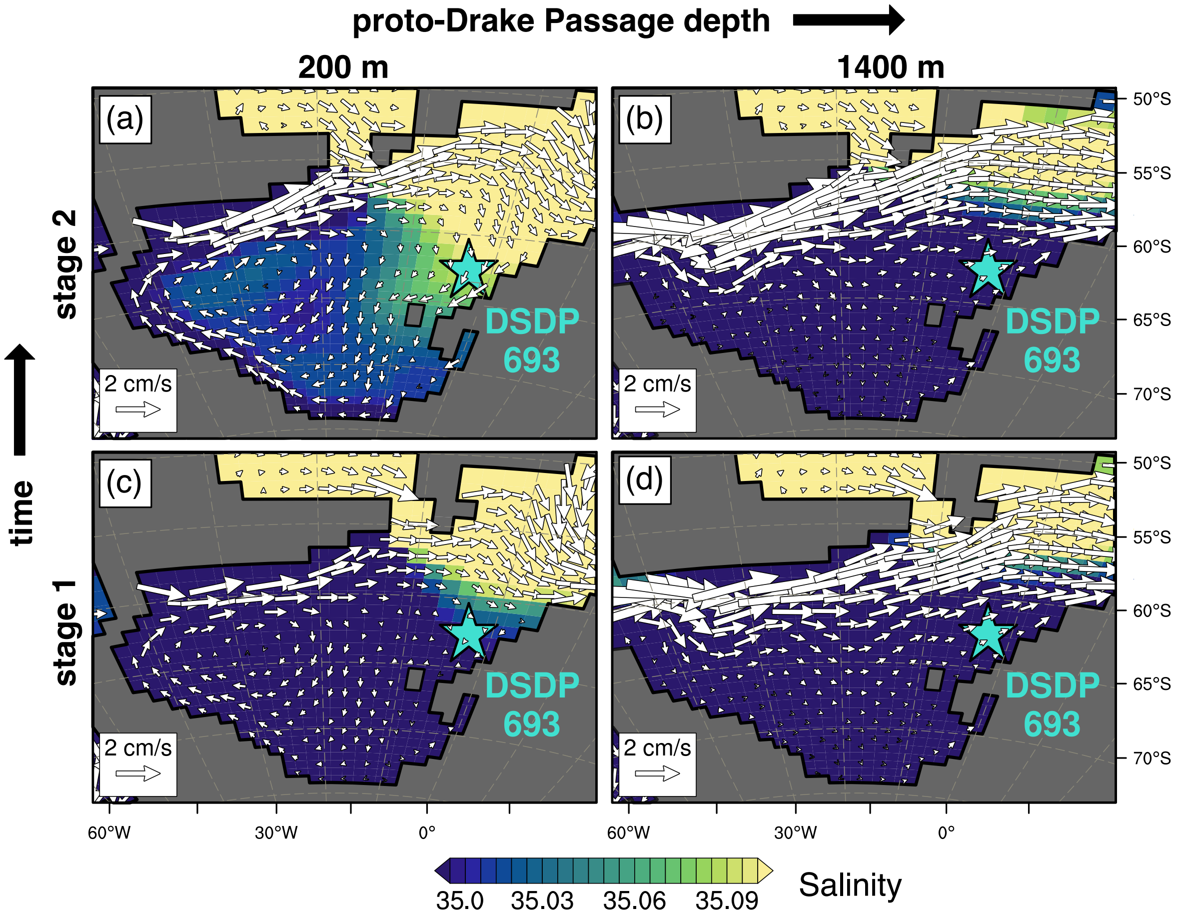

**Figure 4.A11:** Southern Ocean sensitivity to South Atlantic Intermediate Water export. Vectors show ocean velocity in cm/s on contours of salinity, both averaged from 100-600 m. Only grid points with a depth larger than 600 m are shown. Panels depict stages 1 to 2 with DP depths of (left) 200 m and (right) 1400 m. Colormap for salinity only shows a small range of the data to focus on Southern Ocean gradients. Each panel is averaged over 4 ensemble simulations with varying $CO_2$ and WR depth.

# 5 Summary, conclusions and outlook

## 5.1 Summary and conclusions

Our understanding of how the climate system reacts to atmospheric $CO_2$ concentrations significantly above the present-day levels arises solely from examples of past warm periods in the geological record and model-based projections of future warming. As no past greenhouse climate is a perfect analogue to a future anthropogenic warming, a thorough understanding of the processes that characterised the climate sensitivity of individual time periods is a vital step to reduce uncertainties of future warming estimates. The goal of this thesis was to better constrain the main drivers of the Early Cretaceous greenhouse climate and how they differed from our present-day dynamics. To this end, dedicated climate model simulations with Aptian to Albian boundary conditions have been compared to geochemical proxy records of marine surface temperatures, water mass mixing and carbon burial. The main results of this thesis will be summarised by answering the three main research questions of this thesis:

### (1) What controlled the simulated surface temperature distribution during the Early Cretaceous greenhouse?

Climate models still fail to reproduce proxy-predicted polar annual mean temperatures up to 20 °C and single-digit low- to high-latitude temperature gradients, even at the higher end of available $CO_2$ reconstructions. An energy balance flux analysis was applied to new Early Cretaceous climate model simulations to explicitly quantify individual mechanisms that contributed to the surface temperature changes and to increase the comparability of the Early Cretaceous mechanisms to other time slices.

The stronger greenhouse effect under peak OAE 1a $CO_2$ concentrations caused more than 70 % of the overall global mean surface warming of 9.6 °C. The only other significant influence on the global mean temperature was a reduced surface albedo, in consequence of the ice-free land and ocean surface, leading to an additional warming of 2.8 °C. In contrast, the surface albedo changes led to the strongest reduction of the meridional temperature gradient (MTG) due to the pronounced high-latitude warming. The reduced mean elevation of the Antarctic continent further contributed to the enhanced polar warming. In combination, the simulated MTG for the same pre-industrial $CO_2$ level was 24 % lower for the Cretaceous than for the present-day geography. This demonstrates the profound influence of non-$CO_2$ boundary conditions on the simulated surface temperature distribution and needs to be considered for any model-data comparison. The overall meridional heat transport in the ocean and atmosphere was very similar for the present-day and Cretaceous simulations, with the exception of the Arctic Ocean. The Early Cretaceous simulations revealed an increase of local deep water formation and associated oceanic heat advection for higher $CO_2$ concentrations. The resulting influence on the global MTG was low, but important for regional-scale temperatures in the Northern Hemisphere. Furthermore, the onset and strength of deep water formation in the restricted Arctic Ocean basin was sensitive to the applied initial conditions and integration length. This process could therefore contribute to differences in the simulated high-latitude temperatures between different models and spin-up procedures.

While cloud feedbacks did not influence the global mean temperature change, they were the only process strengthening the MTG. The Cretaceous cloud response to enhanced atmospheric $CO_2$ was characterised by a reduced amount of tropical low-level clouds and an increased optical depth of lower high-latitude clouds, especially over the Arctic Ocean. Importantly, the sign and strength of this cloud-induced change of the MTG could be confirmed with a large ensemble of present-day CMIP5 models. Although cloud-related processes continue to be one of the largest sources of intermodel uncertainty, the large-scale mechanisms influencing the latitudinal temperature response to $CO_2$ increases appear to be comparable for both time periods. The overall cloud influence on the Early Cretaceous MTG was even more pronounced than under present-day conditions. The reduced high-latitude surface albedo and increased surface temperatures of the Early Aptian paleogeography were counteracted by a larger polar cloud cover and reduced shortwave heating, even though the seasonal differences of the polar cloud feedbacks were amplified for the Early Cretaceous.

Overall, the results support previous modelling studies showing that the MTG during past greenhouse climates was significantly reduced, but remained above $\sim$20 °C both over land and ocean. Assuming a linear response of the analysed processes, even a further doubling of atmospheric $CO_2$ concentrations to estimated peak mid-Cretaceous levels would not achieve the proxy-derived polar warmth. This misfit implies either an insufficient knowledge of the prevailing boundary conditions, additional feedbacks missing in our current climate models or a warm bias in the proxy-derived temperatures. The latter possibility was addressed in the second main research question of the thesis:

## (2) Can climate models reveal systematic biases in the Early Cretaceous temperature record?

The poor stratigraphic controls for many Aptian-Albian proxy records and the individual uncertainties associated with the different applied techniques make a direct comparison of proxy-derived temperatures with a time-slice simulation difficult. The KCM results were therefore compared to a recent compilation of published TEX$_{86}$-derived temperature records complemented by new data points from the Falkland Plateau. The single-proxy, quality-controlled compilation especially allowed to test the internal consistency of the TEX$_{86}$ record and provided an up-to-date target for the simulated OAE 1a warming.

Reconstructed mean temperatures for commonly applied TEX$_{86}$ calibrations were higher than model-derived ocean temperatures even for the high CO$_2$ simulation. Local temperature offsets of up to 15 °C clearly exceeded the uncertainty ranges associated with both methods. The largest differences between proxy-derived and simulated surface temperatures were found for samples from the young North and South Atlantic, where the restricted circulation led to the evaporatively-driven formation of warm and saline intermediate and deep waters. The simulated oceanographic setting in both basins was more comparable to the present-day Mediterranean and Red Sea than to average open ocean conditions. A similar conclusion could be drawn from the inter-site differences in the isoGDGT fractional abundances that define the resulting TEX$_{86}$ ratio. Samples from the Early Cretaceous North and South Atlantic were characterised by an overall increase in the relative abundances of the crenarchaeol isomer and GDGT-2, while the respective fractional abundances of crenarchaeol were reduced. Based on the combined evidence from the simulated regional circulation and observations of the present-day variability in the TEX$_{86}$ signal formation, the results demonstrate that the oceanographic setting and resulting TEX$_{86}$ export dynamics for large parts of the Early Cretaceous record were probably more similar to the present-day Mediterranean and Red Sea than to the modern global mean conditions. The application of a regional TEX$_{86}$-temperature calibration reduced absolute OAE 1a temperatures for some sites by up to 8 °C. Furthermore, the analysis demonstrated that the anomalous isoGDGT distributions could only be found in Early Cretaceous samples (up to $\sim$100 Ma). It was hypothesised that the progressive opening of the Atlantic Ocean and in particular the establishment of an equatorial connection between the northern and southern basins led to the long-term decline of the salinity-driven intermediate and deep water formation and therefore terminated the Mediterranean-like TEX$_{86}$ signal formation. This would imply that TEX$_{86}$-based reconstructions overestimate the actual surface temperatures for large parts of the Early Cretaceous record.

An important conclusion of the study is that changes in the TEX$_{86}$-temperature relation can occur both on temporal and spatial scales and need to be considered for the reconstruction of absolute temperatures. It was shown that climate model simulations can be a valuable tool to identify spatially-varying modern analogue environments for the TEX$_{86}$ proxy. Accounting for the resulting different TEX$_{86}$-temperature calibrations can help to significantly reduce the apparent model-proxy misfit for OAE 1a temperatures. Given that the physical mechanisms controlling the latitudinal temperature distribution in the KCM experiments were comparable to the CMIP5 results (see question (1)), it can be concluded that the MTG during the Early Aptian OAE 1a was significantly lower than today, but can be reproduced with the current generation of climate models.

Despite the previously discussed long-term maximum in surface temperatures during the onset of OAE 1a, the Aptian was characterised by at least two periods of enhanced carbon burial and associated global-scale cooling events. The simultaneous emergence of the South Atlantic and Southern Ocean in combination with the observed widespread deposition of marine organic-rich black shales raises the question to what extent these young ocean basins might have contributed to the enhanced carbon sequestration and climate perturbations. Changes in the oceanographic conditions are hypothesised to have favoured the transient formation and destruction of regional carbon sinks, which led to the third main research question:

### (3) What controlled the circulation and carbon burial in the Early Cretaceous South Atlantic and Southern Ocean?

This question was addressed by the close integration of dedicated climate model simulations and geochemical data generated within the joint project. Based on the reconstructed circulation history, three idealised stages have been defined to implement the progressive opening of the Falkland Plateau and Georgia Basin Gateway in the KCM. Additionally, multiple ensembles were simulated for each stage to assess the influence of the large uncertainties in key boundary conditions on the simulated circulation changes. Explicitly, the simulations were repeated with different depths of the proto-Drake Passage and the Walvis Ridge as well as with two atmospheric $CO_2$ level endmembers.

The meridional overturning in the South Atlantic was driven by strong evaporation in subtropical latitudes and subsequent salinity-driven formation of intermediate waters. This southward subsurface flow of warm and saline waters was balanced by a northward advection of cold and fresh surface waters from the Southern Ocean. The formation region and subsurface export is supported by the transient occurrence of radiogenic neodymium isotope signatures in the Falkland Basin. Even though each of the total 36 ensemble simulations represented a valid realisation within the limits of the Aptian-Albian boundary conditions, the spread in simulated temperatures between individual ensemble members was locally as high as 15 °C. This demonstrates that the influence of the boundary condition uncertainties increases significantly on smaller geographical scales and needs to be considered in the interpretation of local proxy records. The atmospheric freshwater balance and oceanic surface circulation in the northern Angola Basin showed a high sensitivity to the applied $CO_2$ forcing. The closely related changes in the water column stratification imply a possible control on the observed variability in local organic carbon burial. Furthermore, all experiments indicated the formation of the densest water masses in the highly restricted Angola Basin. The simulated export of this potentially anoxic water mass across the Walvis Ridge supports earlier hypotheses about the importance of overflow waters in maintaining black shale deposition in the deep Cape Basin. The circulation and convection strength in the Southern Ocean was primarily governed by the depth of the proto-Drake Passage. The test of different circulation scenarios for the Weddell Sea against the geochemical record allowed to constrain the most likely depth of the proto-Drake Passage during the Aptian to Albian to $\sim$200 m. Due to the demonstrated influence of the proto-Drake Passage on the global ocean circulation, this result will ultimately improve the model-proxy comparability during the Early Cretaceous. Under this shallower gateway depth, the Weddell Sea convection increased in response to the Falkland Plateau opening and associated salinity advection. The simulations therefore provide an explanation for the reconstructed end of local gray shale deposition.

Overall, the model-proxy synthesis demonstrates the strong geographic controls on the regional circulation. The opening of the Falkland Plateau initiated convection and ventilation of the Southern Ocean, while the opening of the Georgia Basin Gateway enabled deep water exchange between the South Atlantic and Southern Ocean that terminated the black shale deposition in the Cape Basin.

## 5.2 A final remark on evolving ocean basins in the Early Cretaceous greenhouse

One of the goals of this thesis was to identify the characteristic features of the Early Cretaceous climate system that influenced the response to the increased greenhouse gas forcing. In other words, what was similar and what was different to the present-day system? This thesis shows that the simulated changes in the atmospheric radiation balance can, at least as a first-order approximation, be separated in a greenhouse and geographical contribution that allow a direct comparison to the present-day dynamics. In contrast, the largest differences are simulated for the Cretaceous ocean circulation. One feature that emerged in all three chapters are evolving ocean basins. The combination of restricted horizontal circulation due to the presence of narrow gateways in the early stages of seafloor spreading and reduced vertical movement in response to the strong greenhouse forcing led to special oceanographic conditions that influenced the analysis throughout this thesis, but in very diverse ways. Chapter 2 highlighted the close relation between deep water formation in the restricted Arctic Ocean and the amount of poleward oceanic heat transport in the Northern Hemisphere. The larger freshwater inputs in consequence of the enhanced hydrological cycle and limited lateral advection from the proto-North Pacific increased the sensitivity of the local convection strength to the atmospheric $CO_2$. Chapter 3 showed that the restriction of the Early Cretaceous North and South Atlantic led to the formation of warm and saline deep waters that potentially influenced the ecological controls on the $TEX_{86}$ temperature proxy. As over 80% of all Early Cretaceous $TEX_{86}$ data are derived from these young basins, the revealed warm bias has implications for our general view of the Cretaceous temperature evolution. Finally, chapter 4 demonstrated how the evolution of marine gateways in the South Atlantic and Southern Ocean ultimately controlled the regional organic carbon burial during the Aptian and Albian.

Evolving and restricted ocean basins are therefore certainly one of the most characteristic features of the Early Cretaceous climate system. This thesis also shows that they are especially difficult to represent in coupled climate models. The slow water mass renewal in the deeper parts of the basins require extended model spin-ups and make the simulation results sensitive to the choice of initial conditions and applied gateway geometries. The results also raise the question to what extent the basins of the Early Cretaceous North and South Atlantic might be an analogue for restricted basins in the current or future climate system. The deep waters in the modern Mediterranean Sea are well oxygenated, even though the large-scale circulation seems to be comparable to the Aptian to Albian South Atlantic, which was characterised by widespread bottom water anoxia. On the other hand, the geological record also provides evidence for periods of enhanced preservation of organic-rich sediments in the eastern Mediterranean Sea (Calvert et al., 1992; Rohling, 1994). Therefore, an improved understanding of what secondary influences besides the geographical restriction promotes the formation of oxygen-depleted deep waters and burial of organic carbon burial is a key to predict any future changes in our present-day semi-enclosed seas. The young ocean basins of the Early Cretaceous continue to be one of the best opportunities to reveal these underlying dynamics.

## 5.3 Outlook

This thesis addressed two general aspects the Early Cretaceous climate system. While chapters 2 and 3 addressed the causes and strength of the mean state OAE 1a warming, chapter 4 aimed to assess the transient circulation and carbon burial changes in the South Atlantic and Southern Ocean and to provide the physical reasoning behind the reconstructed opening history. The logical next step to understand the global significance of the results of this thesis is to estimate the potential influence of the regional carbon burial changes on the reconstructed carbon cycle perturbations and the global climate trends during the Early Cretaceous. To this end, a biogeochemical box model will be applied to quantify changes in key biogeochemical parameters associated with the proposed opening history that can be directly compared to the geochemical data. The presented ensemble approach in combination with the stratigraphic framework will explicitly allow to quantify the uncertainties in the simulated carbon burial changes.

The comparison of the climate model simulations with the $TEX_{86}$ compilation in chapter 3 revealed the presence of the anomalous isoGDGT distributions for the whole Early Cretaceous. Even if the signal was not detectable for the Late Cretaceous, the proposed mechanism might have also affected other time periods. Differences in the isoGDGT distribution and temperature offsets to other proxy techniques have also been reported for the Pliocene-Pleistocene Mediterranean Sea (Polik et al., 2018). The analysis indicates that the combination of a restricted ocean circulation and high atmospheric $CO_2$ will be the most likely combination to produce Mediterranean-like $TEX_{86}$ export dynamics and could therefore also influence other past greenhouse intervals. A special focus should lie on a comparison to temperature reconstructions derived from other proxy methods to better constrain the magnitude of any potential $TEX_{86}$ warm bias.

The validity of the energy balance model results presented in chapter 2 would also greatly benefit from an expansion to other time slices, as already done for the Eocene (Heinemann et al., 2009; Lunt et al., 2012). The quantification of individual controls on the meridional temperature gradient for several greenhouse intervals might help to increase the signal-to-noise ratio for the separation of the time-slice dependent dynamics from the invariant part that will most likely also influence the future anthropogenic warming.

## References

Calvert, S. E., B. Nielsen, and M. R. Fontugne (1992). “Evidence from nitrogen isotope ratios for enhanced productivity during formation of eastern Mediterranean sapropels”. In: *Nature* 359.6392, pp. 223–225. DOI: `10.1038/359223a0`.

Heinemann, M, J H Jungclaus, and J Marotzke (2009). “Warm Paleocene/Eocene climate as simulated in ECHAM5/MPI-OM”. In: *Clim. Past* 5.1987, pp. 785–802. DOI: `10.5194/cp-5-785-2009`.

Lunt, D. J., T. Dunkley Jones, M. Heinemann, M. Huber, A. LeGrande, A. Winguth, C. Loptson, J. Marotzke, C. D. Roberts, J. Tindall, P. Valdes, and C. Winguth (2012). “A model-data comparison for a multi-model ensemble of early Eocene atmosphere-ocean simulations: EoMIP”. In: *Climate of the Past* 8.5, pp. 1717–1736. DOI: `10.5194/cp-8-1717-2012`.

Polik, Catherine A., Felix J. Elling, and Ann Pearson (2018). “Impacts of Paleoecology on the TEX86 Sea Surface Temperature Proxy in the Pliocene-Pleistocene Mediterranean Sea”. In: *Paleoceanography and Paleoclimatology* 33.12, pp. 1472–1489. DOI: `10.1029/2018PA003494`.

Rohling, Eelco J (1994). “Review and new aspects concerning the formation of eastern Mediterranean sapropels”. In: *Marine Geology* 122.1-2, pp. 1–28. DOI: `10.1016/0025-3227(94)90202-X`.

# Acknowledgements

First of all, I want to thank Sascha Flögel for not only guiding my research over the last three and a half years, but especially for sharing his enthusiasm for the Cretaceous with me. His door was *always* open and countless open-minded discussions did not only spark my fascination for the world of ancient greenhouse climates but also enriched my way of thinking outside of science. I am very grateful to Martin Frank for supervising this thesis and for "adopting" a climate modeller. He made me feel at home in the Paleoceanography department even though I had no idea what everyone was talking about. I also want to thank Birgit Schneider for agreeing to examine this thesis. Without her commitment it would not have been possible to maintain the schedule.

I am especially grateful to Wonsun Park for supporting me since my bachelor studies. His patience and trust during my very first "HiWi" job allowed me discover my passion for climate modelling and "number crunching", while his work on the Cretaceous model set-up gave me a head start for this thesis.

This work would not have been possible without the fruitful and entertaining discussions with my project partners Wolf Dummann, Peter Hofmann, Jens Herrle, Thomas Wagner and Stephanie Kusch. Thank you Wolf for your detailed and patient explanations of your tremendous amounts of data to a chemistry dummy. I learned a lot and the whole project benefitted from your genuine interest to combine our two different approaches.

Special thanks go to Jacky for being such a highly professional office colleague. I really enjoyed the entertaining lunch and coffee breaks with Katriina, Lisa, Peer and Steffen and am grateful to all colleagues that made the department an all-around positive environment.

I thank the German Research Foundation (DFG) for funding this research (FL378/1-1 and FL378/1-2) and the Integrated School of Ocean Sciences (ISOS) for additional funds to attend workshops, conferences and a summer school.

I want to thank my parents for always supporting my decisions and for just so much more. Finally, none of this would have been possible without the love, patience and continued support from my girlfriend Yvonne.

# Erklärung

Hiermit erkläre ich an Eides statt, dass ich die Abhandlung - abgesehen von der Beratung durch meine Betreuer - nach Inhalt und Form eigenständig erarbeitet habe und keine weiteren Quellen und Hilfsmittel als die angegebenen verwendet habe. Die Arbeit wurde weder ganz noch in Teilen einer anderen Stelle im Rahmen eines Prüfungsverfahrens vorgelegt. Teile dieser Arbeit wurden zur Veröffentlichung eingereicht und kenntlich gemacht. Die Arbeit ist unter Einhaltung der Regeln guter wissenschaftlicher Praxis der Deutschen Forschungsgemeinschaft entstanden. Mir wurde kein akademischer Grad entzogen.

Kiel, Juni 2019

Sebastian Steinig